

AN ABSTRACT OF THE THESIS OF

Tracey Spoerer for the degree of Master of Science in Nuclear Engineering presented on June 3, 2022.

Title: Control Rod Shadowing Effects in Control Rod Calibrations of The Oregon State TRIGA® Reactor.

Abstract approved:

Steven Reese

Control rod calibration experiment results for the Oregon State TRIGA® Reactor (OSTR) immediately following LEU conversion in 2008, and MCNP® 5 predicted rod worths from the 2008 LEU Conversion Safety Analysis Report (CSAR) are discussed. The reactivity worth of the four OSTR control rods are measured using the rod-pull method. Reactor power and period measurements in this method rely on the fission chamber power detector on the North side of the reflector. It is proposed that the location of the fission chamber gives rise to a phenomenon known as control rod shadowing, or an inaccurate reactor period measurement due to the asymmetry of the neutron flux distribution in the OSTR core. The effect or asymmetry of the flux is believed to be more pronounced during super-criticality, resulting in error in the time-of-power-rise measurements. As a result, control rod calibration experiments may under-predict or over-predict the reactivity worth of certain control rods. A time-independent Monte-Carlo method for the quantification of control rod shadowing is developed and validated. Thermal flux maps at core axial mid-plane are obtained from the model to inform discrepancies between predicted and observed results.

©Copyright by Tracey Spoerer

June 3, 2022

All Rights Reserved

Control Rod Shadowing Effects in Control Rod Calibrations of The Oregon State TRIGA® Reactor

by

Tracey Spoerer

A THESIS

submitted to

Oregon State University

in partial fulfillment of

the requirements for the

degree of

Master of Science

Presented June 3, 2022

Commencement June 2022

Master of Science thesis of Tracey Spoerer presented on June 3, 2022.

APPROVED:

Major Professor, representing Nuclear Engineering

Head of the School of Nuclear Science & Engineering

Dean of the Graduate School

I understand that my thesis will become part of the permanent collection of Oregon State University libraries. My signature below authorizes release of my thesis to any reader upon request.

Tracey Spoerer, Author

ACKNOWLEDGEMENTS

This work, and the journey that resulted in it, would not be possible without the endless support and encouragement I have received from all my friends, my family, and my colleagues. This list of acknowledgments is extensive, but by no means complete. This work is the result of the efforts of many people, and an innumerable amount of kind actions and charities. The Oregon State University (OSU) School of Nuclear Science & Engineering (NSE), the OSU Radiation Center (RC), and OSU TRIGA® Reactor (OSTR) have been an inviting and accepting community that generously offered me every opportunity to succeed. The OSU NSE faculty, advisors and staff go above and beyond every day to mentor undergraduate and graduate students alike. I hope that this work is becoming of the immense support and patience OSU NSE faculty and staff have had for me over the years.

I want to thank all my lifelong friends from before I arrived at OSU Corvallis in 2017 that helped see me through my early twenties, my enlistment in the United States Army and Operation Enduring Freedom XVIII. I want to also thank all my friends and colleagues at the Oregon Department of Fish and Wildlife (ODFW) who took a chance on hiring a wayward veteran who was looking for a meaningful job outdoors. My summer position working for the ODFW Corvallis Laboratory from 2016-2018 performing juvenile salmonid habitat surveys throughout Oregon provided me the opportunity to find and reinvent myself. A very special thanks goes out to fisheries biologist Andrew Chione, my 2016 survey partner and a true friend. He never let me quit, and we have seen some of the most spectacular features Oregon and Northern California have to offer. No other person has done more to shape my view of the natural world.

I would not be writing this today without the encouragement, support and efforts of the faculty and staff of Central Oregon Community College (COCC) in Bend, Oregon. They showed me it was possible for me to succeed, and that engineering and science were not out of my reach. Dr. Wendi Wampler has been especially influential, and I cannot express enough gratitude for her kind mentorship and sound advice. I certainly would not be here today without her world-class teaching and physics education skills.

This work would also not be possible without the endless support and help the RC and OSTR staff have given me as both an undergraduate and graduate student. Thank you to Robert Schickler, Celia Oney and Chris Kulah for generously devoting their time to train and mentor me as both a Reactor Operator and Senior Reactor Operator at OSTR. I would especially like to thank Robert Schickler giving

me access to resources that have expedited my research. This work would not be possible without the countless kind acts of the RC staff.

I have been fortunate in having two wonderful mentors who have guided me through graduate school. Dr. Steven Reese and Dr. Tianyi Chen have been nothing short of exceptional mentors and advisors and I have learned more in the past two years than I have in the previous ten years. Both have provided me with amazing opportunities and all the tools I've needed to succeed.

Finally, I would like to express my deepest gratitude and love to my parents, Thomas and Laura Spoerer, whose undying love, patience, and support have made this all possible. They do not give themselves enough credit for how amazing of parents they have been since day one. They always help get me back on track when life goes wrong and have done more than most would to put success within my reach. I love both of you and this work is the result of all your efforts.

And to Nicholas Thompson, for being my best friend though all of it.

TABLE OF CONTENTS

	Page
1.0 Introduction	1
1.1 Research Objective	1
1.1.1 Scope	2
1.1.2 Objective.....	3
1.2 Oregon State University TRIGA® Reactor (OSTR) Background	3
1.2.1 OSTR Description	3
1.2.2 OSTR Core Configurations Post-LEU Conversion	4
1.2.3 Control Rod Calibrations at OSTR	5
1.3 The OSTR MCNP® Model.....	6
1.3.1 The OSTR MCNP® Model as Provided	6
1.3.2 Modifications Made to The Model for This Work.....	6
2.0 Literature Review	7
2.1 The Oregon State TRIGA® Reactor (OSTR)	7
2.1.1 General Atomics TRIGA® Reactors.....	7
2.1.2 Description of the OSTR	13
2.1.3 Description of the OSTR core configuration at time of LEU conversion	17
2.1.4 Differences in control rod materials	18
2.2 Control Rod Calibrations	21
2.2.1 Purpose of control rod calibrations	21
2.2.2 Description of the rod-drop method.....	21
2.2.3 Description of the rod-pull calibration method.....	22
2.2.5 Description of control rod calibration procedures at OSTR	23
2.2.6 Results of first control rod calibration after LEU conversion.....	24
2.3 Power Detectors	25
2.3.1 Operating principles of compensated and uncompensated ion chambers	25

TABLE OF CONTENTS (Continued)

	Page
2.3.2 Description of the OSTR uncompensated ion chambers.....	27
2.3.4 Operating principle of fission chamber detectors	28
2.3.5 Description of the OSTR fission chamber	29
2.4 The Control Rod Shadowing Phenomenon	30
2.4.1 Description of the rod shadowing effect.....	30
3.0 Materials and Methods.....	31
3.1 The OSTR MCNP® Model.....	31
3.1.1 Model description.....	32
3.1.2 Normal Core Geometry	33
3.1.3 CLICIT Core Geometry	33
3.2 Fission Chamber Geometry and Materials.....	33
3.2.1 Geometry description	33
3.2.2 Components Included in The Model	34
3.2.3 Placement of fission chambers	35
3.3 Fission Chamber Materials.....	37
3.3.1 Description of materials as advertised.....	37
3.3.2 Modeled materials.....	37
3.3.3 $^{235}\text{UO}_2$ layer thickness calculation	37
3.4 Fission Chamber Tally Specifications	38
3.4.1 Tallied Events.....	38
3.4.2 Tallied Cells	38
3.4.3 Multiplier card	38
3.5 Flux Map Tally Specifications.....	39
3.5.1 Tallied Cells	39
3.5.2 Energy Bins	39

TABLE OF CONTENTS (Continued)

	Page
3.6 Flux Map Interpolation.....	39
3.7 Startup Logs.....	40
3.7.1 Critical rod heights	40
3.7.2 Control rod calibration heights.....	43
3.7.3 The Inhour Equation.....	46
3.7.4 Reactor period calculation.....	46
3.7.5 Reactivity worth calculation	47
3.8 Model Bias Calculation.....	48
3.9 Calculated Control Rod Worth	48
3.9.1 Modeled Control Rod Calibrations.....	48
3.9.2 K-code Specifications	48
3.10 Variance Reduction Method.....	49
4.0 Results/Discussion	50
4.1 Experimental Control Rod Calibrations.....	50
4.1.1 Normal Core Control Rod Calibrations.....	50
4.1.2 CLICIT Core Control Rod Calibrations	52
4.2 Model Bias Calculations.....	54
4.2.1 Normal Core Model Bias Calculation	54
4.2.2 CLICIT Core Model Bias Calculation	57
4.3 MCNP Calculated Control Rod Worths	59
4.3.1 Normal Core Calculated Control Rod Worths.....	59
4.3.2 CLICIT Core Calculated Control Rod Worths.....	62
4.4 Detector Responses	65
4.4.1 Normal Core Detector Responses	65
4.4.2 CLICIT Core Detector Responses	84

TABLE OF CONTENTS (Continued)

	Page
4.4.3 Detector Response Discussion.....	102
4.5 Flux Maps	103
4.5.1 Normal Core Flux Maps.....	103
4.5.2 CLICIT Core Flux Maps	117
4.5.3 Flux Map Discussion.....	129
4.6 Total Rod Worth Comparisons	132
4.6.1 Normal Core Comparisons.....	133
4.6.2 CLICIT Core Comparisons.....	134
4.6.3 Subcritical Experimental Validation	135
5.0 Conclusion.....	137
6.0 References.....	140

LIST OF FIGURES

Page

Figure 1: 2008 LEU normal core configuration.	4
Figure 2: 2008 LEU CLICIT core configuration.	5
Figure 3:TRIGA® fuel element [13].	10
Figure 4: Axial cross section of a TRIGA® Mk. II bioshield [19].	12
Figure 5: Radial cross section of a TRIGA® Mk. II bioshield [19].	12
Figure 6: The OSTR core and reflector assembly [19].	13
Figure 7: Axial reflector assembly schematic [20]....	15
Figure 8: OSTR core and reflector assembly schematic [20].	15
Figure 9: OSTR upper grid plate schematic [20]....	16
Figure 10: 2008 LEU Normal core configuration.	17
Figure 11: 2008 LEU CLICIT core configuration.	18
Figure 12: Radial cross section of an uncompensated ion chamber [31]....	27
Figure 13: Mirion WL-8075 uncompensated ion chamber schematic [33].	28
Figure 14: Reuter-Stokes SA-C3-2510-114 fission chamber schematic [35]....	29
Figure 15: Visualization of the as-provided OSTR model.....	32
Figure 16: OSTR radial core and reflector assembly schematic [20].	36
Figure 17: Modeled fission chamber placement.....	36
Figure 18: Measured and calculated normal core transient rod worth.	59
Figure 19: Measured and calculated normal core safety rod worth.	60
Figure 20: Measured and calculated normal core shim rod worth.	60
Figure 21: Measured and calculated normal core regulating rod worth.	61
Figure 22: Measured and calculated CLICIT core transient rod worth.	62
Figure 23: Measured and calculated CLICIT core safety rod worth.	63
Figure 24: Measured and calculated CLICIT core shim rod worth.	63
Figure 25: Measured and calculated CLICIT core regulating rod worth.	64
Figure 26: Integrated transient rod worth and fission rate in the 348.2° detector.	66
Figure 27: Integrated transient rod worth and fission rate in the 8.2° detector.	66
Figure 28: Integrated transient rod worth and fission rate in the 28.2° detector.	67
Figure 29: Integrated transient rod worth and fission rate in the 148.2° detector.	67
Figure 30: Integrated transient rod worth and fission rate in the 168.2° detector.	68
Figure 31: Integrated transient rod worth and fission rate in the 188.2° detector.	68

LIST OF FIGURES (Continued)

Page

Figure 32: Integrated transient rod worth and fission rate in the 208.2° detector.	69
Figure 33: Integrated transient rod worth and fission rate in the 308.2° detector.	69
Figure 34: Integrated transient rod worth and fission rate in the 328.2° detector.	70
Figure 35: Integrated safety rod worth and fission rate in the 348.2° detector.	70
Figure 36: Integrated safety rod worth and fission rate in the 8.2° detector.	71
Figure 37: Integrated safety rod worth and fission rate in the 28.2° detector.	71
Figure 38: Integrated safety rod worth and fission rate in the 148.2° detector.	72
Figure 39: Integrated safety rod worth and fission rate in the 168.2° detector.	72
Figure 40: Integrated safety rod worth and fission rate in the 188.2° detector.	73
Figure 41: Integrated safety rod worth and fission rate in the 208.2° detector.	73
Figure 42: Integrated safety rod worth and fission rate in the 308.2° detector.	74
Figure 43: Integrated safety rod worth and fission rate in the 328.2° detector.	74
Figure 44: Integrated shim rod worth and fission rate in the 348.2° detector.	75
Figure 45: Integrated shim rod worth and fission rate in the 8.2° detector.	75
Figure 46: Integrated shim rod worth and fission rate in the 28.2° detector.	76
Figure 47: Integrated shim rod worth and fission rate in the 148.2° detector.	76
Figure 48: Integrated shim rod worth and fission rate in the 168.2° detector.	77
Figure 49: Integrated shim rod worth and fission rate in the 188.2° detector.	77
Figure 50: Integrated shim rod worth and fission rate in the 208.2° detector.	78
Figure 51: Integrated shim rod worth and fission rate in the 308.2° detector.	78
Figure 52: Integrated shim rod worth and fission rate in the 328.2° detector.	79
Figure 53: Integrated regulating rod worth and fission rate in the 348.2° detector.	79
Figure 54: Integrated regulating rod worth and fission rate in the 8.2° detector.	80
Figure 55: Integrated regulating rod worth and fission rate in the 28.2° detector.	80
Figure 56: Integrated regulating rod worth and fission rate in the 148.2° detector.	81
Figure 57: Integrated regulating rod worth and fission rate in the 168.2° detector.	81
Figure 58: Integrated regulating rod worth and fission rate in the 188.2° detector.	82
Figure 59: Integrated regulating rod worth and fission rate in the 208.2° detector.	82
Figure 60: Integrated regulating rod worth and fission rate in the 308.2° detector.	83
Figure 61: Integrated regulating rod worth and fission rate in the 328.2° detector.	83
Figure 62: Integrated transient rod worth and fission rate in the 348.2° detector.	84

LIST OF FIGURES (Continued)

Page

Figure 63: Integrated transient rod worth and fission rate in the 8.2° detector.	85
Figure 64: Integrated transient rod worth and fission rate in the 28.2° detector.	85
Figure 65: Integrated transient rod worth and fission rate in the 148.2° detector.	86
Figure 66: Integrated transient rod worth and fission rate in the 168.2° detector.	86
Figure 67: Integrated transient rod worth and fission rate in the 188.2° detector.	87
Figure 68: Integrated transient rod worth and fission rate in the 208.2° detector.	87
Figure 69: Integrated transient rod worth and fission rate in the 308.2° detector.	88
Figure 70: Integrated transient rod worth and fission rate in the 328.2° detector.	88
Figure 71: Integrated safety rod worth and fission rate in the 348.2° detector.	89
Figure 72: Integrated safety rod worth and fission rate in the 8.2° detector.	89
Figure 73: Integrated safety rod worth and fission rate in the 28.2° detector.	90
Figure 74: Integrated safety rod worth and fission rate in the 148.2° detector.	90
Figure 75: Integrated safety rod worth and fission rate in the 168.2° detector.	91
Figure 76: Integrated safety rod worth and fission rate in the 188.2° detector.	91
Figure 77: Integrated safety rod worth and fission rate in the 208.2° detector.	92
Figure 78: Integrated safety rod worth and fission rate in the 308.2° detector.	92
Figure 79: Integrated safety rod worth and fission rate in the 328.2° detector.	93
Figure 80: Integrated shim rod worth and fission rate in the 348.2° detector.	93
Figure 81: Integrated shim rod worth and fission rate in the 8.2° detector.	94
Figure 82: Integrated shim rod worth and fission rate in the 28.2° detector.	94
Figure 83: Integrated shim rod worth and fission rate in the 148.2° detector.	95
Figure 84: Integrated shim rod worth and fission rate in the 168.2° detector.	95
Figure 85: Integrated shim rod worth and fission rate in the 188.2° detector.	96
Figure 86: Integrated shim rod worth and fission rate in the 208.2° detector.	96
Figure 87: Integrated shim rod worth and fission rate in the 308.2° detector.	97
Figure 88: Integrated shim rod worth and fission rate in the 328.2° detector.	97
Figure 89: Integrated regulating rod worth and fission rate in the 348.2° detector.	98
Figure 90: Integrated regulating rod worth and fission rate in the 8.2° detector.	98
Figure 91: Integrated regulating rod worth and fission rate in the 28.2° detector.	99
Figure 92: Integrated regulating rod worth and fission rate in the 148.2° detector.	99
Figure 93: Integrated regulating rod worth and fission rate in the 168.2° detector.	100

LIST OF FIGURES (Continued)

Page

Figure 94: Integrated regulating rod worth and fission rate in the 188.2° detector.	100
Figure 95: Integrated regulating rod worth and fission rate in the 208.2° detector.	101
Figure 96: Integrated regulating rod worth and fission rate in the 308.2° detector.	101
Figure 97: Integrated regulating rod worth and fission rate in the 328.2° detector.	102
Figure 98: Normal core axial mid-plane thermal flux map for transient rod pull 1 configuration.....	104
Figure 99: Normal core axial mid-plane thermal flux map for transient rod pull 2 configuration.....	105
Figure 100: Normal core axial mid-plane thermal flux map for transient rod pull 3 configuration.....	105
Figure 101: Normal core axial mid-plane thermal flux map for transient rod pull 4 configuration.....	106
Figure 102: Normal core axial mid-plane thermal flux map for transient rod pull 5 configuration.....	106
Figure 103: Normal core axial mid-plane thermal flux map for transient rod pull 6 configuration.....	107
Figure 104: Normal core axial mid-plane thermal flux map for safety rod pull 1 configuration.	107
Figure 105: Normal core axial mid-plane thermal flux map for safety rod pull 2 configuration.	108
Figure 106: Normal core axial mid-plane thermal flux map for safety rod pull 3 configuration.	108
Figure 107: Normal core axial mid-plane thermal flux map for safety rod pull 4 configuration.	109
Figure 108: Normal core axial mid-plane thermal flux map for safety rod pull 5 configuration.	109
Figure 109: Normal core axial mid-plane thermal flux map for safety rod pull 6 configuration.	110
Figure 110: Normal core axial mid-plane thermal flux map for shim rod pull 1 configuration.	110
Figure 111: Normal core axial mid-plane thermal flux map for shim rod pull 2 configuration.	111
Figure 112: Normal core axial mid-plane thermal flux map for shim rod pull 3 configuration.	111
Figure 113: Normal core axial mid-plane thermal flux map for shim rod pull 4 configuration.	112
Figure 114: Normal core axial mid-plane thermal flux map for shim rod pull 5 configuration.	112
Figure 115: Normal core axial mid-plane thermal flux map for shim rod pull 6 configuration.	113
Figure 116: Normal core axial mid-plane thermal flux map for regulating rod pull 1 configuration.....	113
Figure 117: Normal core axial mid-plane thermal flux map for regulating rod pull 2 configuration.....	114
Figure 118: Normal core axial mid-plane thermal flux map for regulating rod pull 3 configuration.....	114
Figure 119: Normal core axial mid-plane thermal flux map for regulating rod pull 4 configuration.....	115
Figure 120: Normal core axial mid-plane thermal flux map for regulating rod pull 5 configuration.....	115
Figure 121: Normal core axial mid-plane thermal flux map for regulating rod pull 6 configuration.....	116
Figure 122: Normal core axial mid-plane thermal flux map for regulating rod pull 7 configuration.....	116
Figure 123: Normal core axial mid-plane thermal flux map for regulating rod pull 8 configuration.....	117
Figure 124: CLICIT core axial mid-plane thermal flux map for transient rod pull 1 configuration.....	117

LIST OF FIGURES (Continued)

Page

Figure 125: CLICIT core axial mid-plane thermal flux map for transient rod pull 2 configuration.....	118
Figure 126: CLICIT core axial mid-plane thermal flux map for transient rod pull 3 configuration.....	118
Figure 127: CLICIT core axial mid-plane thermal flux map for transient rod pull 4 configuration.....	119
Figure 128: CLICIT core axial mid-plane thermal flux map for transient rod pull 5 configuration.....	119
Figure 129: CLICIT core axial mid-plane thermal flux map for transient rod pull 6 configuration.....	120
Figure 130: CLICIT core axial mid-plane thermal flux map for safety rod pull 1 configuration.	120
Figure 131: CLICIT core axial mid-plane thermal flux map for safety rod pull 2 configuration.	121
Figure 132: CLICIT core axial mid-plane thermal flux map for safety rod pull 3 configuration.	121
Figure 133: CLICIT core axial mid-plane thermal flux map for safety rod pull 4 configuration.	122
Figure 134: CLICIT core axial mid-plane thermal flux map for safety rod pull 5 configuration.	122
Figure 135: CLICIT core axial mid-plane thermal flux map for shim rod pull 1 configuration.	123
Figure 136: CLICIT core axial mid-plane thermal flux map for shim rod pull 2 configuration.	123
Figure 137: CLICIT core axial mid-plane thermal flux map for shim rod pull 3 configuration.	124
Figure 138: CLICIT core axial mid-plane thermal flux map for shim rod pull 4 configuration.	124
Figure 139: CLICIT core axial mid-plane thermal flux map for shim rod pull 5 configuration.	125
Figure 140: CLICIT core axial mid-plane thermal flux map for shim rod pull 6 configuration.	125
Figure 141: CLICIT core axial mid-plane thermal flux map for regulating rod pull 1 configuration.	126
Figure 142: CLICIT core axial mid-plane thermal flux map for regulating rod pull 2 configuration.	126
Figure 143: CLICIT core axial mid-plane thermal flux map for regulating rod pull 3 configuration.	127
Figure 144: CLICIT core axial mid-plane thermal flux map for regulating rod pull 4 configuration.	127
Figure 145: CLICIT core axial mid-plane thermal flux map for regulating rod pull 5 configuration.	128
Figure 146: CLICIT core axial mid-plane thermal flux map for regulating rod pull 6 configuration.	128
Figure 147: CLICIT core axial mid-plane thermal flux map for regulating rod pull 7 configuration.	129

LIST OF TABLES

Page

Table 2-1: Comparison of Potential Moderator Materials For TRIGA®	8
Table 2-2: Control Rod Effectiveness for Various Materials as Reported in Dayton 1957.	19
Table 2-3: Predicted vs. Measured Control Rod Reactivity Worths for OSTR Normal Core Config. 2008..	24
Table 2-4: OSTR Measured Control Rod Worths for CLICIT Core 2008.	25
Table 3-1: Normal core critical control rod heights [2].	41
Table 3-2: CLICIT core critical control rod heights [2].	42
Table 3-3: Normal core supercritical control rod heights [2].	44
Table 3-4: CLICIT core supercritical control rod heights [2].....	45
Table 3-5: Six-Group Delayed Neutron Precursor Fractions and Decay Constants.....	46
Table 4-1: Normal core transient control rod calibration results.	50
Table 4-2: Normal core safety control rod calibration results.	51
Table 4-3: Normal core shim control rod calibration results.	51
Table 4-4: Normal core regulating control rod calibration results.....	52
Table 4-5: CLICIT core transient control rod calibration results.	53
Table 4-6: CLICIT core safety control rod calibration.	53
Table 4-7: CLICIT core shim control rod calibration results.	54
Table 4-8: CLICIT core regulating control rod calibration results.....	54
Table 4-9: Normal core critical control rod configurations [2] and reactivity bias.	56
Table 4-10: CLICIT core critical control rod configurations [2] and reactivity bias.	58
Table 4-11: Normal core measured and calculated control rod calibration results.	61
Table 4-12: CLICIT core measured and calculated control rod calibration results.....	65
Table 4-13: Non-banked normal core calculated control rod reactivity results using the one-rod-out method.	133
Table 4-14: Banked normal core calculated control rod reactivity results using the one-rod-out method.	134
Table 4-15: Non-banked CLICIT core calculated control rod reactivity results using the one-rod-out method.	134
Table 4-16: Banked CLICIT core calculated control rod reactivity results using the one-rod-out method.	135
Table 4-17: Non-banked CLICIT core one-rod-out method experimental validation.....	136

1.0 Introduction

Oregon State University (OSU) houses a 1 MW Training, Research, Isotope Production General Atomic (TRIGA®) reactor built by General Atomics in 1967. The Oregon State University TRIGA® reactor (OSTR) underwent conversion from high-enriched uranium (HEU) to low-enriched uranium (LEU) fuel in 2008 as part of the U.S. Reduced Enrichment for Research and Test Reactors Program (RERTR) which called for the conversion of all civilian reactors to low-enriched fuels (<20% enrichment) [1]. After the reloading of the core was completed and initial criticality was achieved, control rod reactivity worth measurements, or “control rod calibrations”, were carried out on two core configurations in October 2008 [2].

It is noted in the OSTR startup report that the accuracy of the control rod worth measurement technique was not well characterized, but work in response to a Nuclear Regulatory Commission (NRC) Request for Additional Information (RAI) found it to be less than $\pm 5\%$ per measurement at the time. The result was an integral control rod worth, measured in eight differential measurements, was estimated to have a total measurement accuracy of $\pm 14\%$ [3]. Recent improvements in the accuracy of the control rod calibration procedure, neutronic model of the OSTR, and improvements in computational resources, offered an opportunity to develop and validate a time-independent Monte Carlo method for detecting control rod shadowing effects. In addition, it offered an opportunity to better characterize and understand the error associated with control rod calibrations at OSTR, which was believed to be due to a neutronic phenomenon known as control rod shadowing.

1.1 Research Objective

The objective of this work was to develop and validate a time-independent Monte Carlo method for the detection of control rod shadowing effects in the calibration of the OSTR control rods. Additionally, this work aimed to understand the accuracy of the control rod calibration procedures at OSTR. The reactivity worth of a segment of an OSTR control rod is calculated from the Inhour equation using the measured reactor period induced by the partial withdrawal of the control rod being calibrated [4]. It is noted by Todd Keller in the 2008 post-conversion startup report that the accuracy of the control rod calibration experiment at OSTR was not well characterized prior to the LEU conversion in 2008 [3].

However, in response to NRC RAI question #11, 4/22/2008, rev 10, Keller found that the error associated with each individual measurement at the time was estimated to be less than $\pm 5\%$. This

resulted in an estimated error of $\pm 14\%$ for a total integrated rod worth measurement performed with eight control rod perturbations [3]. This work presented an opportunity to better understand the error associated with control rod calibrations at OSTR as the bias or inaccuracy associated with the current OSTR Monte Carlo N-Particle (MCNP[®]) model was found to be extremely low in this work ($<0.0005\%k/k$ or $<\$0.07$ for the CLICIT core configuration).

During control rod calibrations at OSTR the reactor power level and period are measured using a single detector located on the north side of the reflector [4]. This detector is calibrated at 1 MW during steady-state operation of the reactor where it is assumed the neutron flux profile in the reactor core is relatively flat. During control rod calibrations the discrepancy in control rod heights create an asymmetrical thermal neutron flux and power distribution in the core that changes with each successive control rod perturbation.

It was proposed that this variable asymmetry in flux distribution gives rise to a phenomenon known as control rod shadowing. This phenomenon may lead to inaccurate power and period measurements as the flux profile changes with each successive withdrawal of a control rod and the lowering of the other three in a control rod calibration. Thus, the error in the calculation of the control rod worth due to control rod shadowing may be a function of the detector location.

The most current OSTR MCNP[®] model was validated and modified to introduce fission chamber detectors at nine locations around the reflector. These model changes were made to compare the fission rate in each detector as a function of detector location as the detector output signal is proportional to the fission rate. The goal of these model changes was to determine if control rod shadowing effects introduce error to control rod calibration results at OSTR.

1.1.1 Scope

The scope of this work includes:

1. Validation of the current OSTR MCNP[®] model by the determination of an average model bias for both the normal and CLICIT core configurations. These biases are calculated using the critical rod heights recorded in the reactor logbook during the control rod calibration procedure.
2. Addition of the sensitive volume of nine Reuter-Stokes model SA-C3-2510-114 fission chambers to the model around the reflector assembly in 20-degree increments, except where the thermal and thermalizing columns interfere with detector placement.

3. Comparison of measured and MCNP® predicted integral rod worth curves to the MCNP® predicted integral fission rate in each detector to observe detector response as a function of position.
4. Inclusion of thermal flux tallies at the axial mid-plane of the OSTR core for the production of thermal flux maps.
5. Comparison of the detector fission rate results to thermal flux maps to determine control rod shadowing mechanisms in OSTR.

1.1.2 Objective

The purpose of this work was to determine if control rod shadowing effects exist in the OSTR and if so, to what extent it introduced error into control rod calibration measurements of October 2008. This work presents and validates a time-independent Monte Carlo method for detecting control rod shadowing in the OSTR. This resulted in a more comprehensive understanding of the source of error in control rod worth measurements at OSTR as well as the effect asymmetrical flux distributions in the OSTR core have on the fission chamber detector response.

1.2 Oregon State University TRIGA® Reactor (OSTR) Background

1.2.1 OSTR Description

The nuclear reactor located in the Radiation Center at OSU is a TRIGA® Mk. II type research reactor built by General Atomics in 1967. The OSTR is standard design TRIGA Mk. II open-pool type research reactor that is cooled by the natural convection of de-ionized light water and operates at a nominal 1 MW steady-state (1.1 MW licensed) [1]. As of 2021, the OSTR core consists of 89 standard LEU TRIGA® fuel elements, 3 fuel-followed control rods, an air-followed control rod and 25 graphite reflector elements arranged in a circular array. The safety, shim, and regulating control rods are fuel followed while the transient control rod is air-followed to enable reactor pulsing via pneumatic ejection of the transient rod. The core assembly is surrounded by an aluminum clad graphite reflector [1].

Many experimental irradiation facilities exist at OSTR. Current facilities in use include the 40-position rotating rack (“Lazy Susan”), the neutron radiography facility on the tangential beam port (beam port 3), the prompt gamma neutron activation analysis (PGNAA) facility on the penetrating beam port (beam port 4), the thermal column, a cadmium-lined in-core irradiation tube (CLICIT), a cadmium-lined outer-core irradiation tube (CLOCIT), and an in-core irradiation tube (ICIT).

1.2.2 OSTR Core Configurations Post-LEU Conversion

The core configuration of OSTR as it was at the time of the first control rod calibrations after LEU conversion in 2008 is the configuration of interest in this work. This is because the OSTR MCNP® model was validated in this work against the total control rod worth data for the fresh LEU fuel. After LEU conversion in 2008, OSTR had three different core configurations known as the normal, cadmium-lined in-core irradiation tube (CLICIT), and in-core irradiation tube (ICIT) configurations.

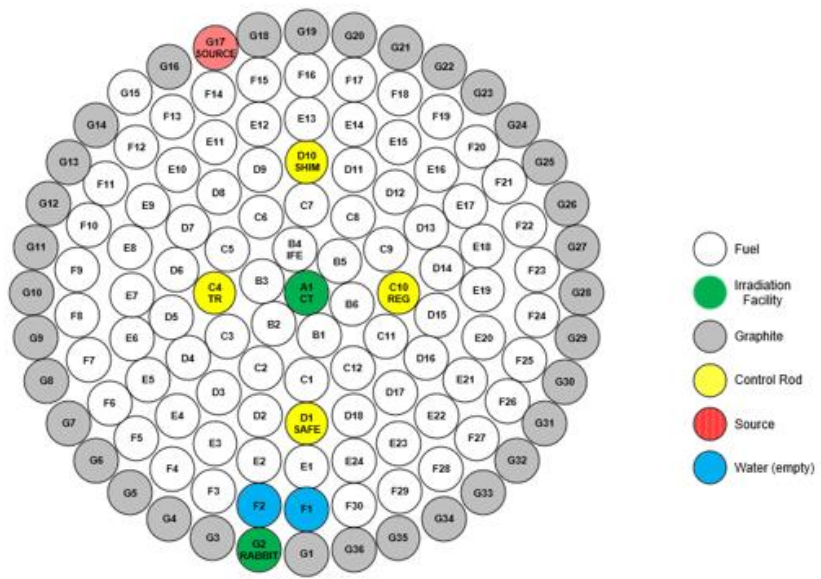


Figure 1: 2008 LEU normal core configuration.

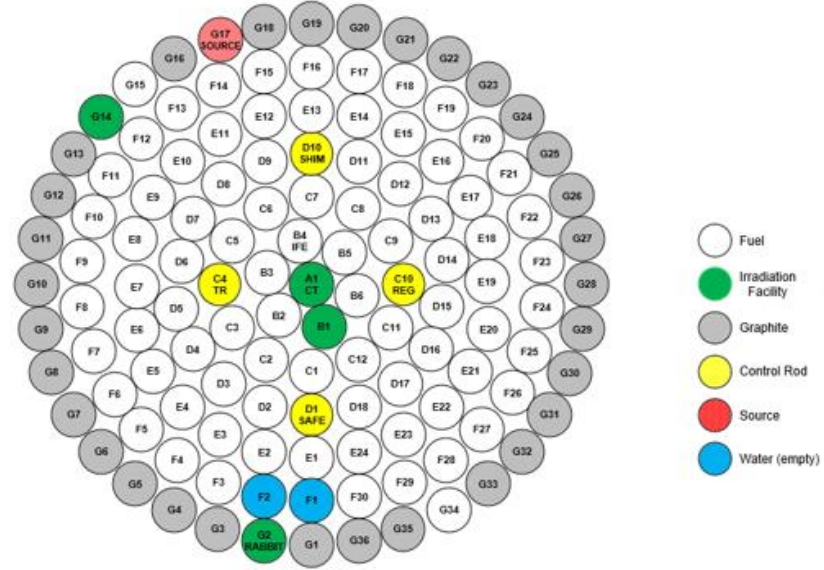


Figure 2: 2008 LEU CLICIT core configuration.

In the CLICIT or ICIT configurations, a fuel element occupying a grid position near the center of the core is removed and replaces a graphite element in a grid position at the core periphery, and either a cadmium lined or unlined aluminum sample irradiation tube is placed in the grid position near the center of the core [1]. The control rod calibrations following the LEU conversion in 2008 were performed in the normal and CLICIT configurations [2]. Therefore, the MCNP® models used in this work reflect the normal and CLICIT configurations as they were in October of 2008.

1.2.3 Control Rod Calibrations at OSTR

Control rod calibrations at OSTR are carried out using an experimental method known as the rod-pull method. In the rod-pull method the reactivity worth of a segment of a control rod is determined by using the rod being calibrated to induce a power rise in OSTR. The OSTR is brought critical by withdrawing three of the control rods to a banked critical height with the rod that is to be measured remaining fully inserted. The reactor power is held constant at a low power level and then the control rod being measured is withdrawn some distance to induce a positive reactor period [4].

A special timer connected to the control console receives signal from the linear power channel and measures the time of power rise from one power level to another, and the average reactor period is

calculated from this data. The Inhour equation is then used to calculate the reactivity insertion associated with the withdrawal of the control rod from the average reactor period during the power rise. This process is repeated until the rod being calibrated is fully withdrawn [4]. However, at the time of LEU conversion in 2008 a stopwatch method was used instead of an integrated timer. This method included some error due to inaccuracies in starting/stopping the stopwatch at the exact moment a certain reactor power was achieved. In response to RAI question #11, 04/22/2008, rev 10 the error associated with the method was found to be $\pm 5\%$ for each rod pull for a total integrated worth accuracy of $\pm 14\%$ for a control rod calibrated in eight pulls [3].

1.3 The OSTR MCNP® Model

1.3.1 The OSTR MCNP® Model as Provided

An existing MCNP® 6 model of OSTR is curated by the OSTR Reactor Administrator, Robert Schickler, who generously provided the model for use in this work. The model was originally created by Tiyapun Kanokrat in 1997 but has been updated many times since then [5]. The provided model uses evaluated nuclear data file seven (ENDF/B-VII.1) from Brookhaven National Laboratory and includes both geometry and materials improvements made by Allyson Kitto in 2012 [6], as well as extensive improvements by Schickler in recent years. The provided model reflects the fresh-fuel CLICIT core configuration as it was post-LEU conversion in 2008.

1.3.2 Modifications Made to The Model for This Work

Initial modifications to the provided MCNP® model of OSTR include altering the CLICIT core configuration to replicate the normal core configuration as both configurations are used in this work. These configurations are no longer used operationally at OSTR. However, they are used in this work to negate burnup effects and compare the fresh fuel model of 2008 to the experimental data collected in 2008. The cells, surfaces, and materials for both configurations exist in the model input file and switching configurations only involved uncommenting and commenting out specific lines of code. Initial modifications also included creating an input file that represented the control rod heights for each critical configuration, and each super-critical configuration for both the CLICIT and normal core configurations during the first control rod calibrations after LEU conversion in 2008. Robert Schickler generously provided an Excel® spreadsheet that outputs the MCNP® code for the control rod surfaces for given control rod height inputs.

The substantive modifications to the OSTR MCNP® model for this work included the addition of nine fission chambers around the graphite reflector. The neutron-sensitive internal parts of the fission chamber were modeled based on drawings provided by Reuter-Stokes upon delivery of the fission chamber. One chamber was placed at its actual location in the OSTR approximately 348.2° of North and eight others were placed at various locations at the same radial distance and height as the actual chamber.

2.0 Literature Review

2.1 The Oregon State TRIGA® Reactor (OSTR)

2.1.1 General Atomics TRIGA® Reactors

TRIGA® nuclear research reactors are renowned for their safety, affordability and variety of applications in both academic and industrial settings [7]. TRIGA® reactors are thermal neutron reactors that consist of a graphite reflected, light-water cooled, uranium-zirconium-hydride metallic fuel system [8]. General Atomics (GA) has constructed 66 TRIGA® reactors in 24 countries [9] since the first TRIGA® Mk. I prototype achieved criticality at the GA campus in Torrey Pines, California in 1958 [7].

The TRIGA® concept has its origins in 1956 when Frederic de Hoffmann of the General Dynamics Corporation convinced the company to form the General Atomic Division (now General Atomics) with the mission of commercializing nuclear reactors. Three teams were formed in the division. One of these groups, led by Edward Teller, also included Massoud Simnad and Freeman Dyson, was tasked with designing a completely inherently safe nuclear reactor [7], [8]. General Atomics defined the idea of “complete operational safety,” in the 1958 report *Technical Foundations of TRIGA®*, to mean that all the excess reactivity of the reactor could be instantaneously inserted, and no accident would occur [8].

The result of their work was an open-pool type research reactor that utilizes metallic fuel that is intrinsically safe due to a large, prompt negative temperature coefficient of reactivity [7]. One key component to this large, prompt negative temperature coefficient of reactivity was the inclusion of a moderator in the fuel matrix itself. Several moderators were considered during the development of TRIGA® including beryllium, beryllium oxide, graphite, and zirconium hydride. Properties of these various moderators as reported in *Technical Foundations of TRIGA®* are shown below in Table 2-1. Beryllium and beryllium oxide were quickly found to be both expensive and problematic to manufacture

due to beryllium's toxicity. Graphite was seen as an attractive option due to its low cost and its known negative temperature coefficient of reactivity [8].

Table 2-1: Comparison of potential moderator materials for TRIGA®.

<i>Properties</i>	Be	BeO	C	ZrH _{1.2}
<i>Moderator:²³⁵U atomic ratio</i>	1300	1000	6000	180
<i>Critical radius, R_C (cm)</i>	20.1	22.2	42.0	12.8
<i>Critical mass, M_C (kg)</i>	1.11	1.11	1.60	0.74
<i>Average thermal neutron flux in core at 10 kW (10¹¹n/cm²s)</i>	2.2	2.2	1.5	3.24
<i>Resonance escape probability, p</i>	0.89	0.89	0.85	0.93
<i>Maximum temperature coefficient [(-1/k) (dk/dt) x10⁴]</i>	2.3	2.5	1.9	1.6

Ultimately, General Atomics chose zirconium hydride because it would result in a lower critical mass of TRIGA® fuel, and thus a higher thermal neutron flux, which was desirable for various experiments. However, little was known about the neutronic properties and metallurgy of zirconium hydride in 1958, motivating General Atomic into creating an extensive research program in these areas. Several neutron scattering experiments were carried out by General Atomics staff on zirconium hydride samples using the highly monochromatic neutron beamlines at the 25 MW Brookhaven Graphite Research Reactor (BGRR). These experiments yielded three important conclusions on the neutronic properties of zirconium hydride: 1) it was found that zirconium hydride is a comparable moderator to free hydrogen for neutron energies above 13 eV, 2) thermal neutrons can gain energy when passing through zirconium hydride in integral multiples of 13 eV, especially as the temperature of the moderator

increases, and 3) these results appear to be independent of the atomic ratio of zirconium to hydrogen [8].

These conclusions, particularly that slow neutrons can gain energy in 13 eV multiples, strongly suggest that the hydrogen atoms in the zirconium hydride lattice act more like Einstein oscillators rather than Debye scatterers. In the Einstein model these harmonic oscillators of a given frequency have quantized energy states that are integer multiples of the fundamental bond vibrational energy. The equation for the bond vibrational energy according to the Einstein model is shown below [8].

$$E = (n + \frac{3}{2})h\nu \quad (2.1)$$

Where n is the quantized vibrational mode, h is the Plank constant, and ν is the bond vibrational energy.

The result is a neutron may gain or lose energy in a scattering event with the oscillator, the hydrogen in zirconium hydride in this case, in integer multiples of 13 eV. If the energy of the incident neutron is just above 13 eV, it is likely to be thermalized in a scattering event with a hydrogen atom. If it is below 13 eV, and the local fuel matrix temperature is elevated, the neutron may gain energy in the scattering event. The fact that a neutron may gain energy in a scattering collision with a hydrogen atom in zirconium hydride is a key safety feature in TRIGA®. Heating of the fuel matrix results in neutron spectrum hardening and reduces the probability that such neutrons will induce fission in ^{235}U [8], [10].

Another key safety feature in TRIGA® fuel is the Doppler broadening of low-energy absorption resonances in ^{238}U and ^{167}Er . Original TRIGA® Mk. I fuel did not contain erbium, but rather relied solely on the Doppler broadening of the low-energy absorption resonances in ^{238}U . The spectrum hardening provided by the zirconium hydride and the Doppler broadening of absorption resonances in ^{238}U resulted in a fuel with a strong, prompt negative fuel temperature coefficient of reactivity that allows TRIGA® reactors to safely pulse [8], [10]. Original TRIGA® fuel was comprised of zirconium hydride and 8.5 wt. % uranium that was 20% enriched in ^{235}U . This original fuel had a negative temperature feedback coefficient of $9.5 \times 10^{-5} \Delta k/k^\circ\text{C}$, but a core lifetime of only 100 MWd [11], [12]. TRIGA® fuel elements consist of three cylindrical fuel slugs 1.47 inches in diameter and 5 inches long with a zirconium pin 0.19 inches in diameter to fill the center void left over from the hydriding process. This center void aids in an even hydriding of the fuel meat. Either end of the fuel element contains a cylindrical graphite slug 1.47 inches in diameter and 3.5 inches in length to reduce neutron leakage [1].

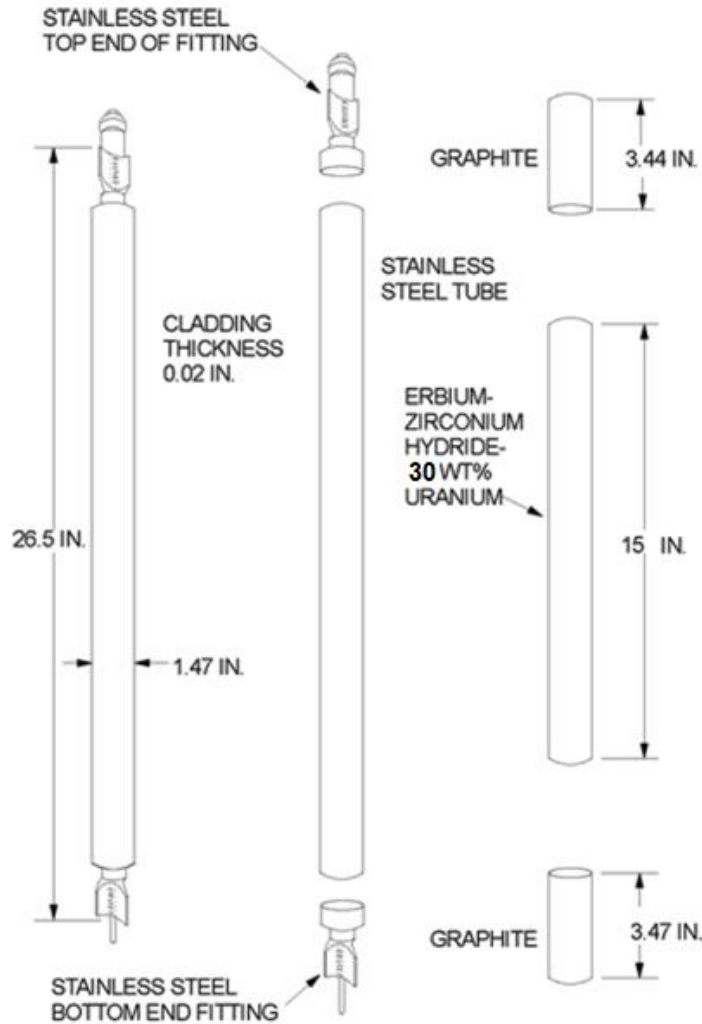


Figure 3:TRIGA® fuel element [13].

In early TRIGA® fuel there were two thin samarium trioxide disks placed between both the upper and lower fuel and graphite slugs to act as a burnable poison [8]. However, modern TRIGA® fuel employs a 0.08 inch thick molybdenum disk placed between the lower fuel slug and lower graphite slug to both prevent bonding and serve as a burnable poison [7], [14]. The entire element is clad in 0.02 inch 304 stainless steel, and two end caps are welded to either end of the rod resulting in a final length of 26.5 inches [1]. Original TRIGA® fuel elements were clad in 1100F aluminum. However, they were later clad in 304 stainless steel to decrease the likelihood of cladding failure [7].

Under General Atomics Fuel Lifetime Improvement Program (FLIP), an 8.5 wt. % uranium, 70% enriched ^{235}U , with 1.6 wt. % natural erbium was developed. The primary purpose of the erbium is to act as a burnable poison which offsets the large core excess reactivity of the FLIP fuel at the beginning of

core life (BOL). However, there also exists a low energy absorption resonance in erbium-167 that undergoes Doppler broadening and aids in the absorption of neutrons that gain energy via the zirconium hydride moderator as fuel temperature increases [11], [15]. This new high enriched uranium (HEU) FLIP fuel saw improvements in both the negative temperature feedback coefficient ($10.5 \times 10^{-5} \Delta k/k^\circ C$) and core lifetime (3500 MWd) [11], [16].

In 1978 the United States implemented the Reduced Enrichment for Research and Test Reactors Program (RERTR) which called for the conversion of all civilian reactors to low-enriched fuels (<20% enrichment) [7], [17]. In response, General Atomics studied three new low enriched uranium (LEU) fuel compositions of 20, 30 and 45 wt. % uranium, 20% enriched, with 0.5, 0.9 and 1.8 wt. % erbium, respectively. Ultimately, a satisfactory compromise was found to be an LEU fuel composition of 30 wt. % uranium, 20% enriched, with 1.1 wt. % erbium [11], [16]. This new LEU 30/20 fuel maintained a large negative temperature coefficient of reactivity ($8 \times 10^{-5} \Delta k/k^\circ C$) and a long core lifetime of 3000 MWd [11].

The original Mk. I design consists of a circular, open-pool water tank set into the ground without neutron beam ports. The core is cylindrical, approximately one meter in height and a half meter in diameter, with fuel elements arranged in concentric rings and an annular graphite reflector just beyond the core periphery. The Mk. II design consists of an above-ground tank, surrounded by a poured-concrete radiological shield (bioshield), with beam ports penetrating the bioshield to enable the use of neutron beams from the reactor core. The Mk. III design is similar to the Mk. II design. However, in the Mk. III design the reactor tank is oval in shape, allowing for movement of the reactor core within the tank [18]. Each specific TRIGA® facility is unique, and there exist a wide variety of configurations that facilitate a diverse range of uses and experiments [7].

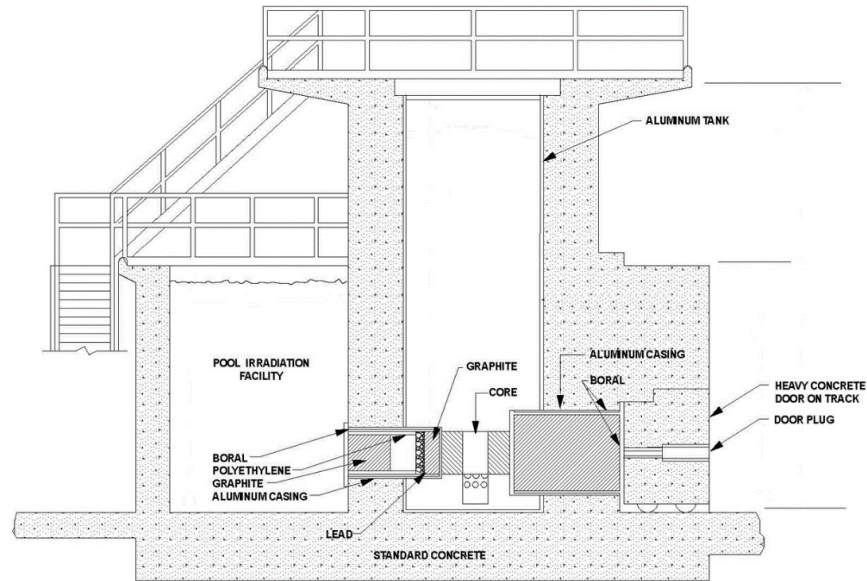


Figure 4: Axial cross section of a TRIGA® Mk. II bioshield [19].

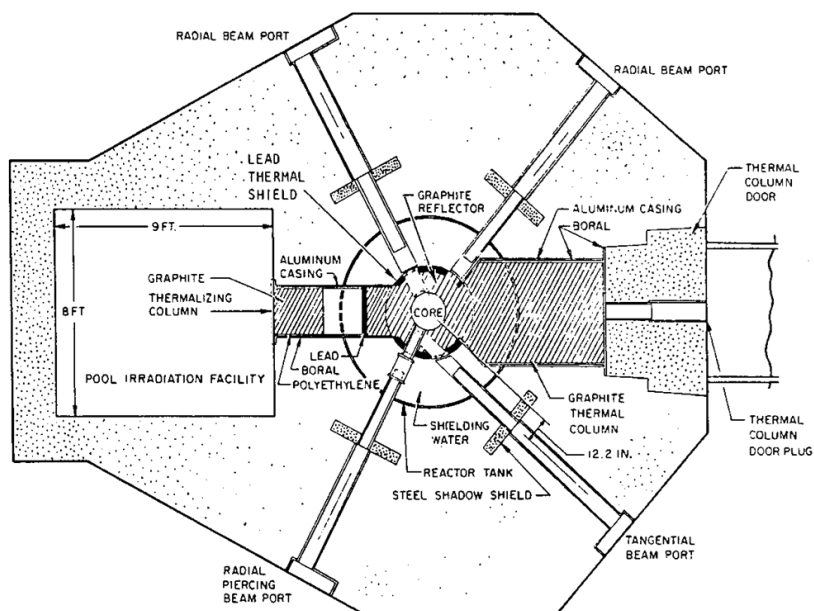


Figure 5: Radial cross section of a TRIGA® Mk. II bioshield [19].

2.1.2 Description of the OSTR

The nuclear reactor located in the Radiation Center at Oregon State University (OSU) is a TRIGA® Mk. II type research reactor built by General Atomics in 1967. The Oregon State TRIGA® Reactor (OSTR) is standard design TRIGA Mk. II. OSTR is an open-pool type research reactor that is cooled by the natural convection of de-ionized light water and operates at a nominal 1 MW steady-state (1.1 MW licensed). Being a Mk. II in design, the OSTR core resides in an above-ground aluminum tank set into a concrete bioshield. The aluminum primary tank is 6.5 feet in diameter and about 20.5 feet deep with a total volume of about 5000 gallons. The bioshield is 21 feet tall and 8.17 feet thick at its base with four beam port lines, a thermalizing column, and a thermal column built into the structure. An auxiliary bulk-shielding experimental tank protrudes from the lower West side of the bioshield. The bulk shield tank is 8 feet wide, 9 feet long and 12 feet deep with a volume of about 6500 gallons [1].

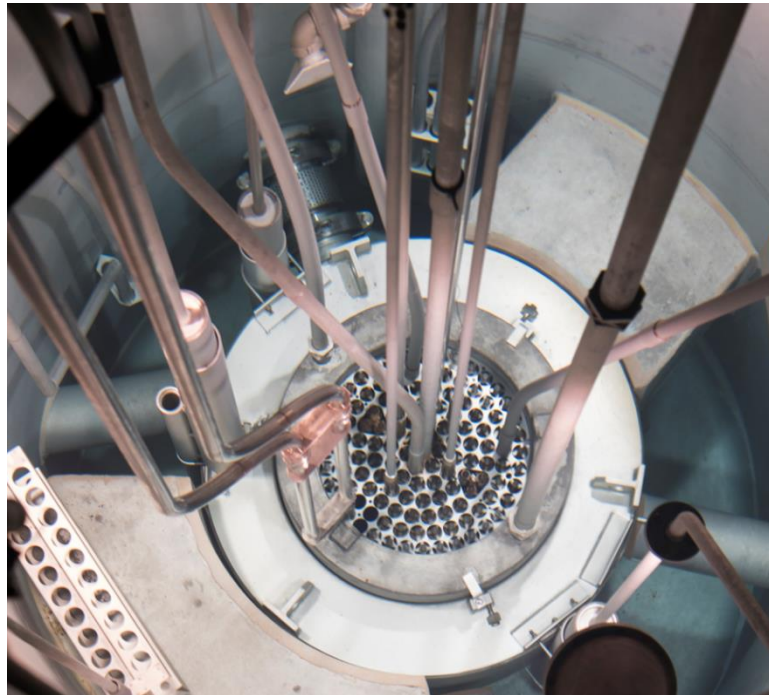


Figure 6: The OSTR core and reflector assembly [19].

The OSTR core is cooled by natural convection of the primary tank water. However, heat is removed from the primary water using a two-loop cooling circuit. The primary loop transfers heat to the secondary loop via a counter flow, parallel-plate type heat exchanger and heat is transferred from the secondary loop to the atmosphere via a cooling tower on the reactor building roof. OSTR was originally

fueled with standard TRIGA® fuel elements from 1967 to 1974 and fueled with HEU FLIP fuel from 1974 to 2008. In 2008 OSTR underwent conversion from HEU FLIP fuel to the modern TRIGA® LEU 30/20 fuel [1], [16]. As of 2021, the OSTR core consists of 89 standard LEU TRIGA® fuel elements, 3 fuel-followed control rods, an air-followed control rod and 25 graphite reflector elements arranged in a circular array. The safety, shim, and regulating control rods are fuel followed while the transient control rod is air-followed to enable reactor pulsing via pneumatic ejection of the transient rod. The core assembly is surrounded by an aluminum clad graphite reflector [1].

The reflector assembly is comprised of an 8-inch-thick, 28.9-inch-tall graphite annulus with 2 inches of lead at the periphery to reduce nuclear heating of the bioshield concrete. The lead is not present at the beam port locations or the thermalizing and thermal column locations. The entire reflector assembly is clad in 0.25 inches of aluminum. Cylindrical air voids exist through the graphite and lead annulus for the penetrating beam port (beam port 4) and the tangential beam port (beam port 3), and beam port 1. The reflector assembly rests freely on an aluminum platform at the bottom of the primary tank, and the reflector assembly supports the upper grid plate, the lower grid plate, and the safety plate. The lower grid plate supports the entire weight of the fuel, reflector elements, control rod guide tubes, and in-core experiments. The safety plate lies below the lower grid plate and is present to prevent control rods from accidentally falling out of the core. The safety plate also supports adapters that enable the placement of fuel elements in locations that allow for control rods to pass through the lower grid plate [1].

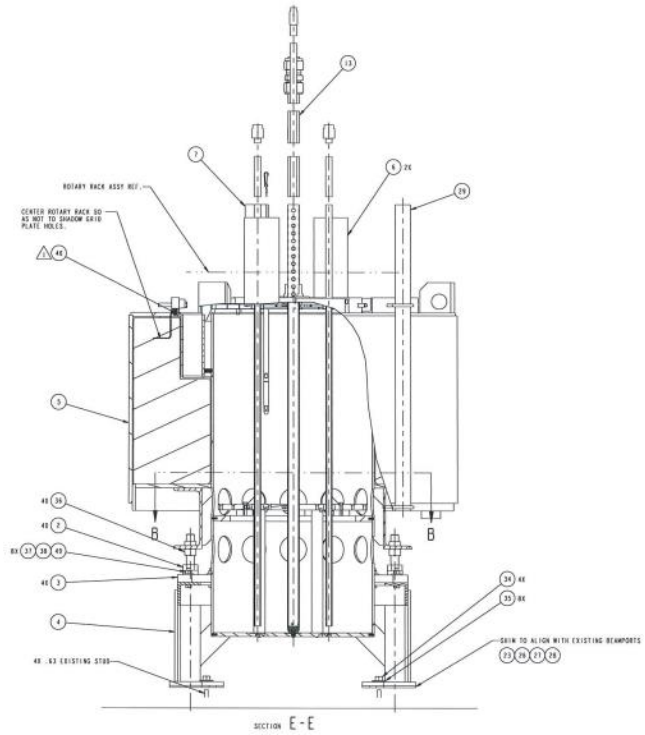


Figure 7: Axial reflector assembly schematic [20].

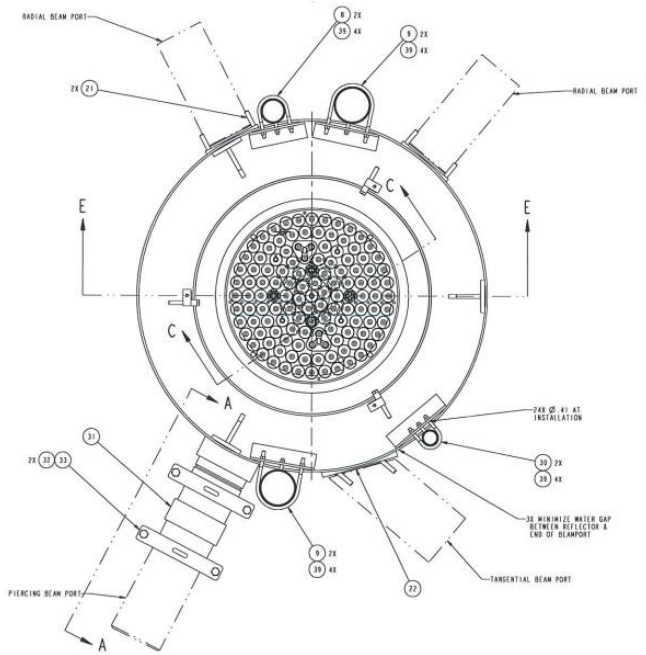


Figure 8: OSTR core and reflector assembly schematic [20].

The upper grid plate provides lateral support for elements and is constructed of 0.625-inch aluminum plate. There are 127 grid plate locations in the upper grid plate to accommodate fuel, control rod guide tubes, reflector elements, and various irradiation tubes. Smaller holes are drilled into various locations in the upper grid plate to accommodate flux mapping experiments. The upper grid plate is supported by a ring welded to the top inside surface of the core barrel, which is affixed to the reflector assembly. A 40-position, nitrogen-purged rotating sample rack is located between the upper regions of the core barrel and the reflector. A hexagonal section in the center of the upper grid plate can be removed to accommodate larger experiments, up to 4.4 inches in diameter, in the region of highest flux. In addition, experiments up to 2.4 inches in diameter can be placed in two triangular-shaped openings cut out of the upper grid plate. When fuel elements are placed in these triangular openings, they are laterally supported with a spacer that fits over the upper pins of the three fuel elements occupying the opening [1].

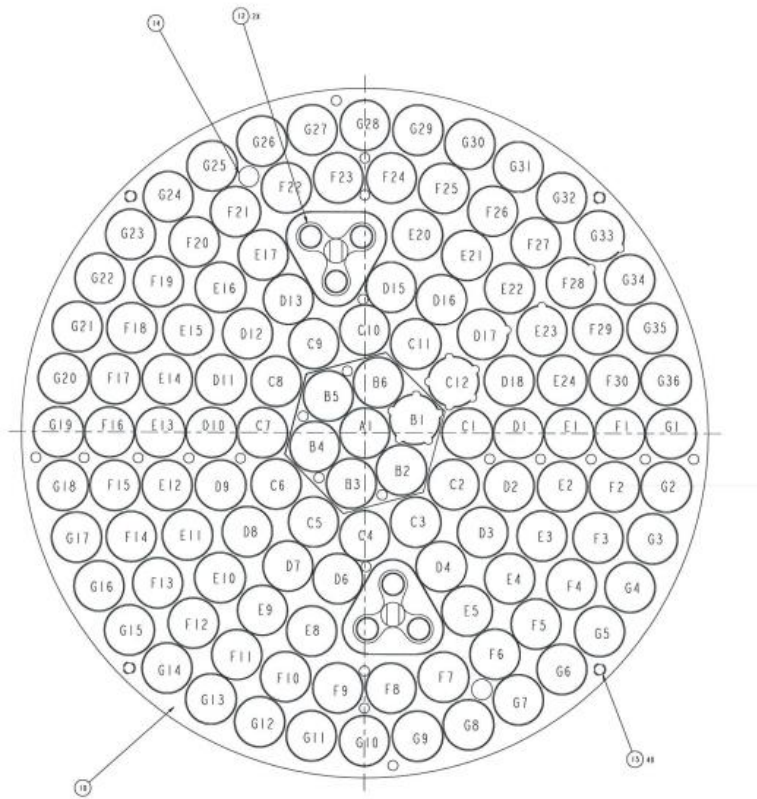


Figure 9: OSTR upper grid plate schematic [20].

2.1.3 Description of the OSTR core configuration at time of LEU conversion

The core configuration of OSTR as it was at the time of the first control rod calibrations after LEU conversion in 2008 was the configuration of interest in this work. This is because the OSTR MCNP® model was validated in this work against the total control rod worth data for the fresh LEU fuel. After LEU conversion in 2008, OSTR had three different core configurations known as the normal, cadmium-lined in-core irradiation tube (CLICIT), and in-core irradiation tube (ICIT) configurations.

In the normal core configuration, all G-ring positions except G-16 and G-2 were filled with graphite reflector elements. The neutron source occupied G-16, and the pneumatic sample transfer tube (rabbit) terminus occupied G-2. The transient rod occupied C-4, the safety rod D-1, the shim rod D-10, and the regulating rod C-10. The A-1 position was occupied by a solid aluminum central thimble rod. All other core positions were occupied by standard TRIGA® LEU 30/20 fuel elements [1].

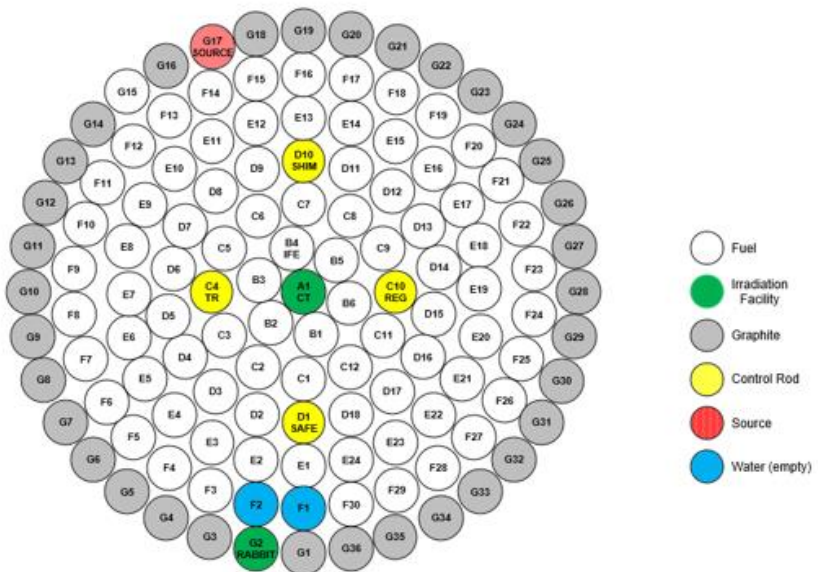


Figure 10: 2008 LEU Normal core configuration.

In the CLICIT or ICIT configurations, the fuel element that occupied B-1 was removed and replaced the graphite element in G34, and either a cadmium lined or unlined aluminum sample irradiation tube was placed in the B-1 position [1]. The control rod calibrations following the LEU

conversion in 2008 were performed in the normal and CLICIT configurations. Therefore, the MCNP® models used in this work reflect the normal and CLICIT configurations of October 2008.

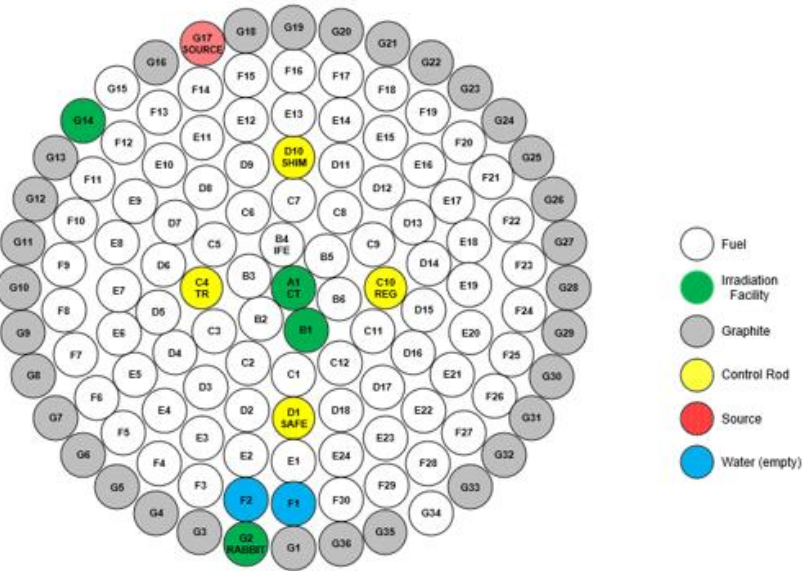


Figure 11: 2008 LEU CLICIT core configuration.

2.1.4 Differences in control rod materials

Control rods or blades, constructed of neutron-absorbing material, that can be mechanically inserted or withdrawn from a reactor core are a common method of reactivity control in many reactors. The reactivity worth of a control rod is a function of its geometry, materials properties, neutronic properties, and the properties of the reactor core in which it is used. The effectiveness of the control rods in any given reactor has important implications on reactor life span and the safety of the reactor. One of the most important components of a control rod's effectiveness or reactivity worth is its neutronic properties and ability to absorb neutrons. A completely effective control rod would absorb all neutrons of any energy incident on the control rod [21]. This control rod would appear to be a neutronic "black body."

However, such a material is not known to exist, and the reactivity worth of the same control rod is not the same in all reactor systems. For this reason, no one material exists as a standard against which to absolutely measure control rod effectiveness. Some early work on the subject by Russel Dayton [21]

used the thermal absorption cross section and the total absorptivity of hafnium as a function of neutron energy as a standard against which to compare the relative absorptivity of various materials. The relative absorptivity of these materials compared to hafnium are presented in Table 2-2 below, and the thermal neutron absorption cross section of a material alone is a poor indicator of its ability to absorb neutrons of any energy. Note that the thermal cross sections in Table 2-2 are multiplied by the thickness of the sample and the overall effectiveness relative to hafnium is the absorption as a function of neutron energy or lethargy [21].

Table 2-2: Control Rod Effectiveness for Various Materials as Reported in Dayton 1957.

Material	Absorptiveness, $\Sigma_a t^{(a)}$	Effectiveness relative to hafnium
<i>3.0 wt. % boron-10 in stainless steel</i>	27.2	1.12
<i>Hafnium</i>	2.40	1.00
<i>0.97 wt. % boron-10 in stainless steel</i>	9.3	0.98
<i>15 wt. % Er_2O_3 in stainless steel</i>	8.7	0.96
<i>Indium</i>	3.68	0.93
<i>Silver</i>	1.85	0.88
<i>Cadmium</i>	77.5	0.80
<i>8.7 wt. % gadolinium in titanium</i>	31.1	0.79
<i>Tantalum</i>	0.60	0.71
<i>2.7 wt. % samarium in stainless steel</i>	3.20	0.71
<i>Haynes 25</i>	0.96	0.68
<i>Titanium</i>	0.16	0.24
<i>Zircaloy 2</i>	--	0.05
<i>2S aluminum</i>	--	0.02

(a) Thermal absorption cross section times the sample thickness

Since the advent of nuclear reactors many neutron absorbing materials and combinations of materials have been developed, tested, and deployed in control rods. Ideally, the material chosen for any given system will absorb neutrons over the entire range of neutron energies present in the reactor

or a combination of materials will work together to individually absorb different sections of the overall neutron energy range [21]. Cost and availability are also factors in the choice of a control rod material.

Hafnium has historically been widely used in pressurized water reactors (PWRs) because the U.S. Navy chose zirconium metal for the cladding and core structural material of S.S.(N) 571 *Nautilus*, the world's first nuclear-powered submarine. Hafnium is the byproduct of the production of pure zirconium metal from zircon sands, and zirconium metal was used as the fuel cladding material in *Nautilus* because it is fairly neutronically transparent with a thermal neutron absorption cross section of just 0.18 b [22]. Natural hafnium has a relatively large thermal neutron absorption cross section at 104 b [23], making it a good control rod material. In addition, it would be cheap as the Navy would gain two required materials for the reactor in the processing of one ore [22].

Several isotopes of hafnium, ^{174}Hf , ^{176}Hf , ^{177}Hf , ^{178}Hf , ^{179}Hf , and ^{180}Hf occur naturally. The most abundant is ^{180}Hf at 35.08%, but ^{180}Hf has a relatively small thermal neutron absorption cross section at 12.9 b. ^{174}Hf has the largest thermal neutron absorption cross section of the naturally occurring hafnium isotopes at 530 b, but an abundance of just 0.16%. The largest contributors to the overall hafnium thermal neutron absorption cross section are ^{177}Hf and ^{178}Hf with abundances of 18.6% and 27.28%, respectively. ^{178}Hf has a thermal neutron absorption cross section of 500 b and a resonance integral of 300 b, while ^{177}Hf has a thermal neutron absorption cross section of 370 b and a large resonance integral of 7200 b [23].

Hafnium was used in subsequent U.S. Naval nuclear reactors and in various U.S. civilian PWRs throughout the 1950s and 1960s due to the excellent performance of the hafnium control rods in *Nautilus*. However, the rapidly growing demand for hafnium and zirconium during the rapid growth of the nuclear sector during these years eventually resulted in limited supply and high costs. In response the U.S. Naval Reactors Program developed silver-indium-cadmium rods as an alternative as these materials were more commercially available at the time [22]. Cadmium is of course chosen as a component due to its very high thermal neutron capture cross section of 2520 b [23], and silver and indium have large absorption resonances at higher neutron energies. As can be seen in Table 2.2; silver, indium, and cadmium are also more effective thermal neutron absorbers than hafnium, but they are slightly overall less effective when absorption is a function of neutron lethargy [21].

Problems with this replacement arose in the 1970s when uncertainties in the availability and cost of silver began to increase due to both speculative trading of silver and the listing of silver and cadmium as strategic materials by the U.S. government. This was especially of concern as silver-indium-cadmium control rods are 80% silver. Yet another problem with the Ag-In-Cd replacement is that the

absorber has a melting temperature of 800 °C compared to 2156 °C for hafnium rods [22]. In the 1980s the world supply of hafnium increased, and once again became a viable control rod material. Westinghouse developed both hafnium and boron carbide (B_4C) replacements for the absorber material in a standard 17 X 17 PWR fuel array [22].

B_4C is found by Keller et al. 1982 to have advantages and disadvantages compared to hafnium. Being a ceramic, the melting point of B_4C is slightly higher than hafnium at 2350 °C. Two downsides to B_4C are it undergoes significant irradiation swelling and it is water soluble in certain conditions. In the event of a control rod cladding breach there is the potential for the absorber to dissolve and leave the control rod. The most significant advantage of B_4C over hafnium is that it has a higher reactivity worth resulting in less material needed to control the reactor. In addition, the precursor materials for the sintering of B_4C ceramic pellets are graphite and boron, both of which are cheap and in plentiful supply. The absorber material in the control rods at OSTR is B_4C in the form of four solid boron carbide rods 15 inches long [1].

2.2 Control Rod Calibrations

2.2.1 Purpose of control rod calibrations

An important quantity that must be known to both predict the behavior of a reactor and ensure operational safety is the change in the reactivity state of the reactor caused by the movement of a control rod [24]. Knowing the resultant reactivity insertion caused by the incremental withdraw or insertion of a control rod allows reactor operators to predict reactor behavior before a manipulation is performed. By knowing the reactivity effect of completely removing all the control rods, one can know both the core excess reactivity, or the amount of reactivity that would be inserted if all control rods were removed from the reactor, and the shutdown margin, the negative reactivity with which to make the reactor subcritical if all control rods were inserted. These are important quantities that must be known for the safe operation of a nuclear reactor in all modes of operation. The experimental measurement of control rod reactivity worth is commonly referred to as a control rod calibration [4], [24], [25].

2.2.2 Description of the rod-drop method

One method for measuring the reactivity worth of control rods is known as the rod-drop method. The rod-drop method measures the power transient induced by rapidly and fully inserting a

control rod from its fully withdrawn state. In the rod-drop method the experiment begins with the reactor in a critical state at some power level with the control rod to be measured completely withdrawn. Then the reactor power detector response or reactor power level is recorded. The control rod to be measured is then released and allowed to fall freely to a fully inserted position and reactor power after the rod is dropped is recorded [26]. The reactivity worth of the entire rod ρ can be calculated from Equation 2.2 shown below, where C_1 is the power detector response prior to the rod drop, C_2 is the power detector response immediately after the rod drop, and β is the effective delayed neutron fraction of the reactor [24].

$$\frac{C_2 - C_1}{C_2} = \frac{\rho}{\beta} \quad (2.2)$$

Note that Equation 2.2 is only valid if the reactor is critical prior to the rod drop. In the rod-drop method the reactivity change is assumed to be instantaneous, and it is assumed that the lifetime of a neutron is significantly shorter than the shortest-lived delayed neutrons. The first assumption is especially problematic in larger reactors because it takes a finite amount of time for a control rod to fall from a fully withdrawn to fully inserted position which can result in significant error in the calculation [24]. However, the most notable problem with the rod-drop method is that it only allows for the measurement of the reactivity of the entire control rod [26], and the differential reactivity worth of the rod axially would be entirely assumed unless the experiment was repeated at multiple drop heights.

2.2.3 Description of the rod-pull calibration method

An alternative control rod calibration method is known as the rod-pull method. In the rod-pull method a reactor is brought critical with the rod to be measured remaining fully inserted, and reactor power is made constant. The control rod being measured is then withdrawn a measured distance to induce a positive reactor period [24]. This resultant reactor period is measured after delayed neutron transients die out and reactor period becomes constant [4]. The reactivity insertion associated with the control rod perturbation can be calculated from the Inhour equation using six delayed neutron precursor groups [4]:

$$\frac{\rho}{\beta_{eff}} = \frac{l^*}{\beta_{eff}T} + \sum_{i=1}^6 \frac{\beta_i}{1 + \lambda_i T} \quad (2.3)$$

where l^* is the prompt neutron generation time, T is the stable reactor period, β_i is the delayed neutron fraction of the i^{th} delayed neutron group, and λ_i is the decay constant for the i^{th} delayed neutron group [4], [27]. This process is repeated until the control rod being measured is completely withdrawn [4]. The rod-pull method is more time consuming than the rod drop method. However, it is more accurate and yields important data about the differential and integral control rod worth as the reactivity of the rod is measured incrementally [24].

2.2.4 Description of control rod calibration procedures at OSTR

The control rods of the OSTR are calibrated using the rod-pull method previously described. Detailed procedures specific to the OSTR are described in Oregon State TRIGA® Reactor Operating Procedure (OSTROP) 9: *Control Rod Calibration Procedures*. The OSTR is brought critical by withdrawing three of the control rods to a banked critical height with the rod that is to be measured remaining fully inserted. The reactor power is held constant at a low power level of 10 W [4], but it should be noted that this power level was 15 W in October 2008 as that was the power core excess and shutdown margin were calculated at [2]. A low power level is required to ensure there are no temperature effects as the OSTR has a strong negative temperature coefficient of reactivity [4], [8]. The control rod being measured is then withdrawn some distance to induce a positive reactor period between 6 and 15 seconds. A special timer connected to the control console receives signal from the linear power channel and measures the time of voltage rise from 2 V to 8 V, which corresponds to a power rise from 200 to 800 W when the linear range switch is in the 1 kW position [4].

These bounds of 200 and 800 W were chosen to ensure reactor period is as constant as possible and that delayed neutron transients immediately after the control rod perturbation have died out. The reactor operator then manually SCRAMs one of the other three control rods after passing 800 W to bring the reactor subcritical. The initial and final heights of the control rods and the time of power rise from 200 to 800 W in milliseconds are recorded. The control rod being measured is left at its previous height and the reactor is brought back to critical at 100 W by re-banking the other three control rods. This process is repeated until the control rod being measured is completely withdrawn. The reactivity insertion associated with each control rod perturbation can be calculated from Equation 2.3. Average period during the power rise is calculated from the time of rise, and curves are fitted to the recorded data to determine the differential and integral control rod worths [4].

2.2.5 Results of first control rod calibration after LEU conversion

The OSTR underwent a conversion from HEU to LEU TRIGA® fuel in 2008 [1], [3]. Control rod calibrations were performed immediately following the establishment of a final normal core configuration on October 14th, 2008. The as-measured control rod worths and the MCNP® 5 predicted rod worths from the LEU Conversion Safety Analysis Report (CSAR) are shown below in Table 2-3 [3].

Table 2-3: Predicted vs. Measured Control Rod Reactivity Worths for OSTR Normal Core Config. 2008.

<i>Control Rod</i>	Measured Rod Worth [\$]	MCNP®5 Predicted Rod Worth [\$]
<i>Shim</i>	2.76	2.55 ± 0.16
<i>Safety</i>	2.66	2.60 ± 0.16
<i>Regulating</i>	3.71	3.36 ± 0.19
<i>Transient</i>	2.86	2.86 ± 0.15
<i>Sum of All Rods</i>	11.99	11.37 ± 0.33

As can be seen, the total worth of the shim and regulating rods disagreed with the MCNP® model of the OSTR at the time. It should be noted that the calibration method at the time used a stopwatch and the method was found to have an estimated accuracy of $\pm 5\%$ for each rod pull [3]. A control rod calibration was performed for the CLICIT core configuration on October 30th, 2008. However, the CLICIT core configuration was not modeled in preparation for LEU conversion and is therefore not reported in the CSAR. The measured rod worths from the October 30th, 2008 CLICIT core control rod calibration are listed below in Table 2-4 [2].

Table 2-4: OSTR Measured Control Rod Worths for CLICIT Core 2008.

<i>Control Rod</i>	Measured Rod Worth [\$]
<i>Shim</i>	2.71
<i>Safety</i>	2.31
<i>Regulating</i>	3.16
<i>Transient</i>	2.57
<i>Sum of All Rods</i>	10.75

2.3 Power Detectors

2.3.1 Operating principles of compensated and uncompensated ion chambers

The reactor power level is one of the most important parameters to measure in a nuclear reactor. The number of fissions per unit time cannot be directly measured except by calorimetric methods. However, the radiation field produced by the reactor can be used to indirectly measure reactor power. Reactor power detectors are used to measure the power rise during control rod calibrations, making them a vital component of reactor instrumentation.

Radiation detectors such as gas-filled ionization chambers rely on the effect ionizing radiation has on gasses [28], [29]. The incident radiation must be an ionizing type such as X-rays, gamma photons, alpha particles, protons, fission fragments, or other heavy ions [30]. The incident ionizing radiation can strip an electron from an atom creating an electron-ion pair in the gas [28], [29]. The electron-ion pairs produced in the gas can be separated and collected to produce an electrical output signal. These ions and electrons can be collected if a voltage gradient is produced between a cathode and anode. The positively charged ions drift and are collected by the cathode and the negatively charged electrons by the anode, resulting in a measurable current that is proportional to the energy imparted on the gas by the incident radiation [28], [29], [31].

The current produced in the detector may either be directly measured or stored in a capacitor where the resulting voltage is measured. These two types or modes of operation are commonly referred to as current mode and pulse mode. Pulse mode counts individual interactions and is commonly used when the magnitude of the radiation field being measured is low because the current produced is also

low [29], [31]. Current mode is commonly used when the magnitude of the radiation field is high because it may not be possible to distinguish between individual ionization events [31].

The type of radiation that is most directly proportional to the number of fissions per unit time is the neutron field or flux. Neutron-sensitive gas-filled ionization chambers are commonly used to measure neutron flux in nuclear reactors. Neutrons do not directly ionize atoms. Therefore, a nuclide(s) that absorbs neutrons and emits directly ionizing particles must be employed [32]. Commonly used nuclides for introducing neutron sensitivity to ionization chambers are ^3He , ^{10}B , ^6Li , and ^{235}U . The chamber itself may be filled with a neutron-sensitive gas such as $^{10}\text{BF}_3$ or ^3He , or the chamber walls may be coated with ^6LiF or ^{10}B [31]. It is desirable for the ionizing particles to cause dense ionization along their path because this results in a higher pulse amplitude or current from the detector [32]. For this reason, a common material used to introduce neutron sensitivity to an ionization chamber is boron as ^{10}B has a high neutron absorption cross section and can emit heavily-ionizing alpha particles in the $^{10}\text{B}(n,\alpha)^7\text{Li}$ reaction [28], [32].

However, other types of ionizing radiation such as gamma photons produced in the reactor will also ionize a neutron-sensitive ion chamber [31], [32]. At high reactor powers the neutron flux may be many orders of magnitude greater than the gamma photon flux and the overall gamma contribution to the detector output may be negligible. At low reactor powers the contribution to the detector signal by the gamma flux may introduce significant error. In an uncompensated ion chamber both gamma and neutron particles will cause ionization events in the gas-filled chamber at the center of the detector [31], [32]. Ion chambers that can distinguish between gamma and neutron radiation are known as compensated ion chambers [28], [30]–[32].

One solution to this problem is to place one chamber within another. In this arrangement the outer chamber is coated with a neutron-sensitive material for producing ions and the center chamber is uncoated. Direct ionization events due to gamma radiation will occur in both chambers while direct and indirect ionization events due to gamma and neutron radiation will occur in the outer chamber [31], [32]. These types of chambers are known as compensated ion chambers.

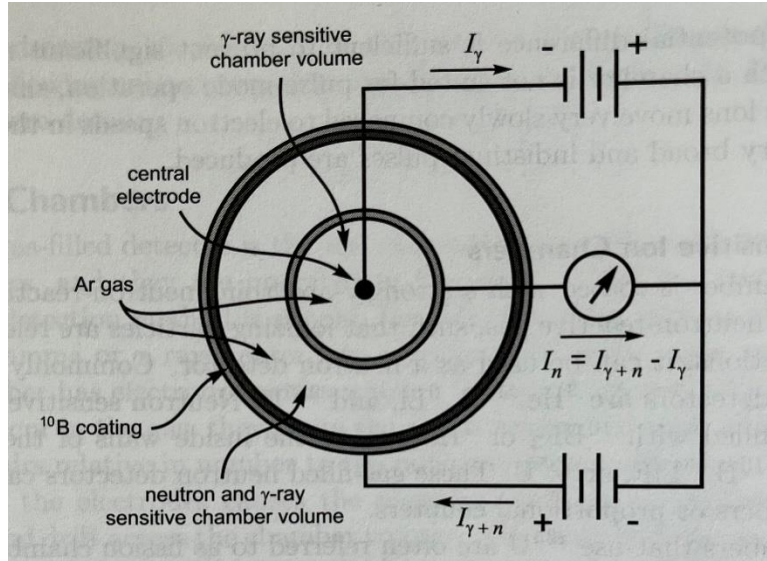


Figure 12: Radial cross section of an uncompensated ion chamber [31].

In the outer neutron-sensitive chamber the current produced by the combined neutron and gamma radiation incident on the detector flows in one direction while the current produced in the inner chamber by only gamma flows in the opposite direction. The subtraction of the gamma-only current from the combined neutron and gamma current results in a signal from the detector that is only due to the indirect ionization events caused by neutron radiation [31].

2.3.2 Description of the OSTR uncompensated ion chambers

OSTR uses two Mirion Technologies model WL-8075 uncompensated ion chambers and are shown below in Figure 13. These uncompensated ion chambers are the detectors for the percent power and safety channels that display reactor power on the control console. The chambers are cylindrical and constructed of aluminum with a diameter of 3 inches and a sensitive length of 7 inches. The neutron-sensitive coating material is ^{10}B with a thickness of 0.8 mg/cm^2 . The primary gas within the ionization chamber is a mixture of argon and diatomic nitrogen. The chambers operate in a voltage range of 200 to 1000 V with a thermal neutron sensitivity of $4.4 \times 10^{-14} \text{ A/n/cm}^2/\text{s}$ and a gamma sensitivity of $4.0 \times 10^{-11} \text{ A/R/hr}$ [33]. Being uncompensated chambers, the OSTR percent power and safety channels are only used to measure reactor power above 10 kW. This is because at powers lower than 10 kW the gamma photon flux is a significant component of the overall radiation field [1].

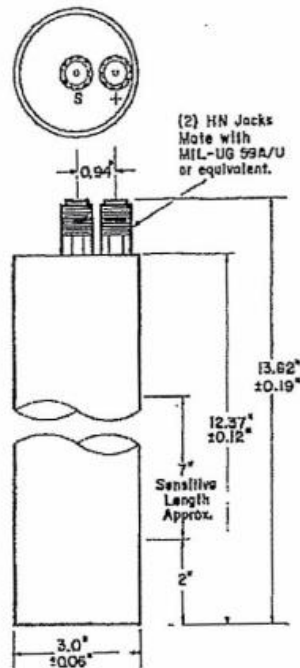


Figure 13: Mirion WL-8075 uncompensated ion chamber schematic [33].

2.3.3 Operating principle of fission chamber detectors

Another type of neutron-sensitive ion chamber is a fission chamber. In fission chambers, neutron sensitivity is introduced with a fissile material such as ^{235}U . Fission chambers, like any neutron-sensitive ion chamber, measure the indirect ionization events caused by neutrons incident on the detector. The incident neutrons will cause some atoms within the fissile material to fission and the resulting fission fragments to ionize the chamber gas [31], [34]. Fission chambers are well-suited for applications where the incident radiation field contains a large gamma photon component because fission fragments can deposit as much as 50 times more energy in the chamber than gamma photons. When operated in pulse mode the pulses from the fission fragment ionizations are many times greater in magnitude than those from gamma photons. A pulse height discriminator circuit can be used to obtain the signal that is only due to incident neutron flux, making fission chambers suitable for reactor power measurements. However, at high reactor powers, fission chambers are typically operated in current mode at high reactor powers due to problems with pulse pileup in high radiation fields [31]. For this reason, the lack of pulse discrimination in current mode is generally not of concern because the neutrons flux component of the radiation field is typically many orders of magnitude larger than that of the gamma component at high reactor powers.

2.3.4 Description of the OSTR fission chamber

The fission chamber used at OSTR is a Reuter-Stokes model number SA-C3-2510-114 type fission chamber that contains 93% enriched UO_2 with a sensitive length of 9.25 inches and is 3.12 inches in diameter. The chamber is constructed of 1100 aluminum and houses an annular aluminum substrate that is coated in 1.62 mg/cm^2 of ^{235}U . The primary gas in the chamber is argon at a pressure of 14.7 psia and the chamber is advertised as being $70\% \pm 20\%$ efficient at the time of manufacturing. The current fission chamber in the primary tank of OSTR was manufactured and delivered in 1982 [35].

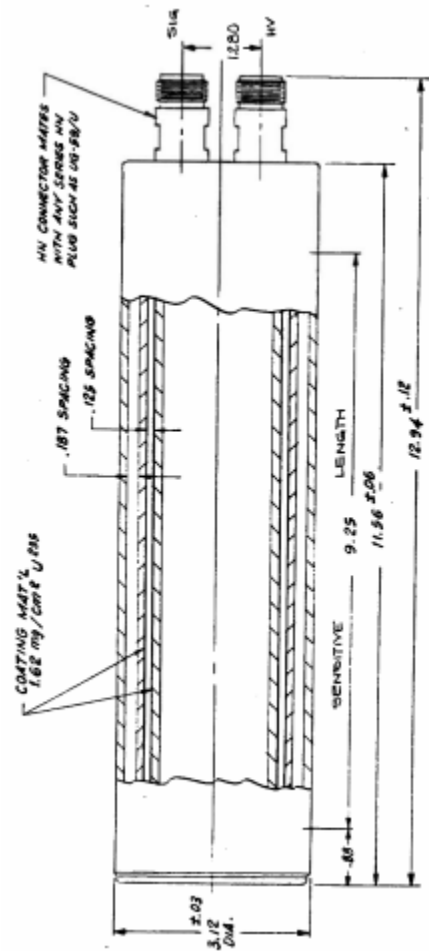


Figure 14: Reuter-Stokes SA-C3-2510-114 fission chamber schematic [35].

The current efficiency of the detector is not known. However, it is possible to estimate the current efficiency of the detector by estimating the burnup of ^{235}U in the chamber. The Reuter-Stokes

advertised sensitivity decrease of 10% per 3×10^{19} n/cm² fluence can be used with the estimated burnup to estimate a current detector efficiency [36]. The voltage range of the chamber is 200 to 800 V and has two operational modes [35]. At reactor powers below 100 W the fission chamber measuring channel operates in counting mode where individual pulses caused by single ionization events are discernable. At reactor powers above 100 W, the channel operates in mean-square voltage mode due to individual ionization events no longer being discernable. Mean-square voltage mode is the operational mode of interest in this work because OSTR control rod calibration data is obtained at powers above 100 W [4].

2.4 The Control Rod Shadowing Phenomenon

2.4.1 Description of the rod shadowing effect

Most nuclear reactors utilize multiple control rods, or in the case of larger reactors, control rod banks distributed throughout the reactor core [37]. Each control rod affects the overall flux profile within the reactor and in situations where there are multiple control rods present, the flux profile can become complex due to the combined effect of all the control rods [37]. This gives rise to a phenomenon where control rods may neutronically interact with one another. These control rod interactions are observed when the reactivity worth of one control rod depends on the presence of other control rods within the core [38].

These changes in control rod reactivity worth may occur in situations at high reactor power where multiple control banks are present, and the orientation and height of one bank relative to the other changes the reactivity worth of certain control rods. This phenomenon has been observed in large-scale reactors where multiple control rod banks are present [37]–[39]. These changes in control rod worth may be perceived as changes in reactivity worth at low powers where the location of the reactor power detectors relative to peak neutron flux has been shifted due to control rod interactions [40].

Recent work by LaPorta 2019 reveals that the close proximity of a control rod being withdrawn relative to a neutron source in the Transient Reactor Test (TREAT) Facility during an initial approach to criticality resulted in a higher reactor power locally near the source than was observed on the startup channel instruments [40]. The reactor was projected to achieve criticality on far lower shim rod reactivity insertion than anticipated [40]. These projections were determined to be unreasonable and disagreed with the historical value of the control rods [40]. Ultimately the effect diminishes in TREAT with increasing rod withdrawal and projected critical worths agree with predicted values [40].

Phenomena in which control rod interactions result in the under-valuing of a control rod's reactivity worth are known as "rod shadowing," and phenomena in which interactions result in over-valuing of their worth are known as "rod anti-shadowing" [37]–[40].

3.0 Materials and Methods

3.1 The OSTR MCNP® Model

3.1.1 Monte Carlo N-Particle (MCNP®)

The equation that describes the behavior of neutrons in a reactor is known as the Neutron Transport Equation [27]:

$$\frac{1}{v} \frac{\partial \varphi}{\partial t} + \hat{\Omega} \cdot \nabla \varphi + \Sigma_t(r, E) \varphi(r, E, \hat{\Omega}, t) = \int_0^{4\pi} d\hat{\Omega}' \int_0^{\infty} dE' \Sigma(E' \rightarrow E, \hat{\Omega}' \rightarrow \hat{\Omega}) \varphi(r, E', \hat{\Omega}', t) + s(r, E, \hat{\Omega}, t) \quad (3.1)$$

Where φ is the angular neutron flux, v is the neutron velocity and s is the source term. Numerical solutions to the neutron transport equation that seek to calculate the neutron multiplication factor of a system (k_{eff}) typically are of a time independent form of Equation 3.1 where the time-dependence of the angular flux is removed. The resulting time-independent transport equation is no longer true for non-critical systems and an eigenvalue is added to the source term to balance the equation for non-critical systems [41]. The inverse of the eigenvalue is the neutron multiplication factor (k_{eff}). Monte Carlo or stochastic methods do not solve the neutron transport equation directly. Rather, they simulate particle histories individually and the average behavior of particles in the physical system is inferred from the average behavior of the simulated particles using the central limit theorem. While MCNP® 6.2 is capable of certain time-dependent calculations for the behavior of particles, a k_{eff} calculation is inherently time-independent because the code is iterating or sampling the system with many particles over iterative cycles to converge a solution to the eigenvalue [42]. A k-eigenvalue calculation was of interest in this work because the reactivity insertion caused by a particular control rod configuration can be calculated from k_{eff} using Equation 3.2.

$$\rho = \frac{k_{eff} - 1}{k_{eff}} \quad (3.2)$$

3.1.2 Model description

The as-delivered MCNP® model of the OSTR used in this work includes the four beam ports, the aluminum primary tank, the thermalizing column, the thermal column, the rotating rack, the reflector, the reflector cladding, and all in-core components. Regions below the primary aluminum tank and regions more than 80 cm above the core mid-plane are voided, and storage racks at the tank periphery are omitted. A visualization of the model geometry is shown below in Figure 15. The model uses the ENDF/B-VII.1 library and includes S(α, β) cards for the negative temperature-feedback effects in moderator and fuel materials. However, control rod calibrations at OSTR are performed at low powers to negate these negative temperature-feedback effects, and a cold core ($<30^{\circ}\text{C}$) with negligible ^{135}Xe content ($<\$0.30$) [4].

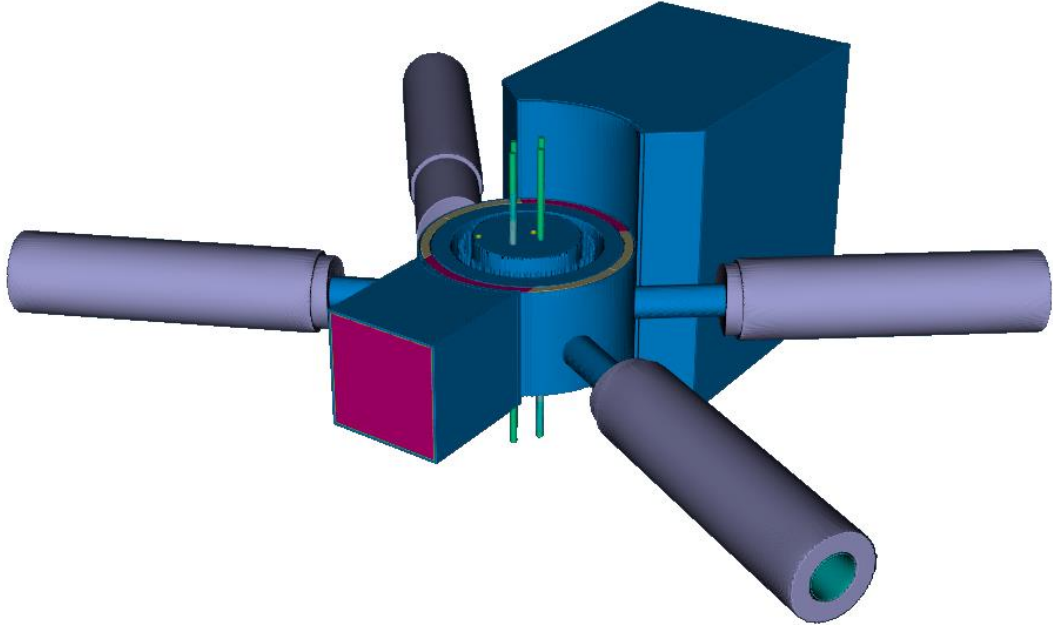


Figure 15: Visualization of the as-provided OSTR model.

3.1.3 Normal Core Geometry

After LEU conversion in 2008, OSTR had three different core configurations known as the normal, cadmium-lined in-core irradiation tube (CLICIT), and in-core irradiation tube (ICIT) configurations. The most reactive of the three was the normal core configuration. For this reason, the normal core configuration was of the most interest for control rod calibrations in 2008 as the normal configuration would be closest to the core excess reactivity limit. In the normal core configuration, position A1 is voided with an aluminum plug (central thimble) and the four control rods occupy their standard locations in C4, D10, C10, and D1. All G-ring positions are filled with graphite reflector elements except G15 (fuel), G16 (neutron source), and G2 (pneumatic transfer system terminus). The normal core diagram can be seen in Figure 10, section 2.1.3.

The as-provided OSTR model input deck was configured for the CLICIT core configuration and had to be modified to reflect the normal configuration. All of the geometry changes needed for these modifications already existed as commented-out lines of code in the input deck. However, it was discovered that the altered model contained an inaccuracy in that the G-ring irradiation tube (GRICIT) had been included in the normal core configuration. This error was corrected, and the model used to perform calculations in this work represents the true normal core configuration as it was in October 2008. The final geometry modifications included altering control rod heights and the addition of the 9 fission chamber assemblies described in section 3.2.

3.1.4 CLICIT Core Geometry

The as-provided OSTR input deck was already in the CLICIT core configuration and the only geometry modifications included the addition of the nine fission chamber assemblies and the changing of control rod heights.

3.2 Fission Chamber Geometry and Materials

3.2.1 Geometry description

The Reuter-Stokes model number SA-C3-2510-114 fission chamber at OSTR is a cylindrical neutron-sensitive ion chamber that resides in an 11.56 ± 0.06 -inch-long, 3.12 ± 0.03 -inch diameter aluminum housing. The DC high voltage connectors at the top of the housing are made of magnesium and insulated with alumina ceramic. The internal sensitive length of the detector consists of a 0.125-inch-thick, 9.25-inch-long aluminum tube substrate that is coated on both its inner and outer surface

with UO_2 enriched to 93% ^{235}U . There is a 0.187-inch argon-filled gap from the inner surface of the housing to the outer surface of the coated substrate, and an argon-filled zone within the inner surface of the coated substrate. The argon-filled regions of the chamber are pressurized to 14.7 psia [35].

3.2.2 Components Included in The Model

The quantity of interest for modeling detector response was the fission rate in the UO_2 ceramic layers, making the UO_2 layers the most important part of the detector to model. The fission rate can easily be tallied in MCNP® and is directly proportional to the ionization rate in the detector at low reactor powers when a pulse height discriminator is used to discriminate between fission fragment ionization events and photon ionization events.

Since the quantity of interest in the detector was the fission rate in the UO_2 layers in the detector, the modeling of ionization events in the argon gas was determined to be of no concern. In addition, the thermal neutron absorption cross section of argon is 0.66 b [23], making the shielding effects of the argon regions on the UO_2 regions negligible. The mean free path of a neutron in a given material can be calculated using Equations 3.3 and 3.4:

$$\Sigma_{tr} = \Sigma_s(1 - \mu_0) \quad (3.3)$$

$$\lambda = \frac{1}{\Sigma_{tr}} \quad (3.4)$$

Where Σ_{tr} is the macroscopic transport cross section, Σ_s is the macroscopic scattering cross section, $1 - \mu_0$ is the cosine of the scattering angle, and λ is the mean free path. Based on values from Appendix A in Duderstadt and Hamilton 1976, the mean free path of a thermal neutron in aluminum was estimated to be 12.2 cm [27]. Therefore, the aluminum outer shell of the detector was determined to be of little neutronic importance.

For the previously mentioned reasons, the argon and aluminum regions are of little neutronic importance and could have likely been omitted from the model. However, the inclusion of all the components of the sensitive length of the detector were not computationally expensive and were included in the model for increased accuracy. The modeled detector geometries included the outer aluminum shell, the outer argon gap, the outer UO_2 layer, the aluminum substrate, the inner UO_2 layer, and the inner argon chamber. The non-sensitive upper and lower ends of the detectors were omitted from the model.

3.2.3 Placement of fission chambers

Three values needed to be known for the correct placement of the original fission chamber in the model. These included the radial distance from the core centerline, the axial distance from the core mid-plane, and the angle from 0° of north. The Cartesian coordinates for the detector surfaces were calculated from these estimated values. The radial distance from the core center line was estimated from the known radius of the reflector, the known radius of the detector, and the fact that the two are not quite in contact because the detector rests in an aluminum cup that is affixed to the reflector cladding. This aluminum cup acts as a guide tube and prevents the detector from being dropped to the bottom of the tank when height adjustments are made during power calibrations. The water-filled gap between the two was not known and not easily measurable with available tools. Therefore, the gap was visually estimated with the OSTR underwater drone to be approximately 8 mm.

The axial distance from the core mid-plane was estimated by physically measuring the height difference between the top of the reflector and the top of the detector with a tool used to work on OSTR from the reactor top. Since the height of the top of the reflector and the total length of the detector are known, the difference between the two were used to calculate the vertical placement of the detector. This resulted in vertical placement of the center of the detector 23.495 cm above the core mid-plane. The angular offset from 0° of north was estimated from the core and reflector schematic shown below in Figure 16. An image processing tool, ImageJ, was used to measure the angle between 0° and the line formed from the core center to detector cup center. This angle is estimated to be 348.2° of north. A visualization of fission chamber placement is shown below in Figure 17.

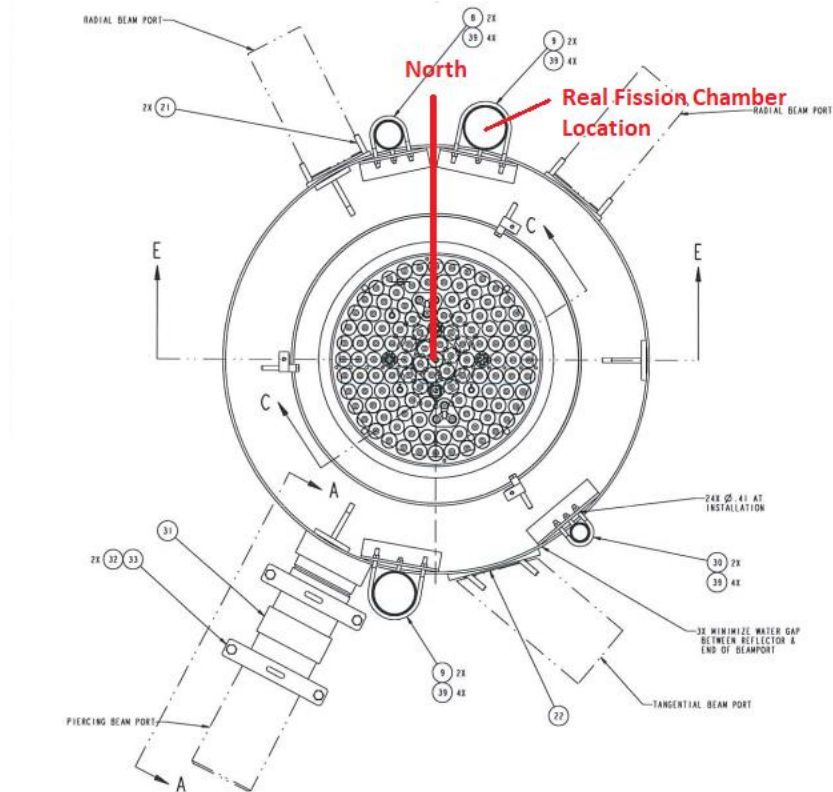


Figure 16: OSTR radial core and reflector assembly schematic [20].

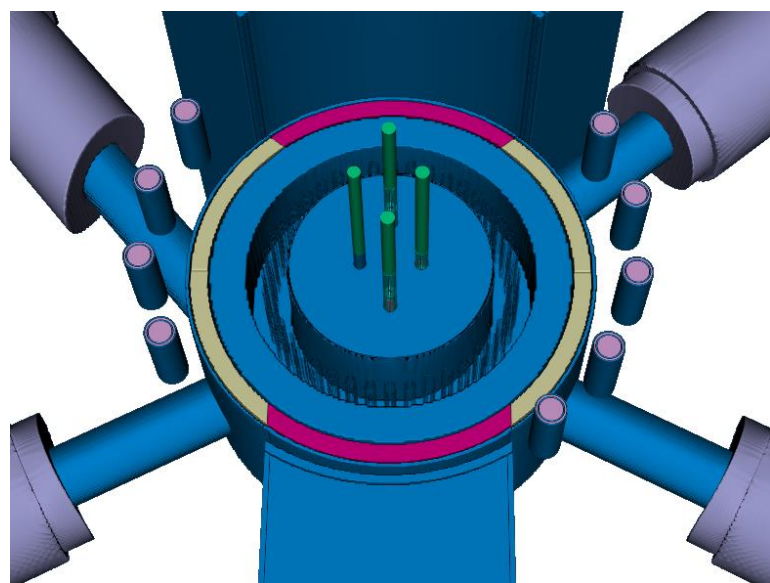


Figure 17: Modeled fission chamber placement.

3.3 Fission Chamber Materials

3.3.1 Description of materials as advertised

The body material of the fission chamber and the substrate for the UO₂ coating are both constructed of 1100 aluminum alloy which is at minimum 99% pure aluminum [43]. The UO₂ fissile material was advertised as being 93% enriched [35]. However, the percent composition of impurities was unknown. The same is true for the argon gas in the detector which was assumed to be pure argon at natural isotopic abundance since an exact composition was not given.

3.3.2 Modeled materials

The aluminum parts of the detector were of little neutronic importance because the mean free path of a thermal neutron in aluminum was found to be many times the thickness of the parts. For this reason, the aluminum parts of the detector were modeled as 6061-T6 aluminum alloy which is close in composition to 1100 aluminum alloy but contains Si and Mg for the formation of Mg₂Si for precipitation formation during heat treatment. 6061-T6 is tempered to provide precipitation hardening and increase the yield strength [43] but this is also of little neutronic importance. This substitution was performed for simplification of model alterations since the materials card for 6061-T6 aluminum alloy was already present in the OSTR MCNP® input deck.

3.3.3 ²³⁵UO₂ layer thickness calculation

The only specification relating to the thickness of the UO₂ layers in the fission chamber was a mass per square area specification for ²³⁵UO₂ of 1.62 $\frac{mg}{cm^2}$ [35]. Material number 85 in the MCNP® input deck, the 93% enriched UO₂, included both an atomic fraction of U corresponding to 93% ²³⁵U and natural isotopic abundance for the remaining 7%. All O is assumed to be ¹⁶O. In addition, the mass differences between ²³⁴U, ²³⁵U, and ²³⁸U were assumed negligible on the scale of $\frac{mg}{cm^2}$. Therefore, the assumption was made that the 1.62 $\frac{mg}{cm^2}$ of ²³⁵UO₂ could be reasonably treated as 1.62 $\frac{mg}{cm^2}$ of UO₂ for the purposes of calculating the UO₂ layer thickness. This calculation was made by simply dividing the density of U ($10.97 \frac{g}{cm^3}$) [44] by the advertised mass per area ($1.62 \frac{mg}{cm^2}$) to estimate a layer thickness of 0.15 mm.

3.4 Fission Chamber Tally Specifications

3.4.1 Tallied Events

The OSTR fission chamber is an ionization chamber that generates current when ionizing particles such as gamma photons or fission fragments ionize the gas within it [28]–[31]. The fission rate in the detector is directly proportional to the neutron flux incident on the detector. At low powers it operates in pulse mode and a pulse height discriminator counts only the ionization events due to heavily ionizing fission fragments. The fissions taking place in the detector were the events of interest because they are proportional to the detector signal.

3.4.2 Tallied Cells

Since detector response as a function of location was of interest, a fission rate tally was created in the MCNP® model for the cells containing the UO₂ coating within the detector. There are two cells per detector for the inner and outer UO₂ coating. The overall fission tally for each detector is the sum of these fission rate tallies. This fission rate tally was obtained from a neutron flux *f4* tally and a multiplier card.

3.4.3 Multiplier card

A tally multiplier card must be used to obtain a fission rate tally from a neutron flux tally in MCNP®. First, a multiplier number was arbitrarily chosen to multiply the model flux by. The purpose of this multiplier number is to calculate what the actual flux in the reactor would be if the reactor were operating at a power that involves far more particles than can be computationally modeled. Since a multiplier number had already been calculated for 1 MW steady-state operations, a number that corresponds to 800 W (the upper data collection limit in control rod calibrations) was chosen. However, this number has little meaning and no effect on the statistics associated with the tally as MCNP® reports relative error for *f4* tallies.

Next, an entry was used to specify multiplier type. A -6 following the multiplier specifies that the neutron flux incident on the detector is to be multiplied by the total fission cross section of the material to obtain a fission reaction rate as the tally output. The specification of which total fission cross section to use is an entry following the multiplier type, material 85 for the UO₂ layers in this case.

3.5 Flux Map Tally Specifications

3.5.1 Tallied Cells

Extremely detailed flux tallies were already in existence in the fuel elements and experimental facilities in the OSTR MCNP® model. Each fuel element contains three fuel meat segments that are divided into three zones axially and three zones radially for a total of 27 fuel zones per fuel element. Each of these 27 zones in a fuel element had an *f4* tally associated with it for very accurate burnup calculations at OSTR. These existing flux tallies were utilized to map the thermal neutron flux across the OSTR model using only the cells in the fuel at the core axial mid-plane.

3.5.2 Energy Bins

A flux energy bin card was associated with the *f4* flux tallies in the fuel at core mid-plane. The upper limit energy cutoff for thermal neutrons was 0.5 eV and fast neutrons were tallied from 100 keV to 20 MeV. An epithermal tally was taken between 0.5 eV and 100 keV. However, the epithermal and fast flux distributions were not mapped or considered in this work because OSTR is a thermal reactor and the movement of the power peak location in the core during control rod calibrations was the phenomenon of interest. Fast neutrons from the core are the most likely to reach the power detectors and the location of maximum fission neutron birth will occur at the location of maximum thermal neutron flux. Therefore, the location of peak thermal neutron flux relative to the fission chamber detector was of interest.

3.6 Flux Map Interpolation

The thermal flux maps shown in section 4.5 are interpolated surfaces fitted to the normalized thermal flux tallies taken at core axial mid plane in each fuel element and control rod. The tallies were first parsed out of the MCNP® output files and normalized, then comma-separated value (CSV) files were generated that included the x-y location of each tally and the normalized thermal flux values were the z value. These CSVs were then imported into MatLab® and an interpolated surface was fit to each data set using the *griddata* function for cubic spline fitting of a mesh. This process was repeated for each control rod pull for both the normal and CLICIT core configurations. These Figures show how the thermal flux distribution changed as control rod positions changed in the calibration process.

3.7 Startup Logs

3.7.1 Critical rod heights

Before each control rod pull was performed in the 2008 OSTR control rod calibration procedure the reactor was stabilized at 15 W and the critical control rod heights were recorded. These critical control rod heights were used to calculate the OSTR MCNP® model bias. The control rods in the MCNP® were set to the recorded critical heights and a *kcode* problem was run for each critical configuration to calculate an average departure from criticality for the normal and CLICIT core models to quantify the accuracy of each. The critical control rod heights used for each were taken from OSTR Logbook #150 [2] and are listed below in Tables 3-1 and 3-2.

Table 3-1: Normal core critical control rod heights [2].

<i>Critical Configuration</i>	Transient	Safety	Shim	Regulating
<i>Transient 1</i>	0.0	48.0	48.0	48.3
<i>Transient 2</i>	22.1	44.8	44.8	44.8
<i>Transient 3</i>	34.3	41.5	41.5	41.6
<i>Transient 4</i>	45.2	38.1	38.1	38.3
<i>Transient 5</i>	56.4	34.7	34.7	34.7
<i>Transient 6</i>	69.3	31.3	31.3	31.4
<i>Safety 1</i>	47.4	0.0	47.4	47.3
<i>Safety 2</i>	44.1	23.3	44.1	44.2
<i>Safety 3</i>	41.2	35.6	41.1	41.1
<i>Safety 4</i>	37.9	46.7	37.9	37.8
<i>Safety 5</i>	34.6	58.1	34.6	34.6
<i>Safety 6</i>	31.4	70.7	31.4	31.5
<i>Shim 1</i>	47.7	47.7	0.0	47.8
<i>Shim 2</i>	44.4	44.4	23.2	44.4
<i>Shim 3</i>	41.2	41.2	35.4	41.2
<i>Shim 4</i>	37.9	37.9	46.3	37.8
<i>Shim 5</i>	34.6	34.6	57.1	34.5
<i>Shim 6</i>	31.2	31.2	69.4	31.2
<i>Regulating 1</i>	51.7	51.7	51.7	0.0
<i>Regulating 2</i>	47.9	47.9	47.9	19.3
<i>Regulating 3</i>	44.1	44.1	44.1	30.2
<i>Regulating 4</i>	40.3	40.3	40.3	39.2
<i>Regulating 5</i>	36.4	36.4	36.4	48.0
<i>Regulating 6</i>	32.6	32.6	32.5	56.8
<i>Regulating 7</i>	28.7	28.7	28.7	66.5
<i>Regulating 8</i>	24.6	24.6	24.6	77.9

Table 3-2: CLICIT core critical control rod heights [2].

<i>Critical Configuration</i>	Transient	Safety	Shim	Regulating
<i>Transient 1</i>	0.0	63.1	63.1	63.1
<i>Transient 2</i>	24.4	58.7	58.6	59.1
<i>Transient 3</i>	36.9	55.7	55.7	54.0
<i>Transient 4</i>	49.2	52.0	52.0	49.4
<i>Transient 5</i>	61.6	48.0	48.0	46.6
<i>Transient 6</i>	72.2	44.5	44.5	46.5
<i>Safety 1</i>	61.0	0.0	61.0	61.7
<i>Safety 2</i>	57.3	26.4	57.4	57.3
<i>Safety 3</i>	53.7	40.0	53.7	53.8
<i>Safety 4</i>	50.2	51.7	50.2	50.6
<i>Safety 5</i>	46.9	65.8	46.9	46.8
<i>Shim 1</i>	63.6	63.6	0.0	64.0
<i>Shim 2</i>	59.7	59.7	24.7	59.7
<i>Shim 3</i>	55.5	55.5	37.0	55.4
<i>Shim 4</i>	51.5	51.5	47.7	52.0
<i>Shim 5</i>	48.1	48.0	58.7	48.1
<i>Shim 6</i>	44.9	44.9	69.6	45.0
<i>Regulating 1</i>	68.3	67.8	67.8	0.0
<i>Regulating 2</i>	62.9	62.8	62.9	22.1
<i>Regulating 3</i>	58.3	58.2	58.3	33.5
<i>Regulating 4</i>	53.9	53.8	53.8	43.3
<i>Regulating 5</i>	49.7	49.7	49.6	52.9
<i>Regulating 6</i>	45.8	45.8	45.8	63.4
<i>Regulating 7</i>	42.3	42.4	42.4	75.3

3.7.2 Control rod calibration heights

After the reactor was stabilized at 15 W a positive period was induced by withdrawing the control rod being calibrated. Once a desired period was achieved the rod would stop being withdrawn and the reactor was allowed to be supercritical at that control rod configuration until 800 W was achieved. These supercritical configurations were used to model the control rod calibration process using the OSTR MCNP® model and calculate detector response. These supercritical rod heights were taken from OSTR Logbook #150 [2] and listed below in Tables 3-3 and 3-4

Table 3-3: Normal core supercritical control rod heights [2].

<i>Critical Configuration</i>	Transient	Safety	Shim	Regulating
<i>Transient 1</i>	22.1	48.0	48.0	48.3
<i>Transient 2</i>	34.3	44.8	44.8	44.8
<i>Transient 3</i>	45.2	41.5	41.5	41.6
<i>Transient 4</i>	56.4	38.1	38.1	38.3
<i>Transient 5</i>	69.3	34.7	34.7	34.7
<i>Transient 6</i>	100.0	31.3	31.3	31.4
<i>Safety 1</i>	47.4	23.3	47.4	47.3
<i>Safety 2</i>	44.1	35.6	44.1	44.2
<i>Safety 3</i>	41.2	46.7	41.1	41.1
<i>Safety 4</i>	37.9	58.1	37.9	37.8
<i>Safety 5</i>	34.6	70.7	34.6	34.6
<i>Safety 6</i>	31.4	100.0	31.4	31.5
<i>Shim 1</i>	47.7	47.7	23.2	47.8
<i>Shim 2</i>	44.4	44.4	35.4	44.4
<i>Shim 3</i>	41.2	41.2	46.3	41.2
<i>Shim 4</i>	37.9	37.9	57.1	37.8
<i>Shim 5</i>	34.6	34.6	69.4	34.5
<i>Shim 6</i>	31.2	31.2	100.0	31.2
<i>Regulating 1</i>	51.7	51.7	51.7	19.3
<i>Regulating 2</i>	47.9	47.9	47.9	30.2
<i>Regulating 3</i>	44.1	44.1	44.1	39.2
<i>Regulating 4</i>	40.3	40.3	40.3	48.0
<i>Regulating 5</i>	36.4	36.4	36.4	56.8
<i>Regulating 6</i>	32.6	32.6	32.5	66.5
<i>Regulating 7</i>	28.7	28.7	28.7	77.9
<i>Regulating 8</i>	24.6	24.6	24.6	100.0

Table 3.4

Table 3-4: CLICIT core supercritical control rod heights [2].

<i>Critical Configuration</i>	Transient	Safety	Shim	Regulating
<i>Transient 1</i>	24.4	63.1	63.1	63.1
<i>Transient 2</i>	36.9	58.7	58.6	59.1
<i>Transient 3</i>	49.2	55.7	55.7	54.0
<i>Transient 4</i>	61.6	52.0	52.0	49.4
<i>Transient 5</i>	72.2	48.0	48.0	46.6
<i>Transient 6</i>	100.0	44.5	44.5	46.5
<i>Safety 1</i>	61.0	26.4	61.0	61.7
<i>Safety 2</i>	57.3	40.0	57.4	57.3
<i>Safety 3</i>	53.7	51.7	53.7	53.8
<i>Safety 4</i>	50.2	65.8	50.2	50.6
<i>Safety 5</i>	46.9	100.0	46.9	46.8
<i>Shim 1</i>	63.6	63.6	24.7	64.0
<i>Shim 2</i>	59.7	59.7	37.0	59.7
<i>Shim 3</i>	55.5	55.5	47.7	55.4
<i>Shim 4</i>	51.5	51.5	58.7	52.0
<i>Shim 5</i>	48.1	48.0	69.6	48.1
<i>Shim 6</i>	44.9	44.9	100.0	45.0
<i>Regulating 1</i>	68.3	67.8	67.8	22.1
<i>Regulating 2</i>	62.9	62.8	62.9	33.5
<i>Regulating 3</i>	58.3	58.2	58.3	43.3
<i>Regulating 4</i>	53.9	53.8	53.8	52.9
<i>Regulating 5</i>	49.7	49.7	49.6	63.4
<i>Regulating 6</i>	45.8	45.8	45.8	75.3
<i>Regulating 7</i>	42.3	42.4	42.4	100.0

3.7.3 The Inhour Equation

The reactivity worth, in dollars, associated with the stable reactor period induced by the withdrawal of a control rod is given by the Inhour equation (Eq. 2.3):

$$\frac{\rho}{\beta_{eff}} = \frac{l^*}{\beta_{eff} T} + \sum_{i=1}^6 \frac{\beta_i}{1 + \lambda_i T}$$

Where l^* is the prompt neutron generation time, T is the stable reactor period, β_i is the delayed neutron fraction of the i^{th} delayed neutron group, and λ_i is the decay constant for the i^{th} delayed neutron group. The delayed neutron fractions and decay constants are given below in Table 3-5 for a ^{235}U fueled reactor [4], [27].

Table 3-5: Six-group delayed neutron precursor fractions and decay constants.

<i>Delayed Neutron Group (i)</i>	Delayed Neutron Fraction (β)	Decay Constant (λ) [s^{-1}]
1	0.038	0.012716
2	0.213	0.031738
3	0.188	0.115525
4	0.407	0.310828
5	0.128	1.397474
6	0.026	3.872331

3.7.4 Reactor period calculation

The only quantity that must be measured to calculate the reactivity worth of a segment of control rod from Equation 2.3 is the stable reactor period, where the reactor period is the time for reactor power to increase by a factor of e . The reactor power as a function of time and the reactor period is given as [4], [27]:

$$P(t) = P_0 e^{\frac{t}{T}} \quad (3.5)$$

Solving for the reactor period yields:

$$T = \frac{t}{\ln\left(\frac{P(t)}{P_0}\right)} \quad (3.6)$$

In the control rod calibration procedures at OSTR this stable period is calculated as an average over a specified power range:

$$T = \frac{\Delta t}{\ln\left(\frac{P_2}{P_1}\right)} \quad (3.7)$$

Where P_2 and P_1 are 800 W and 200 W, or 80% and 20% of the 1 kW range, respectively. This power range is chosen to measure the power rise because it is low enough to negate negative temperature feedback effects in the fuel, yet high enough to accurately measure reactor period. The control rod perturbations in the OSTR control rod calibration procedures are performed at a critical power of 15 W and data is not collected until 200 W to negate the effects of delayed neutron precursors, ensuring a constant reactor period [4].

3.7.5 Reactivity worth calculation

The reactivity worth of a control rod perturbation in dollars can be calculated by substituting Equation 3.7 into Equation 2.3 and multiplying by β_{eff} :

$$\rho [\$] = \frac{l^*}{\frac{\Delta t}{\ln\left(\frac{P_2}{P_1}\right)}} + \beta_{eff} \cdot \sum_{i=1}^6 \frac{\beta_i}{1 + \lambda_i \left(\frac{\Delta t}{\ln\left(\frac{P_2}{P_1}\right)} \right)} \quad (3.8)$$

It can be seen in Equation 3.8 that the only way to skew the reactivity measurement for a given control rod pull is to alter the time of power rise Δt from P_1 to P_2 which are constant at 200 W and 800 W respectively in the control rod calibration procedure. This implies that control rod shadowing on a single detector is a time-dependent phenomenon. However, it was believed that modeling identical detectors at multiple points in space at a singular moment in time would reveal control rod shadowing effects. The difference in detector response as a function of location is due to differences in neutron flux incident on each detector.

3.8 Model Bias Calculation

After the normal and CLICIT core models were updated and the detectors were added, it was necessary to determine the neutron multiplication factor bias in the OSTR model so that the bias could be subtracted from the modeled control rod calibration results. This was accomplished for both normal and CLICIT configurations by running a k-eigenvalue problem with 300,000 neutrons for 100 cycles for each critical control rod configuration listed in Tables 3.1 and 3.2 just before each rod pull was performed. It is assumed that OSTR was exactly critical on average over a time span of about 5 minutes at these control rod configurations [45]. The difference between the model k_{eff} for each configuration and $k_{eff} = 1$ was calculated and an average taken across all configurations. The bias in the OSTR model is found to be very low for both normal core and CLICIT core configurations at -0.04 ± 0.04 and 0.07 ± 0.04 , respectively.

3.9 Calculated Control Rod Worth

3.9.1 Modeled Control Rod Calibrations

Once a model bias was established, the next task was to calculate the integrated reactivity worth of each control rod in each configuration. This was accomplished by altering the control rod heights in the model to match the rod heights after a withdrawal was performed to induce a positive reactor period. The rod heights corresponding to these supercritical configurations can be found in Tables 3.3 and 3.4.

3.9.2 K-code Specifications

k-eigenvalue problems (*kcode*) were run in MCNP® for the model bias calculations, control rod calibration pulls, and flux mapping runs with 3 source points (*ksrc*) per fuel element. The model bias calculation runs and flux mapping runs were performed with 100,000 neutrons per cycle for 100 cycles where the first 25 cycles were omitted from the statistical analysis and the initial guess for the eigenvalue (k_{eff}) is 1.0. Due to extreme challenges in transporting an appreciable neutron flux beyond the reflector to the detectors, the control rod calibration runs were performed using 1,000,000 neutrons per cycle for 100 cycles where the first 25 cycles were omitted from the statistical analysis and the initial guess for the eigenvalue (k_{eff}) is 1.0. A very large number of particles per cycle was required to reduce the relative error associated with the fission rate in the detectors and a variance reduction method was employed to further reduce the error.

3.10 Variance Reduction Method

Variance reduction techniques built into MCNP® can be used to obtain results of sufficient precision using less computer time than creating more particle histories. The time per particle history and the particle history variance in a Monte Carlo calculation are affected by tally type and random walk sampling. Time per particle history may be reduced at the expense of variance if less random walks are sampled (i.e., less particle histories) or the tally dimensions are reduced (i.e., a point detector versus a surface flux). Conversely, the particle history variance may be reduced at the expense of time per particle history if more computational resources are used to sample more random walks or increase tally dimensions [42]. MCNP® estimates tallies of the form:

$$\langle T \rangle = \int d\vec{r} \int d\vec{v} \int dt N(\vec{r}, \vec{v}, t) T(\vec{r}, \vec{v}, t) \quad (3.9)$$

Where $N(\vec{r}, \vec{v}, t)$ is the particle density and $T(\vec{r}, \vec{v}, t)$ is the tally function. Analog Monte Carlo calculations sample all particles or random walks according to their natural physical probability, i.e., any given event, particle or region has a weight of one [42].

Nonanalog Monte Carlo calculations do not directly simulate nature because $N(\vec{r}, \vec{v}, t)$ and $T(\vec{r}, \vec{v}, t)$ may be weighted accordingly as long as $\langle T \rangle$ is preserved. MCNP® variance reduction techniques attempt to produce better statistical estimates of $N(\vec{r}, \vec{v}, t)$ in regions where $T(\vec{r}, \vec{v}, t)$ is assigned a higher importance at the expense of random walk sampling in regions where $T(\vec{r}, \vec{v}, t)$ is assigned less importance. Particle splitting is one such nonanalog method for variance reduction in MCNP®. Particle splitting involves dividing the particle's weight among the specified number of progeny particles at the tally boundary and following each of the progeny independently within the tally region [42].

In MCNP® particle splitting is achieved by altering the importance of a cell or region of interest. The cell importance can be used to either continue the particle history when it enters the cell (importance equal to one) or terminate the particle history upon entering the cell (importance equal to zero). In addition, assigning a cell an importance higher than one results in particle splitting. For example, an importance of two splits the particle of interest into two progeny and $N(\vec{r}, \vec{v}, t)$ is increased in the cell at the expense of $T(\vec{r}, \vec{v}, t)$ in regions with an importance of one to reduce tally variance while preserving computational efficiency [42]. In this work, variance reduction in the form of particle splitting

was employed to reduce the relative error involved in the fission rate tallies associated with the nine fission chambers. This was accomplished by assigning the UO₂ cells in each detector an importance of three.

4.0 Results/Discussion

4.1 Experimental Control Rod Calibrations

4.1.1 Normal Core Control Rod Calibrations

The control rod calibration procedure detailed in OSTROP 9 [4] was performed for both the normal and CLICIT core configurations at LEU core BOL in October 2008. The differential reactivity worth for each section of control rod is calculated from the average reactor period induced by withdrawing the segment of control rod. This average period is calculated from the measured time of power rise from 200 to 800 W [4]. The measured differential integral control rod worths for the normal core configuration are provided in Tables 4-1 through 4-4. These control rod calibration results for the normal core configuration result in a measured total core reactivity worth of \$11.99 [45].

Table 4-1: Normal core transient control rod calibration results.

<i>Configuration</i>	<i>Transient</i>	<i>Safety</i>	<i>Shim</i>	<i>Regulating</i>	<i>Time [ms]</i>	<i>Period [s]</i>	<i>Reactivity [\$]</i>	<i>Cumulative [\$]</i>
<i>Transient 1</i>	22.1	48.0	48.0	48.3	9098	6.56	0.47	0.47
<i>Transient 2</i>	34.3	44.8	44.8	44.8	8753	6.31	0.47	0.94
<i>Transient 3</i>	45.2	41.5	41.5	41.6	8534	6.16	0.48	1.42
<i>Transient 4</i>	56.4	38.1	38.1	38.3	8804	6.35	0.47	1.89
<i>Transient 5</i>	69.3	34.7	34.7	34.7	9704	7.00	0.45	2.34
<i>Transient 6</i>	100.0	31.3	31.3	31.4	6085	4.39	0.54	2.88

Table 4-2: Normal core safety control rod calibration results.

<i>Configuration</i>	Transient	Safety	Shim	Regulating	Time [ms]	Period [s]	Reactivity [\$]	Cumulative [\$]
<i>Safety 1</i>	47.4	23.3	47.4	47.3	9033	6.52	0.47	0.47
<i>Safety 2</i>	44.1	35.6	44.1	44.2	9484	6.84	0.46	0.93
<i>Safety 3</i>	41.2	46.7	41.1	41.1	9307	6.71	0.46	1.39
<i>Safety 4</i>	37.9	58.1	37.9	37.8	9985	7.20	0.45	1.84
<i>Safety 5</i>	34.6	70.7	34.6	34.6	12009	8.66	0.42	2.25
<i>Safety 6</i>	31.4	100.0	31.4	31.5	11481	8.28	0.42	2.68

Table 4-3: Normal core shim control rod calibration results.

<i>Configuration</i>	Transient	Safety	Shim	Regulating	Time [ms]	Period [s]	Reactivity [\$]	Cumulative [\$]
<i>Shim 1</i>	47.7	47.7	23.2	47.8	9019	6.51	0.47	0.47
<i>Shim 2</i>	44.4	44.4	35.4	44.4	9211	6.64	0.46	0.93
<i>Shim 3</i>	41.2	41.2	46.3	41.2	8756	6.32	0.47	1.41
<i>Shim 4</i>	37.9	37.9	57.1	37.8	9638	6.95	0.46	1.86
<i>Shim 5</i>	34.6	34.6	69.4	34.5	10441	7.53	0.44	2.30
<i>Shim 6</i>	31.2	31.2	100.0	31.2	7630	5.50	0.50	2.80

Table 4-4: Normal core regulating control rod calibration results.

<i>Configuration</i>	Transient	Safety	Shim	Regulating	Time [ms]	Period [s]	Reactivity [\$]	Cumulative [\$]
<i>Regulating 1</i>	51.7	51.7	51.7	19.3	8686	6.27	0.47	0.47
<i>Regulating 2</i>	47.9	47.9	47.9	30.2	7536	5.44	0.50	0.98
<i>Regulating 3</i>	44.1	44.1	44.1	39.2	7761	5.60	0.50	1.47
<i>Regulating 4</i>	40.3	40.3	40.3	48.0	7663	5.53	0.50	1.97
<i>Regulating 5</i>	36.4	36.4	36.4	56.8	8112	5.85	0.49	2.46
<i>Regulating 6</i>	32.6	32.6	32.5	66.5	9778	7.05	0.45	2.91
<i>Regulating 7</i>	28.7	28.7	28.7	77.9	11091	8.00	0.43	3.34
<i>Regulating 8</i>	24.6	24.6	24.6	100.0	15623	11.27	0.37	3.71

4.1.2 CLICIT Core Control Rod Calibrations

The control rod calibration procedure detailed in OSTROP 9 [4] was performed for both the normal and CLICIT core configurations at LEU core BOL in October 2008. The differential reactivity worth for each section of control rod is calculated from the average reactor period induced by withdrawing the segment of control rod. This average period is calculated from the measured time of power rise from 200 to 800 W [4]. The measured differential integral control rod worths for the CLICIT core configuration are provided in Tables 4-5 through 4-8. These control rod calibration results for the CLICIT core configuration result in a measured total core reactivity worth of \$10.75 [45].

Table 4-5: CLICIT core transient control rod calibration results.

<i>Configuration</i>	Transient	Safety	Shim	Regulating	Time [ms]	Period [s]	Reactivity [\$]	Cumulative [\$]
<i>Transient 1</i>	24.4	63.1	63.1	63.1	8334	6.01	0.48	0.48
<i>Transient 2</i>	36.9	58.7	58.6	59.1	9536	6.88	0.46	0.94
<i>Transient 3</i>	49.2	55.7	55.7	54.0	7938	5.73	0.49	1.43
<i>Transient 4</i>	61.6	52.0	52.0	49.4	9839	7.10	0.45	1.88
<i>Transient 5</i>	72.2	48.0	48.0	46.6	24184	17.45	0.30	2.18
<i>Transient 6</i>	100.0	44.5	44.5	46.5	14189	10.24	0.39	2.57

Table 4-6: CLICIT core safety control rod calibration.

<i>Configuration</i>	Transient	Safety	Shim	Regulating	Time [ms]	Period [s]	Reactivity [\$]	Cumulative [\$]
<i>Safety 1</i>	61.0	26.4	61.0	61.7	9041	6.52	0.47	0.47
<i>Safety 2</i>	57.3	40.0	57.4	57.3	9625	6.94	0.46	0.92
<i>Safety 3</i>	53.7	51.7	53.7	53.8	10785	7.78	0.44	1.36
<i>Safety 4</i>	50.2	65.8	50.2	50.6	9392	6.77	0.46	1.82
<i>Safety 5</i>	46.9	100.0	46.9	46.8	8169	5.89	0.49	2.31

Table 4-7: CLICIT core shim control rod calibration results.

<i>Configuration</i>	Transient	Safety	Shim	Regulating	Time [ms]	Period [s]	Reactivity [\$]	Cumulative [\$]
<i>Shim 1</i>	63.6	63.6	24.7	64.0	8819	6.36	0.47	0.47
<i>Shim 2</i>	59.7	59.7	37.0	59.7	9219	6.65	0.46	0.94
<i>Shim 3</i>	55.5	55.5	47.7	55.4	9139	6.59	0.47	1.40
<i>Shim 4</i>	51.5	51.5	58.7	52.0	9910	7.15	0.45	1.85
<i>Shim 5</i>	48.1	48.0	69.6	48.1	14390	10.38	0.38	2.24
<i>Shim 6</i>	44.9	44.9	100.0	45.0	8655	6.24	0.48	2.71

Table 4-8: CLICIT core regulating control rod calibration results.

<i>Configuration</i>	Transient	Safety	Shim	Regulating	Time [ms]	Period [s]	Reactivity [\$]	Cumulative [\$]
<i>Regulating 1</i>	68.3	67.8	67.8	22.1	8531	6.15	0.48	0.48
<i>Regulating 2</i>	62.9	62.8	62.9	33.5	8491	6.12	0.48	0.96
<i>Regulating 3</i>	58.3	58.2	58.3	43.3	8041	5.80	0.49	1.45
<i>Regulating 4</i>	53.9	58.2	58.3	52.9	8406	6.06	0.48	1.93
<i>Regulating 5</i>	49.7	49.7	49.6	63.4	9307	6.71	0.46	2.39
<i>Regulating 6</i>	45.8	45.8	45.8	75.3	12153	8.77	0.41	2.80
<i>Regulating 7</i>	42.3	42.4	42.4	100.0	16457	11.87	0.36	3.16

4.2 Model Bias Calculations

4.2.1 Normal Core Model Bias Calculation

The MCNP® model of the normal core was used to produce models reflecting each critical control rod configuration that the reactor was stabilized at before rod pulls were performed during the normal core control rod calibrations of October 2008. A k-code problem was run for each critical

configuration for the purpose of calculating an average model bias or deviation from criticality in the model for control rod heights that the reactor was observed to be critical at. These configurations and calculated biases are shown below in Table 4-9. The average calculated model bias for the normal core configuration was -0.02 ± 0.04 where the error is computed from the total variance.

Table 4-9: Normal core critical control rod configurations [2] and reactivity bias.

<i>Configuration</i>	Transient	Safety	Shim	Regulating	k_{eff}	σ_{keff}	Reactivity [\$]	$\sigma_{\$}$
<i>Transient 1</i>	0.0	48.0	48.0	48.3	0.99973	0.00030	-0.04	0.04
<i>Transient 2</i>	22.1	44.8	44.8	44.8	0.99947	0.00030	-0.07	0.04
<i>Transient 3</i>	34.3	41.5	41.5	41.6	0.99903	0.00033	-0.13	0.04
<i>Transient 4</i>	45.2	38.1	38.1	38.3	0.99965	0.00035	-0.05	0.05
<i>Transient 5</i>	56.4	34.7	34.7	34.7	1.00039	0.00030	0.49	0.04
<i>Transient 6</i>	69.3	31.3	31.3	31.4	0.99976	0.00029	-0.03	0.04
<i>Safety 1</i>	47.4	0.0	47.4	47.3	0.99973	0.00031	-0.04	0.04
<i>Safety 2</i>	44.1	23.3	44.1	44.2	0.99934	0.00032	-0.09	0.04
<i>Safety 3</i>	41.2	35.6	41.1	41.1	1.00035	0.00032	0.05	0.04
<i>Safety 4</i>	37.9	46.7	37.9	37.8	0.99958	0.00025	-0.06	0.03
<i>Safety 5</i>	34.6	58.1	34.6	34.6	0.99952	0.00032	-0.06	0.04
<i>Safety 6</i>	31.4	70.7	31.4	31.5	1.00038	0.00027	0.05	0.04
<i>Shim 1</i>	47.7	47.7	0.0	47.8	1.00020	0.00033	0.03	0.04
<i>Shim 2</i>	44.4	44.4	23.2	44.4	0.99933	0.00033	-0.09	0.04
<i>Shim 3</i>	41.2	41.2	35.4	41.2	0.99923	0.00035	-0.10	0.05
<i>Shim 4</i>	37.9	37.9	46.3	37.8	0.99929	0.00030	-0.09	0.04
<i>Shim 5</i>	34.6	34.6	57.1	34.5	0.99931	0.00033	-0.09	0.04
<i>Shim 6</i>	31.2	31.2	69.4	31.2	1.00014	0.00037	0.02	0.05
<i>Regulating 1</i>	51.7	51.7	51.7	0.0	1.00124	0.00030	0.17	0.04
<i>Regulating 2</i>	47.9	47.9	47.9	19.3	1.00048	0.00033	0.06	0.04
<i>Regulating 3</i>	44.1	44.1	44.1	30.2	1.00001	0.00030	0.00	0.04
<i>Regulating 4</i>	40.3	40.3	40.3	39.2	0.99986	0.00034	-0.02	0.05
<i>Regulating 5</i>	36.4	36.4	36.4	48.0	0.99942	0.00030	-0.08	0.04
<i>Regulating 6</i>	32.6	32.6	32.5	56.8	0.99931	0.00030	-0.09	0.04
<i>Regulating 7</i>	28.7	28.7	28.7	66.5	0.99882	0.00033	-0.16	0.04
<i>Regulating 8</i>	24.6	24.6	24.6	77.9	0.99971	0.00030	-0.04	0.04

4.2.2 CLICIT Core Model Bias Calculation

The MCNP® model of the CLICIT core was used to produce models reflecting each critical control rod configuration that the reactor was stabilized at before rod pulls were performed during the CLICIT core control rod calibrations of October 2008. A k-code problem was run for each critical configuration for the purpose of calculating an average model bias or deviation from criticality in the model for control rod heights that the reactor was observed to be critical at. These configurations and calculated biases are shown below in Table 4-10. The average calculated model bias for the CLICIT core configuration was $\$0.07 \pm 0.04$ where the error is computed from the total variance. Both the normal and CLICIT core model biases are extremely low considering the total observed worth of the 2008 normal and CLICIT cores at BOL were \$10.75 and \$11.99 [45], respectively.

Table 4-10: CLICIT core critical control rod configurations [2] and reactivity bias.

<i>Configuration</i>	Transient	Safety	Shim	Regulating	k_{eff}	σ_{keff}	Reactivity [\$]	$\sigma_{\$}$
<i>Transient 1</i>	0.0	63.1	63.1	63.1	1.00101	0.00031	0.13	0.04
<i>Transient 2</i>	24.4	58.7	58.6	59.1	0.99978	0.00033	-0.03	0.04
<i>Transient 3</i>	36.9	55.7	55.7	54.0	0.99942	0.00034	-0.08	0.05
<i>Transient 4</i>	49.2	52.0	52.0	49.4	1.00098	0.00033	0.13	0.04
<i>Transient 5</i>	61.6	48.0	48.0	46.6	1.00072	0.00037	0.10	0.05
<i>Transient 6</i>	72.2	44.5	44.5	46.5	1.00117	0.00030	0.16	0.04
<i>Safety 1</i>	61.0	0.0	61.0	61.7	1.00171	0.00032	0.23	0.04
<i>Safety 2</i>	57.3	26.4	57.4	57.3	0.99973	0.00034	-0.04	0.05
<i>Safety 3</i>	53.7	40.0	53.7	53.8	0.99991	0.00037	-0.01	0.05
<i>Safety 4</i>	50.2	51.7	50.2	50.6	1.00034	0.0003	0.05	0.04
<i>Safety 5</i>	46.9	65.8	46.9	46.8	1.00049	0.00033	0.07	0.04
<i>Shim 1</i>	63.6	63.6	0.0	64.0	1.00131	0.00031	0.17	0.04
<i>Shim 2</i>	59.7	59.7	24.7	59.7	1.00066	0.00032	0.09	0.04
<i>Shim 3</i>	55.5	55.5	37.0	55.4	1.00019	0.00033	0.03	0.04
<i>Shim 4</i>	51.5	51.5	47.7	52.0	1.00058	0.00024	0.08	0.03
<i>Shim 5</i>	48.1	48.0	58.7	48.1	1.00019	0.00037	0.03	0.05
<i>Shim 6</i>	44.9	44.9	69.6	45.0	1.00003	0.0003	0.00	0.04
<i>Regulating 1</i>	68.3	67.8	67.8	0.0	1.00182	0.00031	0.24	0.04
<i>Regulating 2</i>	62.9	62.8	62.9	22.1	1.00155	0.00032	0.21	0.04
<i>Regulating 3</i>	58.3	58.2	58.3	33.5	1.00111	0.00031	0.15	0.04
<i>Regulating 4</i>	53.9	53.8	53.8	43.3	1.00045	0.00028	0.06	0.04
<i>Regulating 5</i>	49.7	49.7	49.6	52.9	0.99961	0.00028	-0.05	0.04
<i>Regulating 6</i>	45.8	45.8	45.8	63.4	0.99981	0.00032	-0.03	0.04
<i>Regulating 7</i>	42.3	42.4	42.4	75.3	0.99927	0.00031	-0.10	0.04

4.3 MCNP Calculated Control Rod Worths

4.3.1 Normal Core Calculated Control Rod Worths

The MCNP® model of the normal core was used to produce models reflecting each supercritical control rod configuration that resulted in a positive reactor period, or rod pulls, that were performed during the normal core control rod calibrations of October 2008. A k-code problem was run for each supercritical configuration for the purpose of calculating and comparing the model-predicted reactivity for each rod pull with the experimental results. The calculated and measured integral rod worth curves for each control rod in the normal core configuration are shown below in Figures 18 – 21. The normal core model bias of \$-0.02 was subtracted from each calculated reactivity worth of a rod segment. A fourth-order polynomial trendline is fit to the MCNP calculated control rod worth data only for the purpose of aiding in distinguishing between the observed and calculated data. The error associated with each calculated reactivity value is so low that the error bars associated with the calculated values may not be visible.

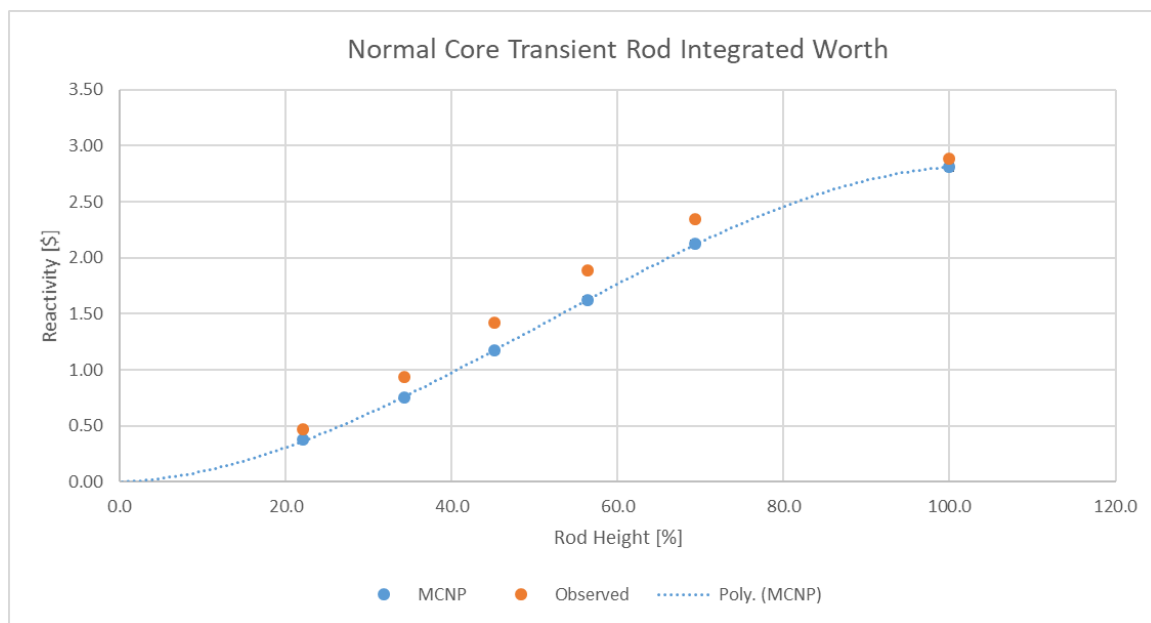


Figure 18: Measured and calculated normal core transient rod worth.

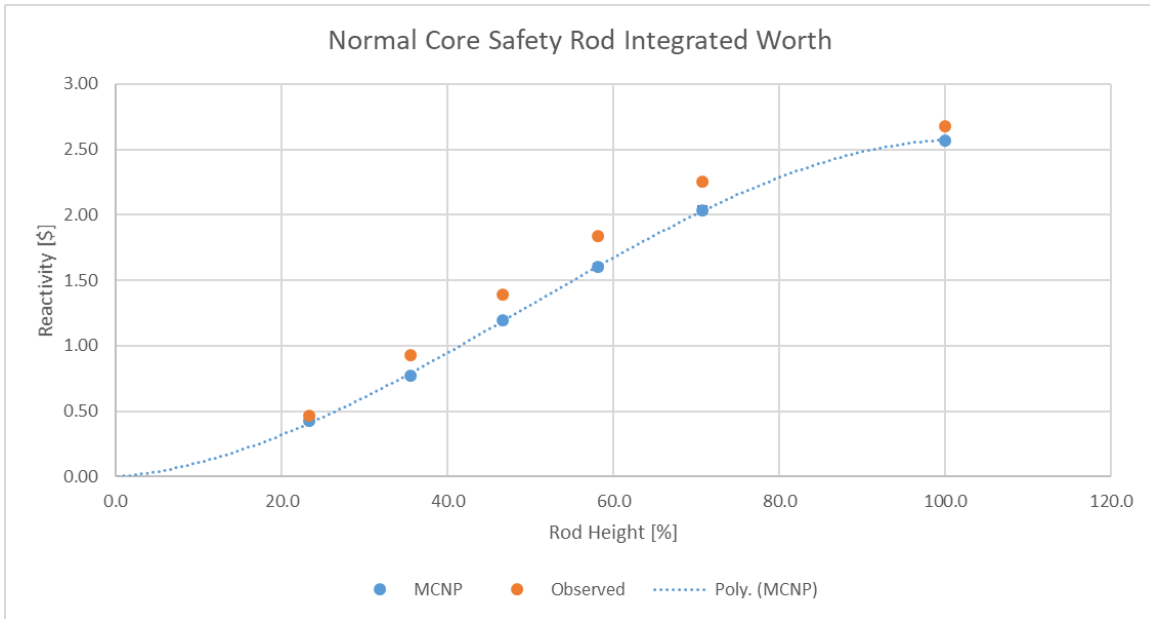


Figure 19: Measured and calculated normal core safety rod worth.

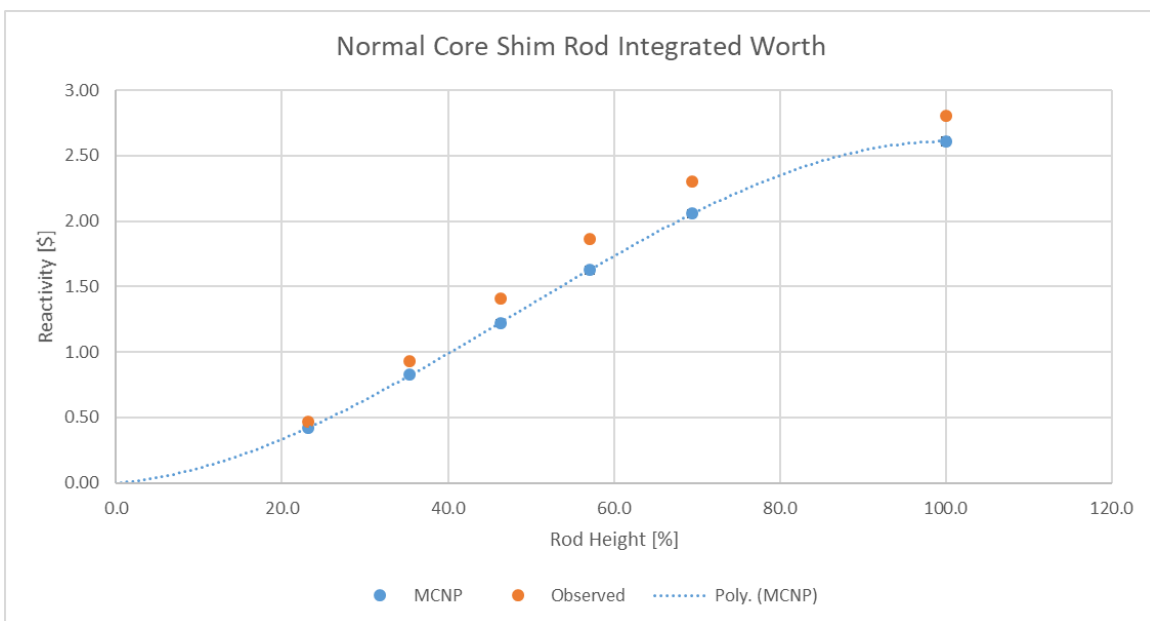


Figure 20: Measured and calculated normal core shim rod worth.

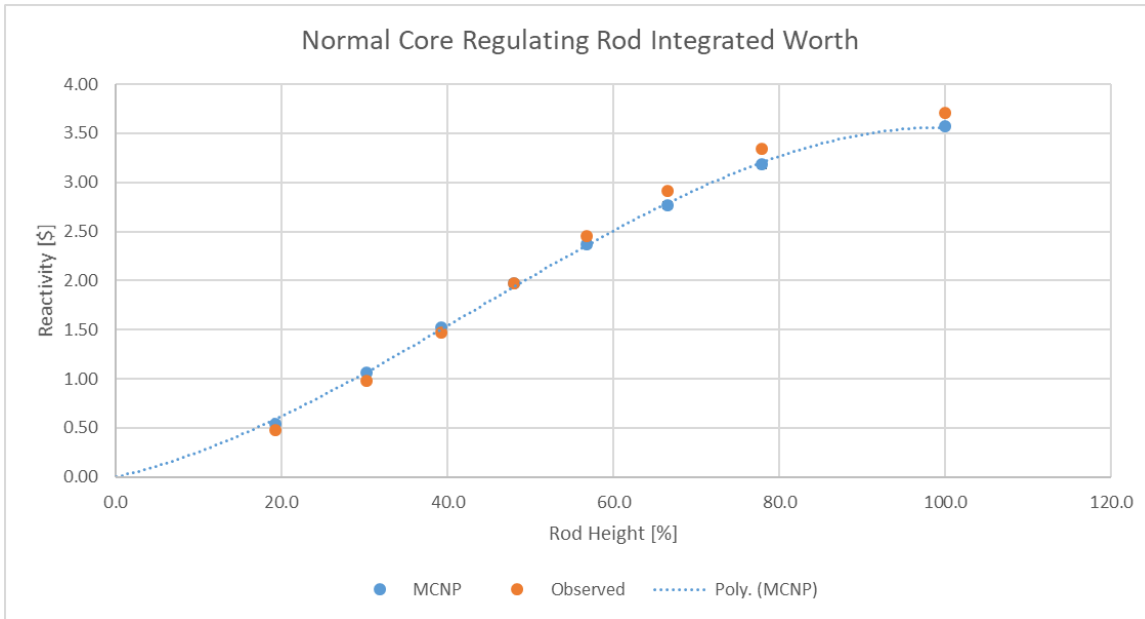


Figure 21: Measured and calculated normal core regulating rod worth.

It can be seen that for the normal core the calculated rod worths generally under predict the control rod worth compared to the measured results. However, the model slightly over-predicts the upper portion of the regulating rod and slightly under predicts its lower portions. The normal core MCNP model of the control rod calibration process results in a total normal core worth of $\$11.56 \pm 0.06$. The cumulative results of both the measured and calculated control rod calibrations are shown below in Table 4.11.

Table 4-11: Normal core measured and calculated control rod calibration results.

Control Rod	Measured worth [\\$]	Calculated worth [\\$]
<i>Transient</i>	2.86	2.81 ± 0.03
<i>Safety</i>	2.66	2.57 ± 0.03
<i>Shim</i>	2.76	2.61 ± 0.03
<i>Regulating</i>	3.71	3.57 ± 0.04
<i>Total</i>	11.99	11.56 ± 0.06

4.3.2 CLICIT Core Calculated Control Rod Worths

The MCNP® model of the CLICIT core was used to produce models reflecting each supercritical control rod configuration that resulted in a positive reactor period, or rod pulls, that were performed during the CLICIT core control rod calibrations of October 2008. A k-code problem was run for each supercritical configuration for the purpose of calculating and comparing the model-predicted reactivity for each rod pull with the experimental results. The calculated and observed integral rod worth curves for each control rod in the CLICIT core configuration are shown below in Figures 22 – 25. The CLICIT core model bias of \$0.07 was subtracted from each calculated reactivity worth of a rod segment. A fourth-order polynomial trendline is fit to the MCNP calculated control rod worth data only for the purpose of aiding in distinguishing between the observed and calculated data.

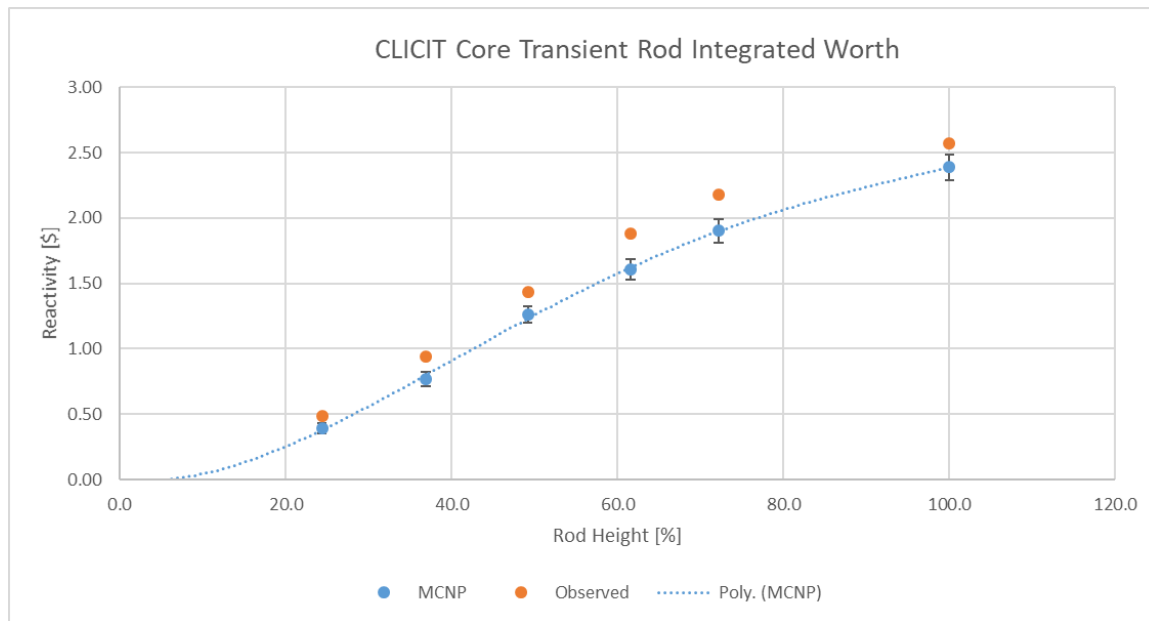


Figure 22: Measured and calculated CLICIT core transient rod worth.

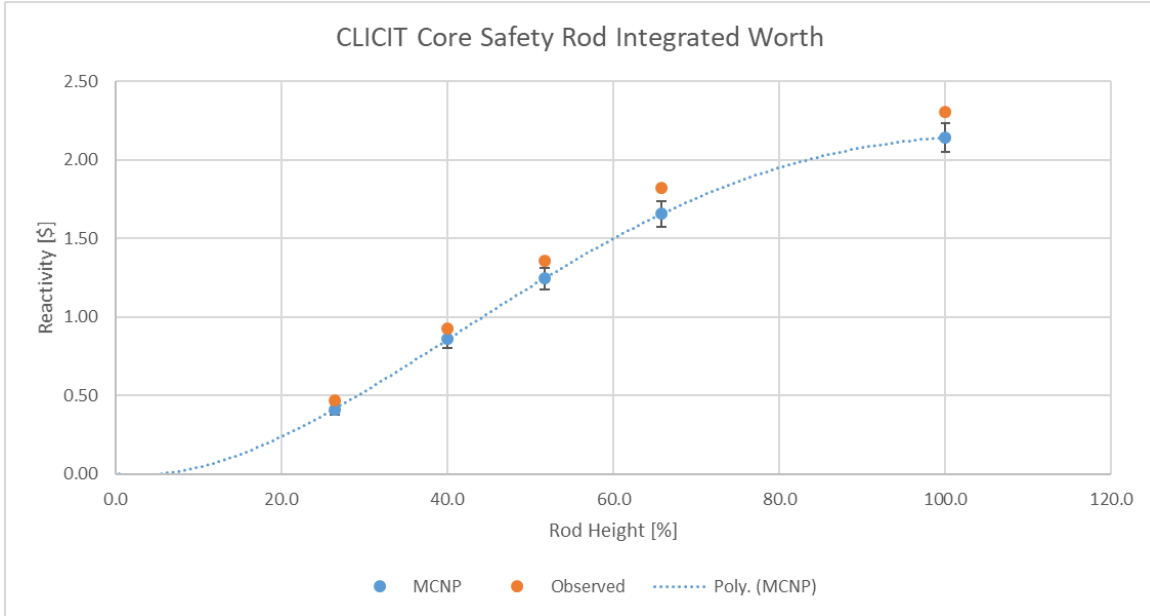


Figure 23: Measured and calculated CLICIT core safety rod worth.

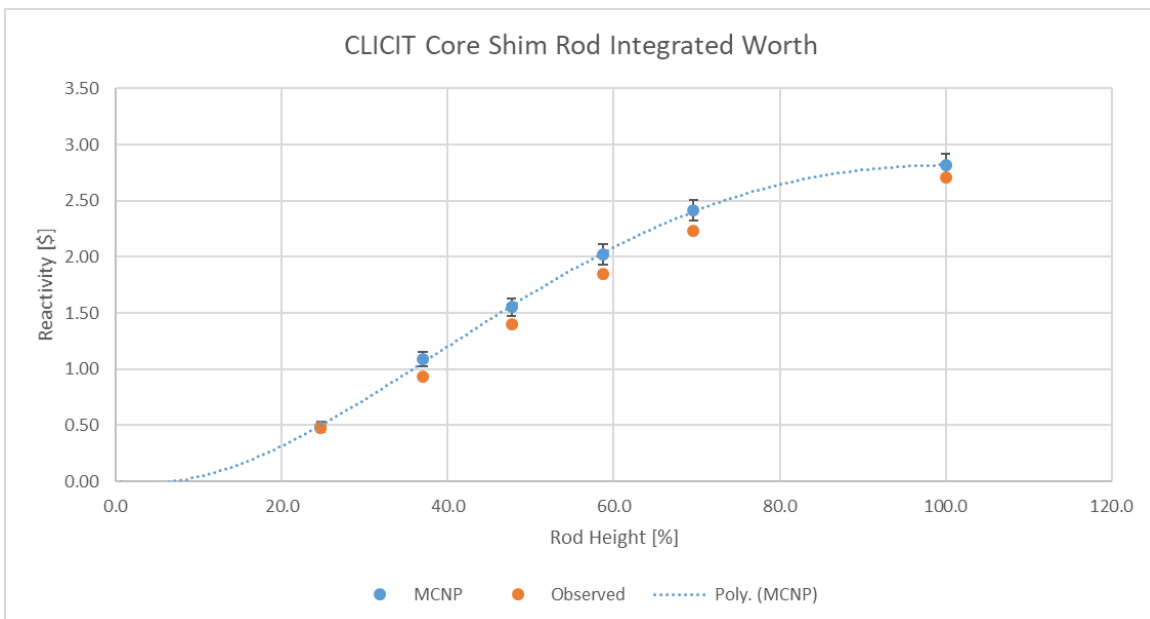


Figure 24: Measured and calculated CLICIT core shim rod worth.

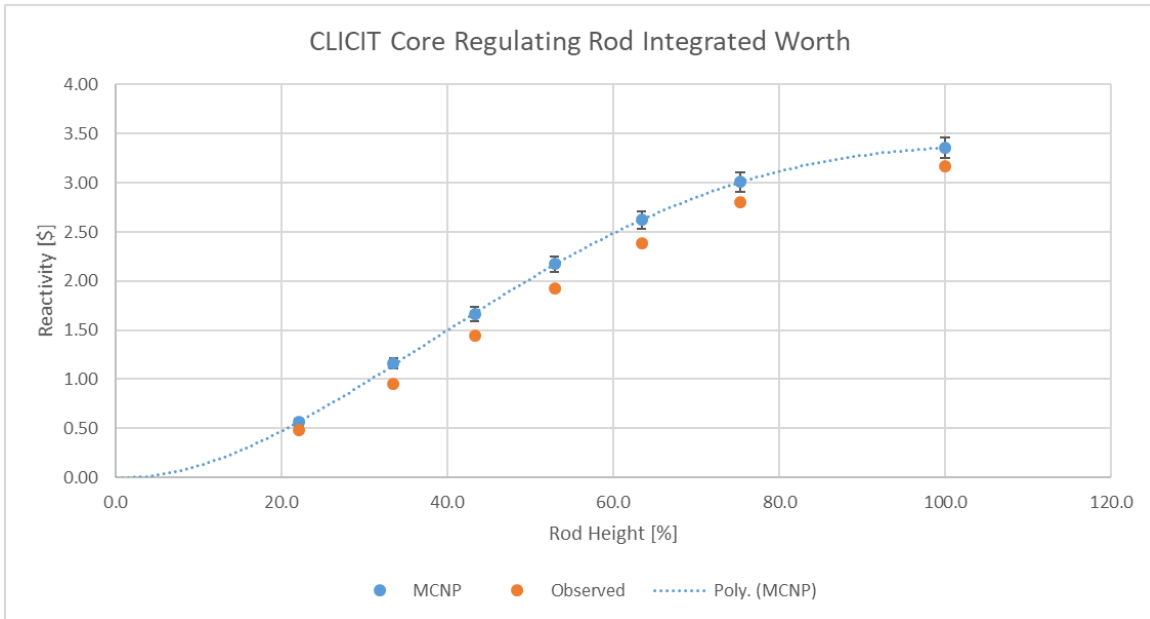


Figure 25: Measured and calculated CLICIT core regulating rod worth.

It can be seen that for the CLICIT core the calculated rod worths for the transient and safety rod under predict both rod worths over the entire integrated rod worth curve and the model over predicts the worth of the shim and regulating rods over the entire integrated rod worth curve. The CLICIT core MCNP model of the control rod calibration process results in a total normal core worth of $\$10.71 \pm 0.20$. The cumulative results of both the measured and calculated control rod calibrations are shown below in Table 4.12. While the calculated and measured total core reactivity worths for the CLICIT core are in better agreement than the normal core, the 1σ standard error for each reactivity manipulation is higher in the CLICIT core model and the under/over prediction for each rod may be offsetting errors.

Table 4-12: CLICIT core measured and calculated control rod calibration results.

<i>Control Rod</i>	Measured worth [\$]	Calculated worth [\$]
<i>Transient</i>	2.57	2.39 ± 0.10
<i>Safety</i>	2.31	2.14 ± 0.09
<i>Shim</i>	2.71	2.82 ± 0.10
<i>Regulating</i>	3.16	3.36 ± 0.11
<i>Total</i>	10.75	10.71 ± 0.20

4.4 Detector Responses

4.4.1 Normal Core Detector Responses

The MCNP® model of the normal core was used to produce models reflecting each supercritical control rod configuration during the normal core control rod calibrations of October 2008 and a *kcode* problem was run for each configuration. The model contained the nine previously described fission chambers, and one million neutrons were born per cycle at various locations in the fuel for 100 cycles with an initial value of 1.0 for k_{eff} and the first 25 cycles are ignored statistically. The fission rate was obtained in the UO₂ regions of each detector by performing a volume-averaged flux tally and using a multiplier card that multiplies the flux by the total fission cross section of the material within the volume.

In addition, a particle-splitting variance reduction method was used to reduce the error associated with the flux tally by assigning the UO₂ regions of the detectors an importance to neutrons of three. The integrated fission rate in each detector is plotted against the measured and MCNP® calculated integral rod worth curves for each rod pull and each detector, where the detector located at 348.2° of North is the physical location of the detector. The comparison of the integrated detector response to the integral control rod worth curves are shown below in Figures 26 – 61 for the normal core configuration.

4.4.1.1 Transient Rod

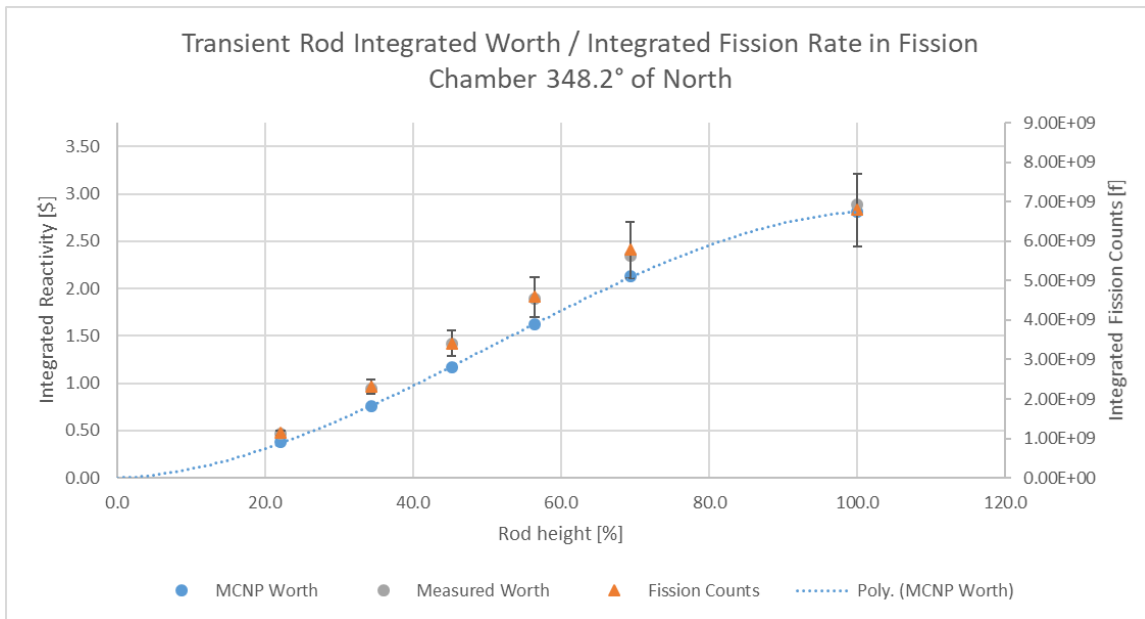


Figure 26: Integrated transient rod worth and fission rate in the 348.2° detector.

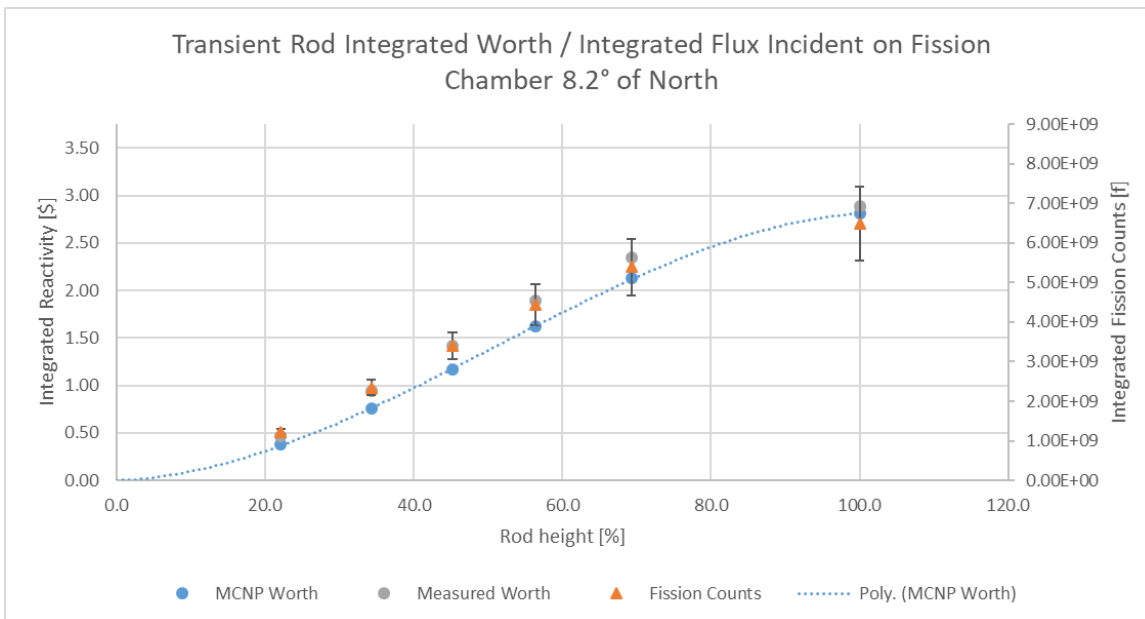


Figure 27: Integrated transient rod worth and fission rate in the 8.2° detector.

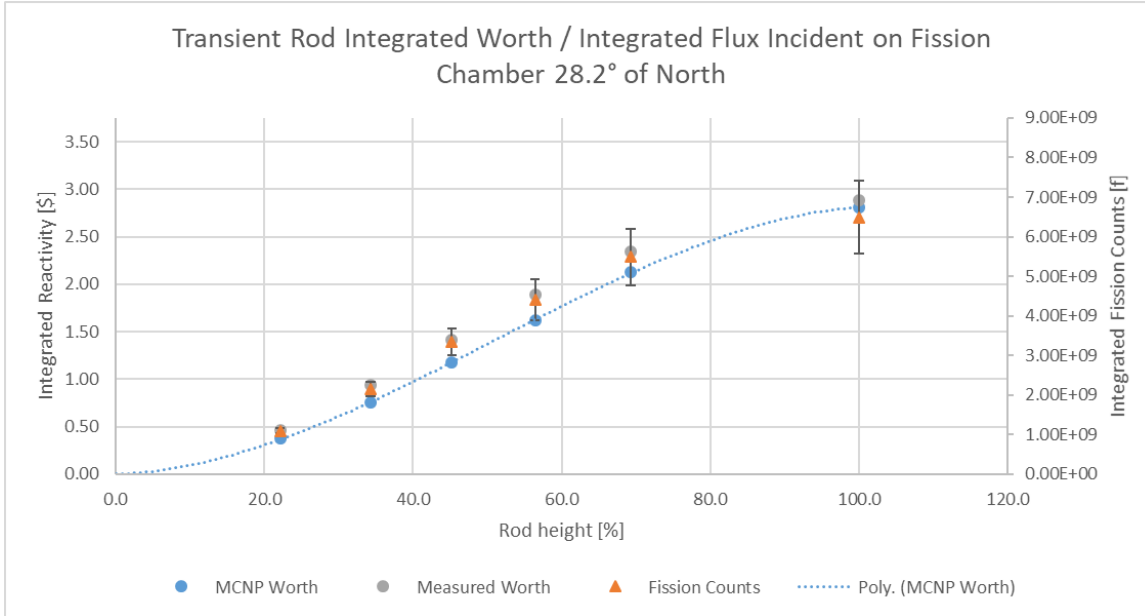


Figure 28: Integrated transient rod worth and fission rate in the 28.2° detector.

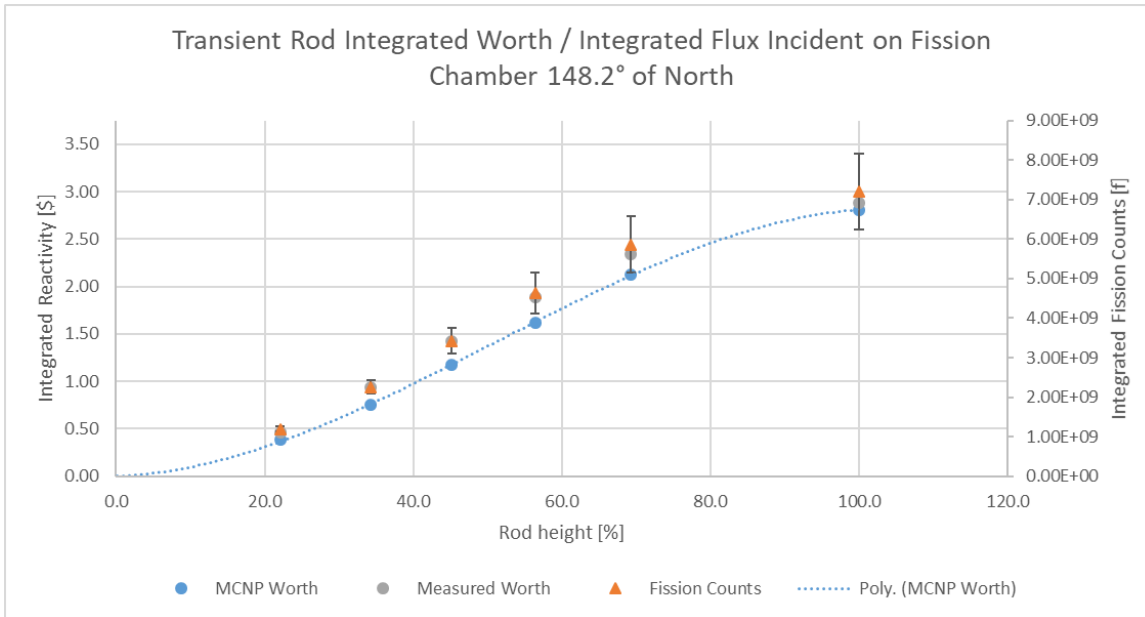


Figure 29: Integrated transient rod worth and fission rate in the 148.2° detector.

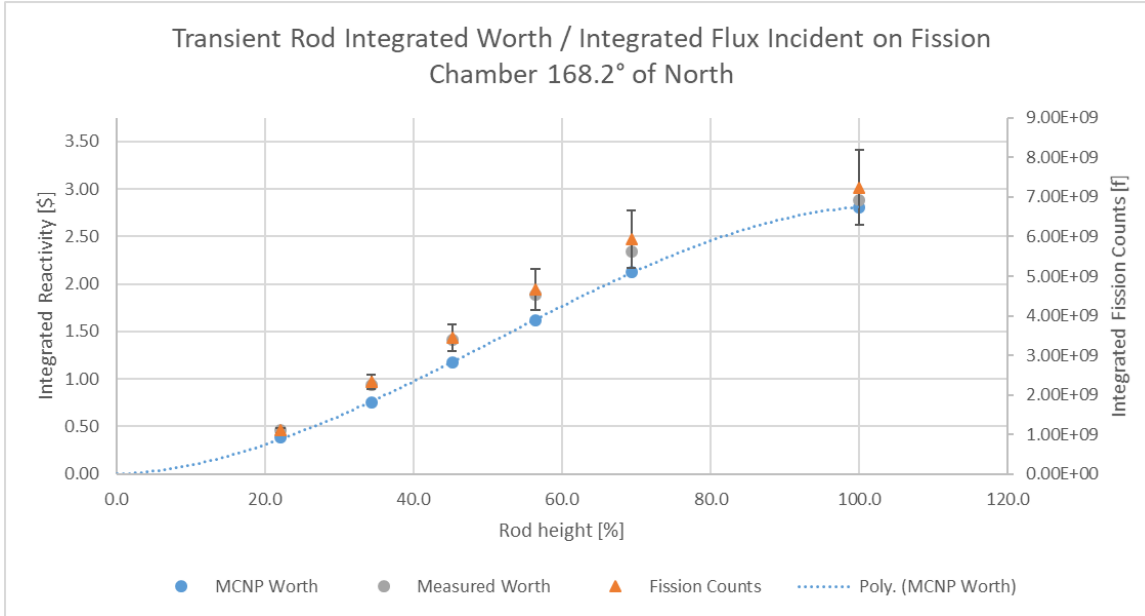


Figure 30: Integrated transient rod worth and fission rate in the 168.2° detector.

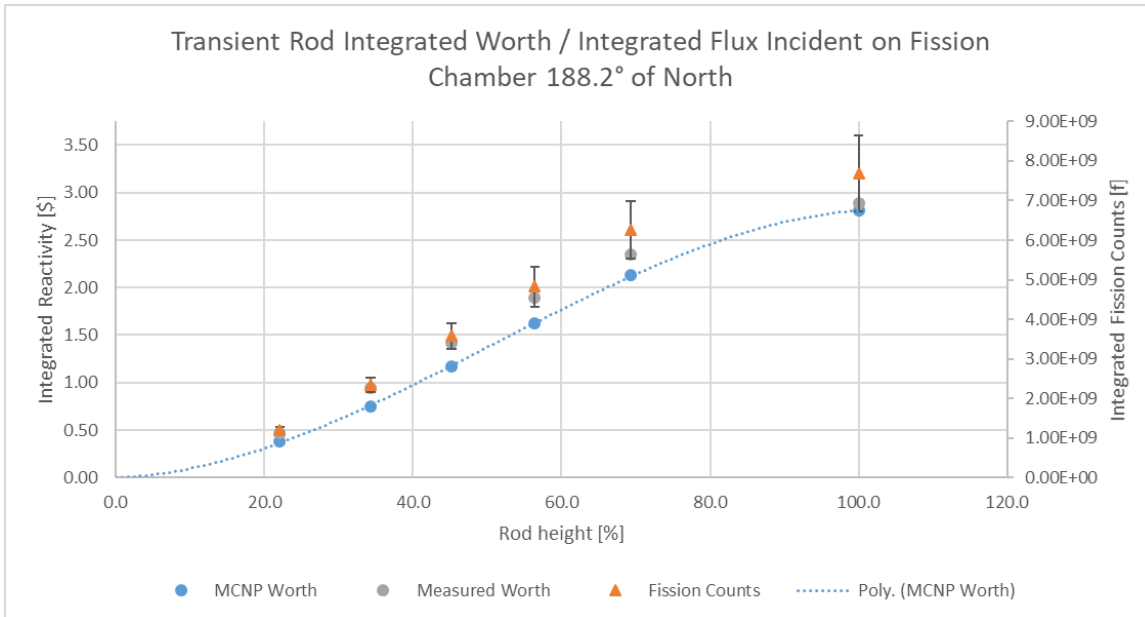


Figure 31: Integrated transient rod worth and fission rate in the 188.2° detector.

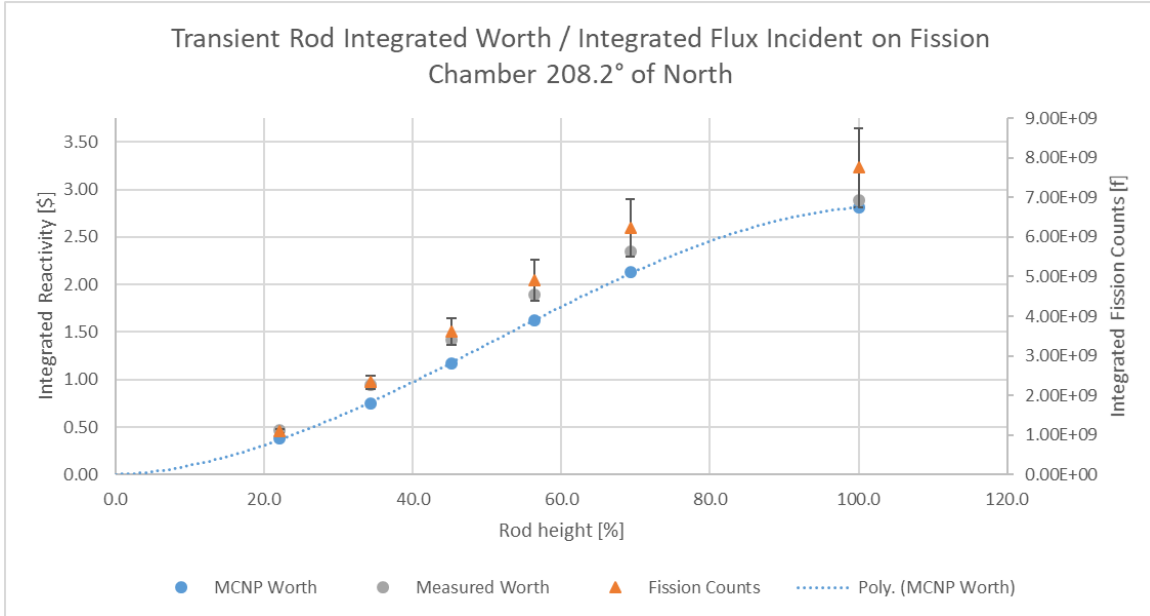


Figure 32: Integrated transient rod worth and fission rate in the 208.2° detector.

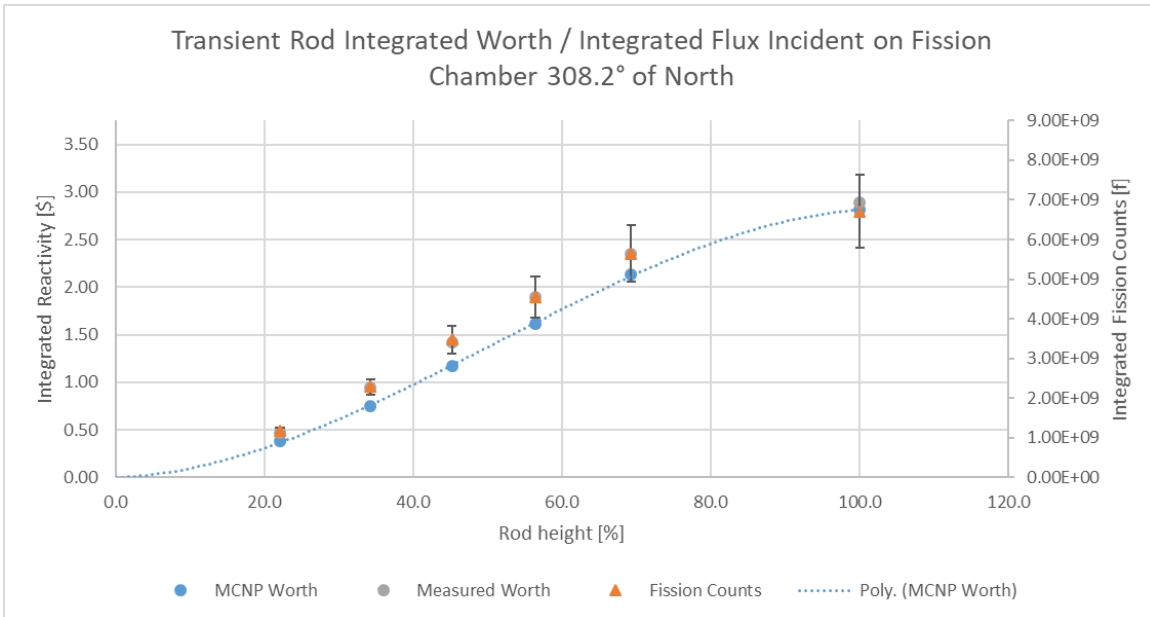


Figure 33: Integrated transient rod worth and fission rate in the 308.2° detector.

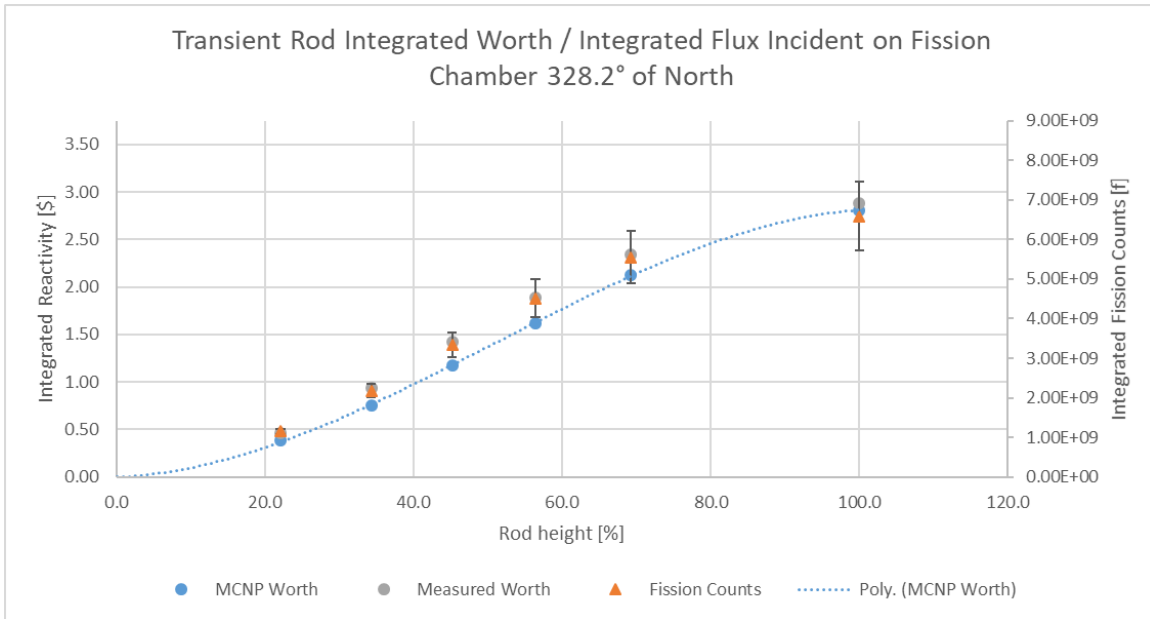


Figure 34: Integrated transient rod worth and fission rate in the 328.2° detector.

4.4.1.2 Safety Rod

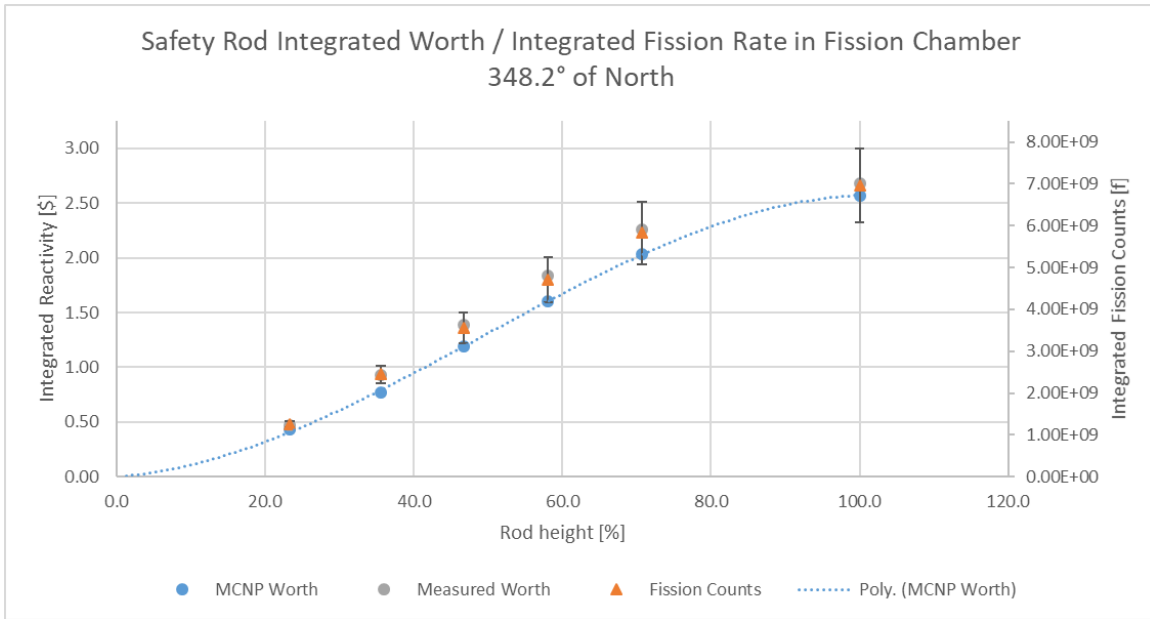


Figure 35: Integrated safety rod worth and fission rate in the 348.2° detector.

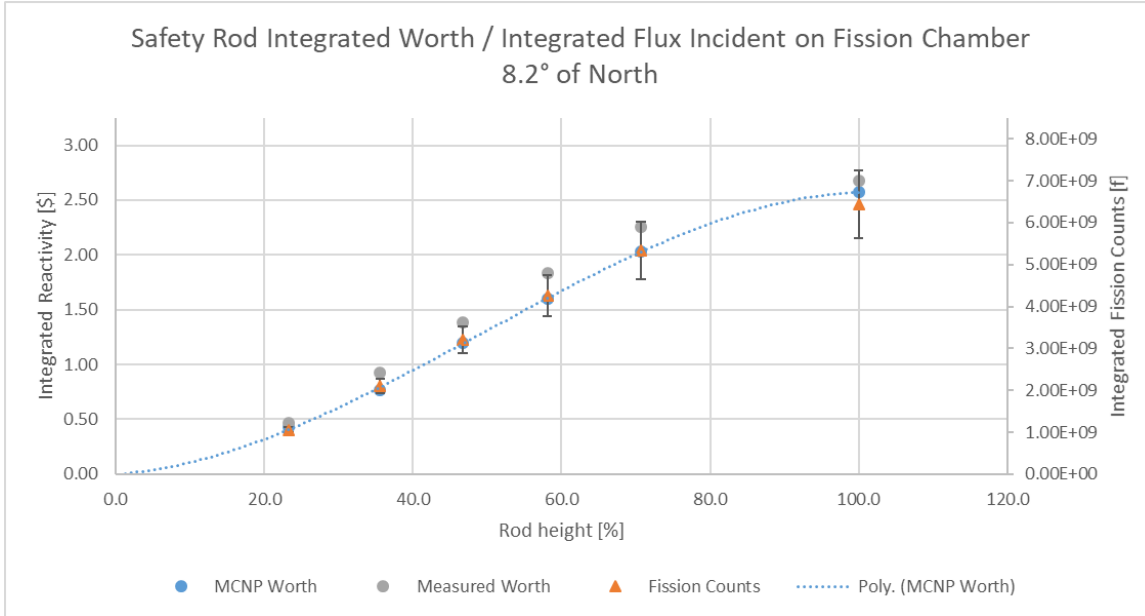


Figure 36: Integrated safety rod worth and fission rate in the 8.2° detector.

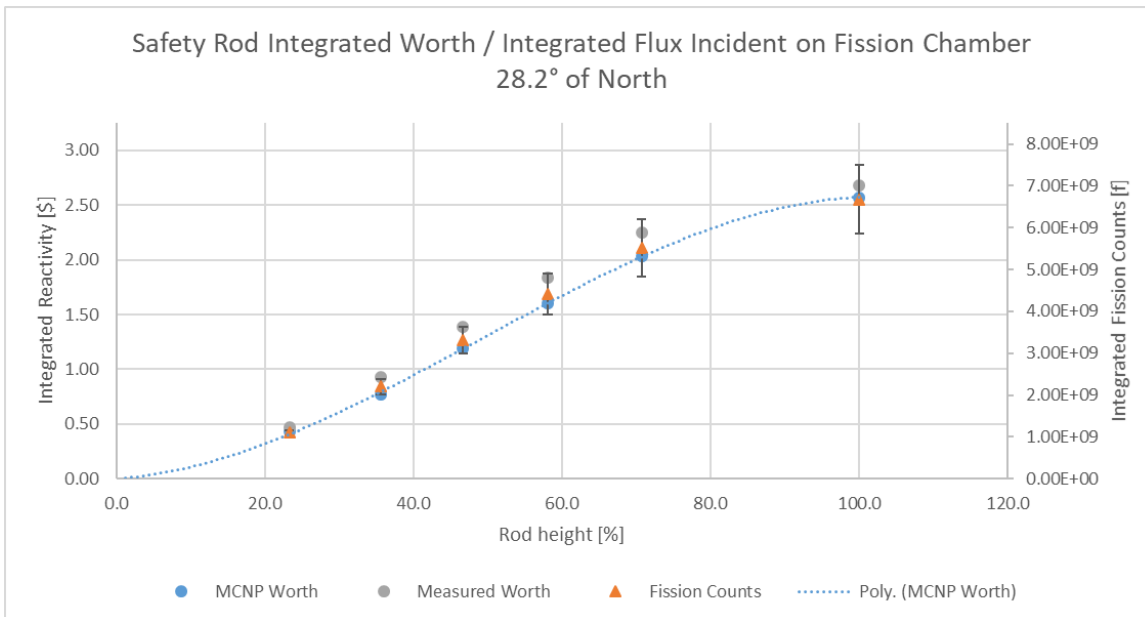


Figure 37: Integrated safety rod worth and fission rate in the 28.2° detector.

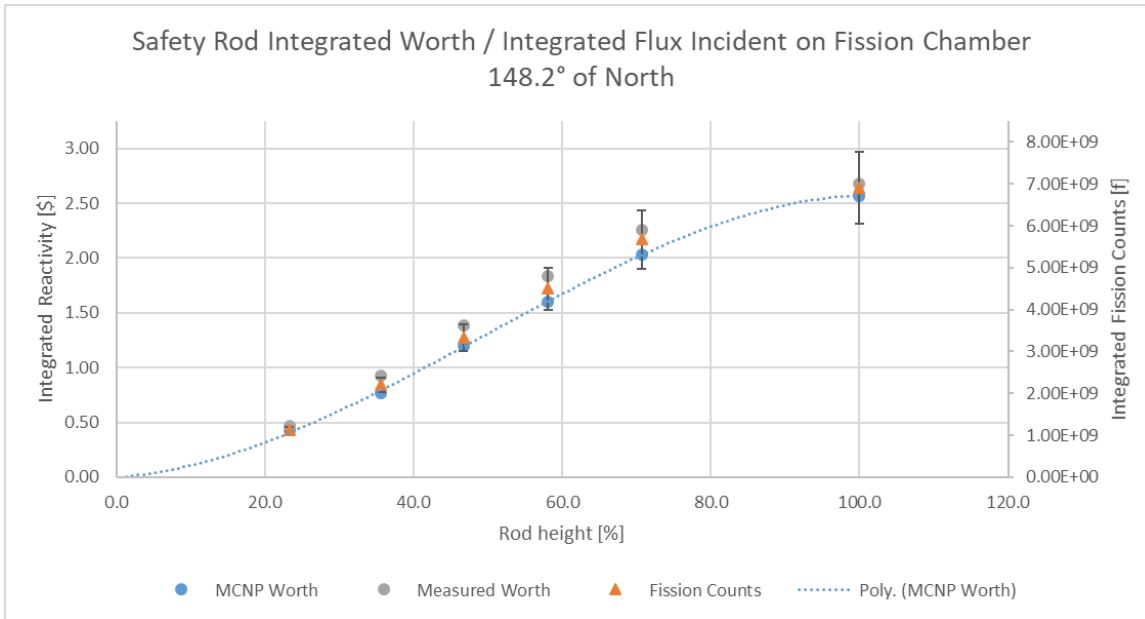


Figure 38: Integrated safety rod worth and fission rate in the 148.2° detector.

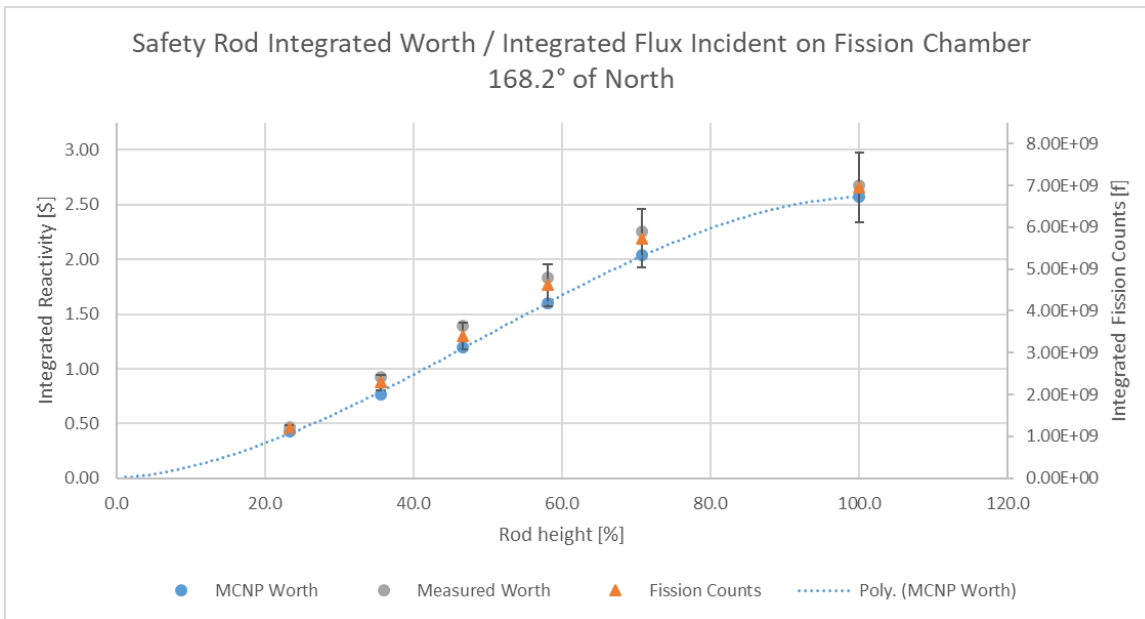


Figure 39: Integrated safety rod worth and fission rate in the 168.2° detector.

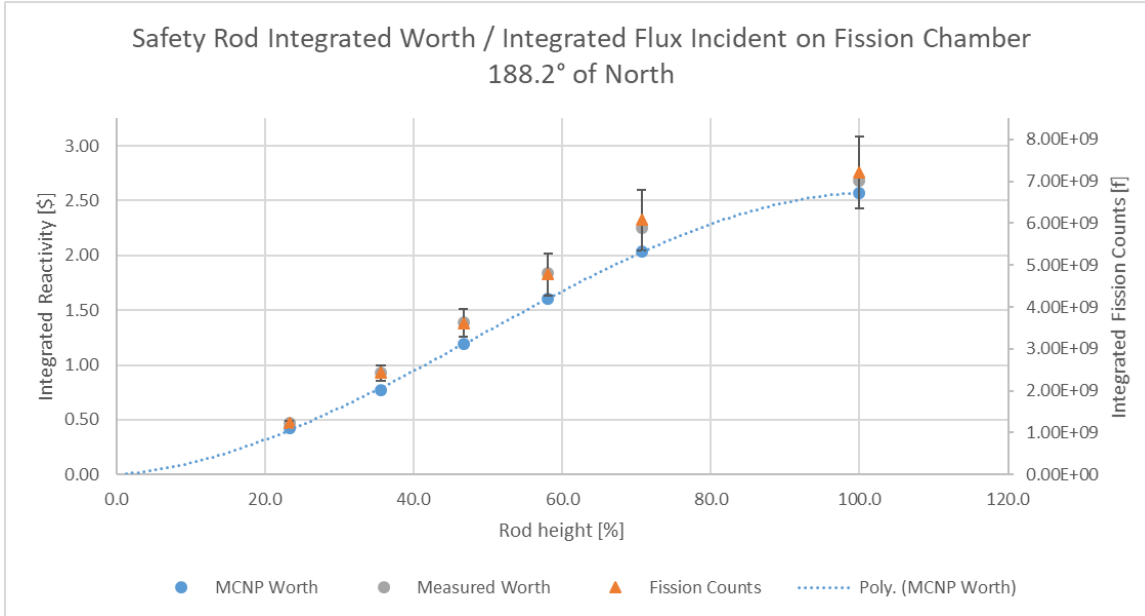


Figure 40: Integrated safety rod worth and fission rate in the 188.2° detector.

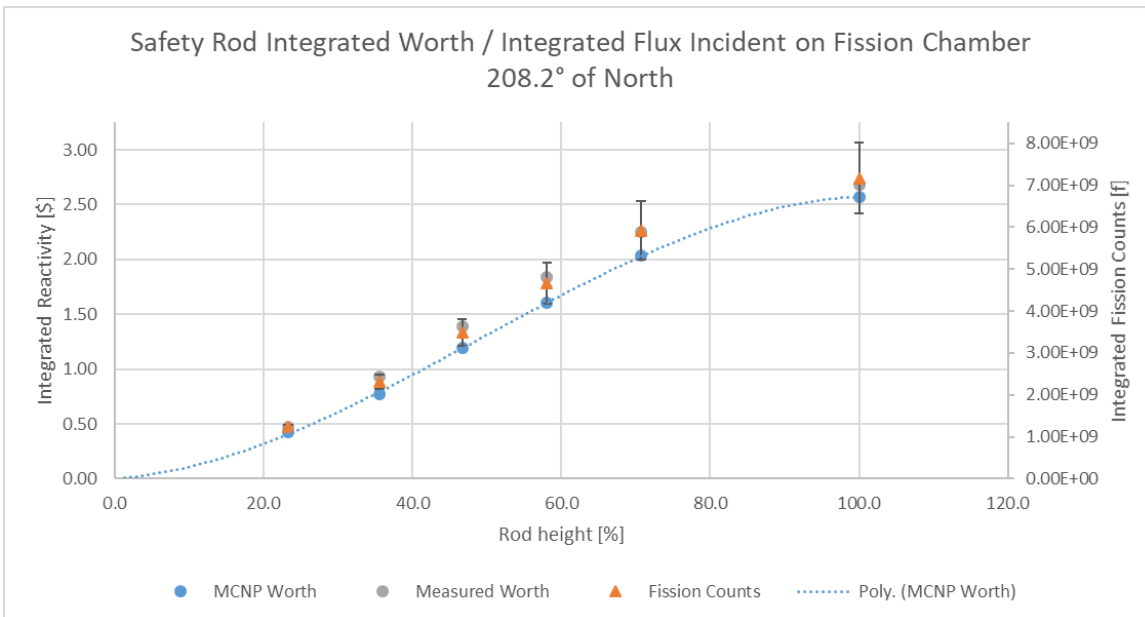


Figure 41: Integrated safety rod worth and fission rate in the 208.2° detector.

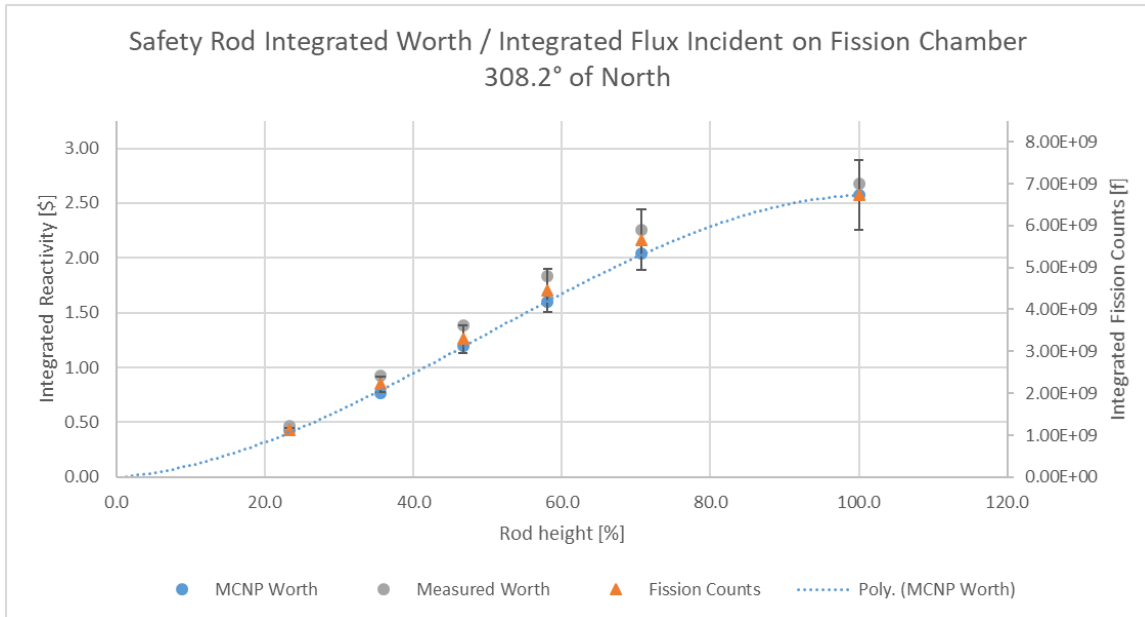


Figure 42: Integrated safety rod worth and fission rate in the 308.2° detector.

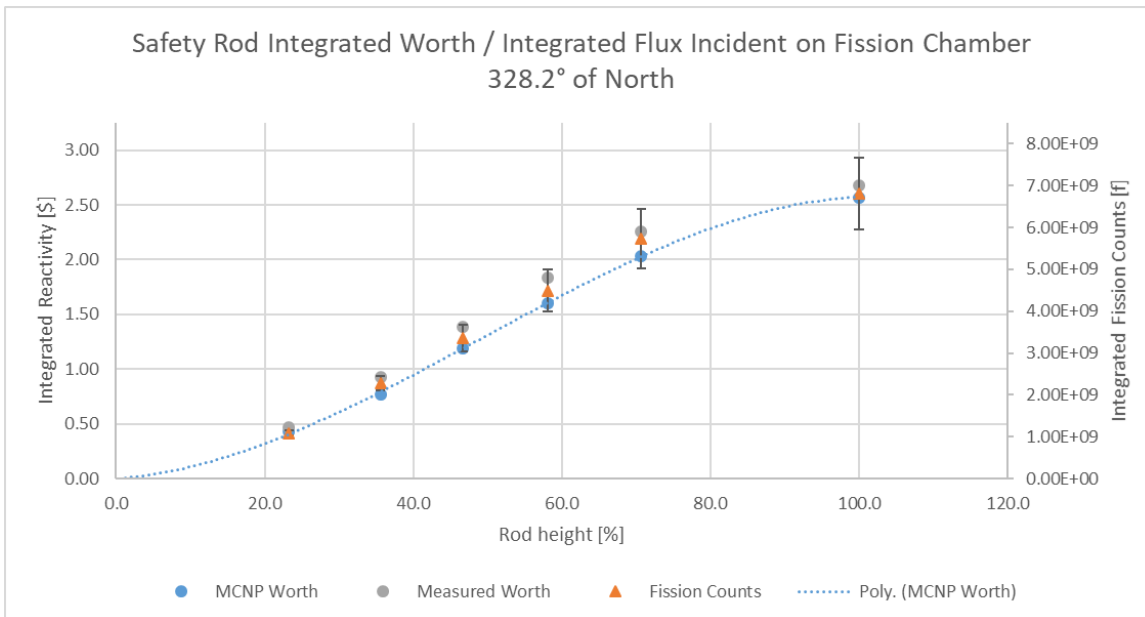


Figure 43: Integrated safety rod worth and fission rate in the 328.2° detector.

4.4.1.3 Shim Rod

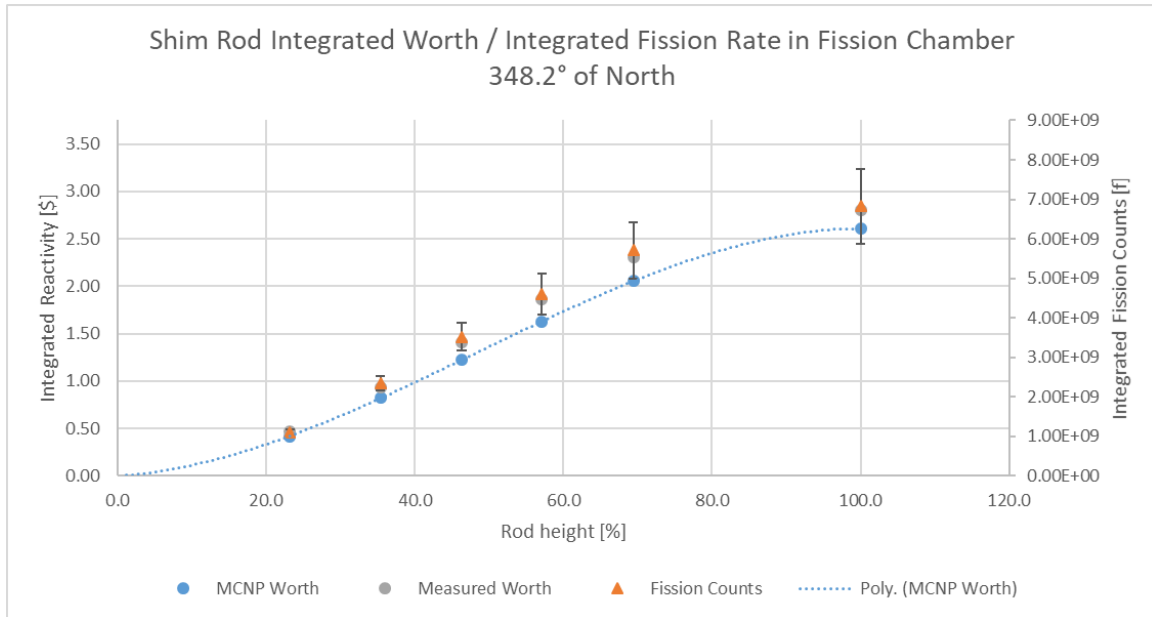


Figure 44: Integrated shim rod worth and fission rate in the 348.2° detector.

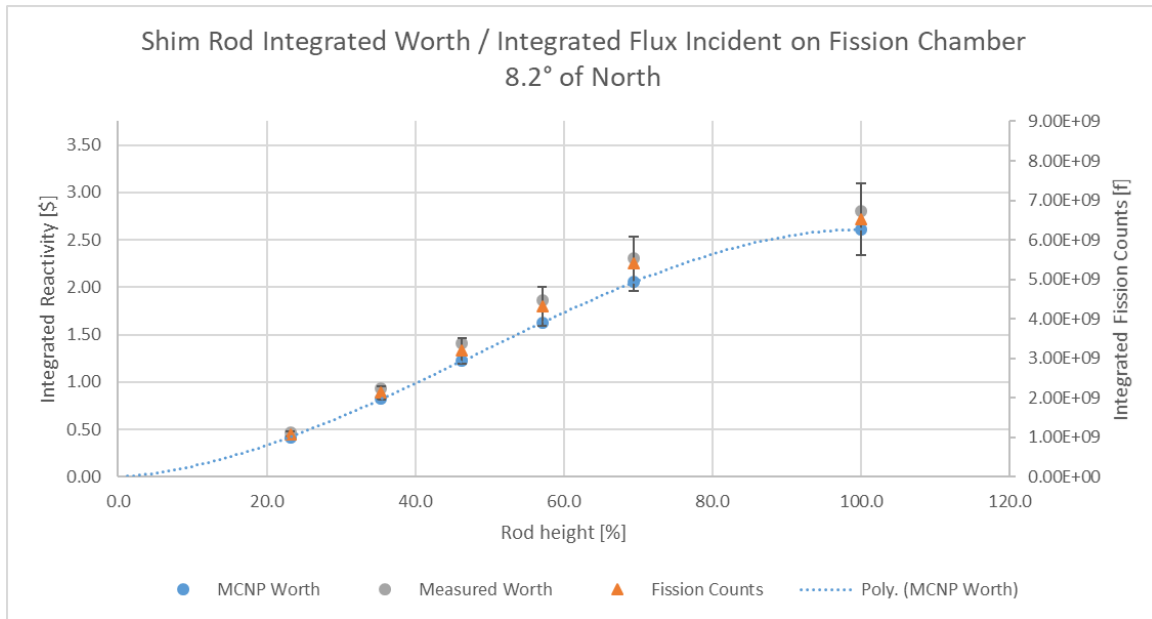


Figure 45: Integrated shim rod worth and fission rate in the 8.2° detector.

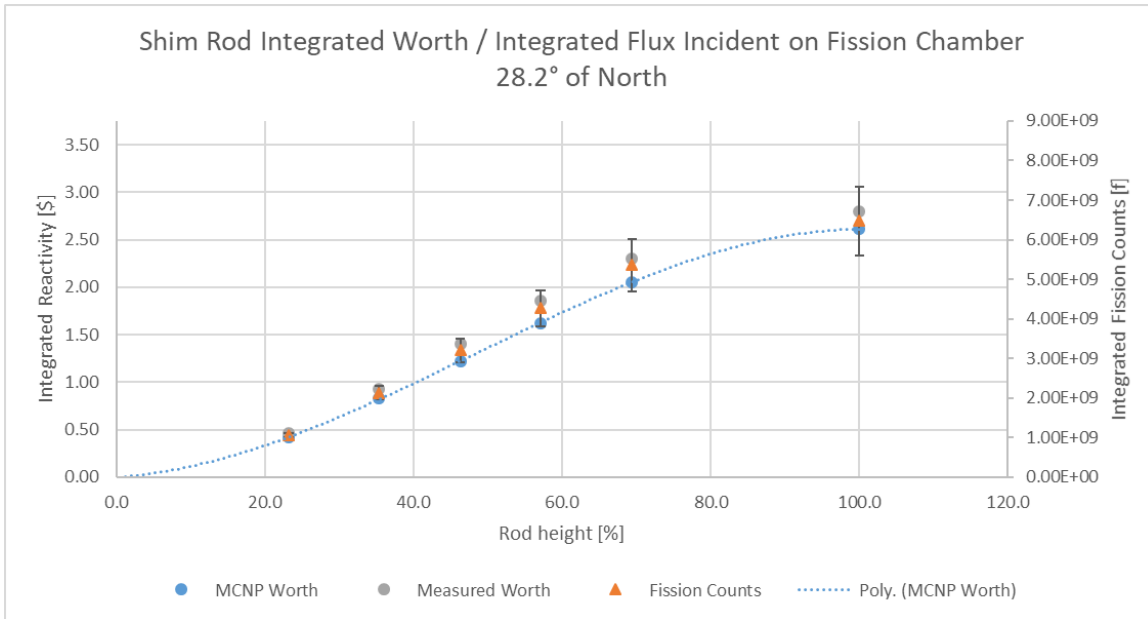


Figure 46: Integrated shim rod worth and fission rate in the 28.2° detector.

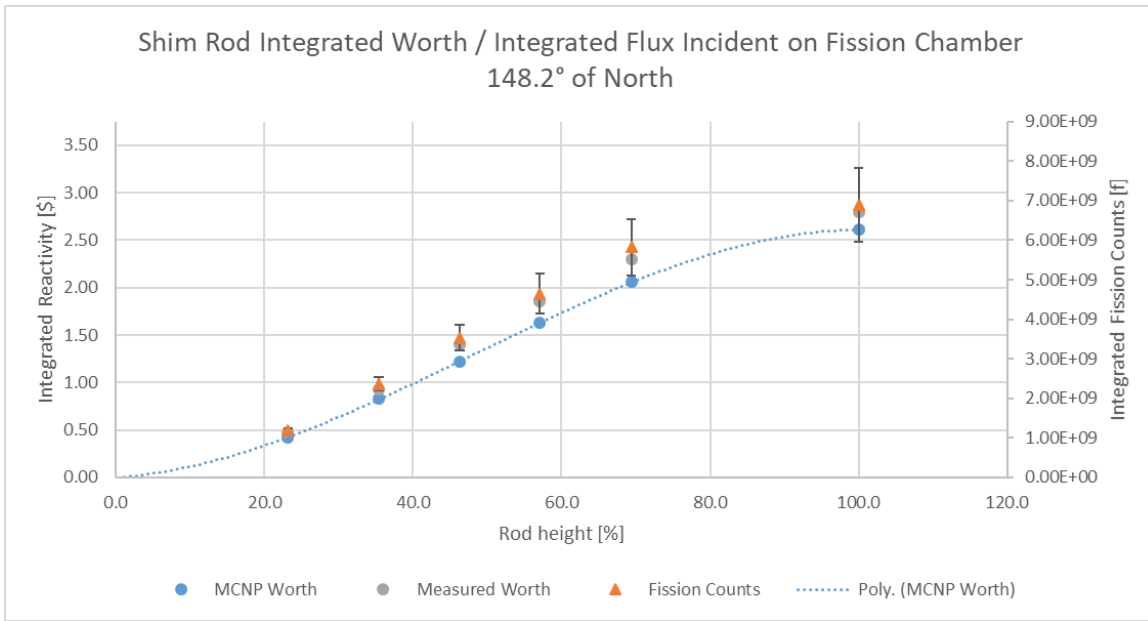


Figure 47: Integrated shim rod worth and fission rate in the 148.2° detector.

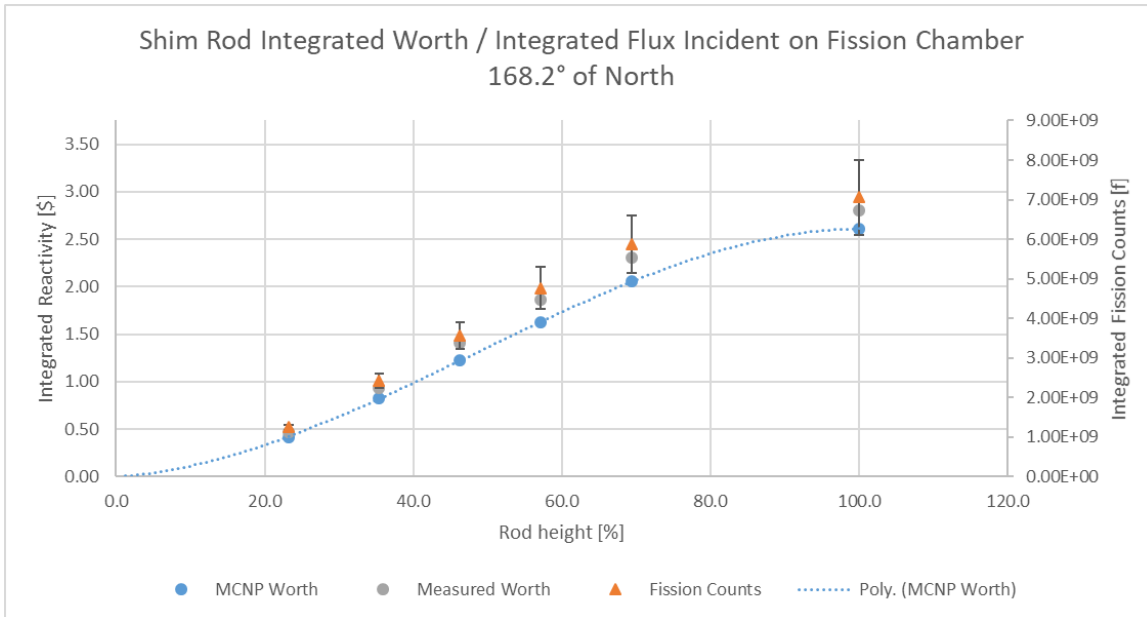


Figure 48: Integrated shim rod worth and fission rate in the 168.2° detector.

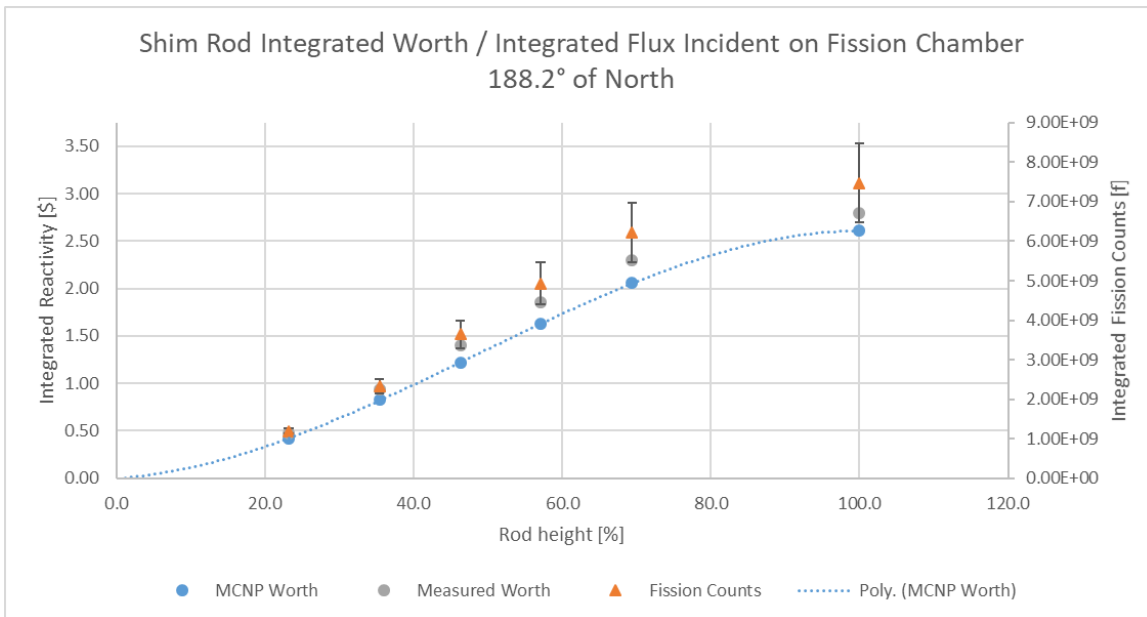


Figure 49: Integrated shim rod worth and fission rate in the 188.2° detector.

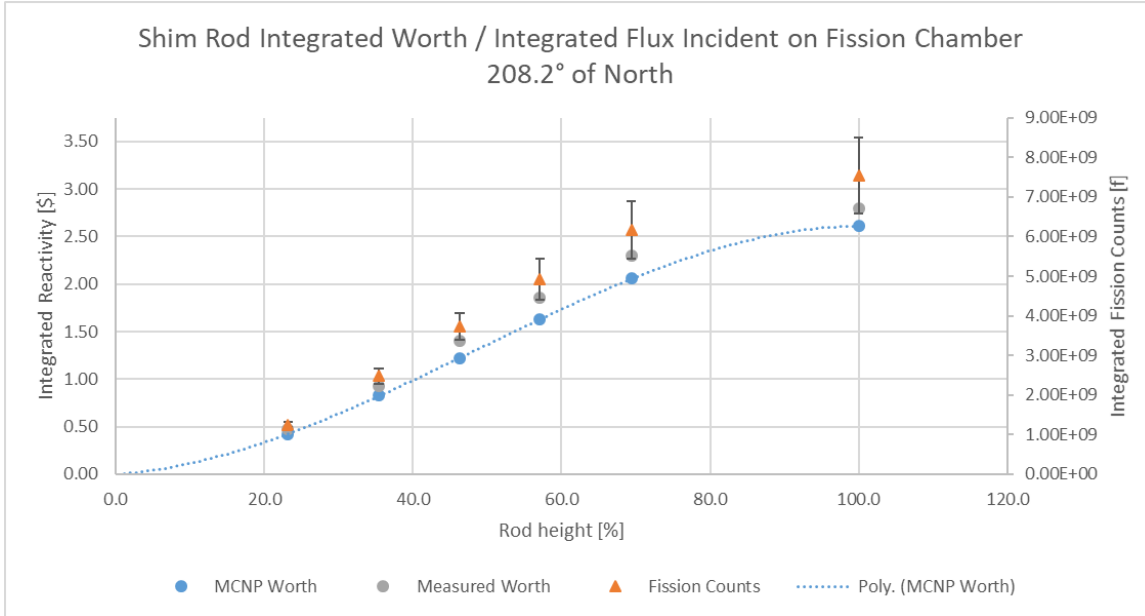


Figure 50: Integrated shim rod worth and fission rate in the 208.2° detector.

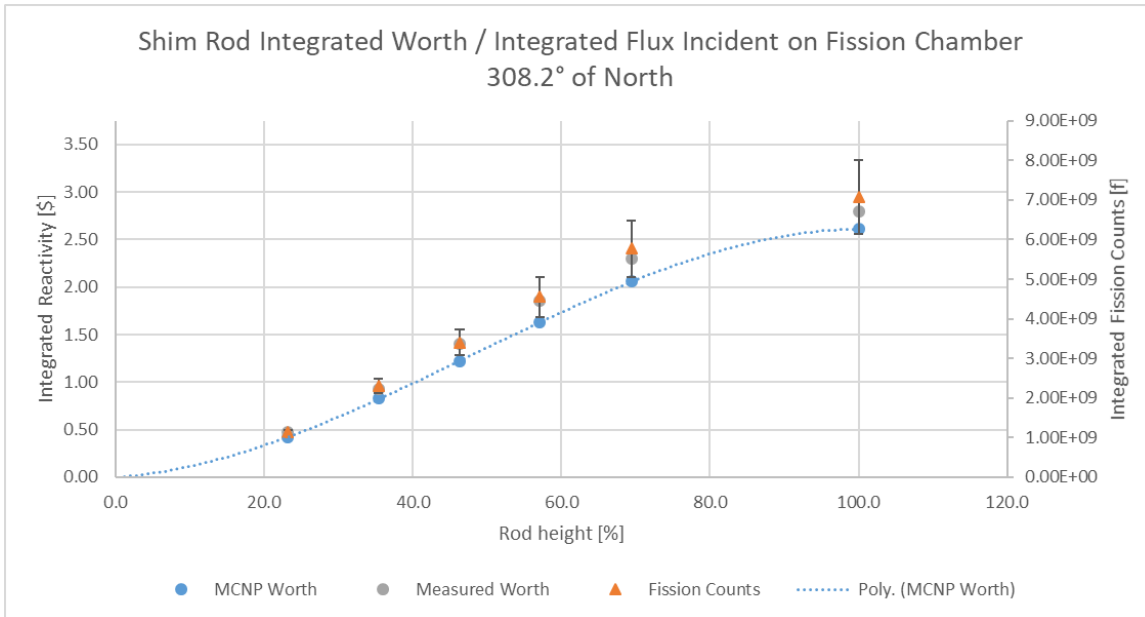


Figure 51: Integrated shim rod worth and fission rate in the 308.2° detector.

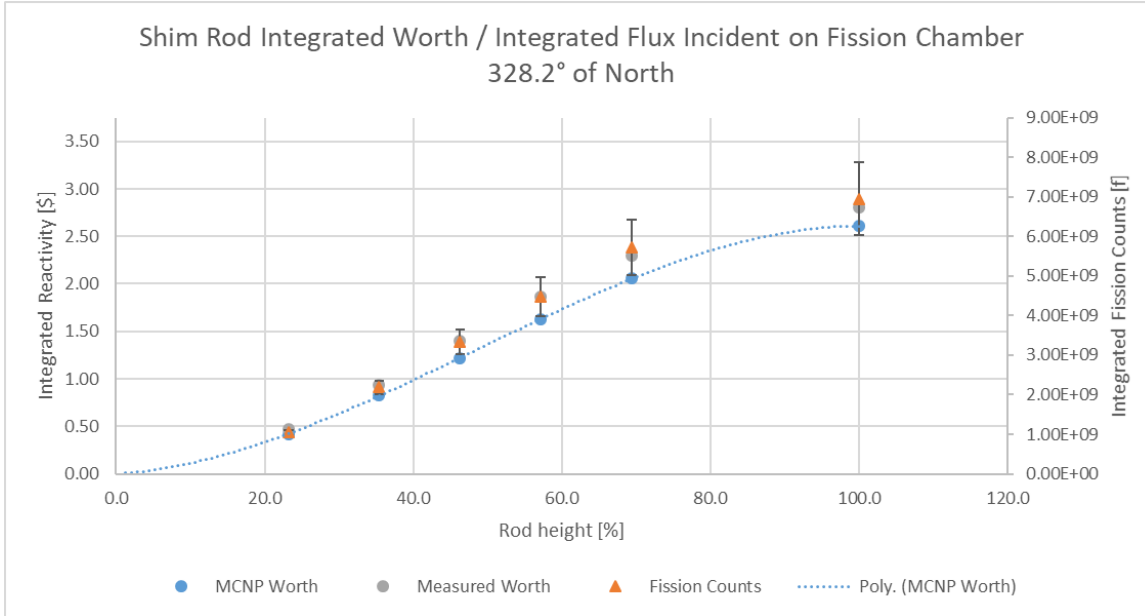


Figure 52: Integrated shim rod worth and fission rate in the 328.2° detector.

4.4.1.4 Regulating Rod

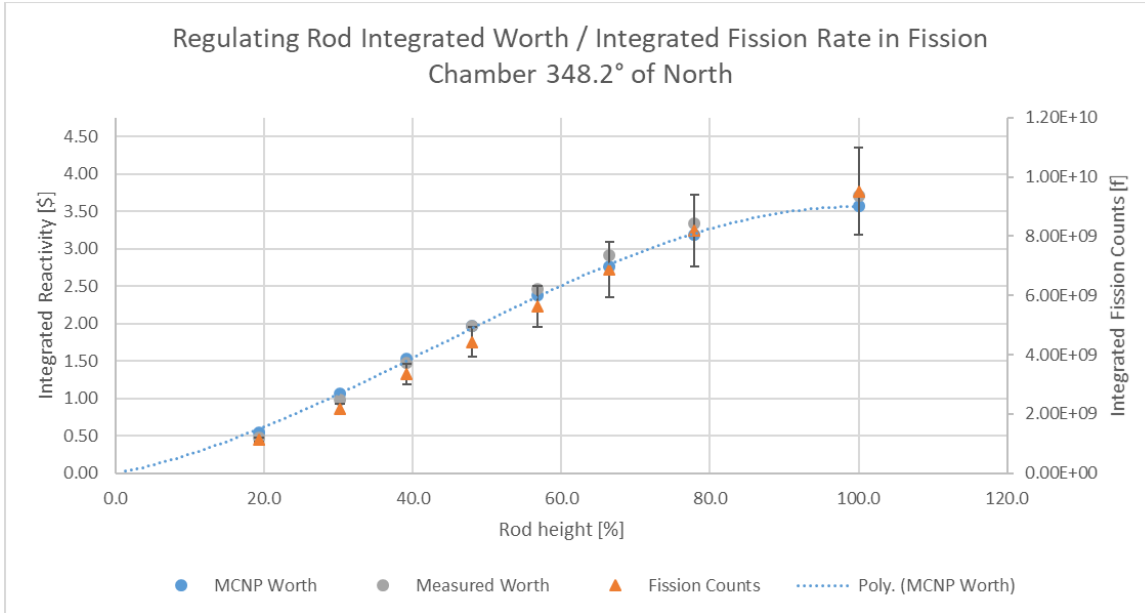


Figure 53: Integrated regulating rod worth and fission rate in the 348.2° detector.

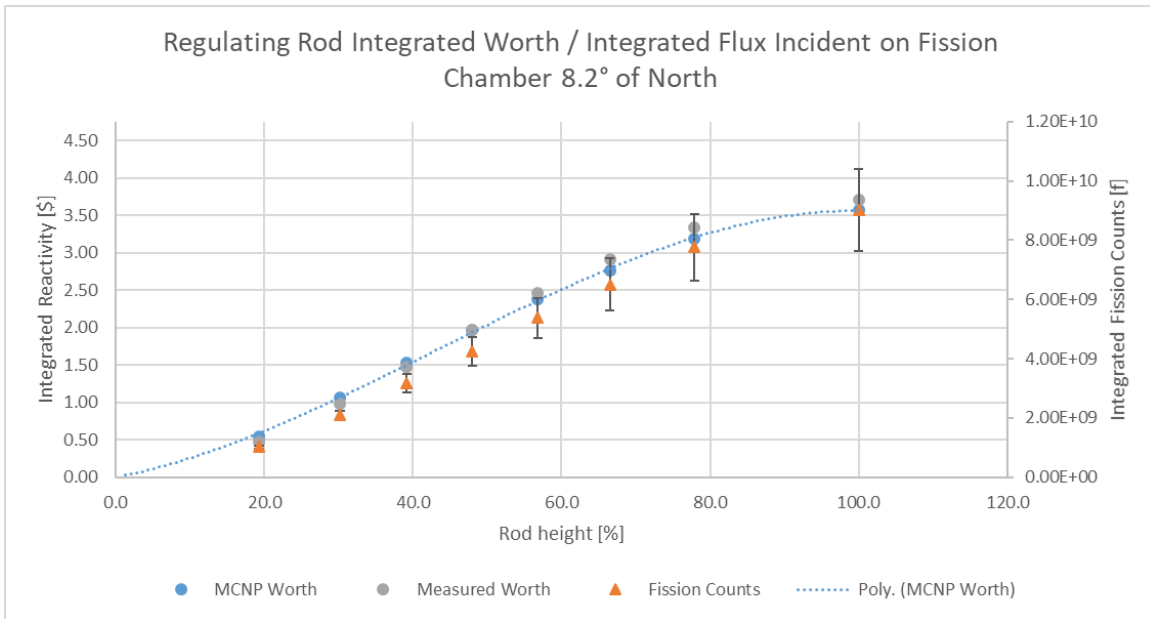


Figure 54: Integrated regulating rod worth and fission rate in the 8.2° detector.

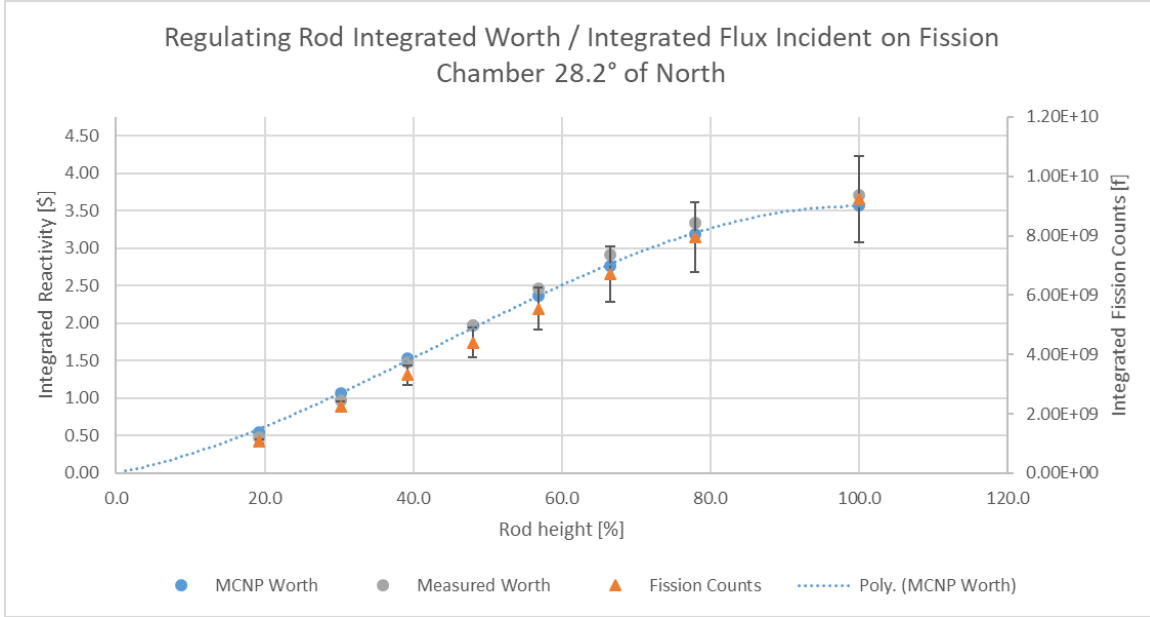


Figure 55: Integrated regulating rod worth and fission rate in the 28.2° detector.

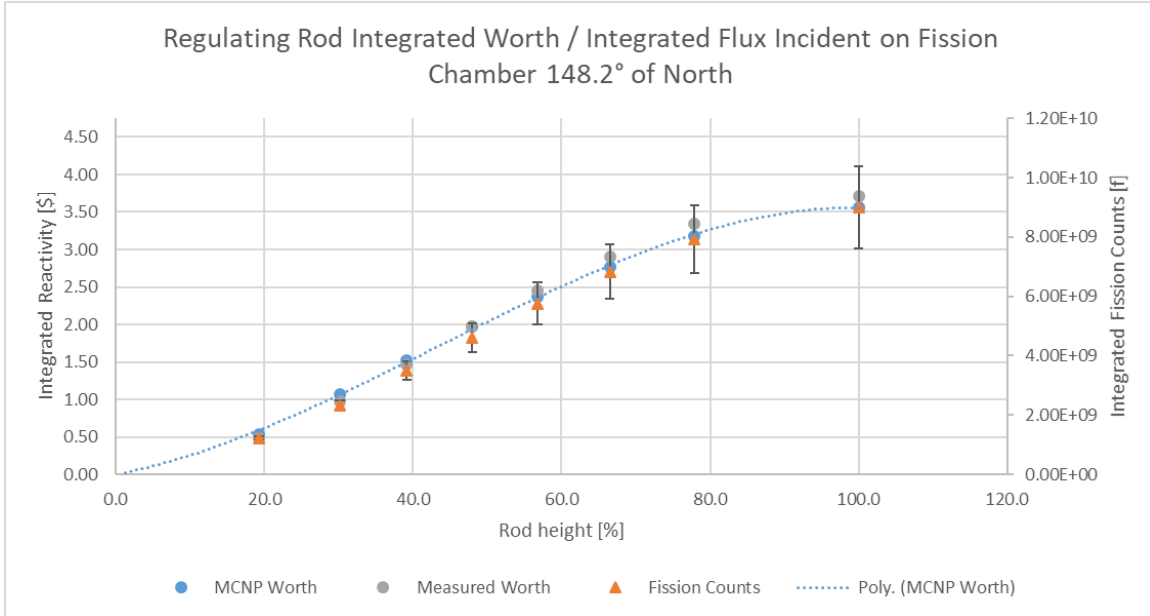


Figure 56: Integrated regulating rod worth and fission rate in the 148.2° detector.

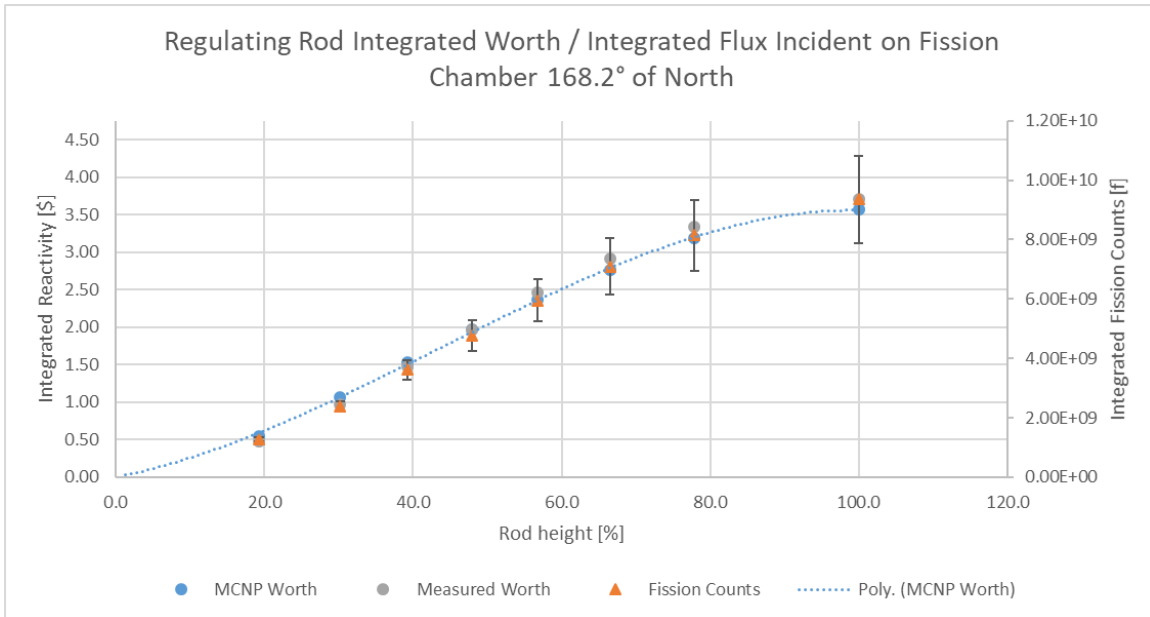


Figure 57: Integrated regulating rod worth and fission rate in the 168.2° detector.

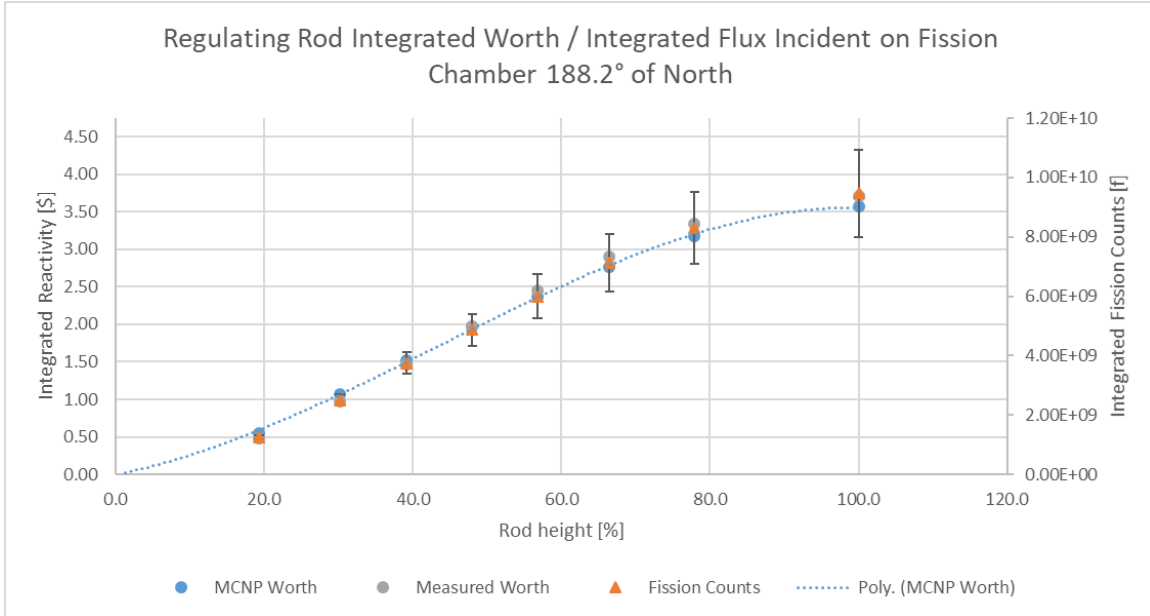


Figure 58: Integrated regulating rod worth and fission rate in the 188.2° detector.

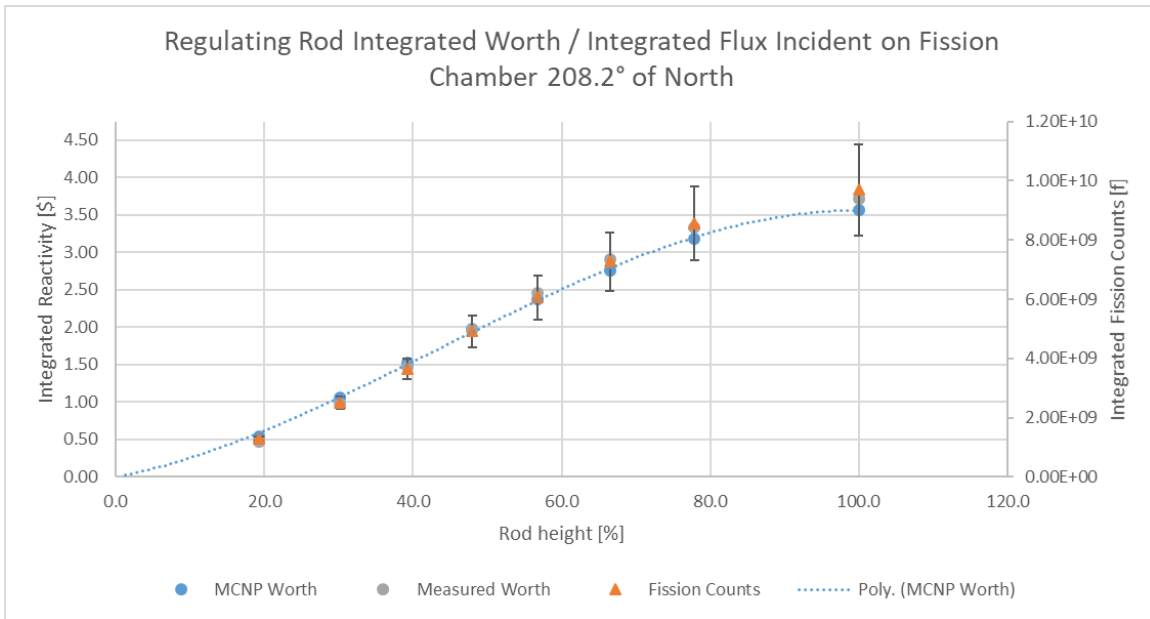


Figure 59: Integrated regulating rod worth and fission rate in the 208.2° detector.

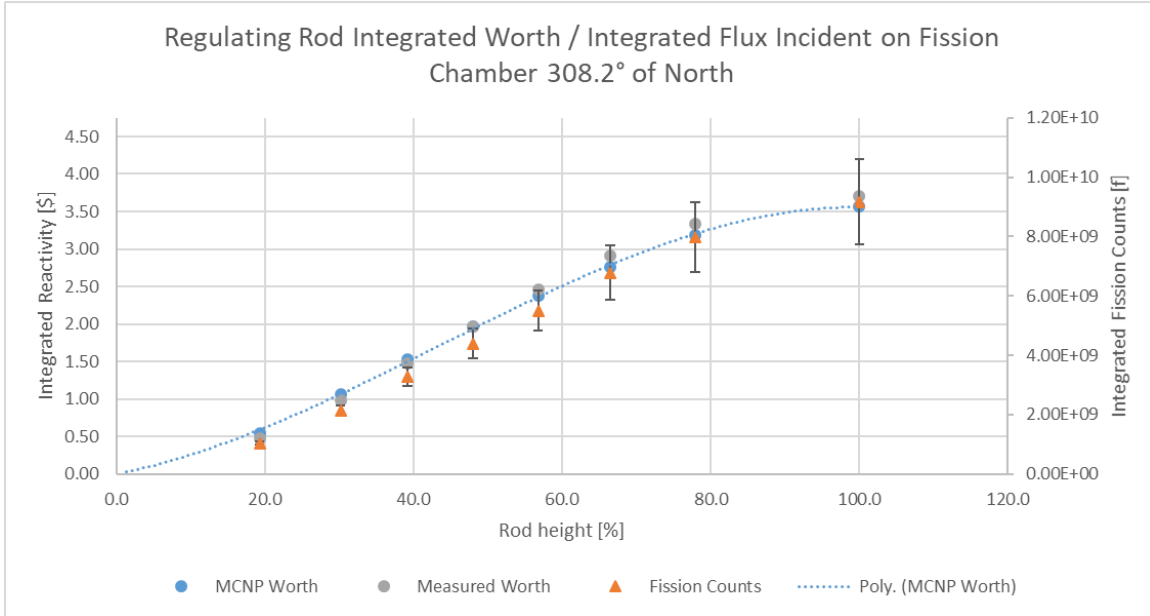


Figure 60: Integrated regulating rod worth and fission rate in the 308.2° detector.

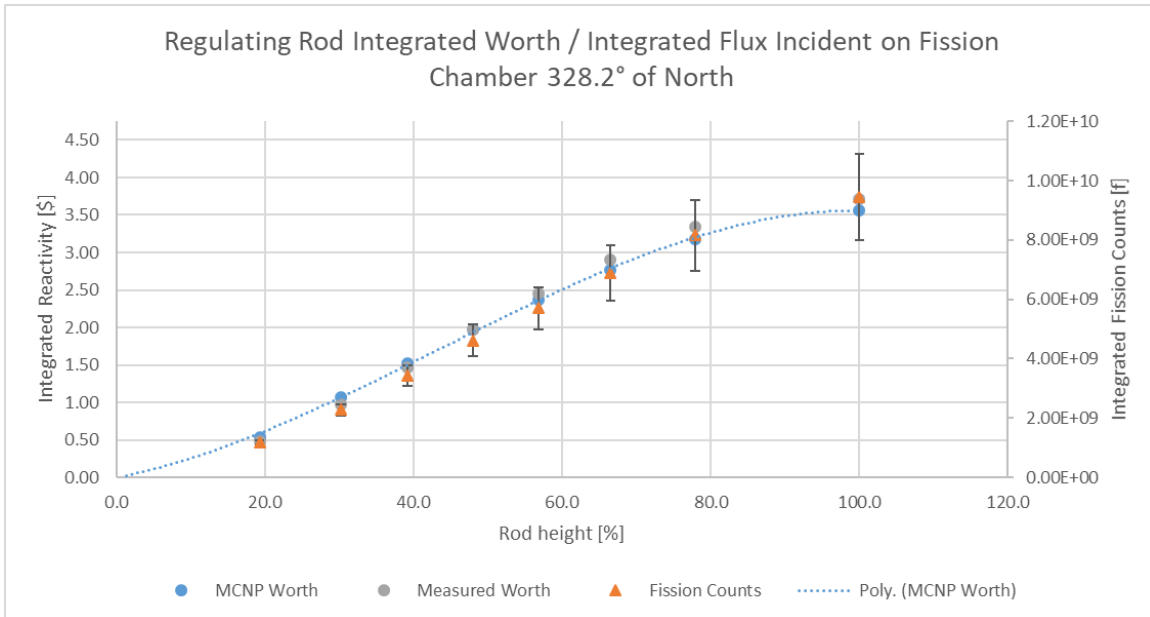


Figure 61: Integrated regulating rod worth and fission rate in the 328.2° detector.

4.4.2 CLICIT Core Detector Responses

The MCNP® model of the CLICIT core was used to produce models reflecting each control rod configuration during the CLICIT core control rod calibrations of October 2008 and a *kcode* problem was run for each configuration. The model contained the nine previously described fission chambers, and one million neutrons were born per cycle at various locations in the fuel for 100 cycles with an initial value of 1.0 for k_{eff} and the first 25 cycles are ignored statistically. The fission rate was obtained in the UO₂ regions of each detector by performing a volume-averaged flux tally and using a multiplier card that multiplies the flux by the total fission cross section of the material within the volume.

In addition, a particle-splitting variance reduction method was used to reduce the error associated with the flux tally by assigning the UO₂ regions of the detectors an importance to neutrons of three. The integrated fission rate in each detector is plotted against the measured and MCNP® calculated integral rod worth curves for each rod pull and each detector, where the detector located at 348.2° of North is the physical detector. The comparison of the integrated detector response to the integral control rod worth curves are shown below in Figures 62 – 97 for the CLICIT core configuration.

4.4.2.1 Transient Rod

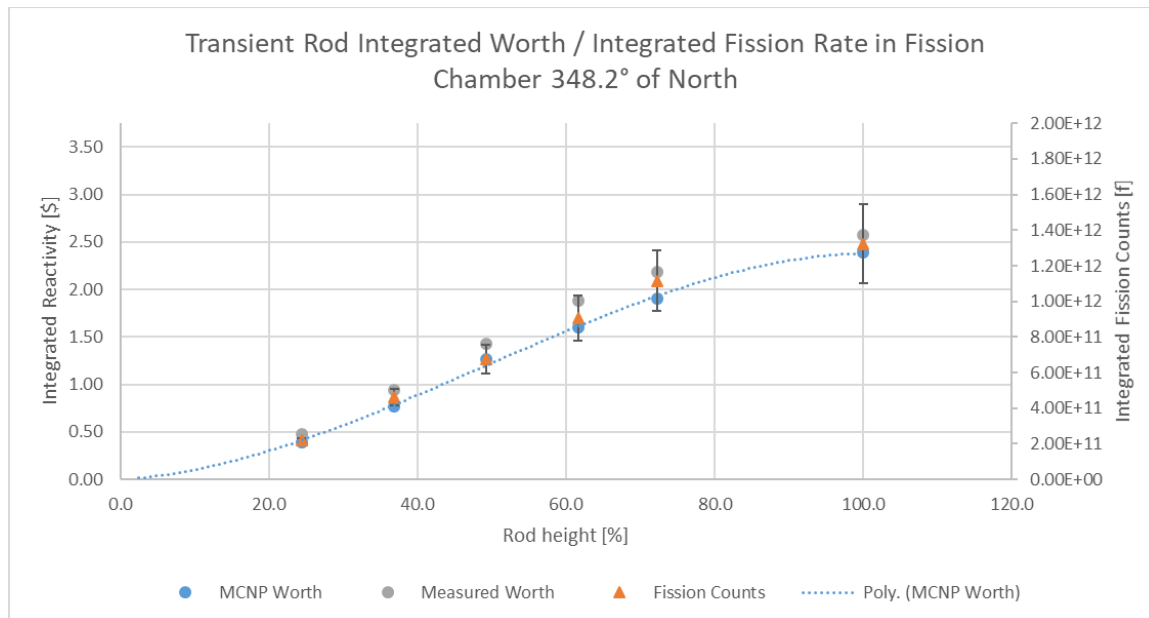


Figure 62: Integrated transient rod worth and fission rate in the 348.2° detector.

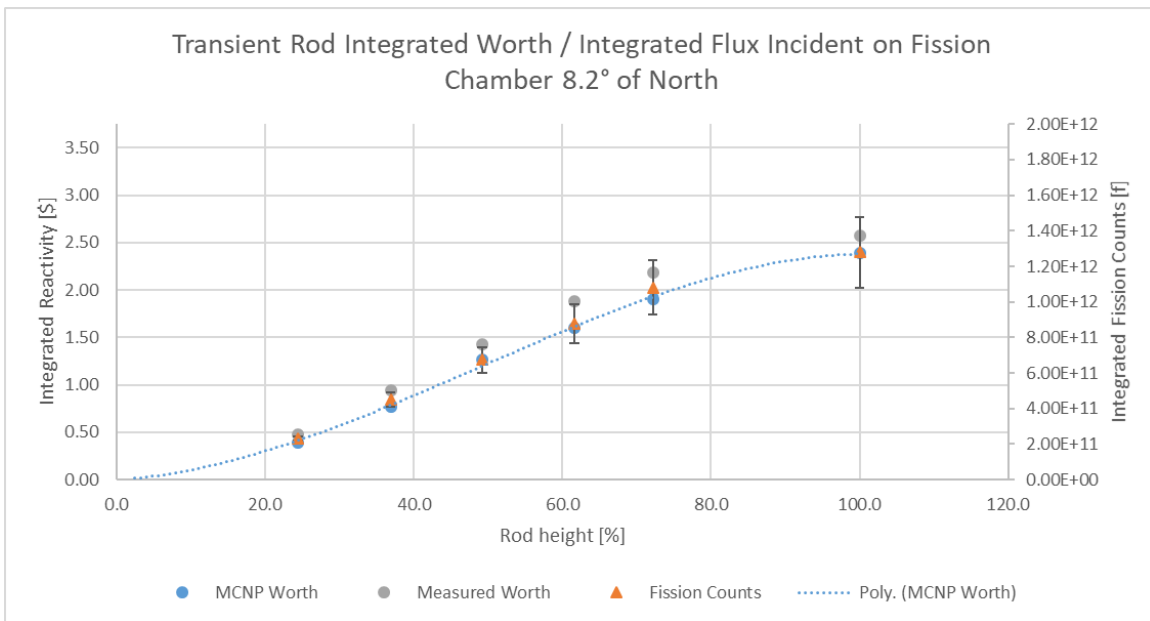


Figure 63: Integrated transient rod worth and fission rate in the 8.2° detector.

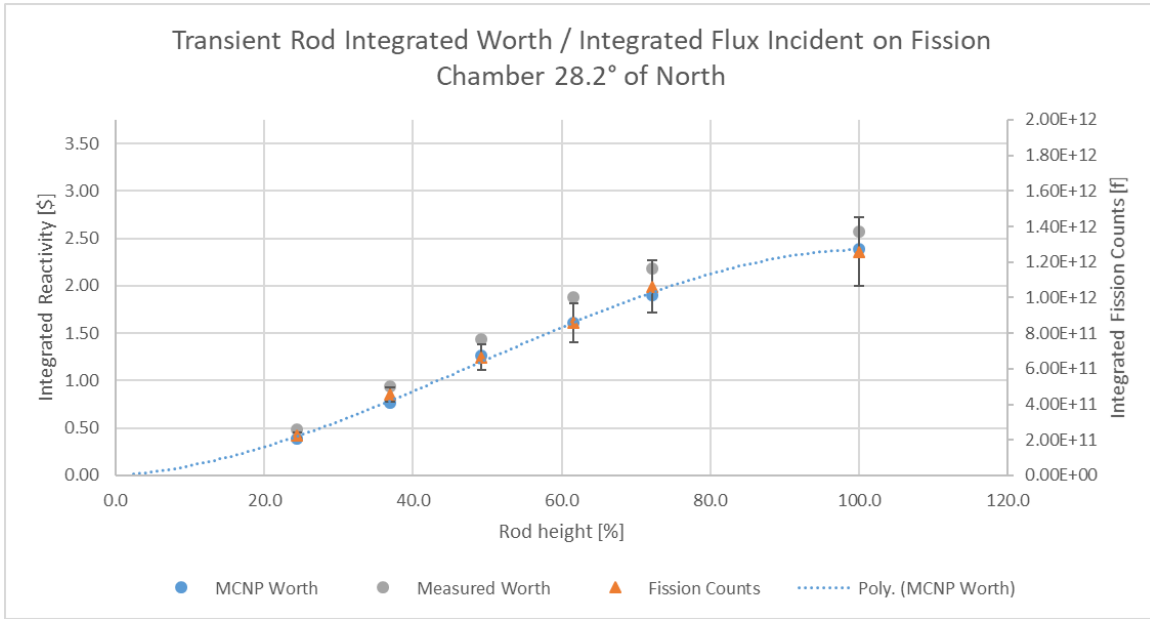


Figure 64: Integrated transient rod worth and fission rate in the 28.2° detector.

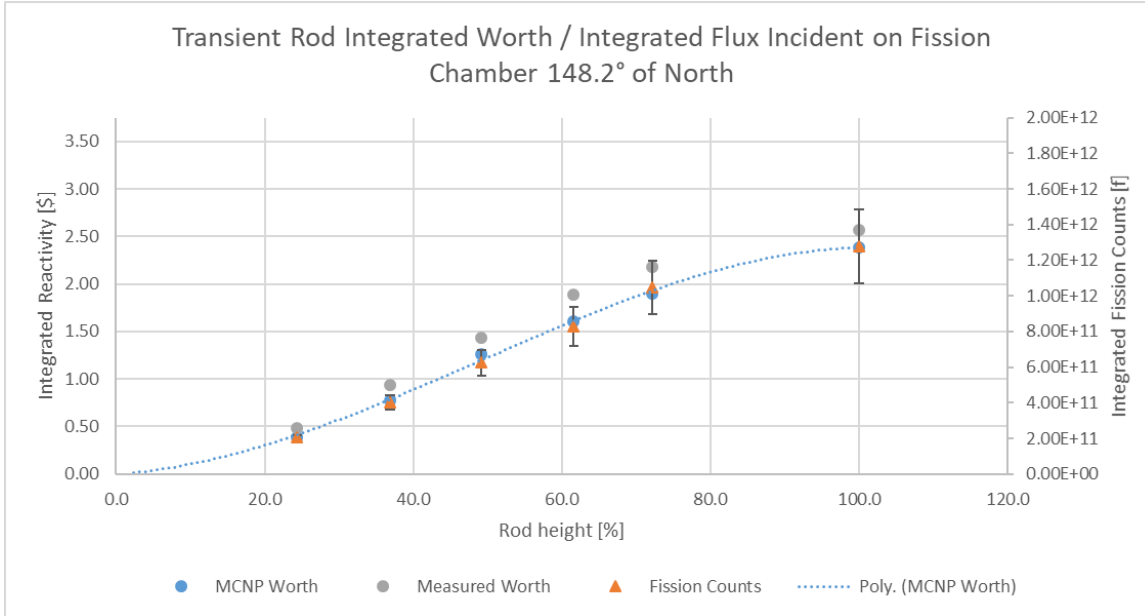


Figure 65: Integrated transient rod worth and fission rate in the 148.2° detector.

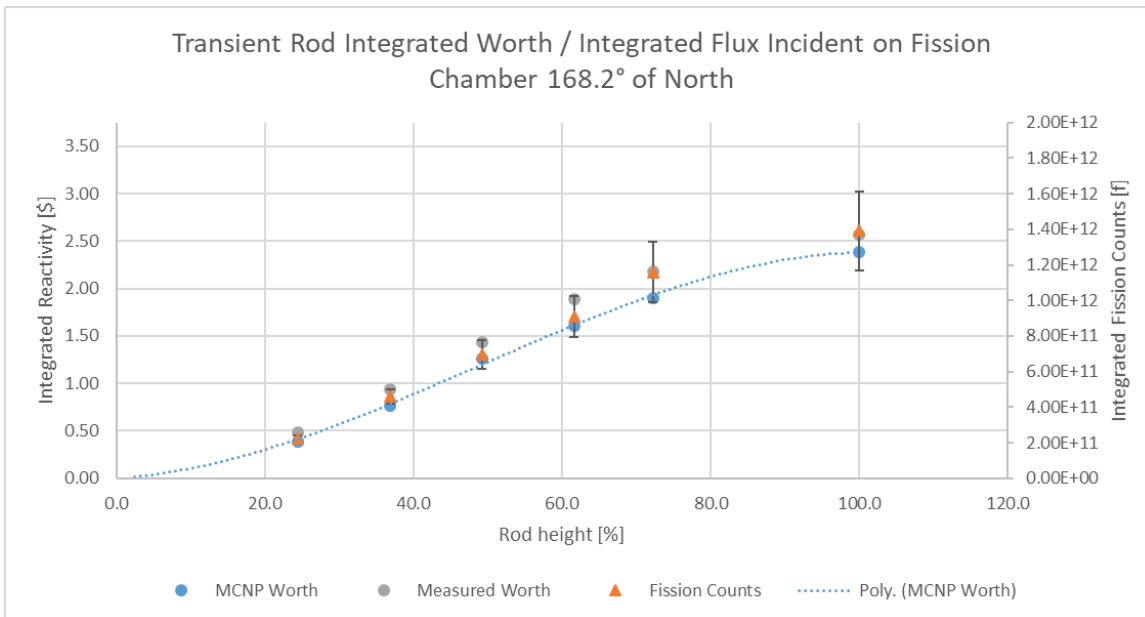


Figure 66: Integrated transient rod worth and fission rate in the 168.2° detector.

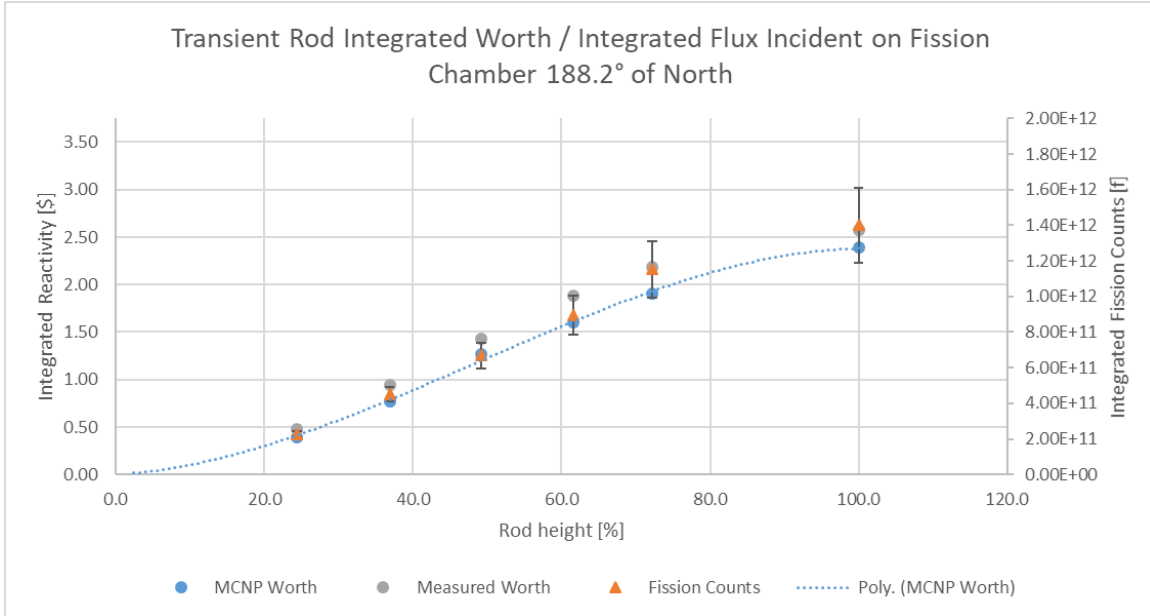


Figure 67: Integrated transient rod worth and fission rate in the 188.2° detector.

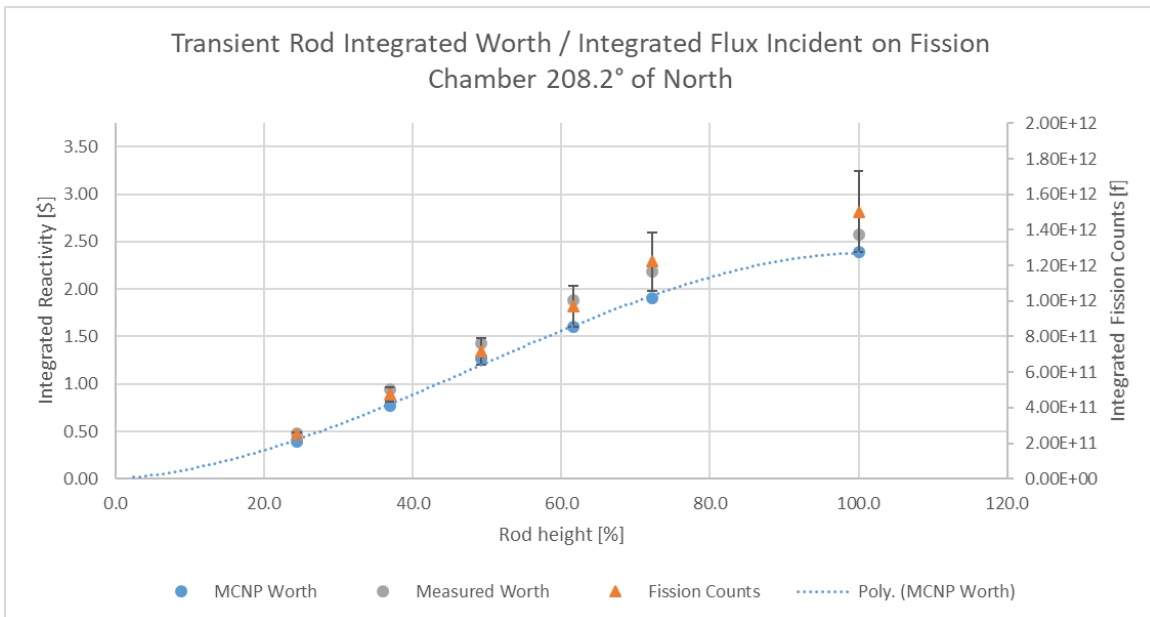


Figure 68: Integrated transient rod worth and fission rate in the 208.2° detector.

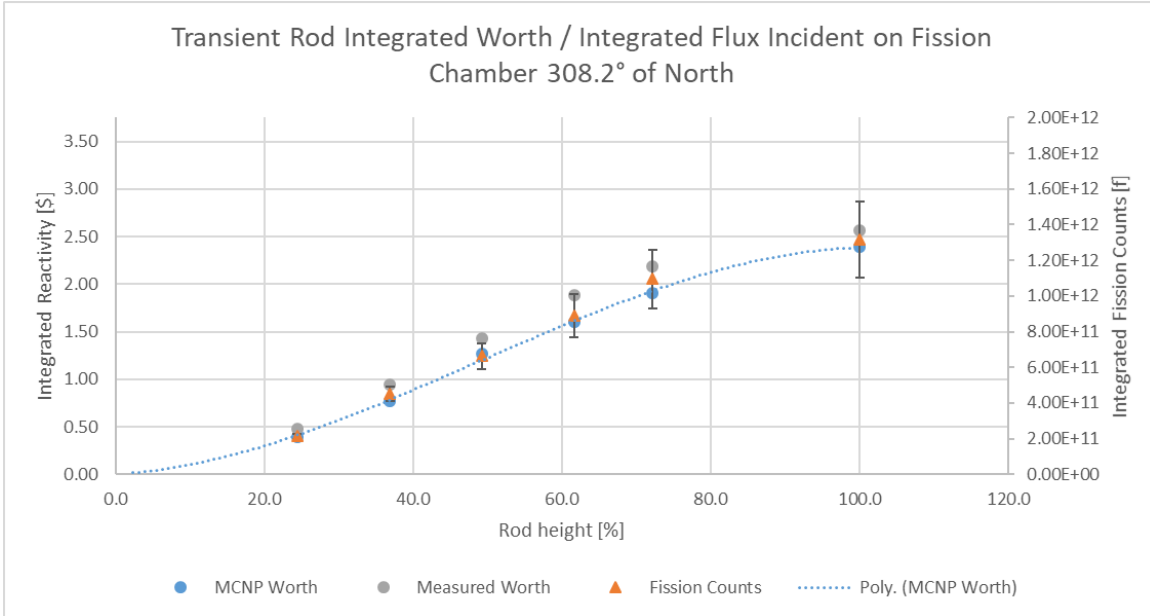


Figure 69: Integrated transient rod worth and fission rate in the 308.2° detector.

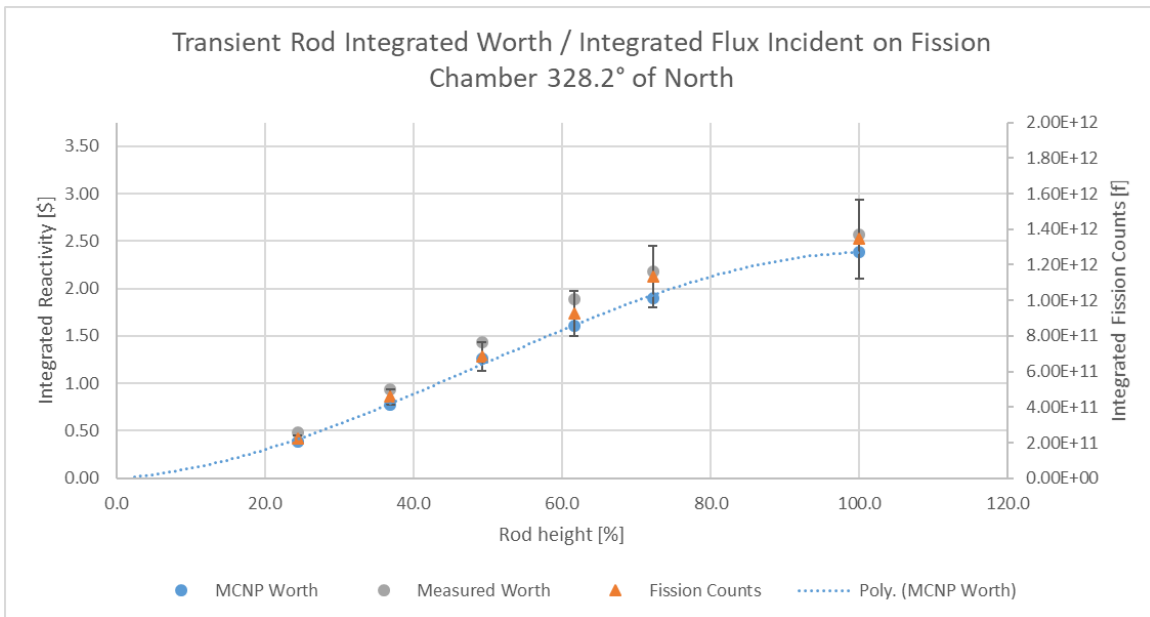


Figure 70: Integrated transient rod worth and fission rate in the 328.2° detector.

4.4.2.2 Safety Rod

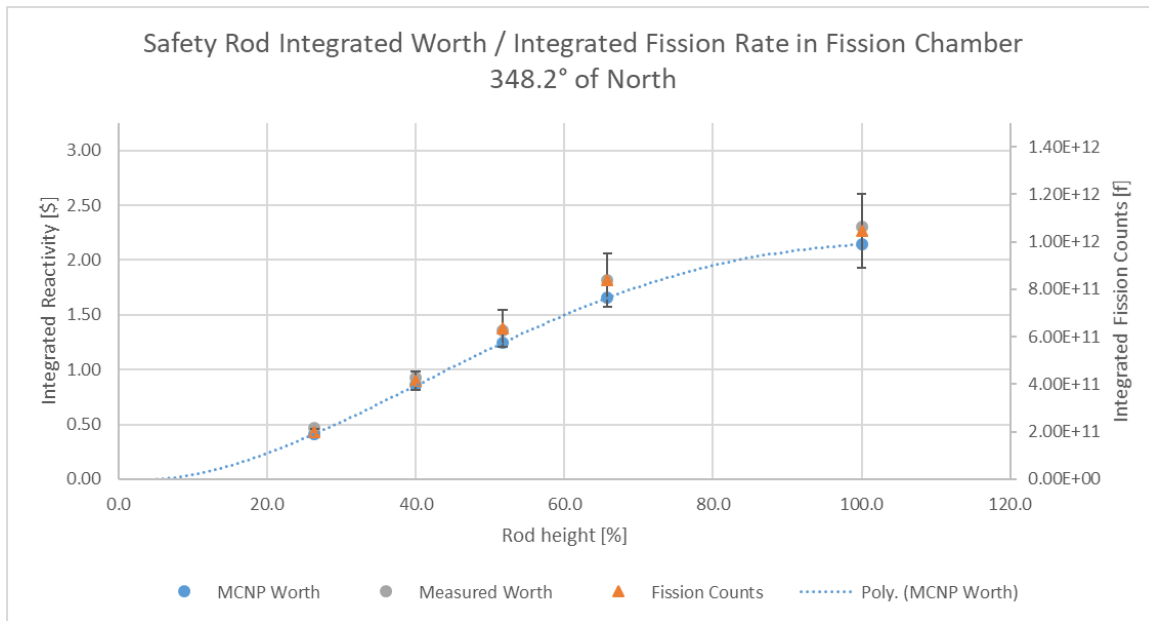


Figure 71: Integrated safety rod worth and fission rate in the 348.2° detector.

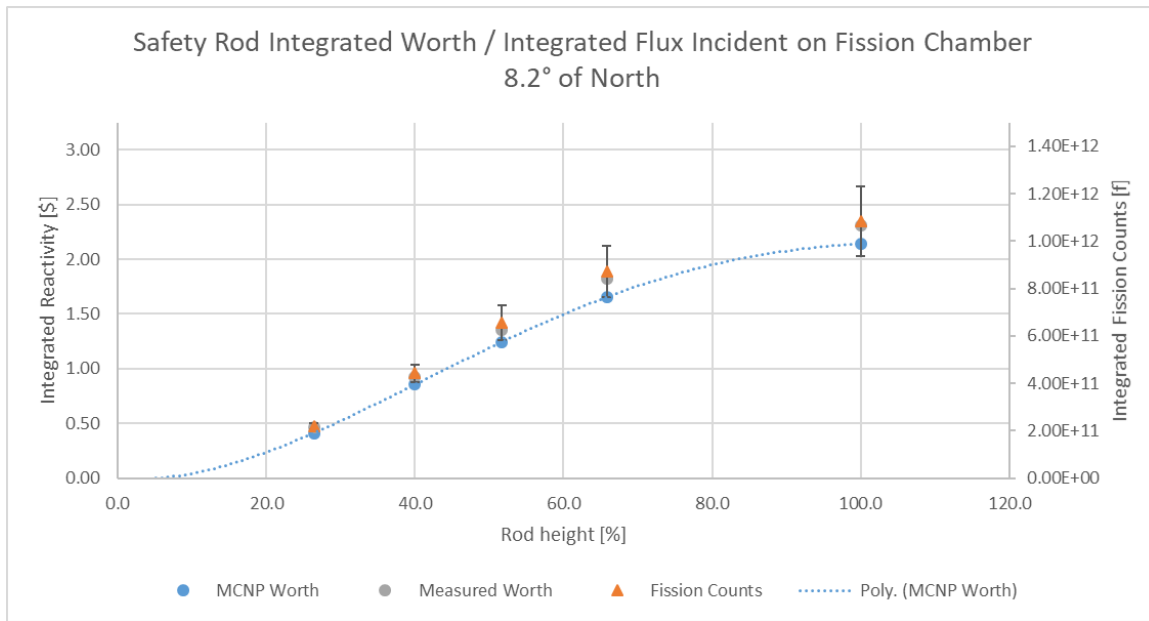


Figure 72: Integrated safety rod worth and fission rate in the 8.2° detector.

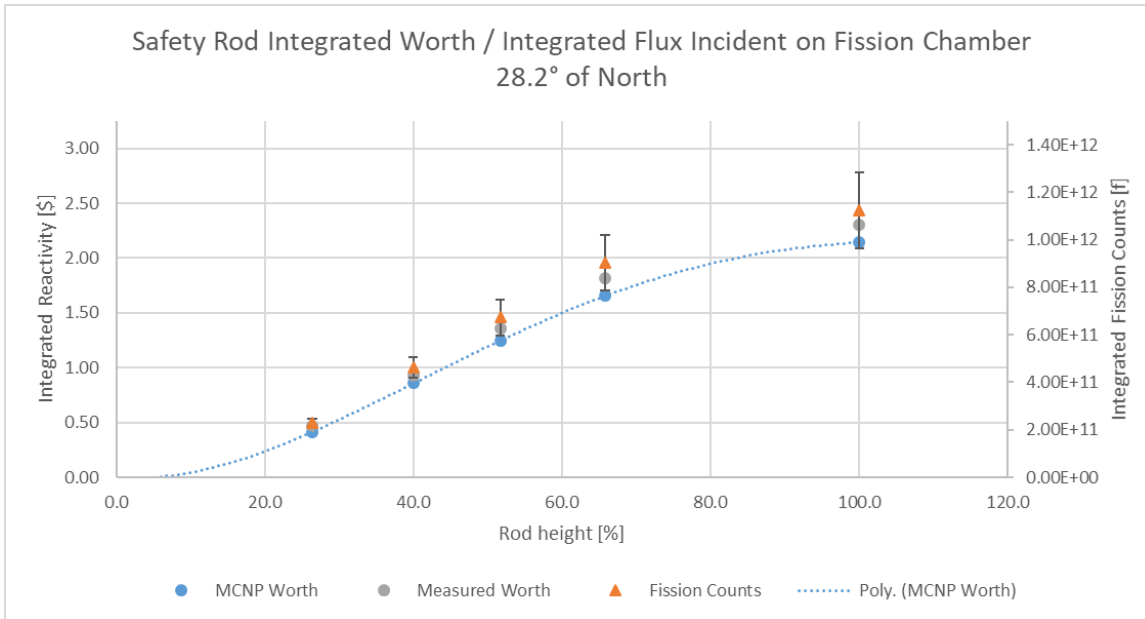


Figure 73: Integrated safety rod worth and fission rate in the 28.2° detector.

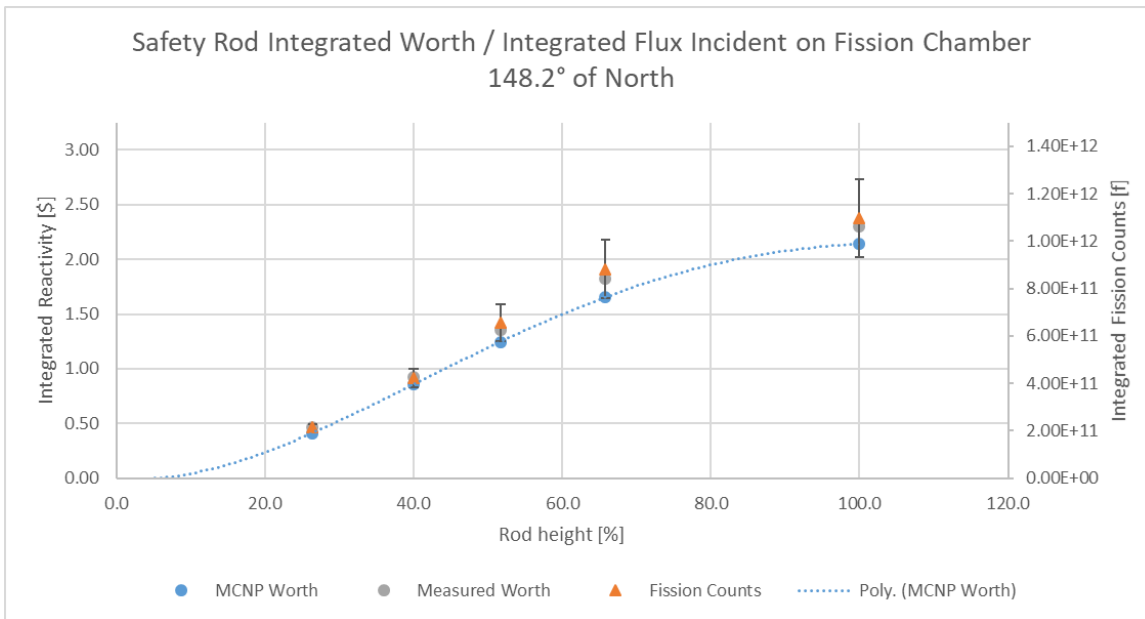


Figure 74: Integrated safety rod worth and fission rate in the 148.2° detector.

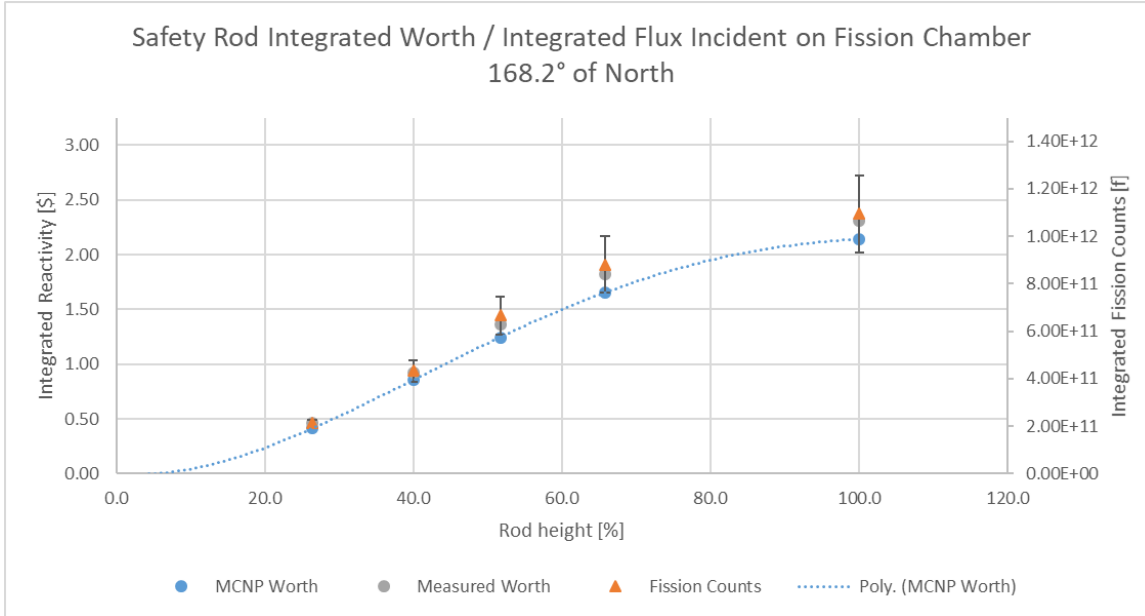


Figure 75: Integrated safety rod worth and fission rate in the 168.2° detector.

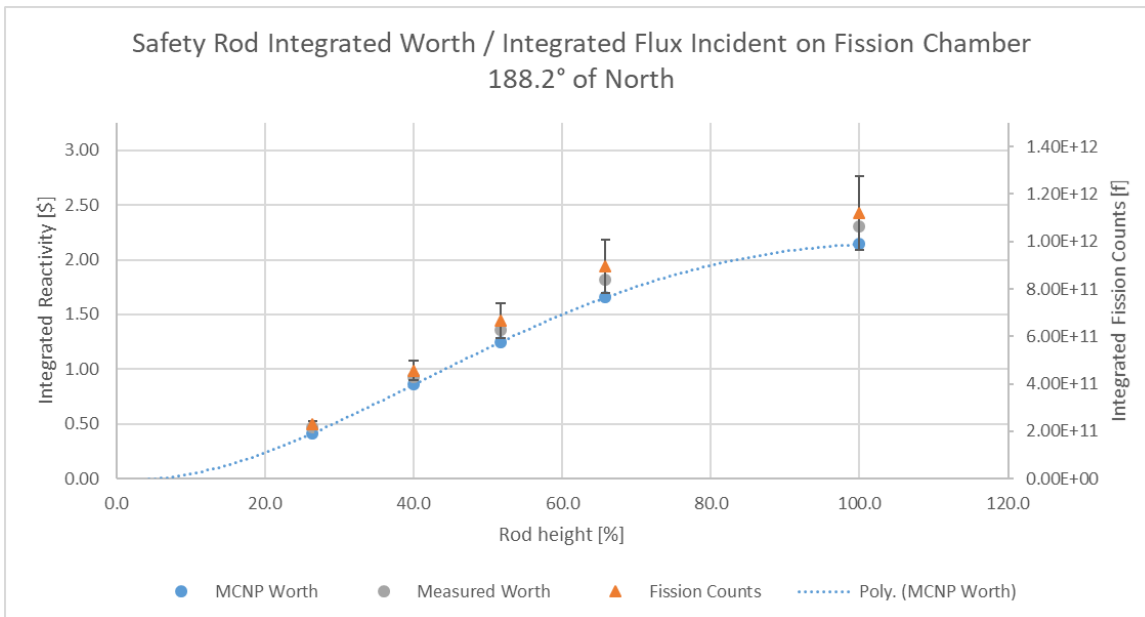


Figure 76: Integrated safety rod worth and fission rate in the 188.2° detector.

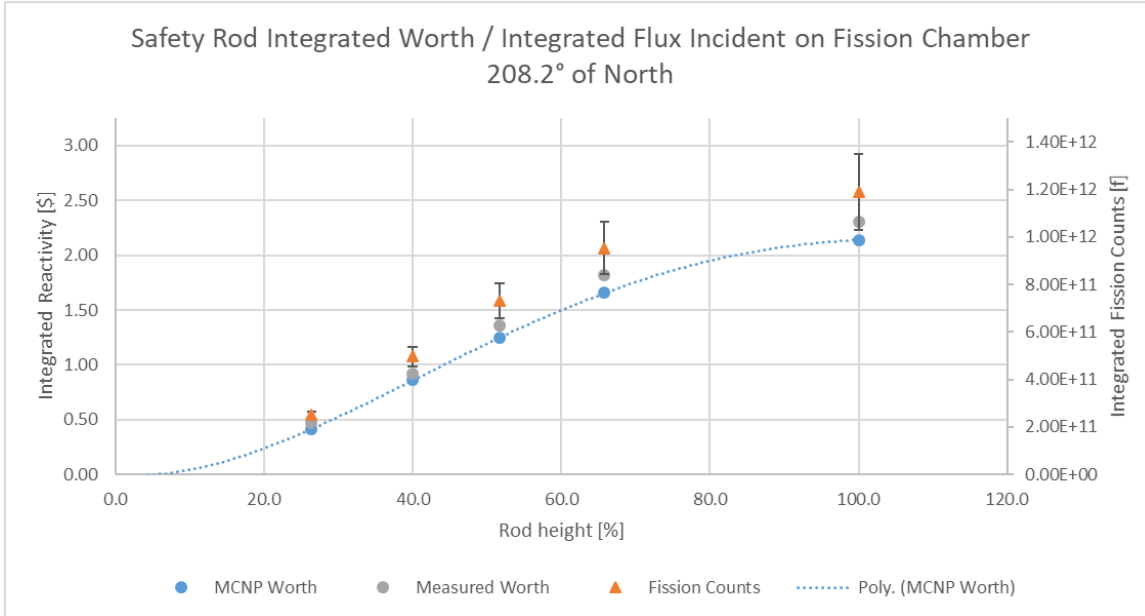


Figure 77: Integrated safety rod worth and fission rate in the 208.2° detector.

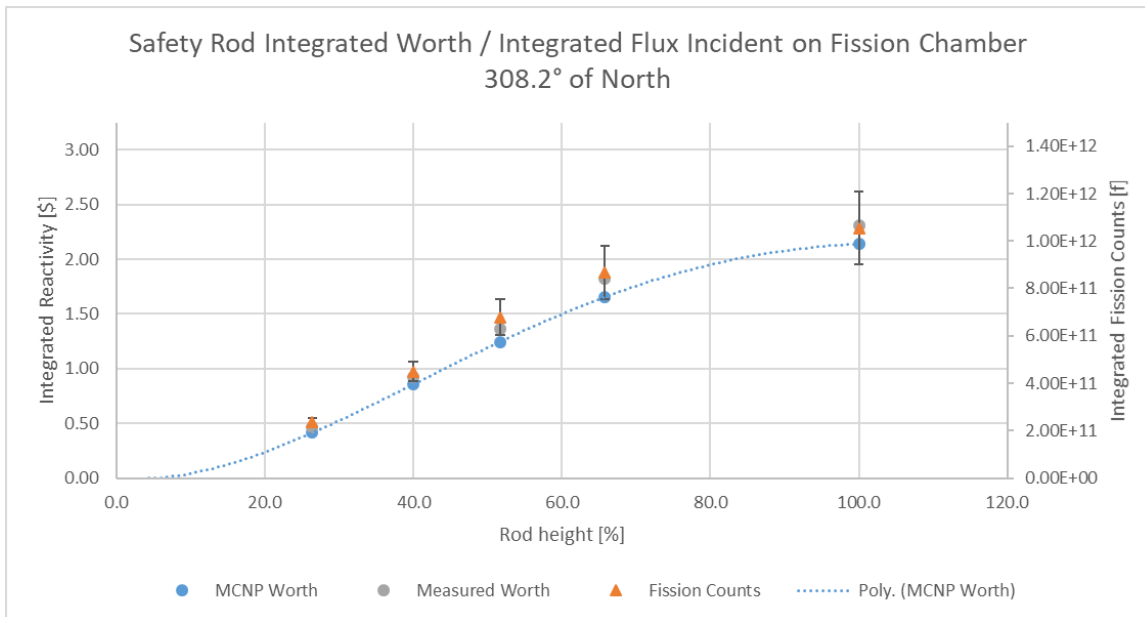


Figure 78: Integrated safety rod worth and fission rate in the 308.2° detector.

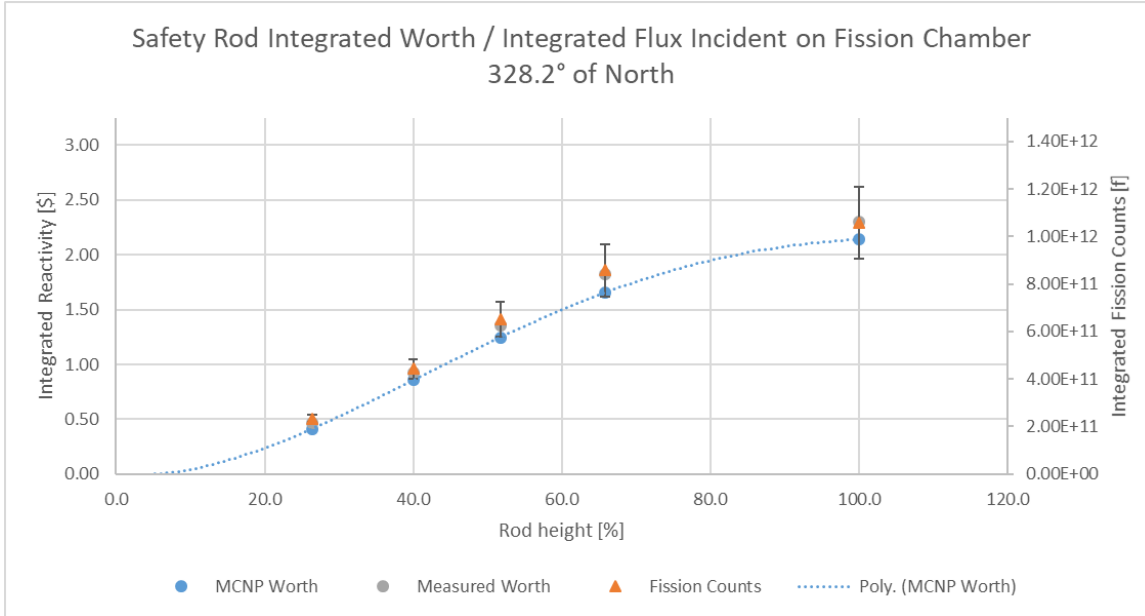


Figure 79: Integrated safety rod worth and fission rate in the 328.2° detector.

4.4.2.3 Shim Rod

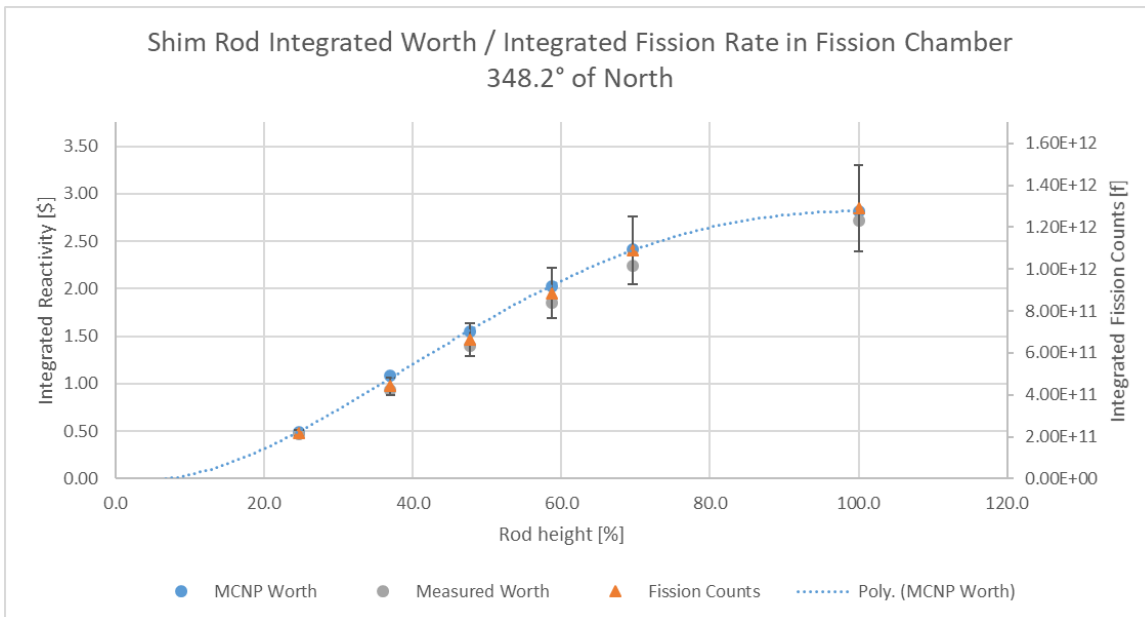


Figure 80: Integrated shim rod worth and fission rate in the 348.2° detector.

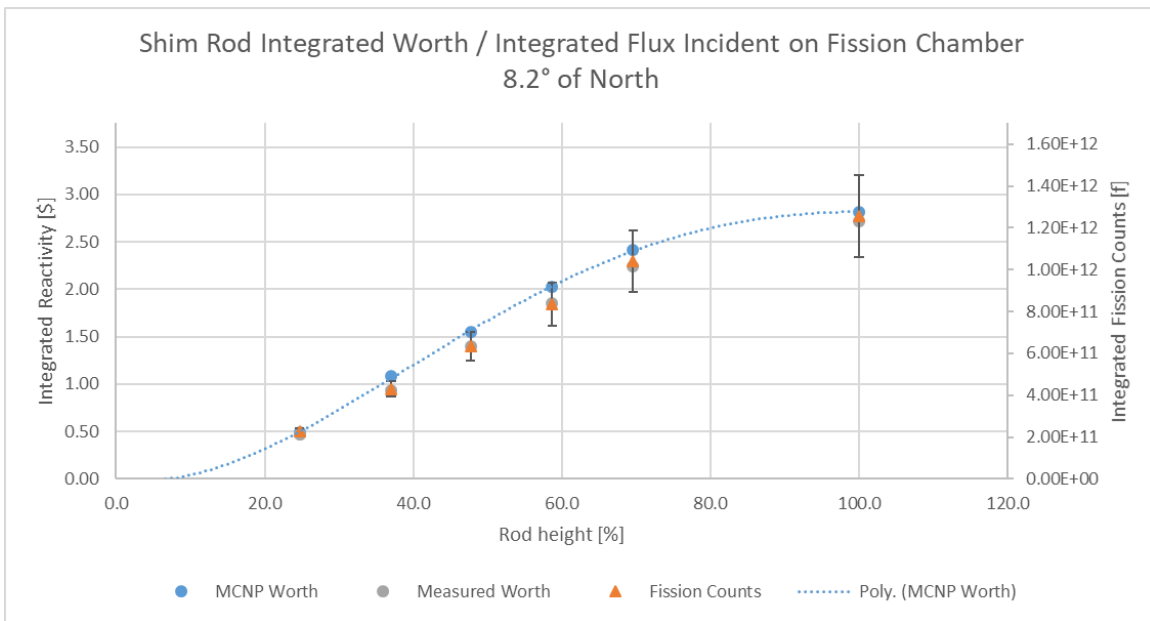


Figure 81: Integrated shim rod worth and fission rate in the 8.2° detector.

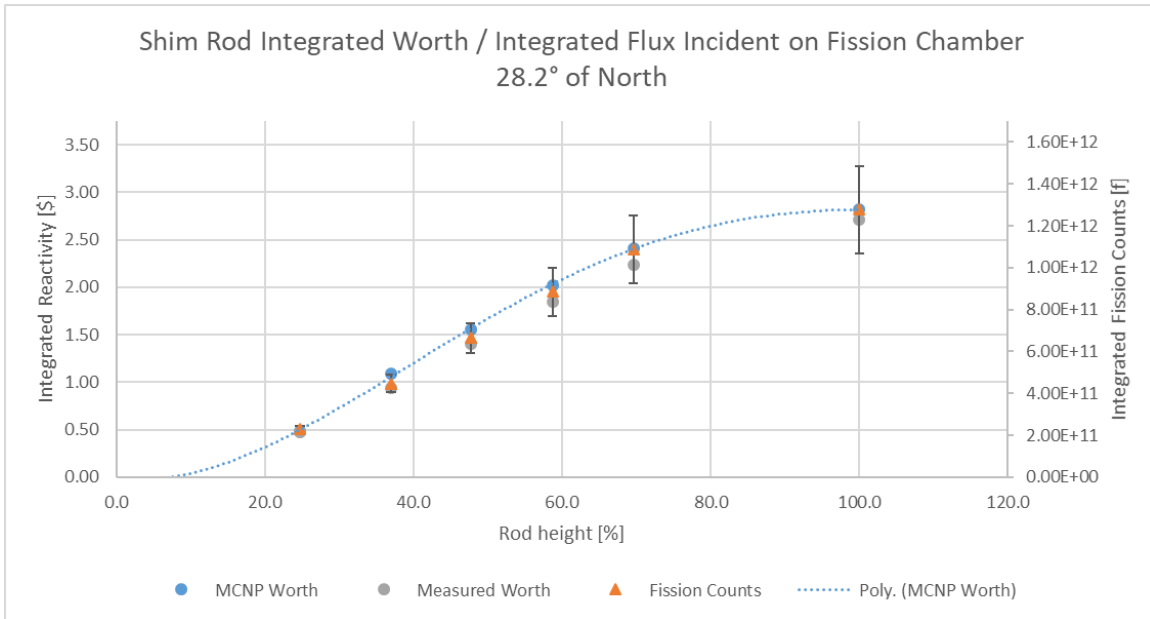


Figure 82: Integrated shim rod worth and fission rate in the 28.2° detector.

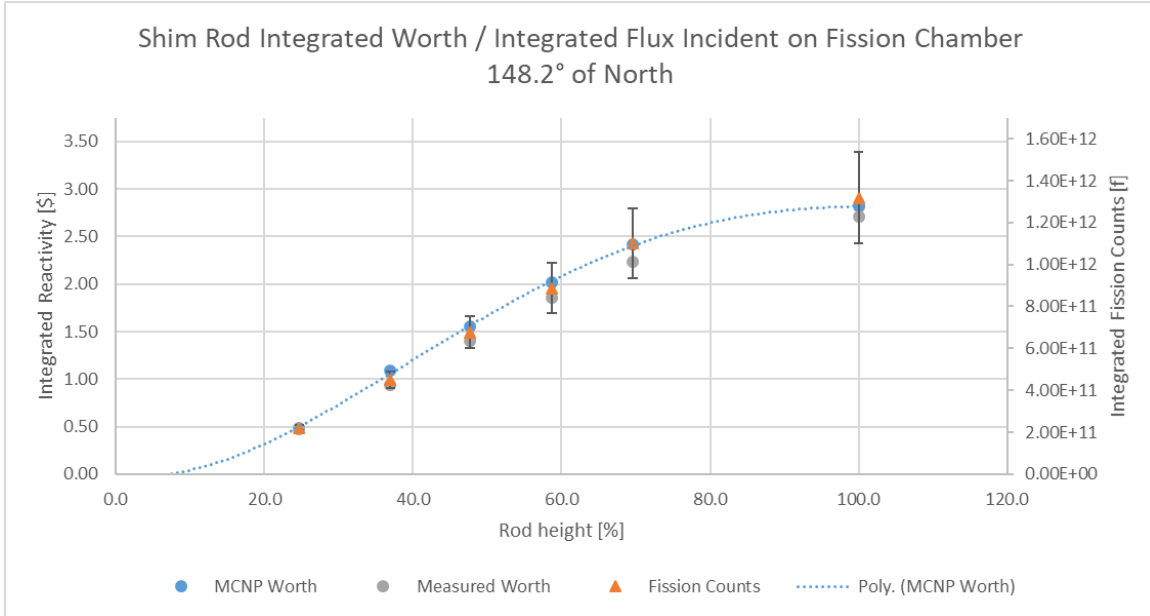


Figure 83: Integrated shim rod worth and fission rate in the 148.2° detector.

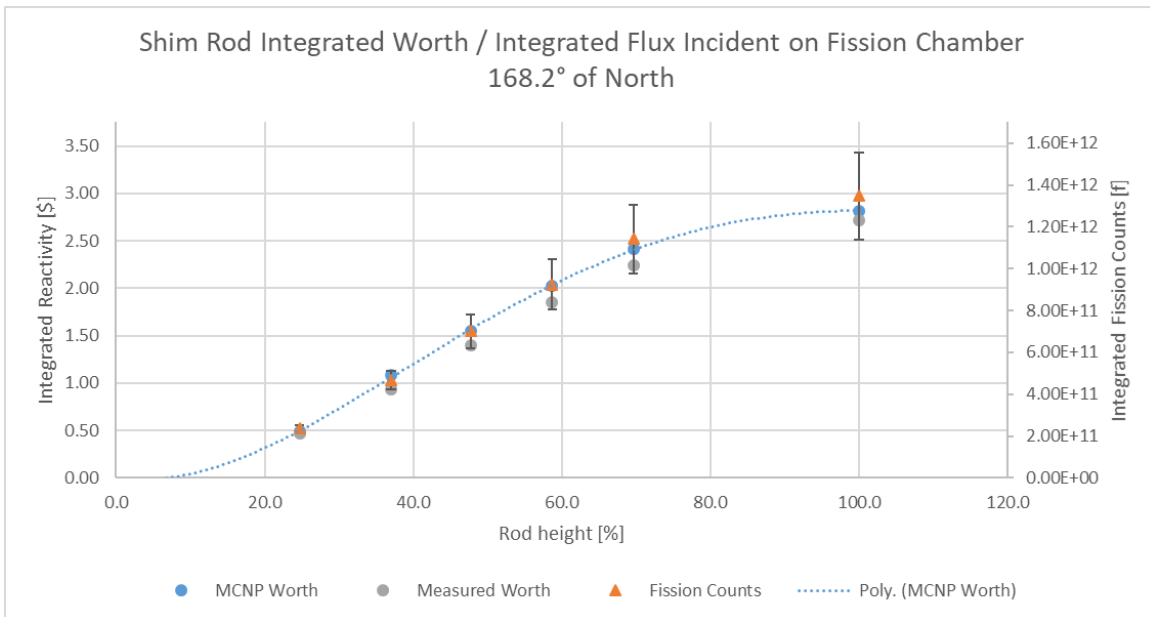


Figure 84: Integrated shim rod worth and fission rate in the 168.2° detector.

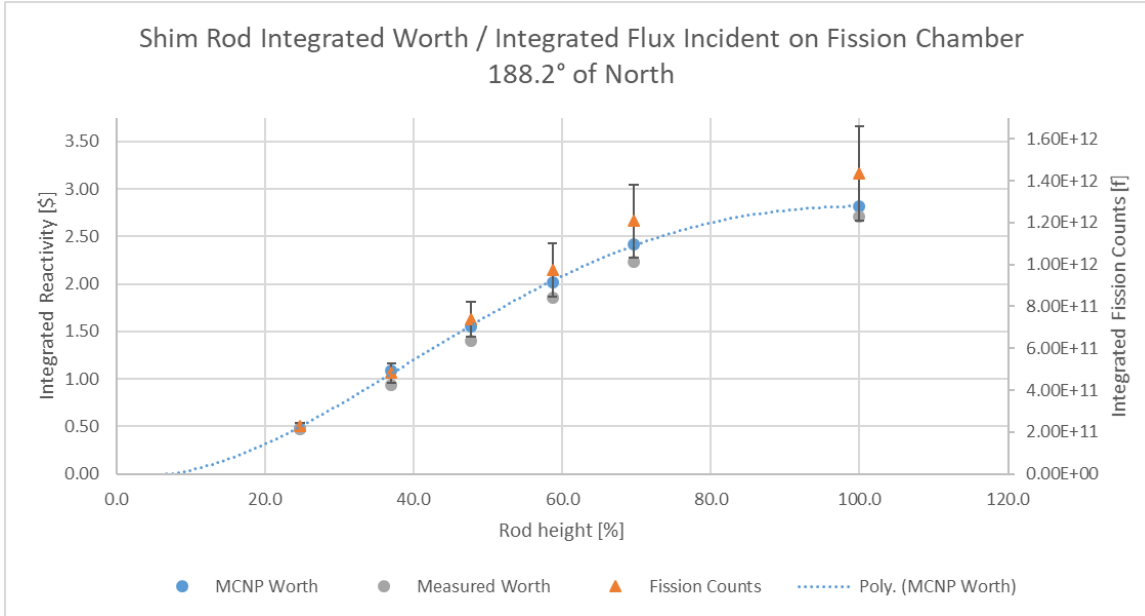


Figure 85: Integrated shim rod worth and fission rate in the 188.2° detector.

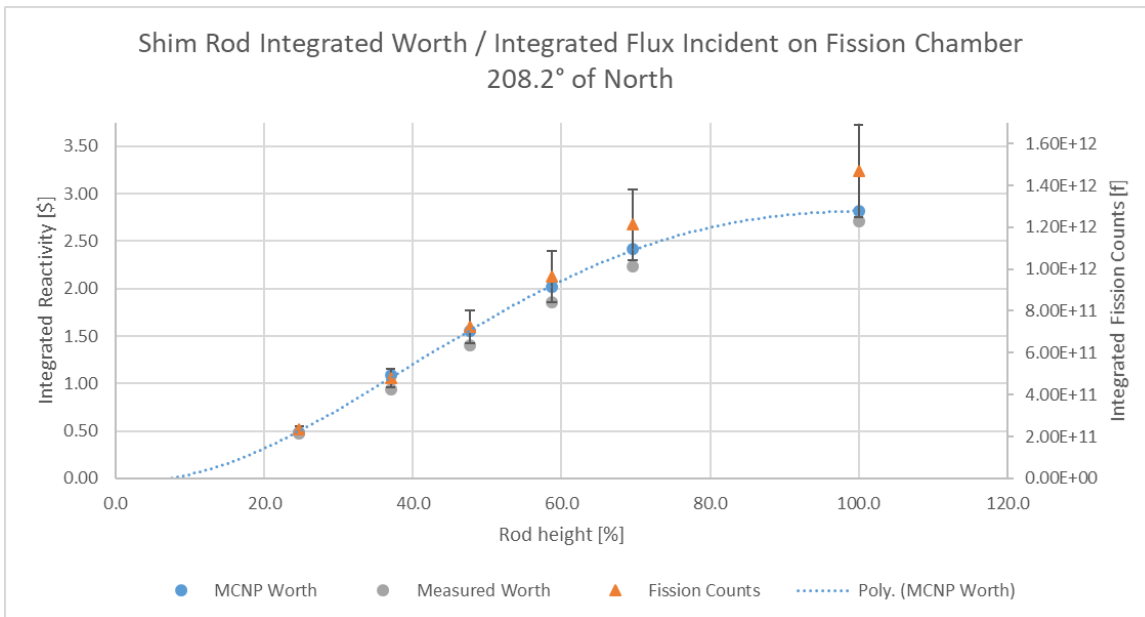


Figure 86: Integrated shim rod worth and fission rate in the 208.2° detector.

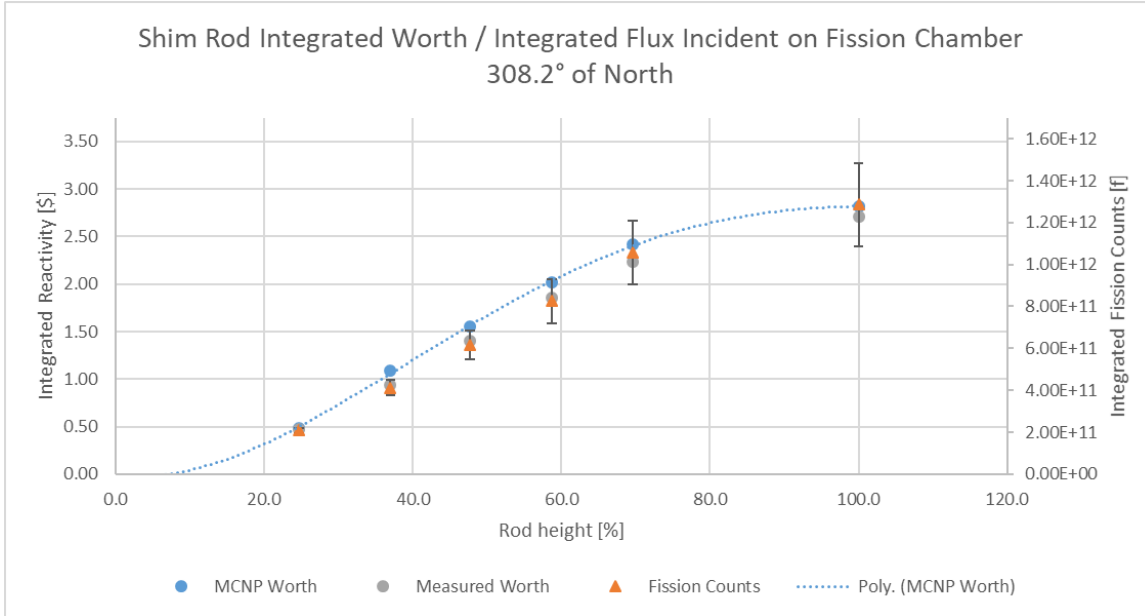


Figure 87: Integrated shim rod worth and fission rate in the 308.2° detector.

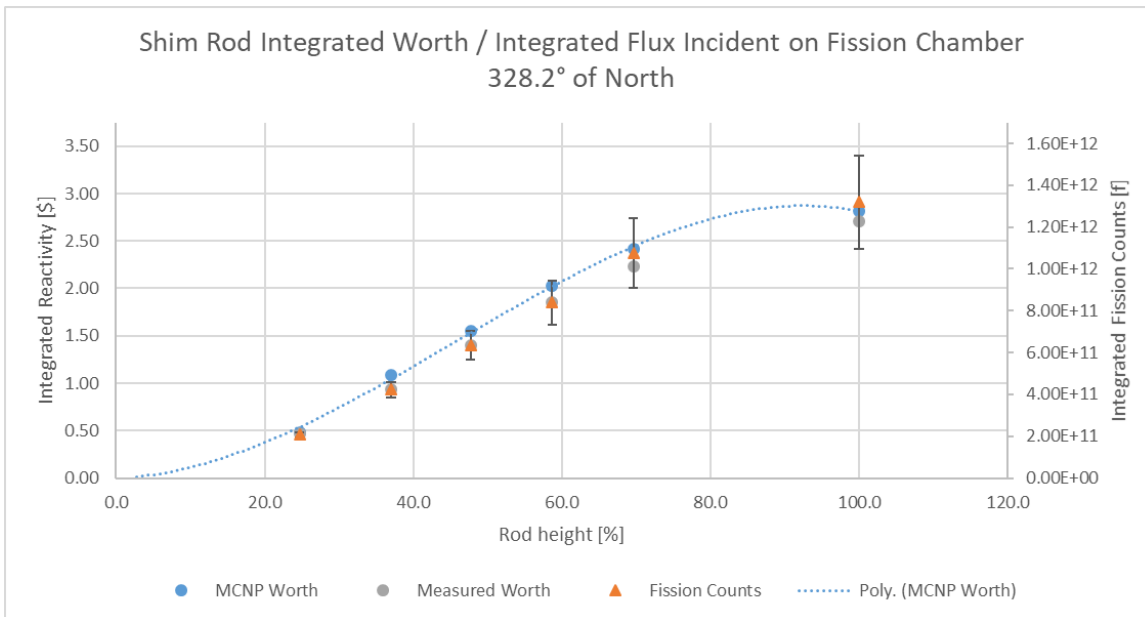


Figure 88: Integrated shim rod worth and fission rate in the 328.2° detector.

4.4.2.4 Regulating Rod

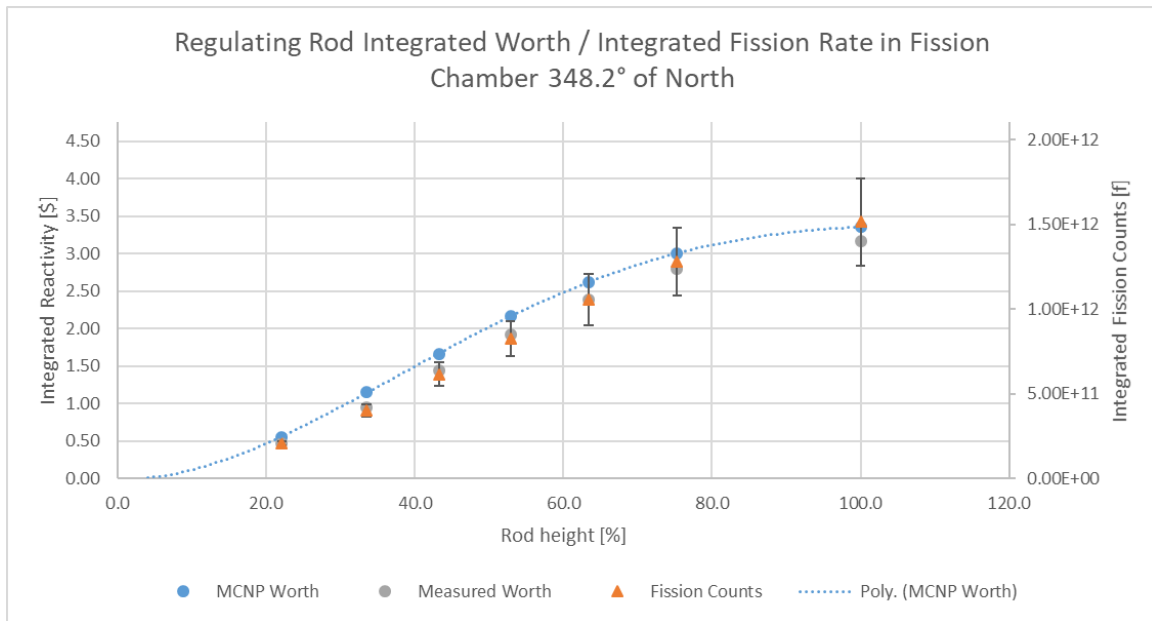


Figure 89: Integrated regulating rod worth and fission rate in the 348.2° detector.

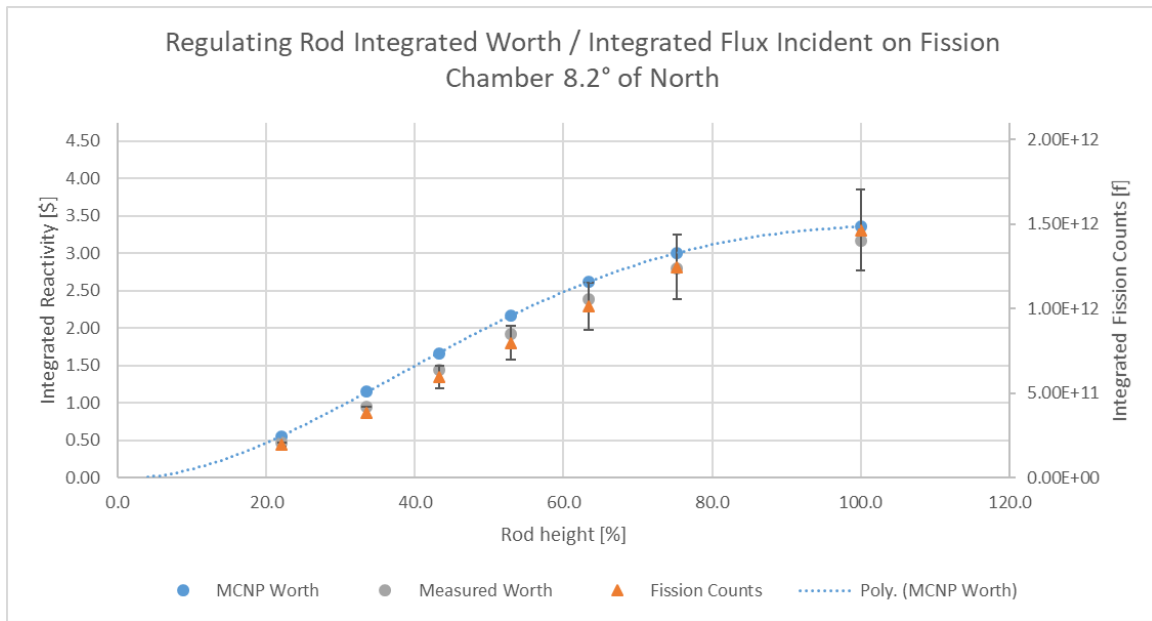


Figure 90: Integrated regulating rod worth and fission rate in the 8.2° detector.

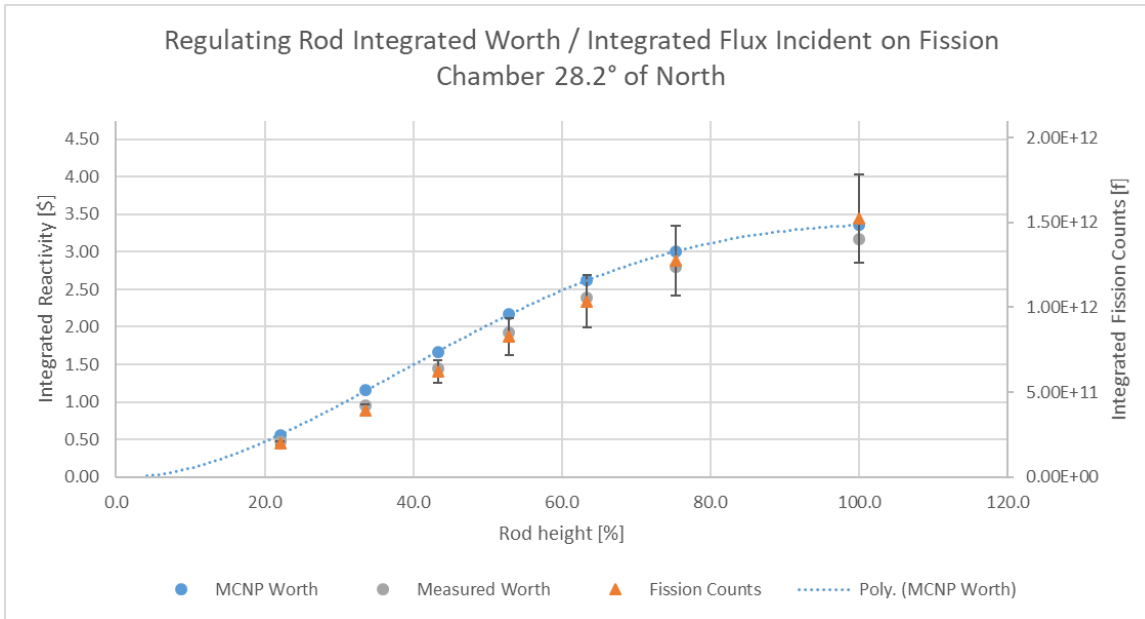


Figure 91: Integrated regulating rod worth and fission rate in the 28.2° detector.

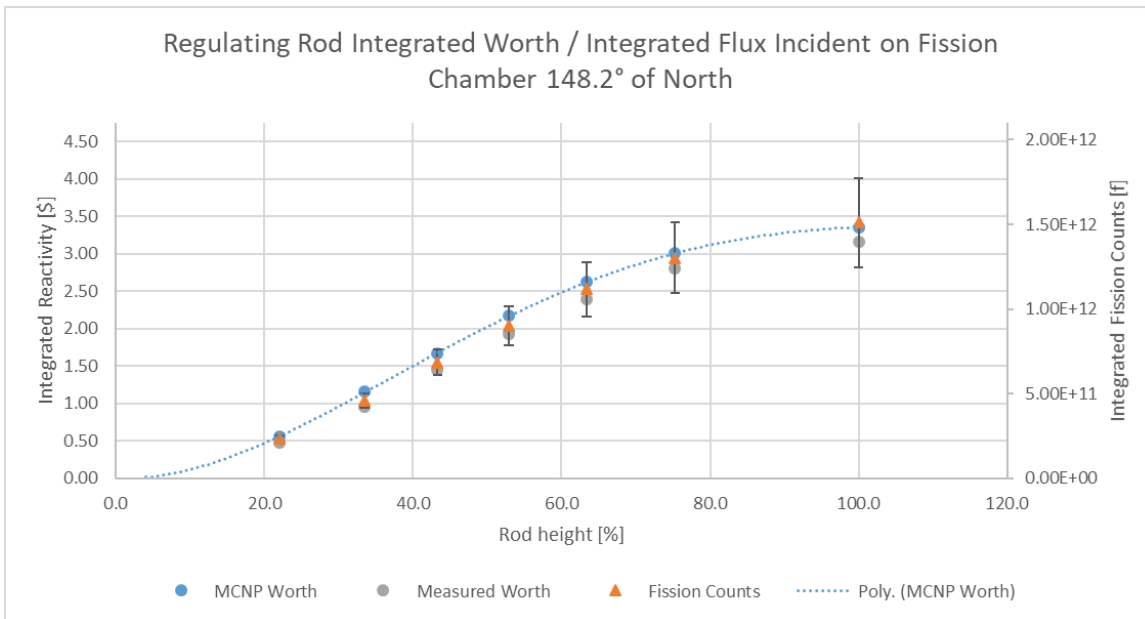


Figure 92: Integrated regulating rod worth and fission rate in the 148.2° detector.

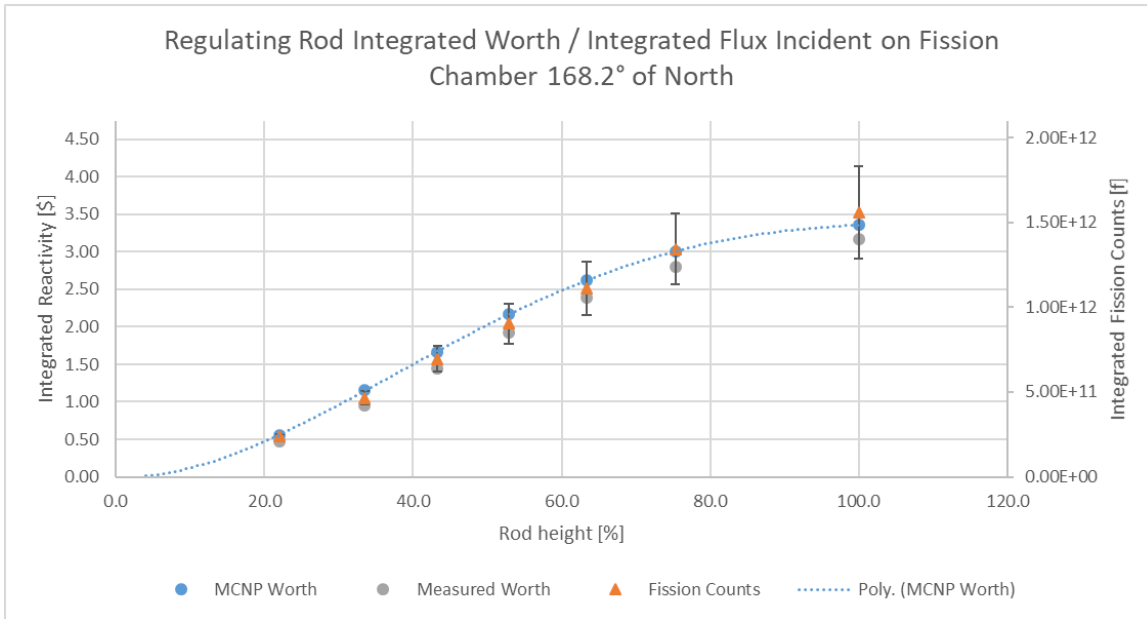


Figure 93: Integrated regulating rod worth and fission rate in the 168.2° detector.

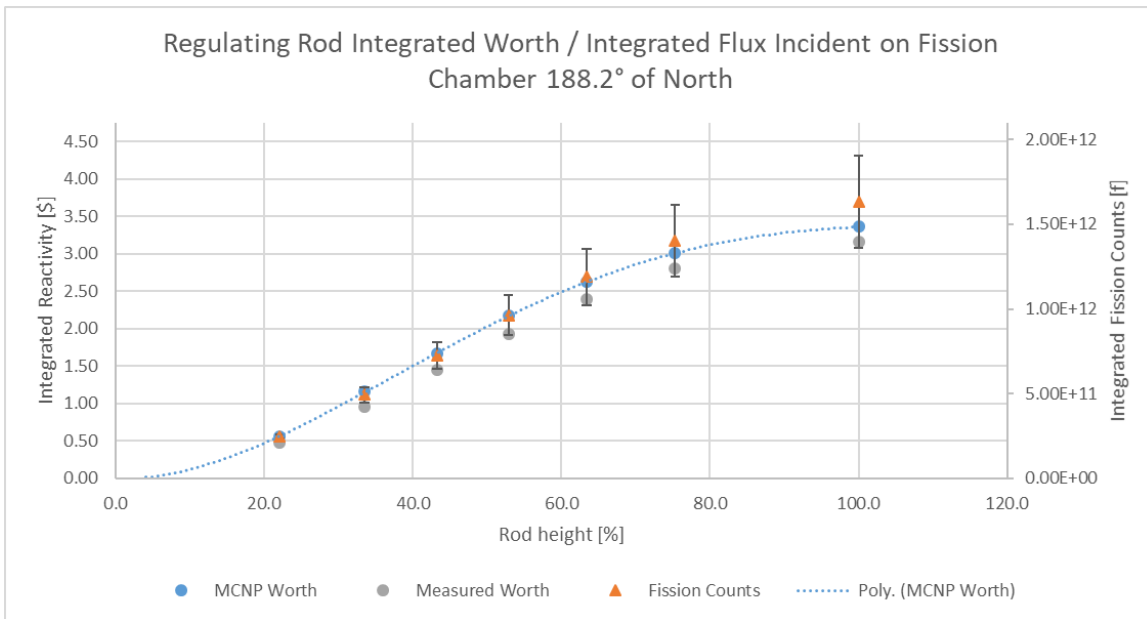


Figure 94: Integrated regulating rod worth and fission rate in the 188.2° detector.

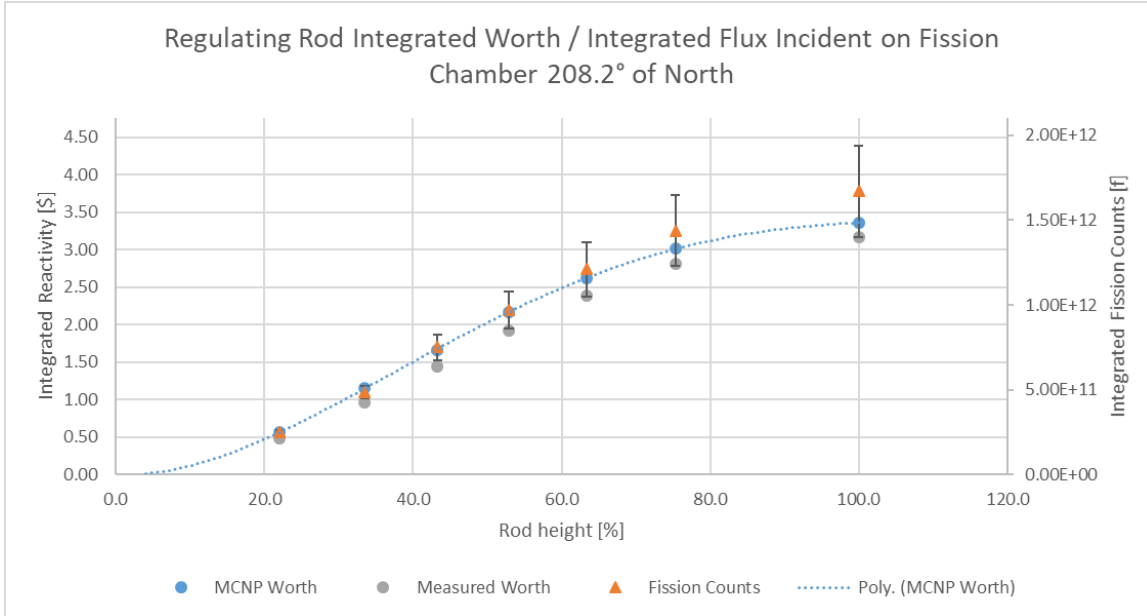


Figure 95: Integrated regulating rod worth and fission rate in the 208.2° detector.

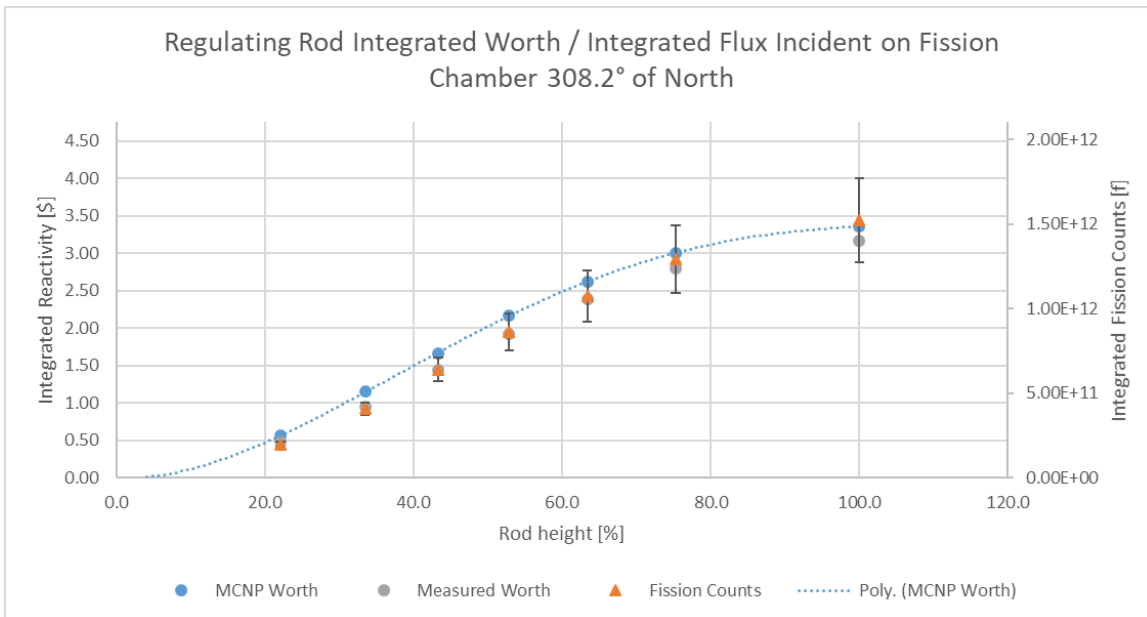


Figure 96: Integrated regulating rod worth and fission rate in the 308.2° detector.

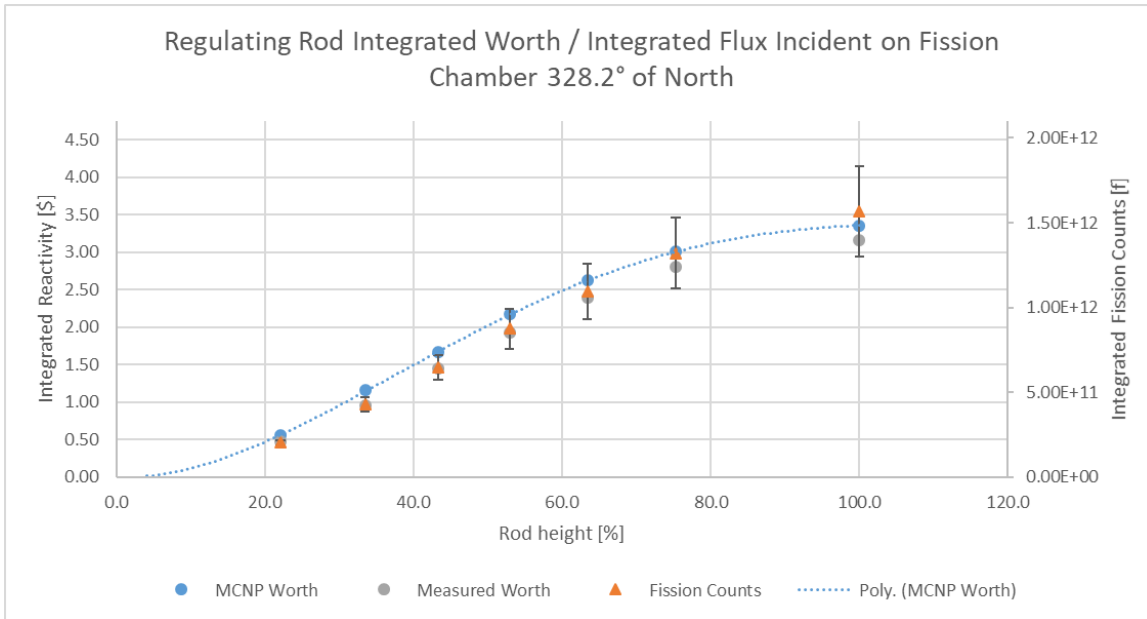


Figure 97: Integrated regulating rod worth and fission rate in the 328.2° detector.

4.4.3 Detector Response Discussion

The secondary axis for the integrated response of the true fission chamber detector located at 348.2° of North is adjusted such that it agrees with the final measured integrated reactivity worth for each control rod, and the secondary axis limits were held constant for all detectors based on the values for the detector at 348.2°. It is observed that each modeled integrated detector response deviates from the modeled integrated detector response for the true fission chamber located at 348.2° of North for all control rod pulls in both the normal and CLICIT core configurations. This implies that the flux seen by any of the nine modeled detectors is different at the moment of supercriticality for the same control rod movement. This phenomenon is known as control rod shadowing, where the orientation of the control rods relative to each other and their current heights relative to each other cause an asymmetry in the core flux and power distributions such that the response of any one detector to the same event is a function of detector location. Thermal neutron flux profiles across the core at core axial mid-plane for each control rod pull are shown in section 4.5 and discussed further in section 4.5.3.

Work by Kim and Kim 2022 [46], Mazaher et al. 2019 [47], and Shaner 2018 [48] shows that these asymmetries become more pronounced in time-dependent models of reactor power transients. This can lead to a skewing of the Δt term in Equation 3.7, which in turn may lead to an inaccurate

calculation of the reactivity worth of a particular control rod pull when Equation 3.7 is substituted into the Inhour equation. This is because the reactor power detectors are calibrated using a calorimetric method at 1 MW with a banked control rod configuration that has its own unique neutron flux profile. The neutron flux incident on the detector at any power level below 1 MW is assumed to be a percent of the neutron flux that was incident on the detector at 1 MW. However, the data in Figures 98 – 147 shows that non-banked configurations, where one control rod has an extreme height disparity relative to the other three, result in a diverse range of flux profile asymmetries. The result is that the detector may be reading a flux level that corresponds to 200 or 800 W when the core-wide power level is not and the implications of which are discussed further in section 4.5.3. Since the time of power rise in Equation 3.7 is taken between 200 and 800 W, a power peaking shift closer to the detector can result in a shorter Δt and a power peaking shift away can result in a longer Δt . The control rod shadowing effect on a particular detector location can be observed using the time-independent method presented in this work. However, to properly quantify the effect and the resulting skewing of the time of power rise (Δt) as seen by a detector at a particular location would require a time-dependent method as the development of the core power and flux asymmetries over the power rise would be required. This information is needed to model the detector response over the entire power rise.

4.5 Flux Maps

4.5.1 Normal Core Flux Maps

The dependence of detector response on detector location was believed to be due to a neutronic phenomenon known as control rod shadowing where the control rods interact with one another neutronically to produce asymmetrical flux distributions in the reactor core [37], [38]. This effect is caused by extreme differences in control rod heights relative to each other. If the detector response is different for different detectors, and control rod configurations, then the response of any one detector will vary per control rod configuration in the calibration of any one control rod. This is due to the asymmetrical flux and power distribution in the core changing between configurations. These asymmetries are especially pronounced in configurations where there is an extreme disparity in heights between the rod being calibrated and the other three.

To illustrate this phenomenon, volume-averaged flux tallies were taken in the fuel meat at core axial mid-plane with an arbitrary multiplier card representing the reactor at 800 W. Normalized flux values for these tallies are plotted to show the normalized flux distribution in the core for each control

rod configuration during the October 2008 control rod calibration. These flux maps for the LEU BOL normal core configuration are shown below in Figures 98 through 123 and for the LEU BOL CLICIT core configuration in Figures 124 through 147 for each control rod perturbation during the calibration process.

4.5.1.1 Transient Rod

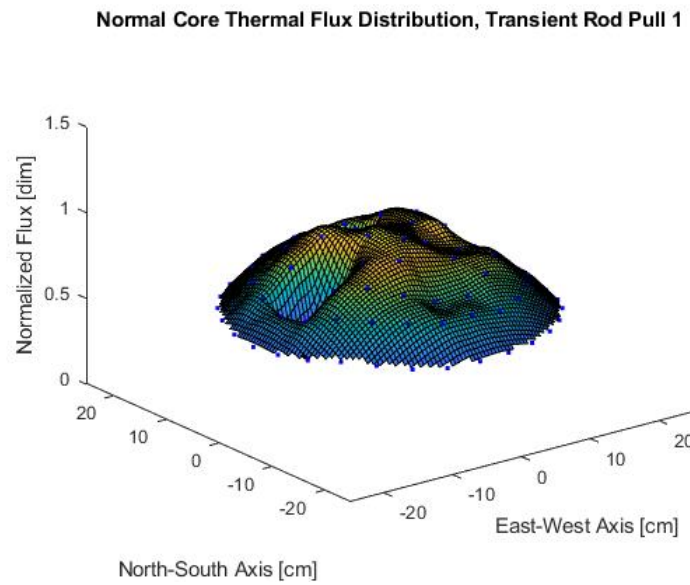


Figure 98: Normal core axial mid-plane thermal flux map for transient rod pull 1 configuration.

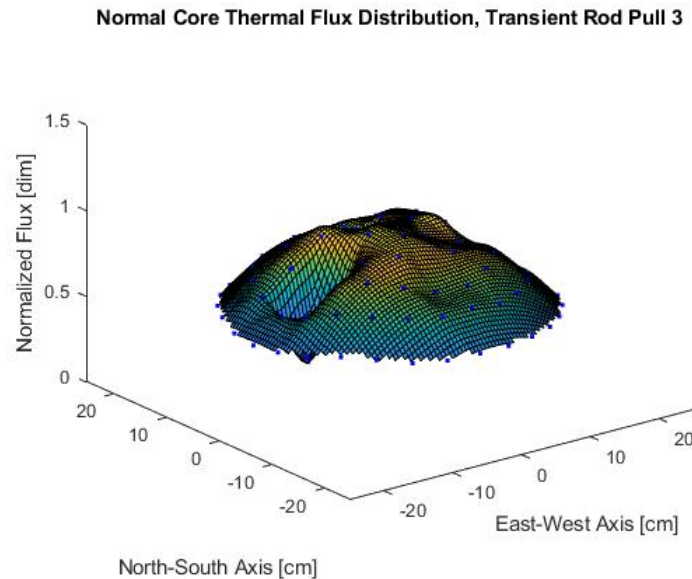


Figure 99: Normal core axial mid-plane thermal flux map for transient rod pull 2 configuration.

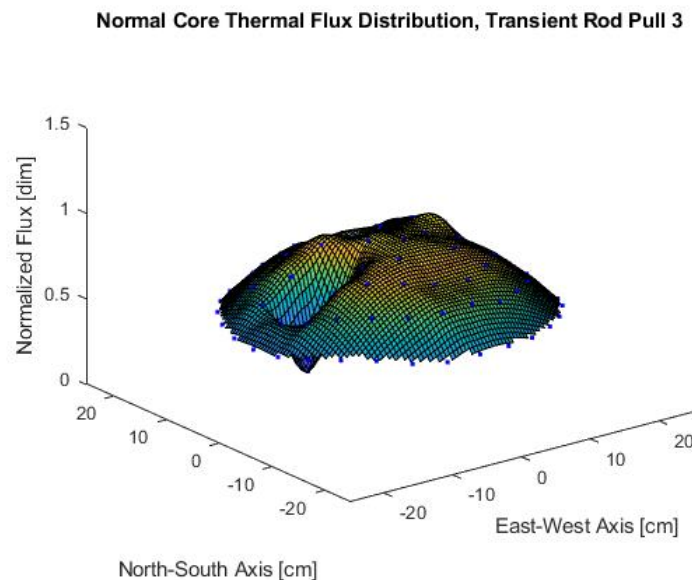


Figure 100: Normal core axial mid-plane thermal flux map for transient rod pull 3 configuration.

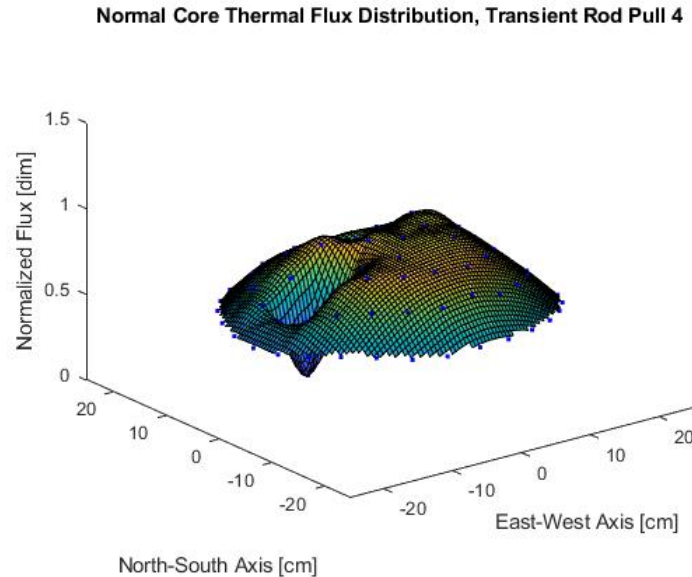


Figure 101: Normal core axial mid-plane thermal flux map for transient rod pull 4 configuration.

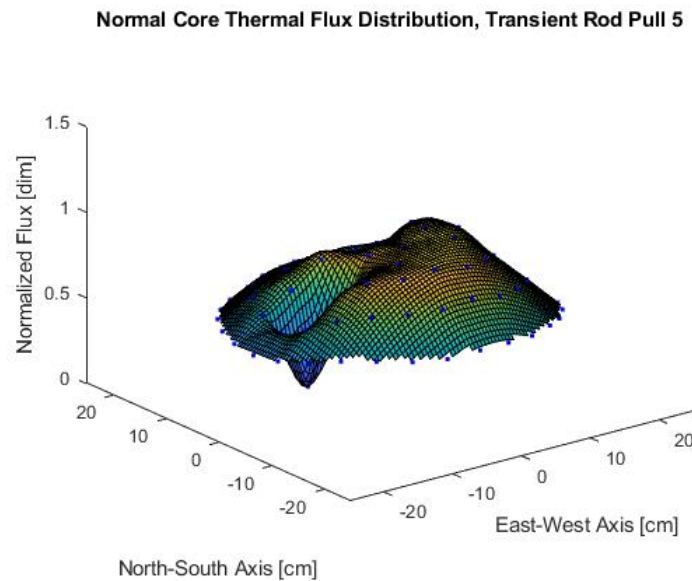


Figure 102: Normal core axial mid-plane thermal flux map for transient rod pull 5 configuration.

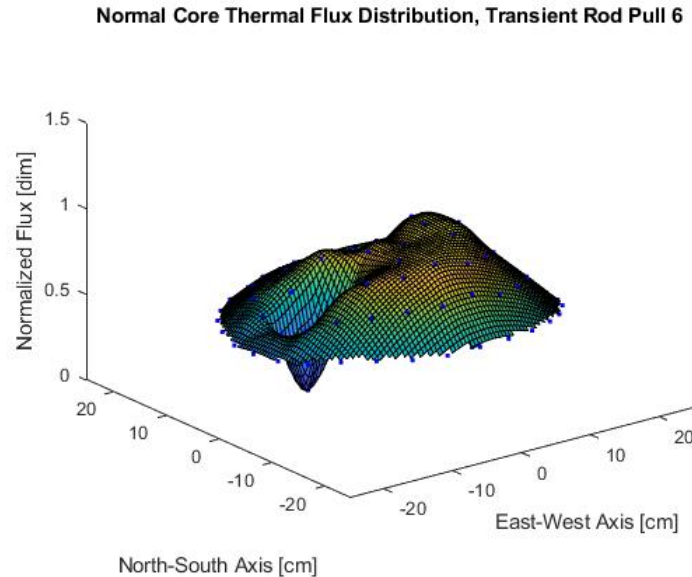


Figure 103: Normal core axial mid-plane thermal flux map for transient rod pull 6 configuration.

4.5.1.2 Safety Rod

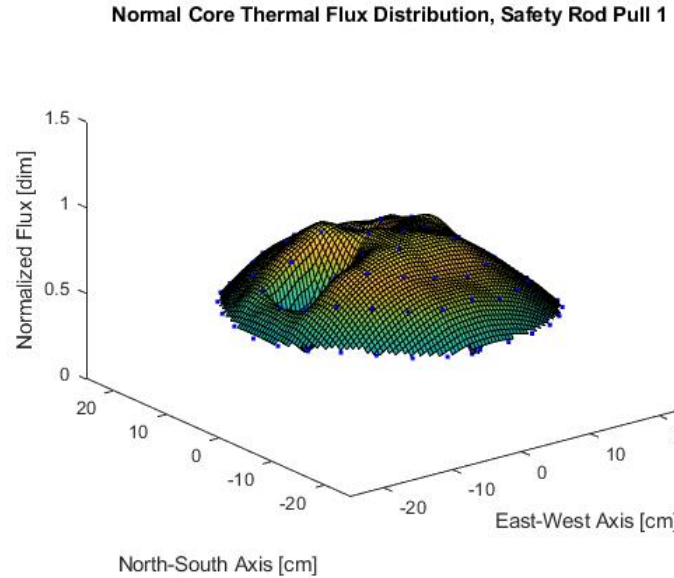


Figure 104: Normal core axial mid-plane thermal flux map for safety rod pull 1 configuration.

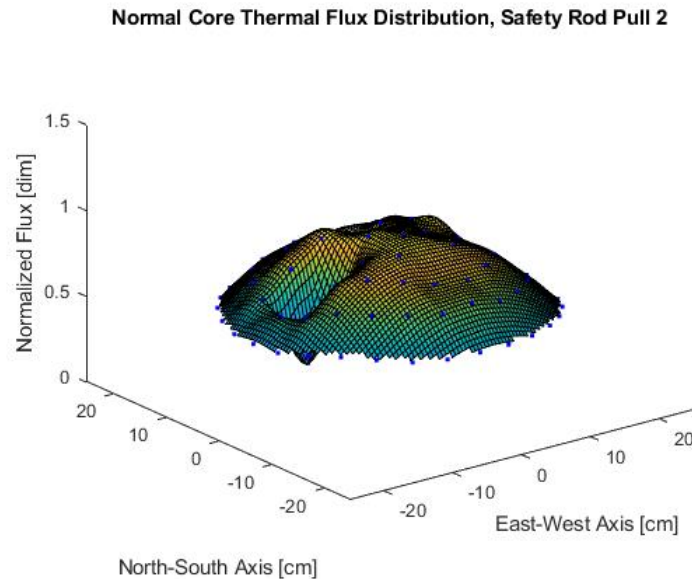


Figure 105: Normal core axial mid-plane thermal flux map for safety rod pull 2 configuration.

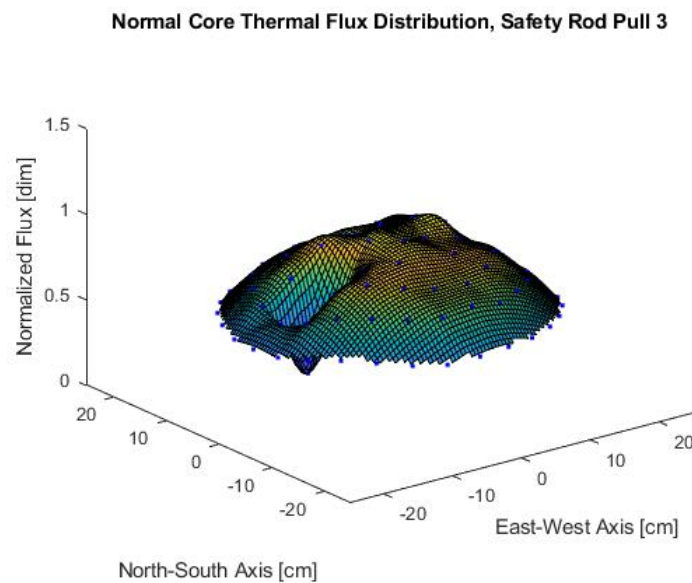


Figure 106: Normal core axial mid-plane thermal flux map for safety rod pull 3 configuration.

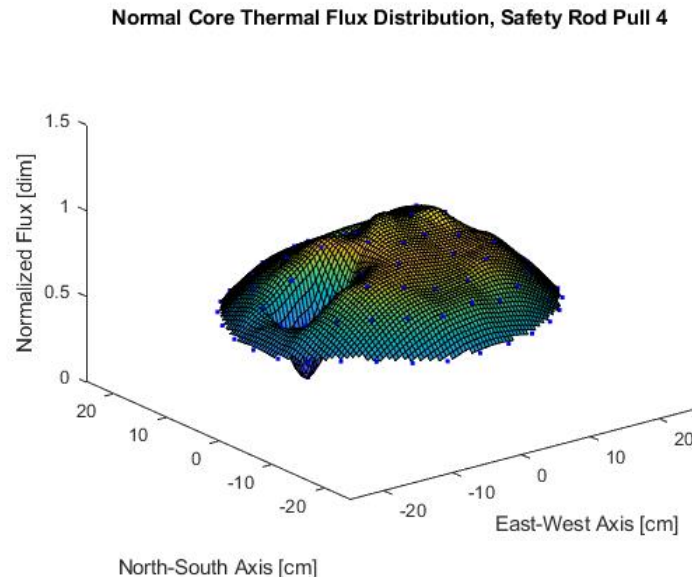


Figure 107: Normal core axial mid-plane thermal flux map for safety rod pull 4 configuration.

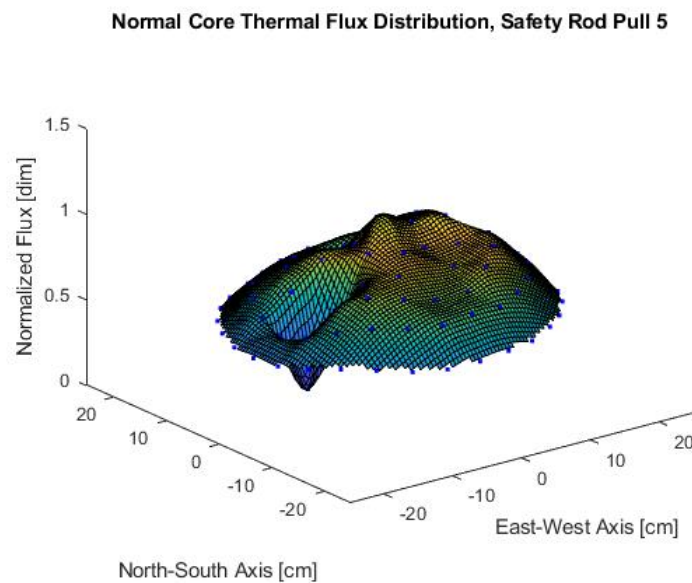


Figure 108: Normal core axial mid-plane thermal flux map for safety rod pull 5 configuration.

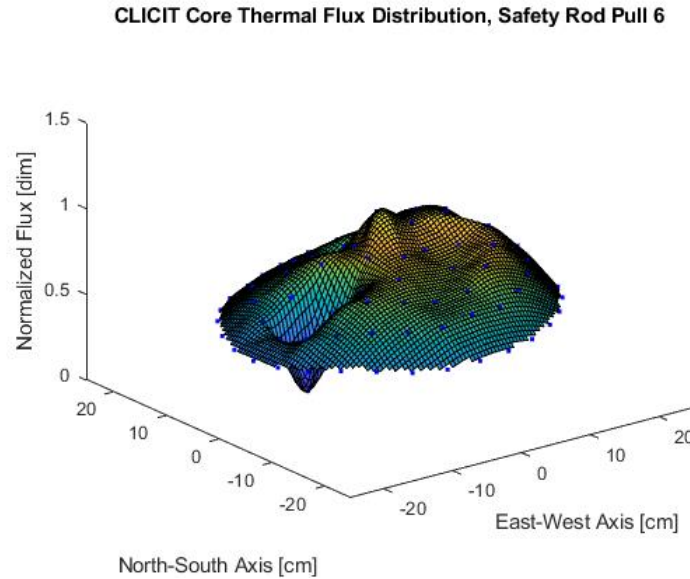


Figure 109: Normal core axial mid-plane thermal flux map for safety rod pull 6 configuration.

4.5.1.3 Shim Rod

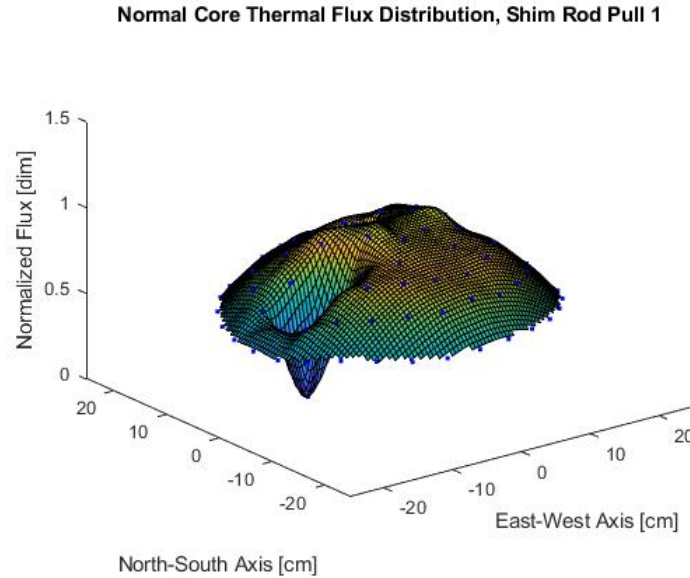


Figure 110: Normal core axial mid-plane thermal flux map for shim rod pull 1 configuration.

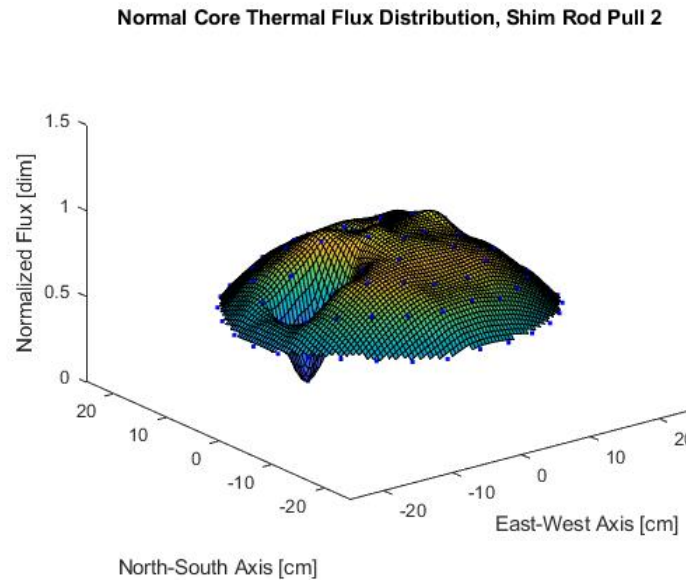


Figure 111: Normal core axial mid-plane thermal flux map for shim rod pull 2 configuration.

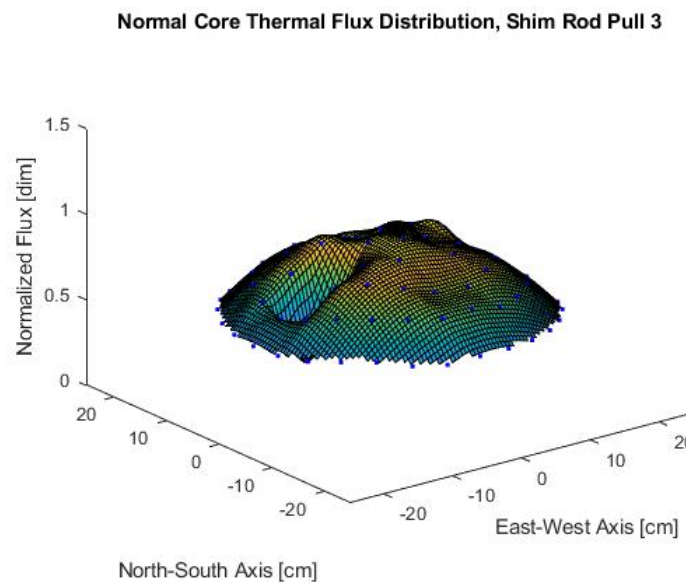


Figure 112: Normal core axial mid-plane thermal flux map for shim rod pull 3 configuration.

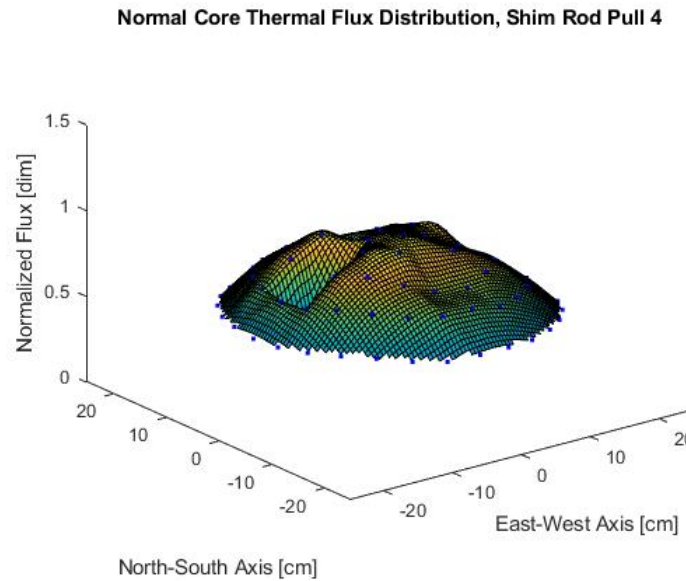


Figure 113: Normal core axial mid-plane thermal flux map for shim rod pull 4 configuration.

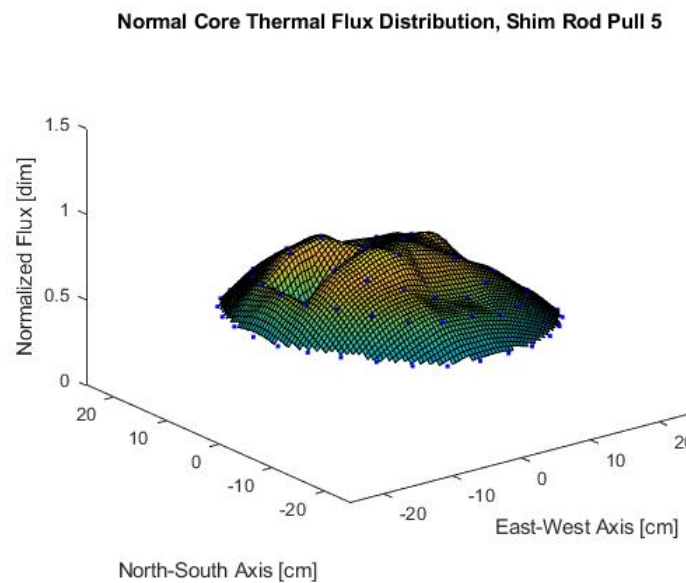


Figure 114: Normal core axial mid-plane thermal flux map for shim rod pull 5 configuration.

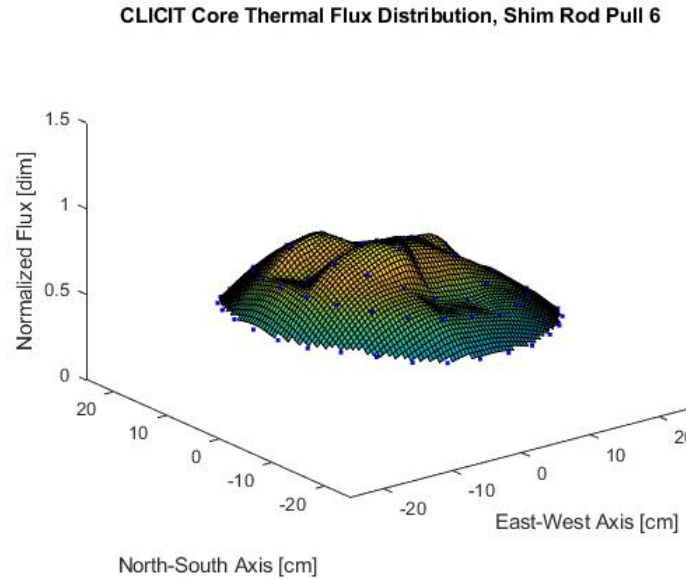


Figure 115: Normal core axial mid-plane thermal flux map for shim rod pull 6 configuration.

4.5.1.4 Regulating Rod

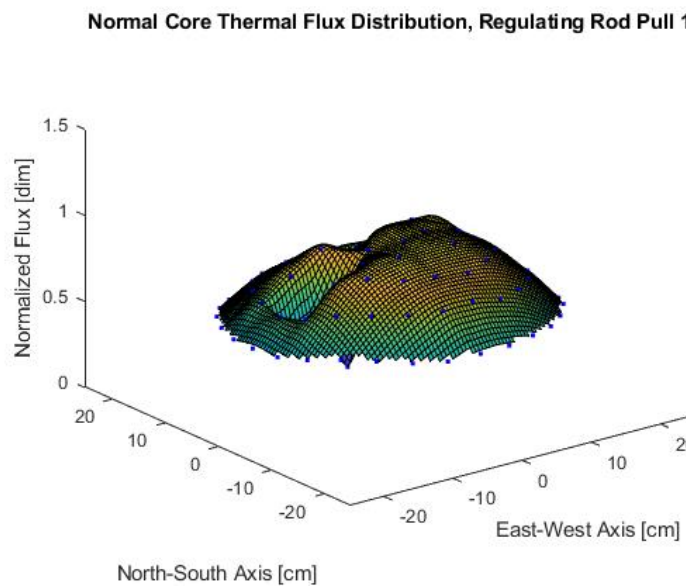


Figure 116: Normal core axial mid-plane thermal flux map for regulating rod pull 1 configuration.

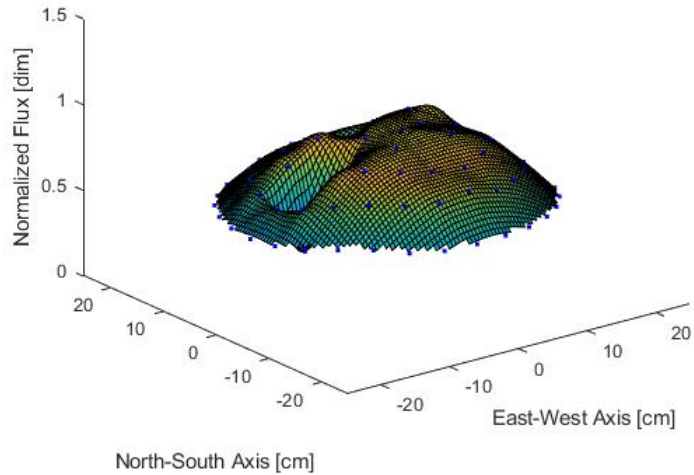
Normal Core Thermal Flux Distribution, Regulating Rod Pull 2

Figure 117: Normal core axial mid-plane thermal flux map for regulating rod pull 2 configuration.

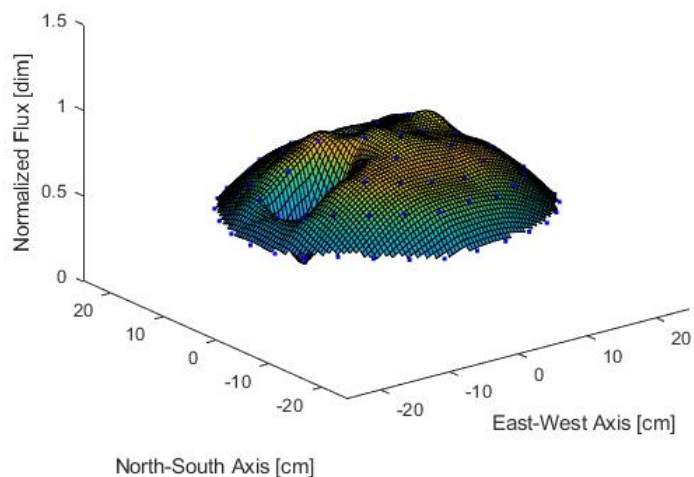
Normal Core Thermal Flux Distribution, Regulating Rod Pull 3

Figure 118: Normal core axial mid-plane thermal flux map for regulating rod pull 3 configuration.

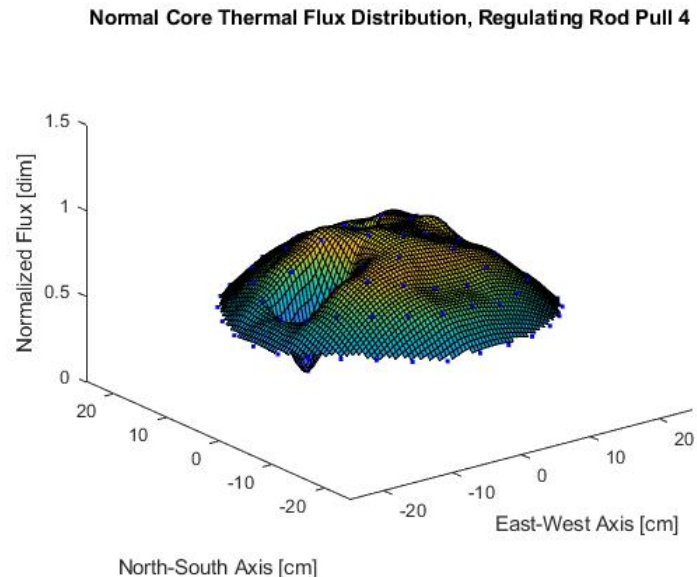


Figure 119: Normal core axial mid-plane thermal flux map for regulating rod pull 4 configuration.

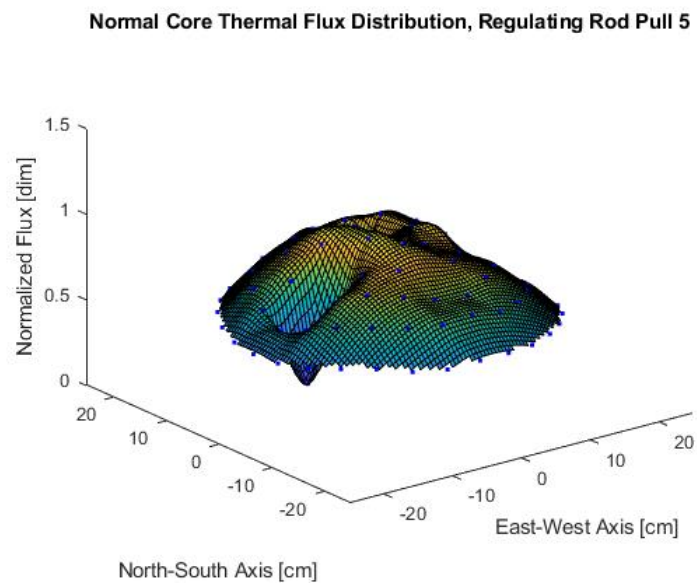


Figure 120: Normal core axial mid-plane thermal flux map for regulating rod pull 5 configuration.

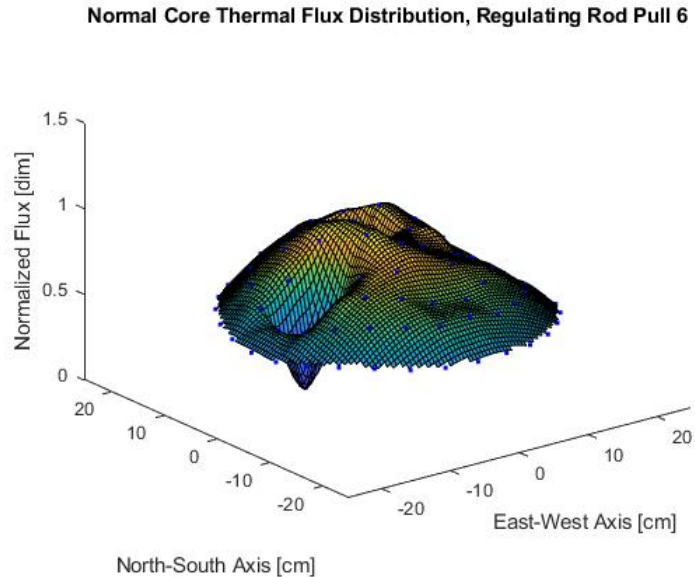


Figure 121: Normal core axial mid-plane thermal flux map for regulating rod pull 6 configuration.

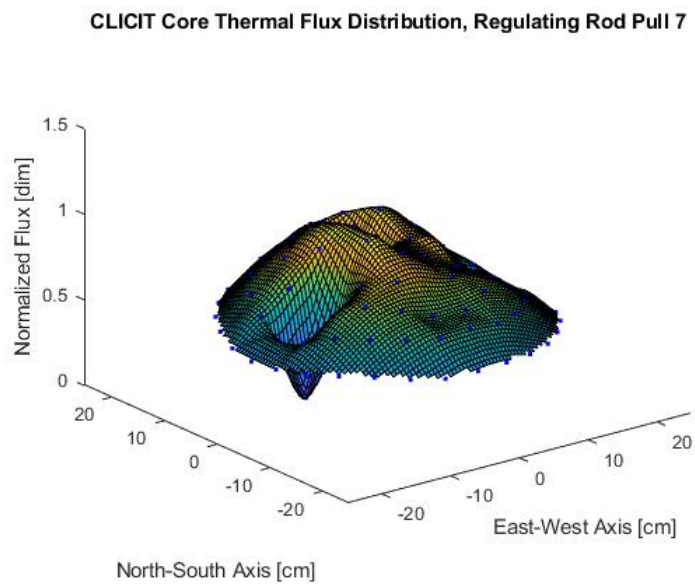


Figure 122: Normal core axial mid-plane thermal flux map for regulating rod pull 7 configuration.

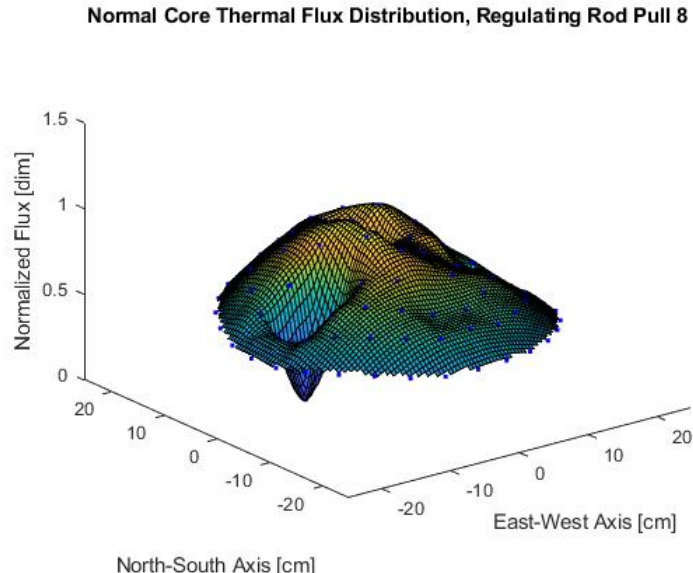


Figure 123: Normal core axial mid-plane thermal flux map for regulating rod pull 8 configuration.

4.5.2 CLICIT Core Flux Maps

4.5.2.1 Transient Rod

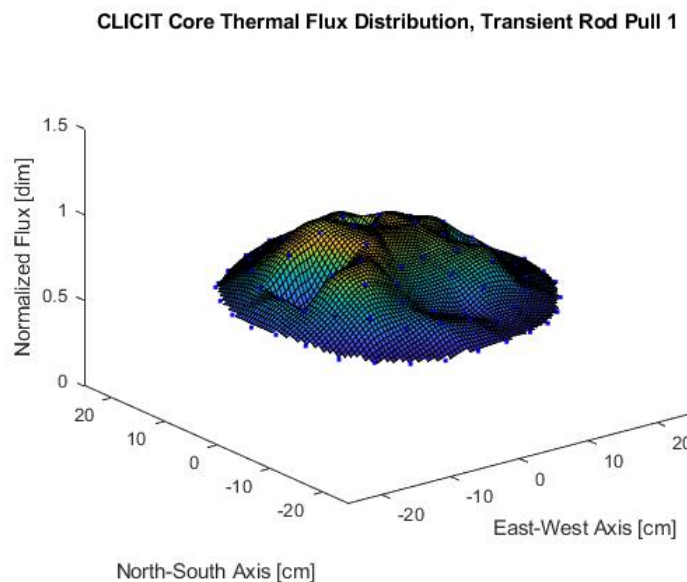


Figure 124: CLICIT core axial mid-plane thermal flux map for transient rod pull 1 configuration.

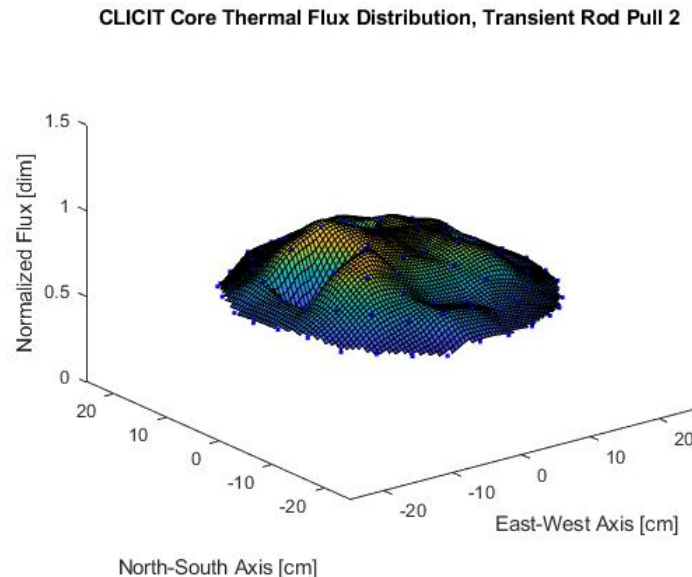


Figure 125: CLICIT core axial mid-plane thermal flux map for transient rod pull 2 configuration.

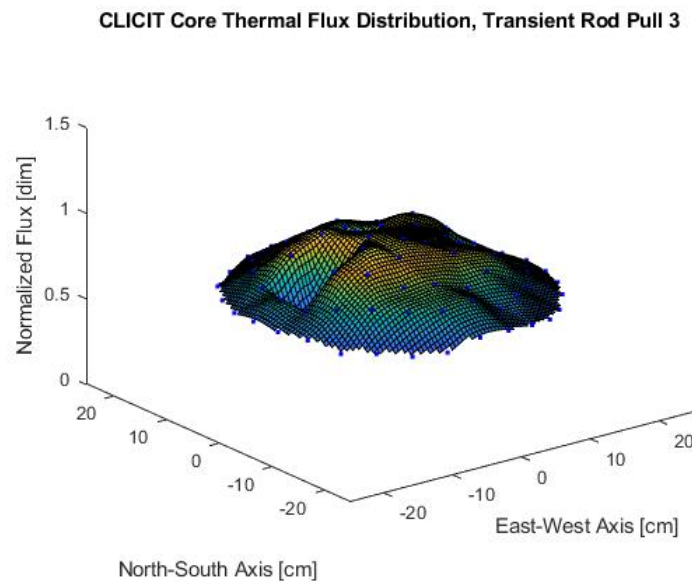


Figure 126: CLICIT core axial mid-plane thermal flux map for transient rod pull 3 configuration.

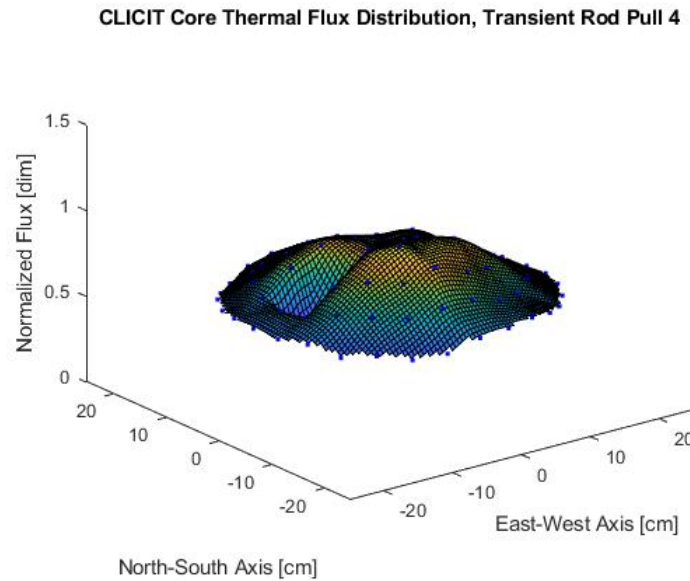


Figure 127: CLICIT core axial mid-plane thermal flux map for transient rod pull 4 configuration.

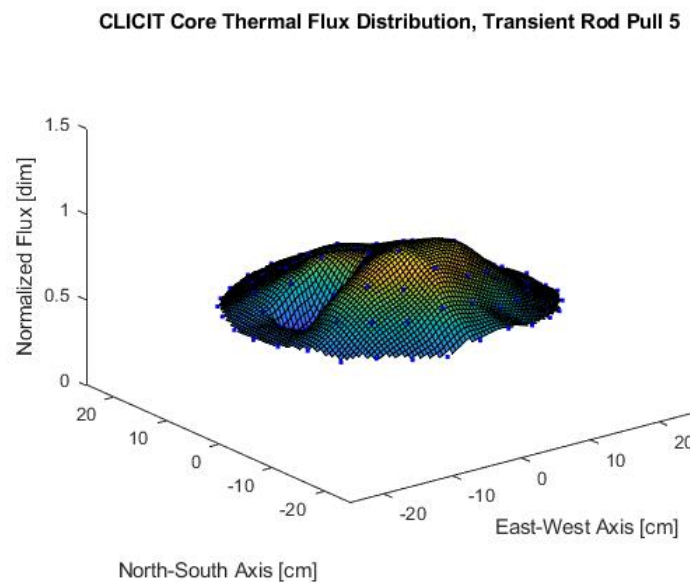


Figure 128: CLICIT core axial mid-plane thermal flux map for transient rod pull 5 configuration.

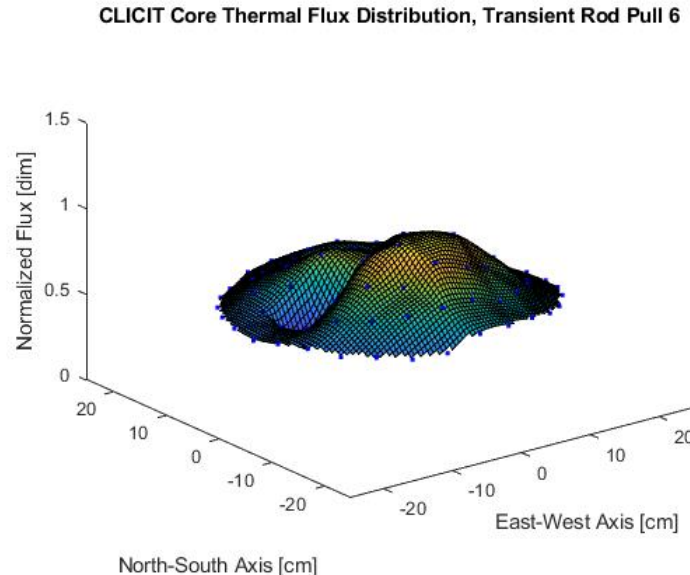


Figure 129: CLICIT core axial mid-plane thermal flux map for transient rod pull 6 configuration.

4.5.2.2 Safety Rod

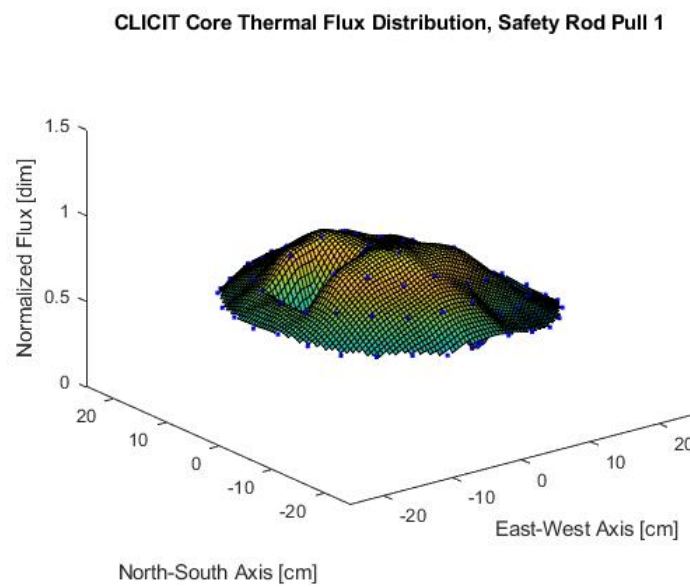


Figure 130: CLICIT core axial mid-plane thermal flux map for safety rod pull 1 configuration.

CLICIT Core Thermal Flux Distribution, Safety Rod Pull 2

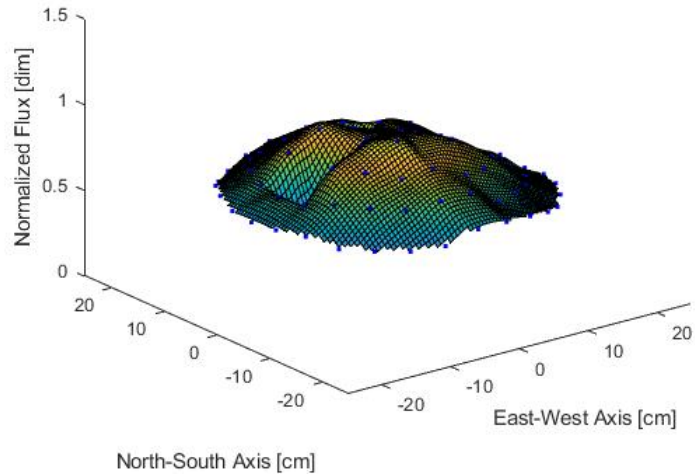


Figure 131: CLICIT core axial mid-plane thermal flux map for safety rod pull 2 configuration.

CLICIT Core Thermal Flux Distribution, Safety Rod Pull 3

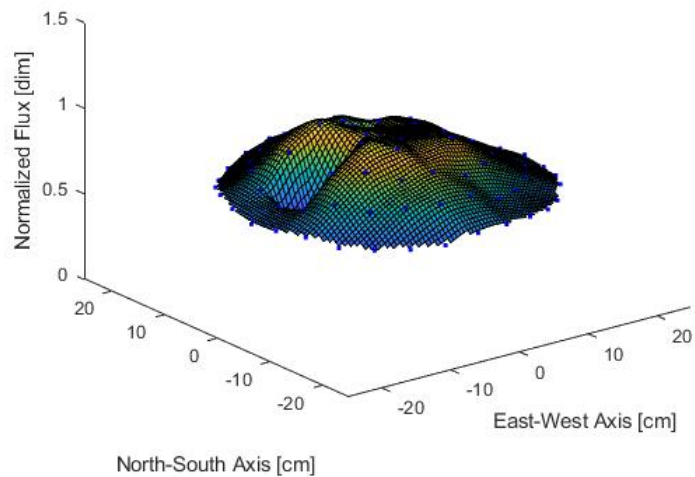


Figure 132: CLICIT core axial mid-plane thermal flux map for safety rod pull 3 configuration.

CLICIT Core Thermal Flux Distribution, Safety Rod Pull 4

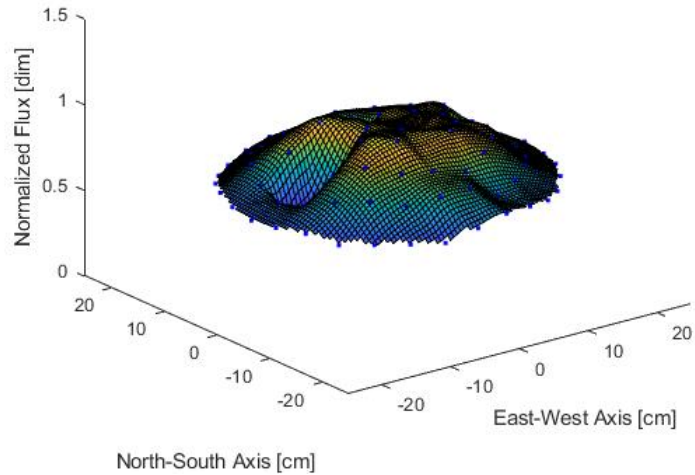


Figure 133: CLICIT core axial mid-plane thermal flux map for safety rod pull 4 configuration.

CLICIT Core Thermal Flux Distribution, Safety Rod Pull 5

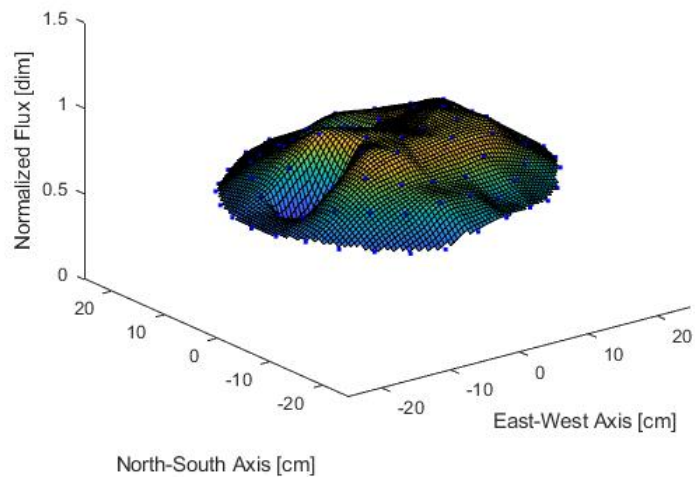


Figure 134: CLICIT core axial mid-plane thermal flux map for safety rod pull 5 configuration.

4.5.2.3 Shim Rod

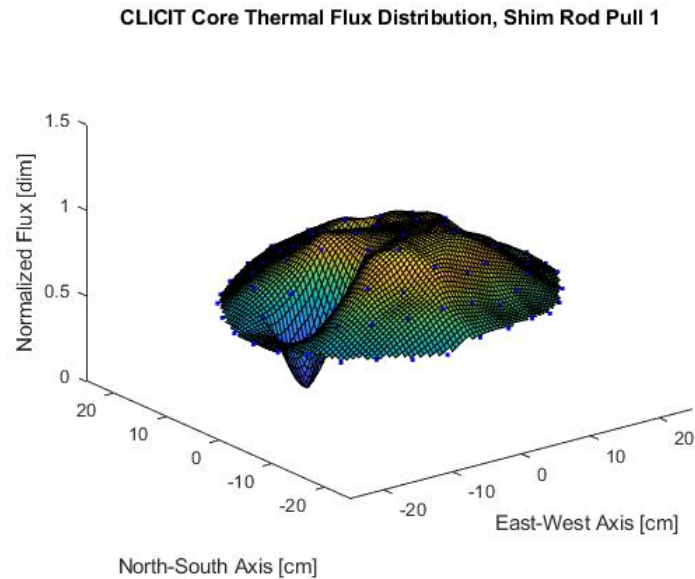


Figure 135: CLICIT core axial mid-plane thermal flux map for shim rod pull 1 configuration.

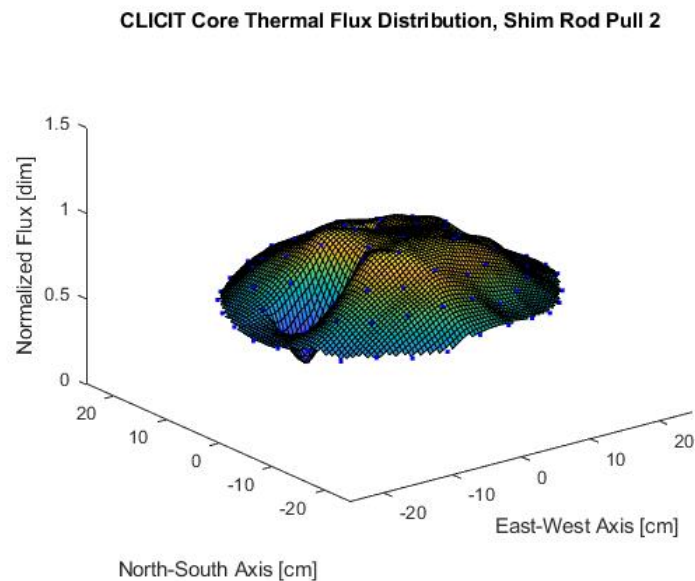


Figure 136: CLICIT core axial mid-plane thermal flux map for shim rod pull 2 configuration.

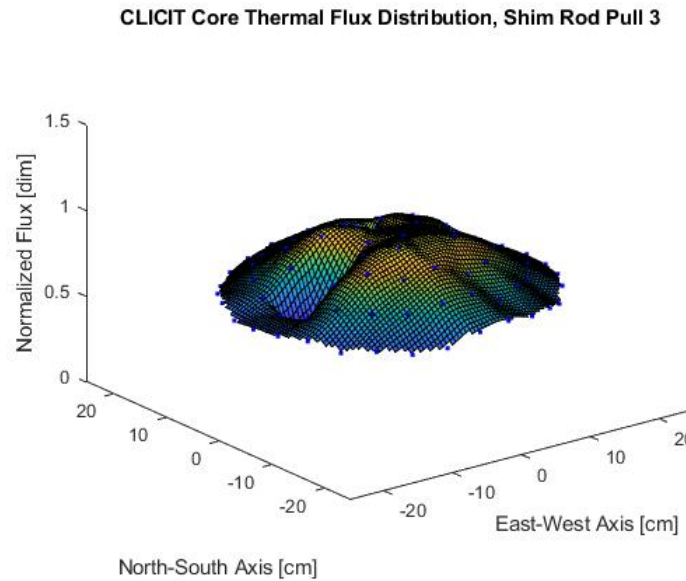


Figure 137: CLICIT core axial mid-plane thermal flux map for shim rod pull 3 configuration.

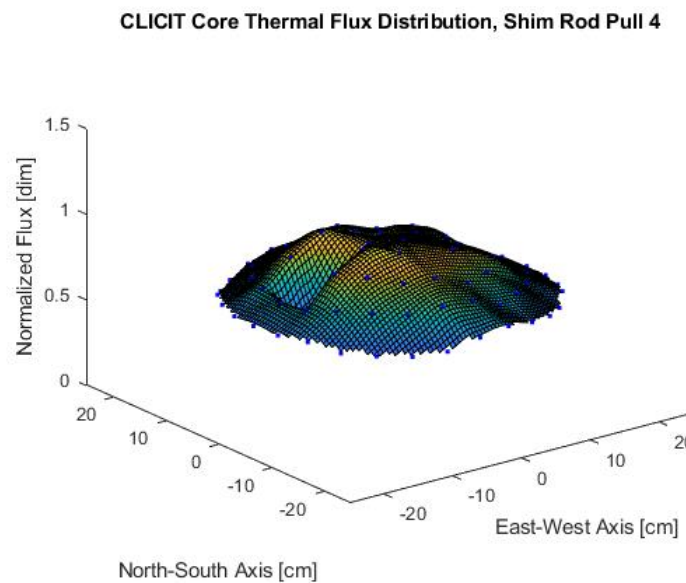


Figure 138: CLICIT core axial mid-plane thermal flux map for shim rod pull 4 configuration.

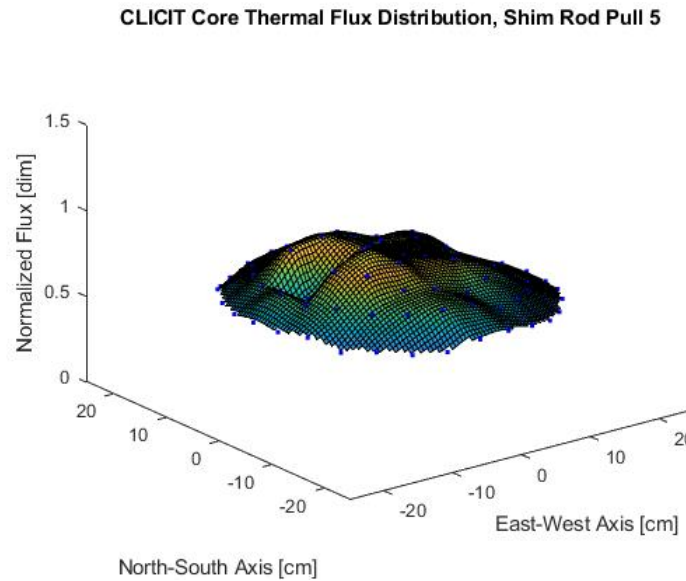


Figure 139: CLICIT core axial mid-plane thermal flux map for shim rod pull 5 configuration.

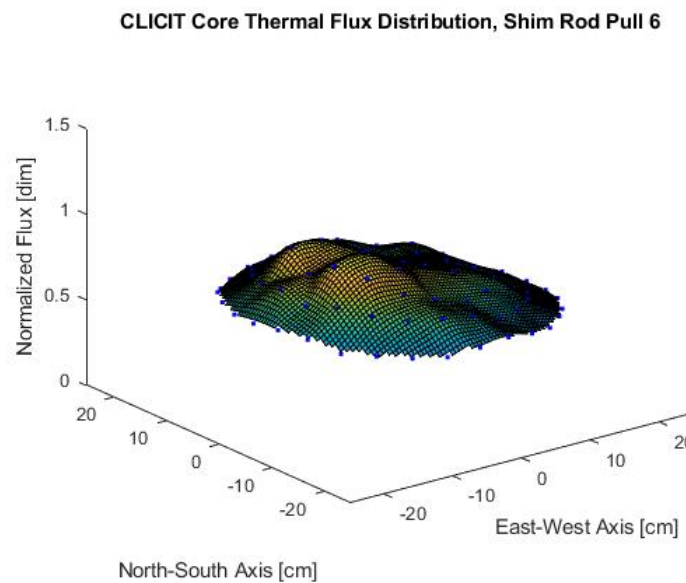


Figure 140: CLICIT core axial mid-plane thermal flux map for shim rod pull 6 configuration.

4.5.2.4 Regulating Rod

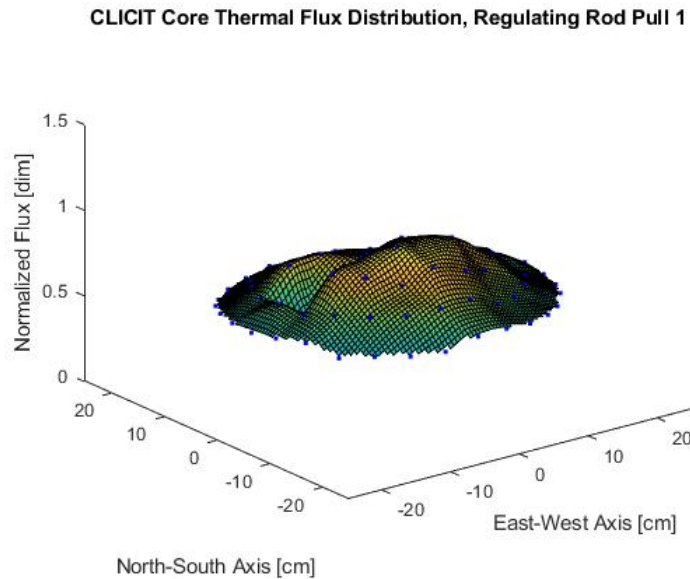


Figure 141: CLICIT core axial mid-plane thermal flux map for regulating rod pull 1 configuration.

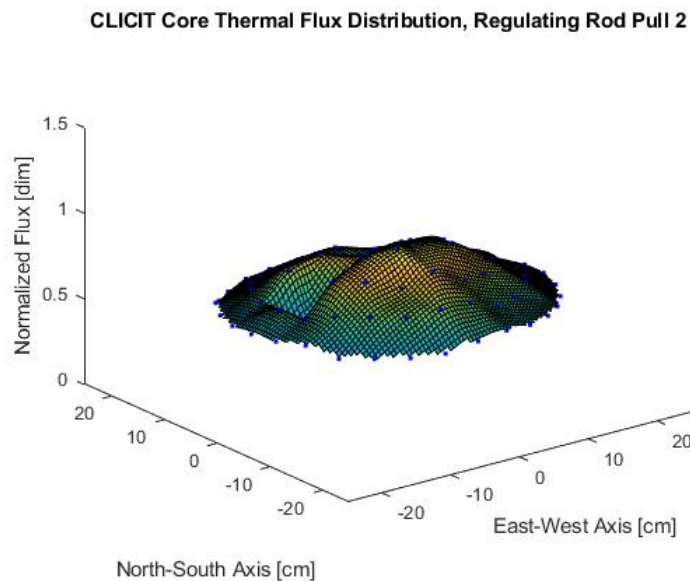


Figure 142: CLICIT core axial mid-plane thermal flux map for regulating rod pull 2 configuration.

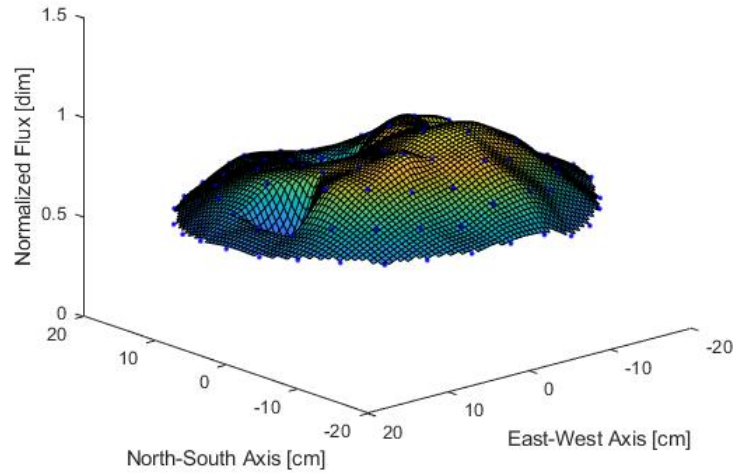
CLICIT Core Thermal Flux Distribution, Regulating Rod Pull 3

Figure 143: CLICIT core axial mid-plane thermal flux map for regulating rod pull 3 configuration.

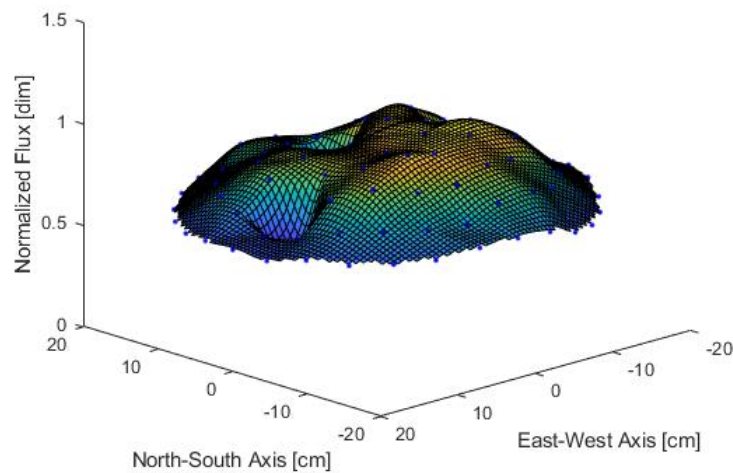
CLICIT Core Thermal Flux Distribution, Regulating Rod Pull 4

Figure 144: CLICIT core axial mid-plane thermal flux map for regulating rod pull 4 configuration.

CLICIT Core Thermal Flux Distribution, Regulating Rod Pull 5

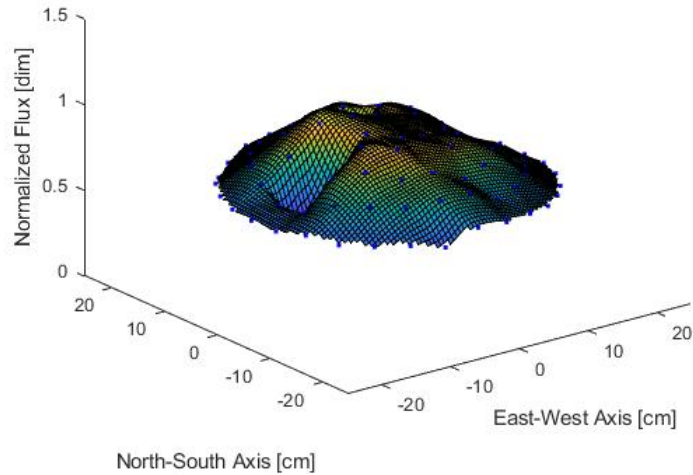


Figure 145: CLICIT core axial mid-plane thermal flux map for regulating rod pull 5 configuration.

CLICIT Core Thermal Flux Distribution, Regulating Rod Pull 6

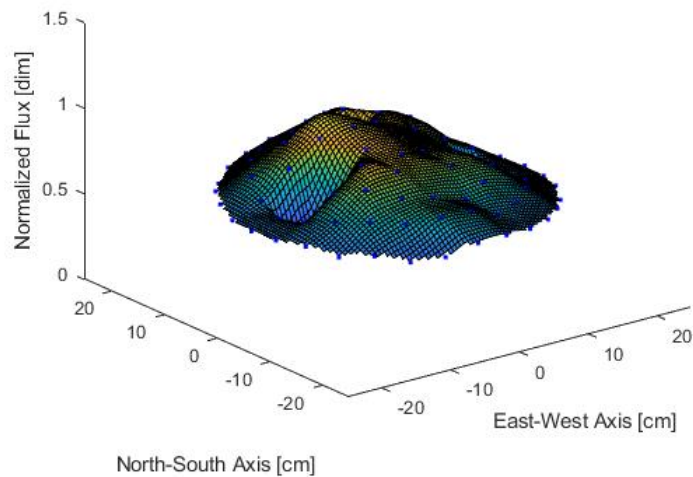


Figure 146: CLICIT core axial mid-plane thermal flux map for regulating rod pull 6 configuration.

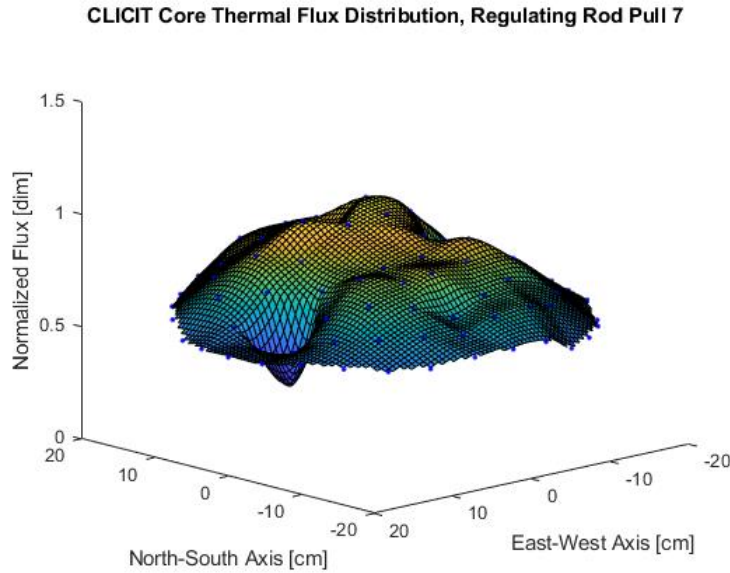


Figure 147: CLICIT core axial mid-plane thermal flux map for regulating rod pull 7 configuration.

4.5.3 Flux Map Discussion

The thermal flux maps shown in Figures 98 – 147 reveal that the shape of the thermal neutron flux distribution in the OSTR is highly dependent on the orientations of the control rods to one another. These thermal flux profiles became particularly asymmetric at extreme control rod height disparities such as when one control rod was fully inserted or withdrawn and the other three were banked at low or high positions. The location of peak thermal neutron flux shifted significantly as the control rod configurations changed during the control rod calibration process. Since measured power is directly proportional to the thermal neutron flux, the location of peak power and fast neutron generation from fission was also shifting with each configuration. Neutrons born fast in the core are those most likely to reach a reactor power detector outside the reflector and the proximity of the peak power location to the detector influences the neutron flux incident on the detector.

The extreme depression or peaking of the thermal neutron flux profile near a reactor power detector due to control rod position illustrates the control rod shadowing and anti-shadowing effect where a depression near the detector shadows the detector and results in an under-response, and a peaking near the detector causes anti-shadowing or an over-response. The disparity between the power rise in the peak power location and the depressed regions of reactor core has been shown to become more pronounced as supercriticality develops over time [46]–[48] which means that detector response would change non-linearly in time especially if the peak power location is near the detector. This would

lead to a skewing of the Δt term in the inhour equation and a skewed reactivity calculation. Time-dependent Monte Carlo methods would be needed to quantify this effect in the calibration of the control rods at OSTR. However, the time-independent method described in this work is capable of qualitatively detecting control rod shadowing and anti-shadowing effects by showing that the same detector responded differently at different locations around the OSTR core due to shifts in thermal flux distribution for each control rod configuration.

These results also imply that extreme control rod configurations at higher powers, those near the NRC licensed limit of 1.1 MW, could potentially result in a core-wide reactor power that is greater than the Limiting Safety System Setting (LSSS) of 1.06 MW or the license limit if the location of peak power is very distant from the reactor power detector(s). This is because each detector is calibrated at 1 MW with a banked control rod configuration. At OSTR the reactor power detectors are calibrated using a calorimetric method where the reactor pool is isolated from the cooling systems and assumed adiabatic. The OSTR is then operated at what is believed to be 1 MW based on the current detector readings on the control console. After some time, the change in the reactor pool temperature is recorded and Equation 4.1 is used to calculate the average power of the OSTR over that time span.

$$\dot{Q} = \frac{mC_p\Delta T}{\Delta t} \quad (4.1)$$

After this calculation is performed each reactor power detector is physically moved either closer to or further away from the core so that the neutron flux incident on it and the corresponding signal read 100% of 1 MW on the control console instrumentation. The problem with this method is that the flux incident on a power detector is a function of location as the neutron flux and power profile of the OSTR is very specific to a particular control rod configuration as shown by Figures 98 – 147. The reactor power detectors see any neutron flux at powers below 1 MW as a percent of the neutron flux incident on the detector at 1 MW. However, as the flux profile deviates from the profile at 1 MW for different control rod configurations, the power level instrumentation may read a power that is not representative of the actual core-wide power level. This implies that it is possible violate the LSSS or licensed power limit if operating OSTR at extreme control rod configurations near 1.1 MW.

However, OSTR uses three reactor power detectors, two uncompensated ion chambers and the fission chamber, at such power levels and all three are at different positions around the reflector periphery. This means that should such an asymmetric power distribution occur, the three power detectors would disagree with each other and the detector reading the highest power would likely be over-responding and reading a higher than actual core-wide power level if the location of power peaking is near that detector. A concerning situation would arise if the location of power peaking was near none of the detectors and the detectors were shadowed by flux depressions near all three. In this situation it would be possible to operate at a higher than allowed power level, but it is extremely unlikely to occur at OSTR due to the placement of the three power detectors around the reflector periphery.

These control rod shadowing and anti-shadowing effects in the OSTR may also affect pulsing operations where the reactor is brought critical at a low power and the transient rod is rapidly ejected from the core to induce a neutronic transient or pulse where the reactor can reach powers exceeding 2000 MW. As other works have shown [46]–[48], flux asymmetries become more pronounced as supercriticality develops and pulsing is a prompt-critical evolution. The limiting condition of operation at OSTR pertaining to pulsing operations is a reactivity insertion limit of \$2.33. Yet, the integral and differential control rod worths of the transient rod are measured at many different control rod configurations throughout the calibration process. As is shown in section 4.6, the worth of a control rod perturbation is a function of many factors including the orientation of the rods relative to each other. It is likely that the rapid ejection of the transient rod to an extreme height relative to the other three control rods results in a reactivity insertion that is not equal to the measured reactivity worth of the same segment of control rod. This effect is observed in both the OSTR MCNP® model and the actual reactor at subcritical configurations when a control rod is completely withdrawn while the other three remain fully inserted. This phenomenon is discussed in greater detail in section 4.6.

This work showed that a reactor power detector's response is a function of location. Detectors at different locations respond differently to the same event due to control rod shadowing effects. This may be the source of disagreement between control rod reactivities measured with an ex-core power detector and MCNP® calculated reactivity worths as MCNP® simply outputs a system-wide neutron multiplication factor. The MCNP® model may be more accurate in situations where the reactivity bias on the model is extremely low and the detector is highly shadowed for a particular rod or core configuration that experiences large shifts in peak power location. However, this does not mean that modeling is a valid replacement for control rod calibration experiments or a solution to problems encountered at reactors

with low core excess. Measuring the reactivity worth of a control rod experimentally is the only method by which reasonable assurance can be given to the regulator that limits on core excess and shutdown margin are met. This work has shown that the two approaches (modeling and measurement) may disagree even for a model with near-zero bias.

4.6 Total Rod Worth Comparisons

It is often assumed in nuclear engineering that the worth of a control rod is only a function of its material properties, temperature, geometry, and the properties of the reactor core within which it is used. Within the category of the properties of the reactor core is the two-dimensional core configuration, i.e., how many fuel rods, experimental facilities and control rods are within the core and where they are located. Less considered is the variation in the three-dimensional core configuration where each unique combination of control rod heights is a unique core configuration for the same two-dimensional core layout. This work showed that a reactor power detector's response is a function of location and detectors at different locations respond differently to the same event due to control rod shadowing effects.

However, another phenomenon was noticed in the course of this work where the reactivity worth of the same control rod was calculated to be different depending on the rod heights relative to one another. This was discovered when an attempt was made to validate the total integral control rod worths by comparing the k_{eff} of the OSTR core with one rod fully ejected and the other three fully inserted to the k_{eff} of the core with all control rods fully inserted. It was found that the total worth of the rods summed separately using this method disagreed significantly despite the MCNP® calculated control rod worths being in good agreement with the measured control rod worths using the control rod configurations in the calibration process. Tables 4-13 and 4-15 below show that fully ejecting one rod in a non-banked configuration resulted in a calculated total core worth of $\$14.12 \pm 0.13$ for the normal core and $\$13.49 \pm 0.13$ for the CLICIT core. Whereas fully ejecting one rod from a banked configuration resulted in a calculated $\$11.56 \pm 0.06$ for the normal core and 10.71 ± 0.20 for the CLICIT core.. Another configuration was modeled where the k_{eff} of the OSTR core with three of the rods 55% withdrawn and one fully ejected was compared to the k_{eff} of the core with three rods 55% and the other fully inserted. The results are shown below in Tables 4-14 and 4-16. This process produced different results than the

other two with total core reactivity worths of $\$10.68 \pm 0.16$ for the normal core and $\$10.51 \pm 0.16$ for the CLICIT core.

4.6.1 Normal Core Comparisons

Table 4-13: Non-banked normal core calculated control rod reactivity results using the one-rod-out method.

<i>Configuration</i>	k_{eff}	σ_{keff}	Reactivity [ρ]	Reactivity [\$]	Std. Error [±\$]
<i>All rods in</i>	0.6523	0.00027	-	-	-
<i>All rods out</i>	1.05169	0.00029	0.0896	11.96	±0.06
<i>Transient out</i>	0.99013	0.00032	0.0258	3.46	±0.07
<i>Safety out</i>	0.98851	0.00035	0.0241	3.23	±0.07
<i>Shim out</i>	0.98949	0.00030	0.0251	3.37	±0.06
<i>Regulating out</i>	0.99449	0.00032	0.0303	4.06	±0.07
<i>Sum of rods separately</i>	-	-	0.1054	14.12	±0.13

Table 4-14: Banked normal core calculated control rod reactivity results using the one-rod-out method.

<i>Configuration</i>	k_{eff}	σ_{keff}	Reactivity [ρ]	Reactivity [\$]	Std. Error [$\pm \$$]
<i>Transient rod in</i>	1.00648	0.00039	-	-	-
<i>Transient rod out</i>	1.02741	0.00034	0.0208	2.71	± 0.09
<i>Safety rod in</i>	1.00864	0.00030	-	-	-
<i>Safety rod out</i>	1.02672	0.00032	0.0179	2.32	± 0.07
<i>Shim rod in</i>	1.00811	0.00032	-	-	-
<i>Shim rod out</i>	1.02645	0.00029	0.0182	2.36	± 0.07
<i>Regulating rod in</i>	1.00320	0.00035	-	-	-
<i>Regulating rod out</i>	1.02845	0.00033	0.0252	3.29	± 0.08
<i>Sum of rods separately</i>	-	-	0.0821	10.68	± 0.15

4.6.2 CLICIT Core Comparisons

Table 4-15: Non-banked CLICIT core calculated control rod reactivity results using the one-rod-out method.

<i>Configuration</i>	k_{eff}	σ_{keff}	Reactivity [ρ]	Reactivity [\$]	Std. Error [$\pm \$$]
<i>All rods in</i>	0.95322	0.00031	-	-	-
<i>All rods out</i>	1.03664	0.00032	0.0875	11.60	± 0.07
<i>Transient out</i>	0.97691	0.00031	0.0249	3.25	± 0.07
<i>Safety out</i>	0.97523	0.00033	0.0231	3.01	± 0.07
<i>Shim out</i>	0.97868	0.00035	0.0267	3.50	± 0.07
<i>Regulating out</i>	0.98036	0.00028	0.0285	3.73	± 0.06
<i>Sum of rods separately</i>	-	-	0.1031	13.49	± 0.13

Table 4-16: Banked CLICIT core calculated control rod reactivity results using the one-rod-out method.

<i>Configuration</i>	k_{eff}	$\sigma_{k\text{eff}}$	Reactivity [ρ]	Reactivity [\\$]	Std. Error [$\pm \$$]
<i>Transient rod in</i>	0.99335	0.00034	-	-	-
<i>Transient rod out</i>	1.01340	0.00037	0.0202	2.63	± 0.09
<i>Safety rod in</i>	0.99507	0.00033	-	-	-
<i>Safety rod out</i>	1.01225	0.00030	0.0173	2.24	± 0.07
<i>Shim rod in</i>	0.99240	0.00030	-	-	-
<i>Shim rod out</i>	1.01332	0.00031	0.0211	2.75	± 0.07
<i>Regulating rod in</i>	0.99164	0.00035	-	-	-
<i>Regulating rod out</i>	1.01370	0.00031	0.0222	2.90	± 0.08
<i>Sum of rods separately</i>	-	-	0.0808	10.51	± 0.16

4.6.3 Subcritical Experimental Validation

These results motivated a need for experimental validation to determine if this phenomenon was a modeling error or real core geometrical effects influencing the reactivity worth of a control rod. A subcritical experiment was devised and carried out at OSTR on the morning of May 2nd, 2022, where the total integrated reactivity worth of each control rod was measured by fully ejecting one rod while the other three remained fully inserted to replicate the non-banked model process for the CLICIT core in Table 4.15. The reactivity worth of a control rod can be measured by comparing the subcritical count rate on the fission chamber detector using:

$$CR_1(1 - k_1) = CR_2(1 - k_2) \quad (4.2)$$

Where the unknown k_1 can be calculated if the shutdown margin is known using:

$$SDM = \frac{1}{k} - 1 \quad (4.3)$$

Substituting Equation 4.3 into 4.2 yields:

$$k_2 = -\left[\frac{CR_1 \left(1 - \frac{1}{SDM + 1} \right)}{CR_2} - 1 \right] \quad (4.4)$$

Where count rates were measured with all rods inserted (CR_1) and with one rod fully ejected (CR_2). Count rates were randomly sampled over a one-minute period and averaged. The core excess and shutdown margin on 05/02/2022 were \$3.97 and \$6.62, respectively. From Equation 4.3, k_1 was calculated to be 0.9527 for the “all rods inserted” configuration. The results of the experiment are presented below in Table 4-17.

Table 4-17: Non-banked CLICIT core one-rod-out method experimental validation.

Configuration	Avg. CR_2 [CPS]	k_2	Reactivity [%k/k]	Reactivity [\$]
All rods in	14.3	-	-	-
Transient rod out	29.4	0.9770	0.0243	3.25
Safety rod out	28.0	0.9759	0.0232	3.10
Shim rod out	34.2	0.9803	0.0276	3.68
Regulating rod out	39.1	0.9828	0.0301	4.01
<i>Sum of rods separately</i>	-	-	0.1053	14.03

The experiment was not carried out for the normal core configuration as it is no longer used operationally at OSTR. The experimental results for the measurement of control rod reactivity using the one-rod-out method for the CLICIT core agree with the calculated results with a measured total core worth of \$14.03 and calculated core worth of $\$13.49 \pm 0.13$. These results suggest that the differences observed in the MCNP® calculations of the control rod worths using the rod-pull method and the one-rod-out are not a model error but a real phenomenon where the reactivity worth of a control rod is partially a function of control rod heights relative to one another. This would suggest that, in addition to control rod shadowing effects causing model and measurement discrepancies, the measured worth of a control rod in OSTR varies depending on the control rod heights during the control rod calibration process, and the real variation in measured reactivity worth due to geometry variation is far greater than any model/measurement discrepancy caused by control rod shadowing.

5.0 Conclusion

This work presented a time-independent Monte Carlo method for the detection of control rod shadowing effects in the Oregon State TRIGA® Reactor (OSTR). Differences in measured and calculated control rod reactivity worths during the first post-LEU conversion control rod calibrations of October 2008 were believed to be due to the shadowing the fission chamber power detector. The OSTR MCNP® model was validated against the critical control rod configurations during the control rod calibrations of 2008 and the model reactivity bias was calculated to be very low at $\$-0.02 \pm 0.04$ for the normal core configuration and $\$0.07 \pm 0.04$ for the CLICIT core configuration.

Nine identical fission chambers were added to the OSTR model with one of the detectors placed at the actual detector location 348.2° of north at the reflector periphery. A *kcode* problem was run in MCNP® 6.2 to compare detector responses to that of the detector located at 348.2° . A particle-splitting variance reduction technique was employed to reduce the relative error associated with the fission rate tally in each detector. It was found that detector response was a function of location and different detectors respond differently to the same control rod manipulation at the moment of supercriticality in the rod-pull method for control rod calibration. This may result in a skewing of the time term in the Inhour equation and be the source of the differences in the measured and calculated control rod reactivity worths observed in October 2008.

The control rod shadowing/anti-shadowing effect was believed to be an asymmetrical flux distribution in OSTR that would result in severe flux profile depression or peaking near the detector during the control rod calibration procedure. Thermal flux tallies were taken at core axial mid plane in the OSTR model for each control rod pull. It was observed that the flux and power distribution in the OSTR core is highly asymmetrical at extreme control rod configurations and can shift significantly as configurations change during the control rod calibration process. A time-dependent method would need to be developed to quantify the control rod shadowing effect. Such a method would enable the study the changes in flux and power asymmetries during supercriticality to quantify the detector response during the power rise in the rod-pull method and the effect this has on the time term in the Inhour equation.

It was also found though both the model and a subcritical experiment that the reactivity worth of a control rod is a function of geometry or the heights of the control rods relative to each other and a control rod manipulation is not an equal reactivity insertion for all configurations. This effect can be significant with a measured total core reactivity worth of \$14.03 and calculated core worth of \$13.49 ±0.13 for the CLICIT core using the one-rod-out method and a measured total core reactivity worth of \$10.75 and calculated core worth of \$10.71 ±0.20 using the rod-pull method.

Control rod shadowing effects are observed in the OSTR using the time-independent method presented in this work. However, these effects have negligible impact on measured reactivity worth compared to the effects control rod geometry has. This implies that the measured reactivity worths of the control rods at OSTR is highly variable and dependent on the configuration of the rods during the control rod calibration process. This variability is not error, but rather the actual worth of the rod at a specific configuration. This phenomenon may be of particular importance for pulsing experiments where the limiting conditions of operation for OSTR specify a reactivity insertion limit taken from the measured control rod worths at a particular banked configuration that may not be representative of the configuration a pulse is initiated from. A time-dependent model would enable the study of such effects.

6.0 Future Work

The control rod shadowing effects and core-wide power level departure from 1 MW for extreme control rod configurations as discussed in section 4.6 could be studied using the time-independent method presented in this work because the reactor is assumed to be at steady-state at 1 MW. This was

found to be beyond the scope of this work, but this process would be relatively straight-forward with the addition of the two uncompensated ion chambers to the OSTR MCNP® model and power-per element tallies in the fuel and control rods. Such work may be a viable capstone project for an undergraduate-level research project.

The aim of this work was to qualitatively show the control rod shadowing effect on particular detector locations. To properly quantify the control rod shadowing effect, and the resulting skewing of the time of power rise (Δt) as seen by a detector at a particular location, would require a time-dependent method as the quantification of the changes core power and flux asymmetries over some time span would be required. This information would be needed to model the detector response over the entire power rise.

7.0 References

- [1] "Safety Analysis Report for the Conversion of the Oregon State TRIGA® Reactor from HEU to LEU Fuel." Oregon State University, 2008.
- [2] "OSTR Logbook #150." Oct. 14, 2008.
- [3] S. T. Keller, "Oregon State University TRIGA Reactor Post Conversion Reactor Startup Report," p. 80.
- [4] R. Schickler, "OSTROP 9: Control Rod Calibration Procedures." 2019.
- [5] K. Tiypun, "Epithermal neutron beam design at the Oregon State University TRIGA Mark II reactor (OSTR) based on Monte Carlo methods," Mar. 1997, Accessed: Sep. 15, 2021. [Online]. Available: https://ir.library.oregonstate.edu/concern/graduate_thesis_or_dissertations/1g05fg170?locale=de
- [6] A. K. Kitto, "Determination of a calculation bias in the MCNP model of the OSTR," Dec. 2012, Accessed: Aug. 30, 2021. [Online]. Available: https://ir.library.oregonstate.edu/concern/graduate_thesis_or_dissertations/rr172174p?locale=en
- [7] "History, Development and Future of TRIGA Research Reactors," Jul. 20, 2016. <https://www.iaea.org/publications/10943/history-development-and-future-of-triga-research-reactors> (accessed Nov. 02, 2021).
- [8] G. D. C. G. A. Division, "Technical Foundations of TRIGA," *UNT Digital Library*, Aug. 27, 1958. <https://digital.library.unt.edu/ark:/67531/metadc304052/> (accessed Nov. 02, 2021).
- [9] "TRIGA Nuclear Reactors," *General Atomics*. <https://www.ga.com/triga/> (accessed Nov. 02, 2021).
- [10] R. S. Stone, H. P. S. Jr, R. H. Stahl, and G. West, "Transient Behavior of TRIGA, a Zirconium-Hydride, Water-Moderated Reactor," *Nuclear Science and Engineering*, May 2017, doi: 10.13182/NSE59-A28840.
- [11] "NUREG-1282, 'Safety Evaluation Report on High-Uranium Content, Low-Enriched Uranium-Zirconium Hydride Fuels for TRIGA Reactors,'" p. 14.
- [12] M. R. Hartman *et al.*, "Neutronic Analysis of the Oregon State TRIGA Reactor in Support of Conversion from HEU Fuel to LEU Fuel," *Nuclear Science and Engineering*, vol. 174, no. 2, pp. 135–149, Jun. 2013, doi: 10.13182/NSE12-5.
- [13] W. R. Marcum, B. G. Woods, M. R. Hartman, S. R. Reese, T. S. Palmer, and S. T. Keller, "Steady-State Thermal-Hydraulic Analysis of the Oregon State University TRIGA Reactor Using RELAP5-3D," *Nuclear Science and Engineering*, Apr. 2017, doi: 10.13182/NSE08-63.
- [14] M. Ravnik, "Description of TRIGA Reactor," p. 14.

- [15] "Burnable Poison-Doped Fuel," pp. 106–124, Jan. 2020, doi: 10.1016/B978-0-12-803581-8.11699-6.
- [16] M. R. Hartman *et al.*, "Neutronic Analysis of the Oregon State TRIGA Reactor in Support of Conversion from HEU Fuel to LEU Fuel," *Nuclear Science and Engineering*, May 2017, doi: 10.13182/NSE12-5.
- [17] "Civilian HEU: Past and Current Reduction Efforts," *James Martin Center for Nonproliferation Studies*, Dec. 20, 2017. <https://nonproliferation.org/past-and-current-civilian-heu-reduction-efforts/> (accessed Nov. 12, 2021).
- [18] H. BÖCK, M. VILLA, and R. BERGMANN, "Five Decades of TRIGA Reactors," in *25th Int. Conf. Nucl. Energy New Eur.*, 2016, pp. 1–8.
- [19] C. Oney, "NSE 455/555 Lecture 2: OSTR Facility Overview."
- [20] "OSTR Core and Reflector Drawings." General Atomics, Jan. 08, 2014.
- [21] R. W. Dayton, *The Effectiveness of Control-rod Materials*. Battelle Memorial Institute, 1957.
- [22] H. W. Keller, J. M. Shallenberger, D. A. Hollein, and A. C. Hott, "Development of Hafnium and Comparison with Other Pressurized Water Reactor Control Rod Materials," *Nuclear Technology*, May 2017, doi: 10.13182/NT82-A33005.
- [23] E. M. Baum, Knolls Atomic Power Laboratory, and Bechtel Marine Propulsion Corporation, *Nuclides and isotopes: chart of the nuclides*. Schenectady, N.Y.: KAPL : Bechtel, 2010.
- [24] F. J. Jankowski, "Calibration of Control Rods," *Nuclear Science and Engineering*, vol. 2, no. 3, pp. 288–302, 1957.
- [25] H. R. Fike, *Control Rod Calibrations in the Standard Pile*. E.I. du Pont de Nemours & Company, Explosives Department, Atomic Energy Division, Technical Division, Savannah River Laboratory, 1959.
- [26] W. Rothenstein, "CALIBRATION OF CONTROL RODS USING THE ROD DROP METHOD," Israel. Atomic Energy Commission. Soreq Research Establishment, Rehovoth, IA-820, Jun. 1963. Accessed: Dec. 06, 2021. [Online]. Available: <https://www.osti.gov/biblio/4694562>
- [27] J. J. Duderstadt and L. J. Hamilton, *Nuclear reactor analysis*. New York: Wiley, 1976.
- [28] W. D. Loveland, D. J. Morrissey, and G. T. Seaborg, *Modern nuclear chemistry*, Second edition. Hoboken, NJ, USA: Wiley, 2017.
- [29] G. F. Knoll, *Radiation Detection and Measurement*. John Wiley & Sons, 2010.
- [30] N. Tsoulfanidis and S. Landsberger, *Measurement & detection of radiation*, 4th edition. Boca Raton: CRC Press, Taylor & Francis Group, 2015.

- [31] J. K. Shultz and R. E. Faw, *Fundamentals of nuclear science and engineering*, 2nd ed. Boca Raton: CRC Press, 2008.
- [32] H. S. McCreary and R. T. Bayard, "A Neutron-Sensitive Ionization Chamber with Electrically Adjusted Gamma Compensation," *Review of Scientific Instruments*, vol. 25, no. 2, pp. 161–164, Feb. 1954, doi: 10.1063/1.1771011.
- [33] "Model WL-8075 Uncompensated Ion Chamber Data Sheet." Mirion Technologies, Jul. 28, 2011.
- [34] H. L. Anderson, E. T. Booth, J. R. Dunning, E. Fermi, G. N. Glasoe, and F. G. Slack, "The Fission of Uranium," *Phys. Rev.*, vol. 55, no. 5, pp. 511–512, Mar. 1939, doi: 10.1103/PhysRev.55.511.2.
- [35] "Model SA-C3-2510-114 Fission Chamber Sales Specifications." GE Reuter-Stokes, May 21, 1982.
- [36] "Neutron Fission Counters and Chambers | Baker Hughes Digital Solutions." <https://www.bakerhughes.com/reuter-stokes/radiation-measurement-monitoring/neutron-fission-counters-and-chambers> (accessed Dec. 06, 2021).
- [37] "Control rod shadowing effect in PWR core utilizing Urania-Gadolinia fuel," *Progress in Nuclear Energy*, vol. 142, p. 103993, Dec. 2021, doi: 10.1016/j.pnucene.2021.103993.
- [38] G. Girardin, "7329 - Control Rod Shadowing and Anti-shadowing Effects in a Large Gas-cooled Fast Reactor," p. 8, 2007.
- [39] M. ITAGAKI, Y. MIYOSHI, K. GAKUHARI, N. OKADA, and T. SAKAI, "Control-Rod Interference Effects Observed during Reactor Physics Experiments with Nuclear Ship 'MUTSU,'" *Journal of Nuclear Science and Technology*, Mar. 2012, Accessed: Dec. 07, 2021. [Online]. Available: <https://www.tandfonline.com/doi/abs/10.1080/18811248.1993.9734503>
- [40] A. W. LaPorta, "Transient Reactor Test (TREAT) Facility Initial Approach to Restart Criticality Following Extended Standby Operation," *Nuclear Technology*, Feb. 2019, Accessed: Dec. 07, 2021. [Online]. Available: <https://www.tandfonline.com/doi/abs/10.1080/00295450.2019.1565471>
- [41] E. E. Lewis and W. F. Miller, *Computational methods of neutron transport*. New York: Wiley, 1984.
- [42] X-5 Monte Carlo Team, "MCNP - A General Monte Carlo N-Particle Transport Code, Version 5, Volume I: Overview and Theory." Feb. 01, 2008. [Online]. Available: https://mcnp.lanl.gov/pdf_files/la-ur-03-1987.pdf
- [43] J. R. Davis, Ed., *Alloying: understanding the basics*. Materials Park, OH: ASM International, 2001.
- [44] "CRC Handbook of Chemistry and Physics," *Routledge & CRC Press*. <https://www.routledge.com/CRC-Handbook-of-Chemistry-and-Physics/Rumble/p/book/9780367712600> (accessed Feb. 07, 2022).
- [45] "OSTR Reactor Logbook #150." 01/.

- [46] H. Kim and Y. Kim, "Pin-by-Pin Coupled Transient Monte Carlo Analysis Using the iMC Code," *Front. Energy Res.*, vol. 10, p. 853222, Mar. 2022, doi: 10.3389/fenrg.2022.853222.
- [47] M. G. Mazaher, A. A. Salehi, and N. Vosoughi, "A time dependent Monte Carlo approach for nuclear reactor analysis in a 3-D arbitrary geometry," *Progress in Nuclear Energy*, vol. 115, pp. 80–90, Aug. 2019, doi: 10.1016/j.pnucene.2019.03.024.
- [48] S. C. Shaner, "Development of High Fidelity Methods for 3D Monte Carlo Transient Analysis of Nuclear Reactors," p. 140.